DOCTORAL THESIS

ANDRIA AROTI

Study of the effect of Hofmeister anions on monolayer, bilayer and micelle lipid model systems through experiments and theory

Research advisor

Associate Professor Epameinondas Leontidis

UNIVERSITY OF CYPRUS

DEPARTMENT OF CHEMISTRY

OCTOBER 2005

ΔΙΔΑΚΤΟΡΙΚΗ ΔΙΑΤΡΙΒΗ

ΑΝΤΡΙΑ ΑΡΟΤΗ

Μελέτη της επίδρασης των ανιόντων της σειράς Hofmeister σε λιπιδικά μοντέλα μονοστοιβάδων, διπλοστοιβάδων και μικυλίων μέσω πειραμάτων και θεωρίας

Υπεύθυνος Έρευνας

Αναπληρωτής Καθηγητής Επαμεινώνδας Λεοντίδης

ΠΑΝΕΠΙΣΤΗΜΙΟ ΚΥΠΡΟΥ

ΤΜΗΜΑ ΧΗΜΕΙΑΣ

ΟΚΤΩΒΡΙΟΣ 2005

DOCTORAL THESIS

ANDRIA AROTI

EXAMINATION COMMITTEE

Prof. Dr. Werner Kunz

University of Regensburg - Germany

Dr. Aris Xenakis

National Hellenic Research Foundation – Greece

Associate Professor Epameinondas Leontidis

University of Cyprus – Cyprus

Associate Professor Costas Patrickios

University of Cyprus – Cyprus

Assistant Professor Ioannis Paschalides

University of Cyprus – Cyprus

ABSTRACT

In this thesis, we attempt to understand the mechanisms behind specific anion effects by studying the effects of sodium salts (NaX) of different monovalent anions belonging to the Hofmeister series on three model systems: (a) Langmuir monolayers of phospholipids at the air-water interface, (b) bilayers of phospholipids dispersed in excess water, and (c) micelles of phospholipid compounds. The double-chain zwitterionic lipid 1,2-Dipalmitoyl-sn-Glycero-3-Phosphocholine (DPPC) was used to form monolayers and bilayers, and the single-chain lipid Dodecylphosphocholine (DPC) was used to form micellar solutions. The salts used were NaCl, NaBr, $NaNO_3$, NaI, $NaBF_4$, $NaClO_4$ and NaSCN.

The phase behavior and the morphology and structure of DPPC Langmuir monolayers in the presence of electrolytes in the subphase were studied by surface pressure – area isotherms, Brewster Angle Microscopy (BAM), Grazing Incidence X-ray Diffraction (GIXD) and Infrared Reflection-Absorption Spectroscopy (IRRAS). The presence of salts was found to increase the surface pressure at a fixed area per molecule at the low-pressure part of the isotherm, indicating a stabilization of the liquid-expanded phase of the monolayer. This increase depends on the type of the anion and the electrolyte concentration. X-Ray diffraction and infrared spectroscopy experiments show that moderate concentrations of large polarizable anions, such as I^-, do not significantly change the conformation and packing properties of the hydrocarbon chains while smaller, less polarizable anions such as Br^- do not alter the packing properties at all. The lattice parameters and the ordering of the lipid molecules in the liquid-condensed phase remain essentially unaffected even at quite high electrolyte concentrations, suggesting that anions partition into or bind to the looser liquid-expanded phase, but do not penetrate into or bind to the domains of the liquid-condensed phase.

The effect of the NaX salt solutions on the L_α Phase of DPPC bilayers was investigated using Small-Angle X-Ray Scattering (SAXS) and the Osmotic Stress (OS) technique. The plots of the applied osmotic pressure, Π, versus the interbilayer separation, d_w, ($\log\Pi$ vs. d_w) were compared for different Hofmeister anions and different salt concentrations. It was observed that for the same osmotic pressure the water bilayer separation increases in the presence of salts, depending on the type of the anion and the concentration of the electrolyte used. The effect of the different anions on the bilayer structural parameters follows the Hofmeister series with SCN^- inducing the most pronounced changes. In addition, the maximum swelling

separation of DPPC bilayers increases in the presence of electrolytes in a manner following the Hofmeister series.

The micellar properties of the surfactant DPC in the presence of different Hofmeister anions were studied using Dynamic Light Scattering (DLS). The critical micelle concentration (cmc), the hydrodynamic radius, the aggregation number and the surface headgroup area of the DPC micelles are all affected by the type and concentration of anion used. The effect of the anions is in the order of the Hofmeister series.

In order to obtain "binding constants" of anions on the lipid models examined in this thesis, fitting of the experimental results was carried out with appropriate theoretical models. The fitting results indicate that the monolayer experimental data cannot be explained with models based on chemical binding of the anions on the headgroups of the lipid molecules. For both the bilayer and micellar geometries the computed binding constants (using a binding model) depend on the type of the anions but also on the concentration of the salt solutions. The binding constants increase with electrolyte concentration and follow the Hofmeister series of anions. In addition, the binding constants obtained for each anion, using the two geometries, do not agree; those calculated for micelles were found to be greater by a factor of 50-100 than those computed for the bilayer geometry.

The monolayer results can be fitted quite well with an ion-partitioning model, which assumes that anions can penetrate a surface lipid layer. However, the computed partitioning constants U_{-} of anions cannot be correlated with individual physicochemical properties of anions indicating that the Hofmeister effect may depend on their combination. The same partitioning model when applied to lipid bilayers does not perform well providing results comparable to those of the binding model.

ΠΕΡΙΛΗΨΗ

Σε αυτή την διατριβή επιχειρούμε να κατανοήσουμε τους μηχανισμούς των ειδικών επιδράσεων απλών ανιόντων σε φυσικοχημικά και βιολογικά συστήματα. Για τον σκοπό αυτό μελετούμε τις επιδράσεις διαφόρων αλάτων του νατρίου με μονοσθενή ανιόντα (NaX) που ανήκουν στη σειρά Hofmeister χρησιμοποιώντας τρία πρότυπα συστήματα: (α) Μονοστοιβάδες φωσφολιπιδίων στην διεπιφάνεια νερού-αέρα. (β) Διπλοστοιβάδες φωσφολιπιδίων διεσπαρμένες σε περίσσεια νερού. (γ) Μικκύλια φωσφολιπιδίων. Για τον σχηματισμό των μονοστοιβάδων και των διπλοστοιβάδων χρησιμοποιήθηκε το διπολικό (zwitterionic) φωσφολιπίδιο 1,2-Dipalmitoyl-sn-Glycero-3-Phosphocholine (DPPC) με δύο αλειφατικές αλυσίδες, ενώ για τον σχηματισμό μικκυλίων χρησιμοποιήθηκε το συγγενές λιπίδιο Dodecylphosphocholine (DPC) με μια αλειφατική αλυσίδα. Τα άλατα που χρησιμοποιήθηκαν στην μελέτη αυτή είναι: NaCl, NaBr, $NaNO_3$, NaI, $NaBF_4$, $NaClO_4$ και NaSCN.

Η φασική συμπεριφορά και η δομή των μονοστοιβάδων του DPPC στην διεπιφάνεια νερού-αέρα στην παρουσία ηλεκτρολυτών στο υδατικό υπόστρωμα μελετήθηκαν με ισόθερμες επιφανειακής πίεσης ως προς την επιφάνεια ανά μόριο, με μικροσκοπία γωνίας Brewster (BAM), με περίθλαση ακτινών Χ υπό μικρή γωνία (GIXD) και με υπέρυθρη φασματοσκοπία ανάκλασης-απορρόφησης (IRRAS). Στην παρουσία αλάτων σημειώθηκε σημαντική αύξηση της επιφανειακής πίεσης σε σταθερή επιφάνεια ανά μόριο, υποδεικνύοντας έτσι σταθεροποίηση της υγρής-εκτεταμένης φάσης της μονοστοιβάδας. Αυτή η αύξηση εξαρτάται από το είδος του ανιόντος και την συγκέντρωση του ηλεκτρολύτη. Η περίθλαση ακτινών Χ και η υπέρυθρη φασματοσκοπία έδειξαν ότι συγκεντρώσεις μέχρι 0.5 Μ των ανιόντων με μεγάλη πολωσιμότητα, όπως το I^-, δεν επηρεάζουν σημαντικά τη μέση διαμόρφωση και την διευθέτηση των υδρογονανθρακικών αλυσίδων του λιπιδίου DPPC, ενώ τα μικρότερα ανιόντα με μικρότερες πολωσιμότητες, όπως το Br^-, δεν αλλάζουν *καθόλου* τη δομή της μονοστοιβάδας και τη μέση διαμόρφωση των λιπιδίων. Οι παράμετροι πλέγματος και η διάταξη των λιπιδικών μορίων στην υγρή-συμπυκνωμένη φάση παραμένουν ουσιαστικά ανεπηρέαστες ακόμη και σε αρκετά υψηλές συγκεντρώσεις ηλεκτρολυτών. Αυτό υποδεικνύει ότι τα ανιόντα διαχέονται ή δεσμεύονται στην λιγότερο πυκνή υγρή-εκτεταμένη φάση, αλλά δεν διαπερνούν ή δεν δεσμεύονται στην περιοχή της υγρής-συμπυκνωμένης φάσης.

Η επίδραση των αλάτων νατρίου (NaX) στην υγρή φυλλώδη φάση L_α των διπλοστοιβάδων DPPC μελετήθηκε με σκέδαση ακτινών Χ υπό μικρή γωνία (SAXS) σε συνδυασμό με

επιβολή ωσμωτικής πίεσης (OS). Τα διαγράμματα της εφαρμοζόμενης ωσμωτικής πίεσης, Π, στις διπλοστοιβάδες του DPPC ως προς την απόσταση διαδοχικών διπλοστοιβάδων, d_w, (logΠ - d_w) συγκρίθηκαν στην παρουσία διαφορετικών ανιόντων Hofmeister και διαφορετικών συγκεντρώσεων αλάτων. Διαπιστώθηκε ότι σε σταθερή ωσμωτική πίεση η απόσταση των διπλοστοιβάδων αυξάνει στην παρουσία αλάτων και η αύξηση αυτή εξαρτάται από το είδος του ανιόντος και τη συγκέντρωση του άλατος, με το ανιόν SCN^- να εμφανίζει τη μεγαλύτερη επίδραση. Επιπλέον, η απόσταση των διπλοστοιβάδων του DPPC σε συνθήκες μέγιστης διόγκωσης (maximum swelling) αυξάνεται παρουσία των ηλεκτρολυτών, ακολουθώντας και πάλι τη σειρά ανιόντων Hofmeister.

Οι ιδιότητες των μικκυλίων του επιφανειοενεργού DPC στην παρουσία των διαφόρων ανιόντων Hofmeister μελετήθηκαν χρησιμοποιώντας δυναμική σκέδαση φωτός (DLS). Η κρίσιμη συγκέντρωση μικκυλιοποίησης (cmc), η υδροδυναμική ακτίνα, ο αριθμός συσσωμάτωσης και η επιφάνεια της κεφαλής των μορίων DPC επηρεάζονται από το είδος και τη συγκέντρωση του ανιόντος. Η επίδραση των ανιόντων ακολουθεί τη σειρά Hofmeister.

Για τον υπολογισμό σταθερών πρόσδεσης των ανιόντων στις διάφορες λιπιδικές γεωμετρίες πραγματοποιείται θεωρητική προσαρμογή (fitting) στα πειραματικά αποτελέσματα με κατάλληλα θεωρητικά πρότυπα. Τα αποτελέσματα δείχνουν ότι μοντέλα, τα οποία βασίζονται στη χημική προσρόφηση των ανιόντων στις κεφαλές των λιπιδικών μορίων, δεν μπορούν να εξηγήσουν τα πειραματικά αποτελέσματα των μονοστοιβάδων. Τόσο για τις διπλοστοιβάδες όσο και για τα μικκύλια, οι υπολογιζόμενες «χημικές» σταθερές πρόσδεσης εξαρτώνται από το είδος του ανιόντος αλλά και από τη συγκέντρωση των αλάτων. Οι σταθερές πρόσδεσης αυξάνονται με τη συγκέντρωση και ακολουθούν τη σειρά ανιόντων Hofmeister. Επιπλέον, οι «χημικές» σταθερές που λαμβάνονται για κάθε ανιόν, από τις δύο γεωμετρίες, δεν συμφωνούν. Οι σταθερές που υπολογίστηκαν για τα μικκύλια βρέθηκαν να είναι 50-100 φορές μεγαλύτερες από αυτές που υπολογίστηκαν για τη γεωμετρία των διπλοστοιβάδων. Τα πειραματικά αποτελέσματα των μονοστοιβάδων μπορούν να εξηγηθούν πολύ ικανοποιητικά με χρήση ενός εναλλακτικού θεωρητικού μοντέλου που βασίζεται στην κατανομή των ανιόντων μεταξύ του διαλύματος και μιας επιφανειακής λιπιδικής στοιβάδας πάχους λίγων Å, μέσω του οποίου σταθερές κατανομής των ανιόντων μεταξύ των δύο φάσεων μπορούν να υπολογισθούν. Τα αποτελέσματα δείχνουν ότι οι σταθερές κατανομής των ανιόντων δεν συσχετίζονται με τις επιμέρους φυσικοχημικές ιδιότητες των ανιόντων υποδεικνύοντας ότι η επίδραση των ανιόντων Hofmeister μπορεί να εξαρτάται από το συνδυασμό των ιοντικών ιδιοτήτων.

Το ίδιο μοντέλο κατανομής δεν συμπεριφέρεται τόσο ικανοποιητικά όταν εφαρμόζεται στις διπλοστοιβάδες λιπιδίων, παρέχοντας αποτελέσματα συγκρίσιμα με το μοντέλο χημικής προσρόφησης.

ACKNOWLEDGMENTS

Enough time has already passed from the moment I sat in front of my computer in order to write the last and perhaps the most difficult part of my doctoral thesis. My mind is flooded with memories, of joy, distress, impatience, sorrow, tiredness but also satisfaction for all that I have achieved in the previous five years in my life. Now is the time, after five years full of unique experiences, to thank all those who helped in their own way for the completion of this doctoral thesis. This thesis would not have been possible without their help!

I would like to thank Associate Professor Dr. Epameinondas Leontidis, my thesis and academic advisor, for his guidance and all the insight, support, and encouragement he has given me during the course of my undergraduate and postgraduate studies. Mr Leontidis encouraged me to set the direction of my own research while with his guidance I learned to undertake initiatives in subjects that concerned my research but also in my own daily life. He also made sure that I learned all the non-laboratory aspects of scientific research, including writing articles and preparing presentations. Mr Leontidis clarity in both written and oral presentations will always be a goal to which I will aspire.

Grateful acknowledgements are made to Professor Thomas Zemb and Dr. Monique Dubois of Centre d'Energie Atomique (CEA), Saclay, France for inviting me and thus giving me the opportunity to work in their lab (Service de Chimie Moleculaire) and complete a large part of my doctoral thesis. Thomas provided useful advice and references, and his genuine excitement and interest in science made it enjoyable for me to work with him. Monique was something between a science advisor and a "mother" to me. She was always very helpful in problems that were presented both in and out of the laboratory, supportive and encouraging, and her generosity and kindness helped make life in France much easier. I wish to thank both of you for your help and friendship during my stay in France.

Special thanks to Dr Luc Belloni of Centre d'Energie Atomique (CEA), Saclay, who has been very helpful with his knowledge and introduced me to the theoretical part of my thesis, the Poisson-Boltzmann equation and its applications.

I would also like to thank Professor Gerald Brezesinski of Max Plank Institute, Potsdam, Germany, and his group, with the help of whom the experiments of Grazing X-ray Diffraction, Brewster angle microscopy and Infrared Reflection Absorption Spectroscopy have been carried out successfully.

Also, I would like to thank Dr Miles Page who was a postgraduate student in France at the time I was there; With Miles we had a great time both in the lab but also in our everyday life. He is an excellent friend. He is a good listener and he always finds a funny way to avoid the different difficulties. Thanks for your friendship and for making the lab such a nice place to work.

Grateful acknowledgments are made to Dr Sylvain Desert of Centre d'Energie Atomique (CEA), Saclay. Besides his help in the lab, he carried out Light Scattering experiments for me and helped me measure refractive indexes, he has been very supportive and he helped me overcome various personal difficulties. Actually, I regard Sylvain as a brother. He and his wife will always be in my heart.

Special thanks to Dr Guillame Brotons of Centre d'Energie Atomique (CEA), Saclay who guided me during my very first steps in France and helped me to learn and use many experimental techniques about which I had little or no prior experience.

I would like also to acknowledge the continuous support and encouragement of my best friends. These are my fellow colleagues Rodoula Moleski, Rodoula Mallouri and Dr Dina Kleitou. They have been wonderful friends and they have provided a constant stream of moral support. Although we didn't spend a lot of time together, since I was in France, the last 1 ½ years we came closer and since then they encourage and support me in any difficulty that I have confronted. I will never forget the "group therapy" as Rodoula Mallouri used to call the time that I wanted to talk to someone and all of the team was gathered together to solve the problem. I will never forget the timetable that Rodoula Moleski used to make to help me whenever I was feeling under pressure. Dina helped me in her own way. She could always turn a bad moment to a funny moment!

Last, but certainly not least, I want to thank my family and my husband.

I am most indebted to my family, and especially to my parents, Telemachos Arotis and Praxoulla Aroti for their understanding and for their love. They encouraged me to pursue my interests, and were always there to offer help or advice. I can never repay the kindness and support they have given me during my life, and especially over the last five years.

Finally, I would like to thank my best friend in life, my husband Marinos Ioannides. The only reason that I was able to make it through this long process and overcome the difficult portions of my postgraduate years is the love and support which he provided me during this time. I thank you for supporting me during my studies, and for putting up with all of the flights, the phone calls, and the seemingly endless separations.

To them I dedicate this thesis with great love!

THANK YOU ALL!

ΕΥΧΑΡΙΣΤΙΕΣ

Έχει περάσει ήδη αρκετή ώρα από την στιγμή που κάθισα μπροστά από την οθόνη του υπολογιστή μου για να γράψω το τελευταίο και ίσως πιο δύσκολο κομμάτι της διδακτορικής μου διατριβής. Με έχουν κατακλύσει διάφορες αναμνήσεις, χαράς, αγωνίας, ανυπομονησίας, λύπης, κούρασης αλλά και ικανοποίησης για όλα όσα έχουν επιτευχθεί τα τελευταία 5 χρόνια στην ζωή μου. Ήρθε η ώρα μετά από 5 χρόνια γεμάτα από μοναδικές εμπειρίες να ευχαριστήσω όλους που βρέθηκαν στον δρόμο μου και βοήθησαν με το δικό τους τρόπο για την ολοκλήρωση αυτής της διδακτορικής διατριβής. Αυτή η διατριβή δεν θα ήταν δυνατή χωρίς την βοήθειά τους!

Θα επιθυμούσα να ευχαριστήσω τον επιβλέποντα σύμβουλό μου, Αναπληρωτή καθηγητή Δρ Επαμεινώνδα Λεοντίδη, για την καθοδήγηση, την υποστήριξη, και την ενθάρρυνση που μου έχει δώσει κατά τη διάρκεια των προπτυχιακών και των μεταπτυχιακών σπουδών μου. Ο κος Λεοντίδης με ενθάρρυνε να καθορίσω την κατεύθυνση της έρευνάς μου ενώ με την καθοδήγησή του έμαθα να αναλαμβάνω πρωτοβουλίες τόσο σε θέματα που αφορούσαν την ερευνά μου αλλά και σε θέματα της καθημερινής μου ζωής. Επίσης επιδίωξε να μάθω όλες τις μη-εργαστηριακές πτυχές της επιστημονικής έρευνας, συμπεριλαμβανομένου του γραψίματος των άρθρων και της προετοιμασίας των παρουσιάσεων. Η ευχέρεια του κου Λεοντίδη στις γραπτές και προφορικές παρουσιάσεις θα είναι πάντα ένας στόχος τον οποίο θα επιδιώκω.

Ιδιαίτερες ευχαριστίες στον καθηγητή Thomas Zemb και τη Δρ Monique Dubois του Κέντρου Ατομικής Ενέργειας (CEA), Saclay, Γαλλία για την πρόσκληση και την ευκαιρία που μου έδωσαν να εργαστώ στο εργαστήριό τους (Υπηρεσία Μοριακής Χημείας) ολοκληρώνοντας έτσι ένα μεγάλο μέρος της διδακτορικής διατριβής μου. Ο Thomas μου παρείχε χρήσιμες συμβουλές και αναφορές, και ο γνήσιος ενθουσιασμός και το ενδιαφέρον του για την επιστήμη γενικά κατέστησαν ευχάριστο το περιβάλλον να συνεργαστώ μαζί του. Η Monique ήταν κάτι μεταξύ ενός συμβούλου επιστήμης και μιας "μητέρας" για μένα. Ήταν πάντα πολύ βοηθητική στα προβλήματα που παρουσιάζονταν στο εργαστήριο και έξω από αυτό, γεμάτη συμπαράσταση και ενθάρρυνση, και η γενναιοδωρία και η ευγένειά της είχαν καταστήσει τη ζωή μου στη Γαλλία πολύ λιγότερο δύσκολη. Επιθυμώ να ευχαριστήσω και

τους δύο σας για τη βοήθεια και για τη φιλία σας κατά τη διάρκεια της παραμονής μου στη Γαλλία.

Ειδικές ευχαριστίες στο Δρ Luc Belloni του Κέντρου Ατομικής Ενέργειας (CEA), Saclay, Γαλλία, ο οποίος με τις γνώσεις του με εισήγαγε στο θεωρητικό μέρος της διατριβής μου ειδικά στην εξίσωση Poisson- Boltzmann και τις εφαρμογές της.

Θα επιθυμούσα επίσης να ευχαριστήσω τον καθηγητή Gerald Brezesinski του Ινστιτούτου Max Plank, Potsdam, Γερμανίας, και την ομάδα του, με τη βοήθεια των οποίων πραγματοποιήθηκαν με επιτυχία τα πειράματα Grazing X-ray Diffraction, Brewster angle microscopy και Infrared Reflection Absorption Spectroscopy.

Επίσης, θα επιθυμούσα να ευχαριστήσω τον Δρα Miles Page που ήταν μεταπτυχιακός σπουδαστής στη Γαλλία τη περίοδο που βρισκόμουν εκεί. Με τον Miles περάσαμε υπέροχα τόσο στο εργαστήριο όσο και στην καθημερινή μας ζωή. Είναι άριστος φίλος. Είναι καλός ακροατής και βρίσκει πάντα έναν αστείο τρόπο να αποφύγει τις διάφορες δυσκολίες. Σε ευχαριστώ για τη φιλία σου και για την ευχάριστη ατμόσφαιρα που δημιουργούσες στο εργαστήριο για να εργαστεί κάποιος.

Θερμές ευχαριστίες στο Δρ Sylvain Desert του Κέντρου Ατομικής Ενέργειας (CEA), Saclay, Γαλλία. Εκτός από τη βοήθειά του στο εργαστήριο, πραγματοποίησε πειράματα Σκέδασης φωτός για μένα και με βοήθησε με τις μετρήσεις δεικτών διάθλασης, ήταν πολύ ενθαρρυντικός και με βοήθησε να υπερνικήσω τις διάφορες προσωπικές δυσκολίες. Πραγματικά, αισθάνομαι τον Sylvain σαν αδελφό. Αυτός και η σύζυγός του θα είναι πάντα στην καρδιά μου.

Ειδικές ευχαριστίες στο Δρ Guillame Brotons του Κέντρου Ατομικής Ενέργειας (CEA), Saclay, Γαλλία που με καθοδήγησε στα πρώτα βήματά μου στη Γαλλία και με βοήθησε να χειρίζομαι πολλές πειραματικές τεχνικές που είχα ελάχιστη ή μη προγενέστερη εμπειρία.

Θα επιθυμούσα επίσης να αναγνωρίσω τη συνεχή υποστήριξη και την ενθάρρυνση των καλύτερων φίλων μου. Αυτές είναι η Ροδούλα Μολέσκη, η Ροδούλα Μαλλούρη και η Δρ Ντίνα Κλείτου. Είναι εκπληκτικές φίλες. Αν και δεν περάσαμε πολύ χρόνο μαζί, δεδομένου ότι ήμουν στη Γαλλία, τον τελευταίο 1 ½ χρόνο ήρθαμε πιο κοντά και από τότε με

ενθαρρύνουν και με υποστηρίζουν σε οποιαδήποτε δυσκολία που έχω αντιμετωπίσει. Δεν θα ξεχάσω ποτέ τις στιγμές "θεραπείας ομάδας" όπως καλεί η Ροδούλα Μαλλούρη το χρόνο που θέλησα να μιλήσω σε κάποιο και όλη η ομάδα μαζεύτηκε για να λύσει το πρόβλημα. Δεν θα ξεχάσω ποτέ το χρονοδιάγραμμα που έφτιαχνε η Ροδούλα Μολέσκη για να με βοηθήσει όποτε αισθανόμουν πίεση με τα μαθήματα. Η Ντίνα με βοήθησε με τον δικό της τρόπο. Μπορούσε πάντα να μετατρέπει μια κακή στιγμή σε μια αστεία στιγμή!

Τέλος, θέλω να ευχαριστήσω την οικογένειά μου και το σύζυγό μου.
Είμαι ευγνώμων στην οικογένειά μου, και ειδικά στους γονείς μου, τον πατέρα μου Τηλέμαχο Αρότη και τη μητέρα μου Πραξούλλα Αρότη για την κατανόηση τους και για την αγάπη τους. Με ενθάρρυναν να ακολουθήσω τα ενδιαφέροντά μου, και πάντα ήταν εκεί να προσφέρουν τη βοήθεια ή τις συμβουλές τους. Δεν θα μπορέσω ποτέ να ξεπληρώνω την αγάπη και υποστήριξη που μου έχουν προσφέρει κατά τη διάρκεια της ζωής μου, και ειδικά κατά τη διάρκεια των τελευταίων πέντε χρόνων.
Τέλος, θα επιθυμούσα να ευχαριστήσω τον καλύτερο μου φίλο στη ζωή, τον σύζυγό μου Μαρίνο Ιωαννίδη. Ο μόνος λόγος που μπόρεσα να αντεπεξέλθω αυτής της μακροχρόνιας διαδικασίας και να υπερνικήσω τις δύσκολες στιγμές των μεταπτυχιακών ετών είναι η αγάπη και η υποστήριξη που μου παρείχε ο Μαρίνος κατά τη διάρκεια αυτής της περιόδου. Σε ευχαριστώ για την υποστήριξη κατά τη διάρκεια των μελετών μου, και για την ανοχή όλων των ταξιδιών, των τηλεφωνημάτων, και των φαινομενικά ατελείωτων χωρισμών.
Αφιερώνω την διατριβή μου στους γονείς μου και στον σύζυγό μου με όλη μου την αγάπη!

ΣΑΣ ΕΥΧΑΡΙΣΤΩ ΟΛΟΥΣ!

SYMBOLS

A = Hamaker constant (kT or J), total surface area available to each DPPC molecule ($Å^2$), headgroup area of DPPC molecules ($Å^2$)

A_0 = excluded area per molecule ($Å^2$), chain cross-sectional area ($Å^2$)

A_{xy} = In-plane unit cell area ($Å^2$)

a = total film area ($Å^2$)

a_i = angle of incidence (◦)

a_c = critical angle for total external reflection (◦)

B = second virial coefficient

b_L = bilayer thickness (Å)

C = aqueous solute concentration (M)

c = concentration of monolayer spreading solution (M), lipid weight concentration

D = distance between two surfaces (m or Å), lamellar repeat spacing (Å), diffusion coefficient (cm^2/sec)

d = monolayer thickness (Å), inter-plane distance of lattice planes (Å)

d_w , d_f = aqueous bilayer separation (Å)

d_{head} = headgroup thickness (Å)

E = Electric field strength (Vm^{-1})

F = Force (N), Faraday constant F = 9.649 x 10^4 $Cmol^{-1}$.

F_m = free energy of micellization (kJ/mole)

K = association constant (M^{-1}), optical constant

k = Boltzmann's constant k = 1.380622 x 10^{-23} JK^{-1}, X-ray wavenumber k = $2\pi/\lambda$

L_β , $L_{\beta'}$ = gel lamellar phase

$L_{\beta I}$ = interdigitated lamellar phase

$P_{\beta'}$ = undulated ripple phase

L_α = liquid-crystalline lamellar phase

L_B = Bjerrum length

l_c = critical hydrocarbon chain length (m)

l_i = distance of each monolayer forming molecule from the nearest neighbours (Å)

M = micellar mass

MW = Molecular weight

N = aggregation number

N_{AV} = Avogadro's number, $N_{AV} = 6.022 \times 10^{23}$ mol^{-1}

n = refractive index of a media, number of segments in a polymer chain, integer number of wavelengths, viscosity of dispersing liquid (cP)

P_0 = hydration coefficient (Pa)

q = scattering vector (cm^{-1} or $Å^{-1}$), electron charge $q = 1.6021892 \times 10^{-19}$ C

R = molar gas constant R = 8.314 $JK^{-1}mol^{-1}$, average radius of a micelle

R_θ = Rayleigh ratio

R_h = hydrodynamic radius (nm)

R_g = radius of gyration (nm)

R_P = Pauling radius (Å), reflection coefficient of p-polarized light

R_s = reflection coefficient of s-polarized light

r_e = electron radius, $r_e = 2.82 \times 10^{-13}$ cm

T = temperature (K or °C)

T_m = main transition temperature or melting temperature (°C)

T_p = transmission coefficient of p-polarized light

T_s = transmission coefficient of s-polarized light

t, t_d = time (s), delay time (s or μs)

V = Ionic volume (cm^3/mol), volume of monolayer spreading solution (L)

v = volume of hydrocarbon chains (m^3)

$\bar{v}_w$, $\bar{v}_L$ = water and lipid partial specific volumes (ml/g)

w = weight percentage

x_b = percentage of lipid molecules that have acquired a charge

z = valency

α = surface or headgroup area of a micellar molecule ($Å^2$), the incompressible area of chains of a lipid molecule ($Å^2$)

α_p = volume polarizability ($Å^3$)

Γ = decay rate (sec^{-1})

γ = surface tension of the monolayer (mNm^{-1} or dyn/cm), distortion lattice angle (◦)

γ_0 = surface tension of water or electrolyte solution (mNm^{-1} or dyn/cm)

δ = diffuse layer thickness (Å)

ε_0 = permittivity of vacuum $\varepsilon_0 = 8.854 \times 10^{-12}$ $C^2J^{-1}m^{-1}$.

ε_r = solvent dielectric constant

θ = angle of incidence (◦), Bragg angle (◦)

θ_{BA} = Brewster angle (◦)

θ_t = tilt angle with respect to the normal (◦)

κ^{-1} = Debye length (m or nm)

κ_c = bending rigidity (kT)

λ = wavelength (nm or Å), line tension, characteristic decay length (Å)

μ = chemical potential, linear absorption coefficient

ν, ν_s, ν_{as} = vibration frequency of (s symmetric and as antisymmetric) stretching modes (cm^{-1})

ξ = correlation length

ρ = electron density of a sample ($e/Å^3$)

σ = surface charge density (Cm^{-2})

Φ = Electrostatic potential (V)

Φ_0 = Electrostatic surface potential (V)

φ = refractive angle (◦), volume fraction

Π = osmotic pressure (Pa)

π = surface pressure (mN/m)

χ = Flory-Huggins interaction parameter

ψ = tilt azimuthal direction of the aliphatic chains (◦)

τ = characteristic decay time constant (μs)

TABLE OF CONTENTS

LIST OF FIGURES

CHAPTER 1

CHAPTER 2

CHAPTER 3

CHAPTER 4

CHAPTER 5

CHAPTER 6

CHAPTER 7

CHAPTER 8

CHAPTER 9

LIST OF TABLES

CHAPTER 1

CHAPTER 3

CHAPTER 4

CHAPTER 6

CHAPTER 7

CHAPTER 8

CHAPTER 9

1 CHAPTER

GENERAL INTRODUCTION – GOALS AND ORIGINALITY OF THE THESIS

1.1 Aim

The starting goal of this work was to provide improved understanding of the mechanism of action of Hofmeister anions. This was done by examining the interactions of Hofmeister anions with three model-systems, in which lipids with the same choline headgroup arrange themselves into the different geometries of monolayers, bilayers and micelles. The effects of the anions on the structures and properties of these model systems have been examined, and a number of theoretical models were applied to obtain "binding" or interaction constants of anions with the lipids. Attempts were made to correlate the binding constants to analogous binding constants on other interfaces or to potential local interactions (hydration, dispersion, electrostatics etc.) in order to identify interaction mechanisms.

1.2 Specific ion effects and the Hofmeister series

The presence of ions in aqueous solutions and their influence on various physicochemical and biological phenomena has been widely studied since 1888. More than 100 years ago, **Hofmeister** (**1888)** and **Lewith (1888)** published experimental results showing the effect of various salts solutions on the solubility of proteins. Specifically, it was found that (a) the log(solubility) of many proteins in electrolyte solutions depends linearly on electrolyte concentration, and that (b) a different log(solubility) vs salt concentration curve is obtained for each electrolyte even for ions with the same charge. Since then, numerous experimental studies have shown the importance of specific ion effects in a multitude of biological and physicochemical phenomena; for example the presence of ions in aqueous solutions affects polymer cloud points (**Schott et al. 1984**), the critical micelle concentration of surfactant molecules (**Ray et al. 1971; Zhang et al. 1996**), pH measurements (**Camoes et al. 1997; Boström et al. 2002**), zeta and surface potentials (**McLaughlin et al. 1975; Tatulian 1983; Clarke et al. 1999; Franks 2002**), the surface tension of electrolytes (**Jarvis et al. 1968; Weissenborn et al. 1996**), the enzymatic activity of biomolecules (**Wright et al. 1977; Hochachka et al. 1984; Hall et al. 1995**) etc. Two very interesting reviews that were published on the topic of specific salt effects by **Collins et al. 1985** and **Cacace et al. 1997** contain more than 900 references! Depending on their "importance" in different phenomena, ions have been ordered into a sequence, which is called either the Hofmeister series or the lyotropic series. Representative Hofmeister series for cations and anions are given below:

$$Mg^{2+} > Ca^{2+} > H^{+} > Na^{+} > K^{+} > Rb^{+} > Cs^{+} > NH_4^{+} > N(CH_3)_4^{+}$$

$$SO_4^{2-} > HPO_4^{2-} > OH^{-} > F^{-} > CH_3COO^{-} > Cl^{-} > Br^{-} > NO_3^{-} > I^{-} > BF_4^{-} \approx ClO_4^{-} > SCN^{-}$$

In these sequences, the ions are ordered depending on their ability to salt-out proteins, with the strongest salting-out ions on the left side of the sequences. Anions were found to have a much stronger impact on protein solubility than cations. This thesis will be exclusively devoted to anion effects. In general, the *anions* that are located on the left of Cl^- decrease protein solubility, therefore they are called salting-out ions, while the ions on the right of Cl^- have the opposite effect and thus they are called salting-in ions. The Cl^- ion is said to be an

indifferent ion and the sign of many specific anion effects is found to change around the Cl^- ion.

Despite the fact that the Hofmeister series plays a significant role in a dramatic range of biological and physicochemical phenomena, the precise origin of action of the Hofmeister ions has not yet been clarified and no generally accepted explanations exist at the molecular level. This may be due to the fact that many phenomena involve the action of both ions of an electrolyte or the fact that Hofmeister ions affect more than one significant interaction in the same system, thus making it impossible to define appropriate Hofmeister parameters that can explain the mechanism of ionic action in various experimental studies.

Different ideas about the nature of specific salt effects have been proposed: The main model idea for many years was that ions interact with water very strongly and thus they modify the structure of water (**Chaplin 1999**). This is why the ions on the left of Cl^- in the Hofmeister series are also known as cosmotropes, meaning that they enhance water structuring (structure makers), while the ions that are on the right of Cl^- are called chaotropes or structure breakers. **Collins** and **Washabaugh (1985)** have developed a molecular model based on the idea that the water surrounding an ion can be divided into three layers. The first layer is adjacent to the ion and the water properties (ordering) are defined by the ion, the third layer represents the water in the bulk solution and the second layer has properties determined by the other two layers. The disadvantage of this model is that it is very complicated (involving the interactions between the three hydration shells) and provides no real quantitative information. Based on a similar idea (water structure), many biologists (**Chaplin 1999**) refer to low-density and high-density water close to biological interfaces and the way that ions affect the two water regions.

A recent proposition by **Ninham et al. 1997** suggests that the origin of the Hofmeister series could be due to the existence of dispersion interactions between ions and surfaces. Since the classical Gouy-Chapman theory cannot fully explain the mechanism of action of Hofmeister ions, it is believed that an ionic dispersion potential acting between ions and interface must be included in the theory; most Hofmeister phenomena can then be understood if ionic polarizability is properly incorporated in double layer models. The model can be applied to various experiments provided that ions do not interact through chemical bonds with surfaces. **Boström et al. 2001** explained the surface tension of electrolytes based on the idea of dispersion forces. They were able to introduce ion specificity into their electrostatic

calculation, which retained the basic picture of **Onsager and Samaras (1934)**, which postulated the existence of a layer free of ions close to the water surface. However these results disagree with recent molecular simulations of electrolyte solution surfaces, which show for example that ions like Cl^- have a higher affinity (higher concentration) for the surface than Na^+ ions (**Jungwirth et al. 2000**) and that large, polarizable anions have strong concentration peaks at the water surface (**Jungwirth et al. 2002**). It is particularly noteworthy that these simulations use a polarizable model for water and ions.

An alternative qualitative model argues that ion specificity arises as a result of the fine balance between ion-water and water-water interactions (**Collins 1997**). Recent computer simulation studies using Monte Carlo and Molecular Dynamics giving emphasis to hydration interactions support this idea and examine specific effects of ions on the hydrogen bond network of water (**Karlström et al. 2002; Hribar et al. 2002**).

It is obvious from the above broad spectrum of alternative explanations that no consensus exists today for the mechanism of specific ion effects, and it remains largely unclear whether ions act through precisely defined, specific, local interactions, or through more delocalized collective interactions. Elucidation of the mechanism of action of the Hofmeister ions in a particular experimental situation will provide valuable insights for a multitude of ion-specific phenomena, and will have a strong impact on biology and chemistry. In particular, the following important questions that remain unanswered today must be addressed:

(a) Is there a concentration threshold for specific ion effects to appear?

(b) Are specific ion effects really interfacial phenomena?

(c) Are specific ion effects based on local or on collective interactions?

(d) Does a unique ion parameter exist to correlate ion effects?

In order to better understand the mechanism of action of Hofmeister anions, we need to work with model interfaces as will be discussed below. However, before proceeding we must discuss the fundamental properties of the Hofmeister anions. For ions of the same charge, the next most important property is their size, quantified by their Pauling radius (**Leontidis 2002**). Generally, the cosmotropic ions have *small* Pauling radii and thus they are *strongly hydrated*, losing their water of hydration with great difficulty. The opposite holds for chaotropic ions, which are *weakly hydrated*. Another fundamental property of ions is their polarizability. The polarizability of an ion is the ability of its electronic shells to undergo deformation in an electric field. Although, the polarizability of an anion can be associated with its size and internal structure, it is often considered as an independent parameter. In

general, cosmotropic ions have *small* polarizabilities and chaotropic ions *large* polarizabilities, although significant exceptions exist (SO_4^{2-} is a cosmotropic ion with high polarizability). **Table 1-1** below gives different properties of Hofmeister anions, as they have been determined experimentally.

Table 1-1. Properties of Hofmeister anions

Property / **Ions**	**R_p Pauling radius (Å)[a]**	**V Ionic Volume (cm^3/mol)[b]**	**α_p Polarizability (Å^3)[c]**		**ΔG_{hyd} Hydration free energy (Kcal/mol)[d]**	**Softness[e]**
SO_4^{2-}	2.30	25.0	5.46	6.33	-258.2	-0.38
OH^-	1.33	1.5	1.84	2.25	-102.8	0.00
F^-	1.33	4.3	0.88	1.30	-111.1	-0.66
CH_3COO^-	1.62	46.2	5.50	----	-87.2	-0.22
Cl^-	1.81	23.3	3.42	3.76	-81.3	-0.09
Br^-	1.96	30.2	4.85	5.07	-75.3	0.17
NO_3^-	1.79	34.5	4.13	4.48	-71.7	0.03
I^-	2.20	41.7	7.51	7.41	-65.7	0.50
SCN^-	2.13	41.2	6.75	----	-66.9	0.85
BF_4^-	2.30	49.7	----	----	-45.4	-0.30
ClO_4^-	2.40	49.6	5.06	5.45	-102.8	-0.30

[a]Pauling radius taken from **Babu et al. 1999** and **Marcus 1997**
[b]Ionic volume taken from **Marcus 1997**
[c]Polarizabilities taken from **Marcus 1997** (column A) and **Pyper et al. 1992** (column B)
[d]Free energies of hydration taken from **Marcus 1991**
[e]Ionic softness taken from **Marcus 1997**

1.3 Model systems used in this thesis – previous work

Since we want to determine if the Hofmeister ions act primarily through dispersion or other interactions with interfaces or solutes, or through some direct or indirect interaction with water molecules, we must use simple model systems, which will yet allow the examination of several possibilities. Three model systems are used in this work (a) Langmuir monolayers of phospholipids at the air-water interface, (b) bilayers of phospholipids, and (c) micelles of phospholipid compounds. These models provide various advantages such as: (i) Possibility to study the effect of Hofmeister anions at three different geometries. (ii) Similar interactions between ions and lipids are expected in the three different geometries, provided that the lipids used have the same headgroups. (iii) We can achieve a regulated change of the hydration of

surface (by changing the headgroups of the phospholipid molecules used). For the formation of these three geometries we have used the phospholipids DPPC (1, 2-Dipalmitoyl-sn-Glycero-3-Phosphocholine) and DPC (Dodecylphosphocholine) (see **Chapter 4**).

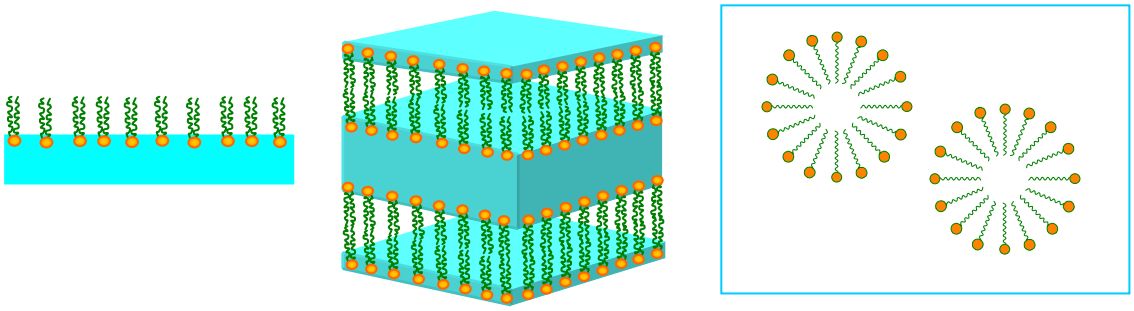

(a) **(b)** **(c)**

Figure 1-1. Different geometries - Langmuir monolayers, (a) bilayers, (b) micelles (c)

Phospholipids offer some significant advantages: They can be charged or uncharged (e.g., serine vs. choline headgroups) and they can be examined as *bilayers* in the form of vesicles or lamellar phases, as *monolayers* at the air-water interface, and even as *micelles* (in the case of single-tail-phospholipids). In addition, the phospholipids DPPC and DPC are bipolar (zwitterionic) and thus they do not demonstrate strong Coulomb interactions with the anions. As a result, the weaker interactions (Van der Waals and electrostatic other than Coulomb) can be studied more easily. Moreover, phospholipids are important components of cellular membranes and are very well characterized by many research groups over the past few years.

The simplicity of a Langmuir monolayer at the air-water interface offers a clear theoretical advantage for the evaluation and comparison of interfacial models of ion binding. In addition, the development of many new experimental techniques that provide details on the structure, ordering and morphology at the mesoscopic and the molecular level, such as grazing X-ray scattering, fluorescence microscopy and Brewster angle microscopy, renders DPPC monolayers especially attractive for our purposes. Several investigations of the effects of cations on monolayers (**Shah et al. 1965; Goddard et al. 1967; Yamaouchi et al. 1968; Gordziel et al. 1982; Grigoriev et al. 1999; Kmetko et al. 2001**) and bilayers (**Simon et al. 1975; Lis et al. 1981; Akutsu et al. 1981; Loosley-Millman et al. 1982; Afzal et al. 1983; Altenbach et al. 1984; Kwok et al. 1986; Roux et al. 1990; Lösche et al. 1989; Rappolt et**

al. 2001; Scarpa et al. 2002) exist in the literature, given the importance of H^+, Na^+, K^+, Ca^{2+} and Mg^{2+} in altering biomembrane behavior. Relatively few studies have concentrated on anions, which are of more interest in terms of the Hofmeister effect. The effects of anions on lipid *monolayers* are mostly concentrated on positively charged lipids for which the Coulomb interactions are overwhelmingly important (**Langmuir et al. 1937; Mara 1986; Helm et al. 1986; Knock et al. 2000; Teppner et al. 2000; Kölsch et al. 2004**). A long time ago, the effect of very low electrolyte concentrations on the surface pressure of lecithin monolayers was also examined, and was concluded that the anions in the subphase do not influence in any significant way the surface pressure – area isotherms (**Shah et al. 1965**).

Phospholipid bilayers are very useful as model systems for the study of ion effects, since they are excellent membrane mimics, and they can be viewed as the next modeling step after monolayers. Anion effects, mainly on the structural properties of lipid bilayers, have been examined in the past (**McLaughlin et al. 1975; Jendrasiak et al. 1972; Chapman et al. 1977; Hauser et al. 1977; Loschilova et al. 1978; Tatulian 1983; Cunningham et al. 1986; McDonald et al. 1988; Cunningham et al. 1988; Tatulian et al. 1991; Rydall et al. 1992; Jendrasiak et al. 1993; Sanderson et al. 1991; Bartucci et al. 1996; Clarke et al. 1999; Sachs et al. 2003; Sachs et al. 2004**). Various methods have been used to study the structural properties of lipid bilayers in the presence of electrolytes such as ^{1}H-NMR, ^{2}H-NMR or ^{31}P NMR, Raman spectroscopy, EPR spectroscopy, as well as X-Ray Diffraction or Neutron Diffraction, Zeta Potential measurements, Differential Scanning Calorimetry and recently Molecular Dynamics Simulations.

Chaotropic anions have been found to "enhance" the binding of lanthanides and divalent ions on PC membranes (**Hauser et al. 1977**). **Jendrasiak (1972)** has found by ^{1}H-NMR studies that the effectiveness of the anions follows the Hofmeister series. Specifically, I^- and SCN^- interact strongly enough with phosphocholines, but the interaction cannot be characterized as binding. **Jendrasiak et al. 1993** studied the effect of the chaotropic anions SCN^- and $SeCN^-$ on EPC bilayers with ^{1}H-NMR and ^{31}P NMR and found that both anions cause splitting of the choline ^{1}H resonances while no changes have been observed in the glycerol and phosphate headgroup region. **Loschilova et al. 1978** have used Raman spectroscopy and have also concluded that the interaction of anions with PC lipids follows a Hofmeister series. However, electrostatics alone could not explain the spectral changes in the presence of anions. Much has been learned from ^{2}H-NMR experiments. The deuterium quadrupolar splitting of deuterated cholines has been used to quantitate the degree of binding of ions to the headgroup.

McDonald et al. 1988 and **Rydall et al. 1992** have carried out an investigation of the influence of Hofmeister series anions on POPC bilayers. They found that the chaotropic anions produce the most significant changes of the deuterium quadrupolar splittings. The effect of anions was found to follow the Hofmeister series. Using the DLVO (Derjaguin-Landau-Verwey-Overbeek) theory, they estimated the surface potential of the bilayers and the binding constants of the ions to the lipids by assuming that the bilayer ions adsorb and create a double layer charge. The influence of anions on the zeta-potential of lipid bilayers (PE and PC vesicles or PC bilayers) has been measured by **McLaughlin et al. 1975, Tatulian 1983 and Clarke et al. 1999** using either electrophoretic mobility or fluorescence spectroscopy (using fluorescent dyes). They have observed a decrease of the zeta-potential which followed the Hofmeister series and thus they have concluded that the lipid membrane potential becomes more negative through adsorption of the anions. **Tatulian (1983)** used the DLVO theory (with some assumptions) to calculate surface potentials and binding constants of anions to the lipids, while **Clarke et al. 1999** have used the fluorescence shift of specific dyes to obtain values of the intrinsic binding constant of ClO_4^- on DMPC.

Binding constants of several anions to PC lipid bilayers as estimated by different groups using different experimental methods are summarized in **Table 1-2**. The binding constants calculated by various binding models always follow the Hofmeister series, increasing for the more chaotropic ions. However, they show significant variability between experiments of different groups or between different experimental methods.

Table 1-2. Binding constants of anions to PC neutral bilayers

Anion	**Cl^-**	**Br^-**	**NO_3^-**	**I^-**	**SCN^-**	**ClO_4^-**
	1.67	4.0	24.0			70
Binding constant	0.2	3.6	2.0	40	10	222
(M^{-1})		2.0	2.8	32	80	115
						10 , 23

The effect of anions on the phase transition temperatures of lipids has also been studied repeatedly (**Chapman et al. 1977, Cunningham et al. 1986, Sanderson et al. 1991; Przyczyna et al. 2002**). The general result is that the chaotropic ions have pronounced effects on the main phase transition of lipids ($L_\beta \rightarrow L_\alpha$). Structural information for lipid bilayers in the presence of salt solutions has also been obtained using X-ray diffraction or

Neutron diffraction measurements. **Cunningham et al. 1986**, have studied the influence of monovalent anions on the structural properties of DPPC bilayers. In general, the DPPC bilayers swell continuously in 1 M potassium salt solutions until the limiting bilayer repeat distance is obtained. In the presence of SCN^- ions, an interdigitated structure was reported. A significant effect of the chaotropic anions I^- and SCN^- on DPPC bilayers was also observed by **Bartucci et al. 1994** with EPR measurements, who also concluded that the chaotropic anions may induce an interdigitation of the DPPC hydrocarbon chains. **Tatulian et al. 1991** performed similar experiments using Neutron diffraction. They observed that addition of NaCl does not affect the DPPC lamellar structure while the effect of $NaClO_4$ drastically influences the lamellar repeat spacing. Information on atomic-level local interactions of anions with lipid bilayers can be deduced by Molecular Dynamic Simulations. Recently **Sachs et al. (2003** and **2004)** have studied zwitterionic phospholipid bilayers in contact with electrolyte solutions. Anion penetration into zwitterionic lipid bilayers was found mostly for large anions (chaotropic anions) that can penetrate deeply into the bilayers. They also found that in the presence of the anions there is a significant change of the average headgroup tilt of the lipids with respect to the lipid-water interface.

The literature on the effects of cations on negatively charged micelles is voluminous. Research on cation binding has involved a wide range of surfactants, while the cations investigated have ranged from monovalent to trivalent cations, including Cr^{3+}, La^{3+}, and Al^{3+}. The effect of anions on micelles was also extensively studied over the years, especially on positively charged micelles, where it was found that the presence of anions induces a spherical to rodlike micelle transition (**Ikeda et al. 1980; Imae et al. 1987; Lin et al. 1994**). The effect was attributed to the reduced repulsion among the micellar polar heads induced by binding of the anions on the micellar headgroups. Recently, new methods have been developed with which one can calculate the interfacial concentration (e.g. ion exchange constants or selectivity coefficients) of ions or the fraction of charged sites due to ion adsorption on the micellar surface. These methods are: chemical trapping (**Loughlin et al. 1990; Chaudhuri et al. 1993; Cuccovia, et al. 1997; Cuccovia, et al. 1999; Keiper et al. 2001**), ion flotation (**Morgan et al. 1994; Thalody et al. 1995; Kellaway et al. 1997**) and several anion selective electrodes (**Morini et al. 1996; Gaillon et al. 1999**). In all of these studies it was found that the chaotropic anions have a higher affinity for the micellar surface than the cosmotropic anions and thus the ion exchange constant or the selectivity coefficient

$K_{chaot/kosm}$ was always larger than 1. In general, the presence of anions on the micellar surface follows the Hofmeister series. Very few studies have concentrated on the effect of anions on zwitterionic micelles. **Ray et al. 1971** and **Zhang et al. 1996** have shown that inorganic anions can influence the critical micelle concentration (cmc) of zwitterionic micelles. The effect of anions decreases in the order $F^- > Cl^- > SO_4^{2-} > Br^- > NO_3^- > I^- > SCN^-$ which follows the Hofmeister series. The effect of anions is explained on the basis of their structure-making (salting-out) and structure-breaking (salting-in) properties. Either using kinetic nucleophilic reactions (**Bunton et al. 1989**), or fluorescence spectroscopy (**Brochsztain et al. 1990; Baptista et al. 1991**) it was shown that inorganic anions such as OH^-, F^-, Cl^-, Br^- can selectively concentrate and/or bind to the micellar surface following the Hofmeister series. A very interesting series of investigations by **Okada** and co-workers (**Okada et al. 1998; Masudo et al. 1999; Iso et al. 2000**) has recently used capillary electrophoresis or potentiometric and chromatographic methods to evaluate ion uptake by zwitterionic micelles. It was found that ion uptake by zwitterionic micelles e.g. by 3-(N-dodecyl-N,N-dimethylammonium)propane-1-sulfonate (DDAPS) is in the order of $ClO_4^- > SCN^- > I^- > Br^- > Cl^-$ which agrees with the Hofmeister series. Binding constants of the chaotropic anions were computed using binding models; these were of the order of 1 M^{-1}. Specifically, $K_I = 0.12$ M^{-1}, $K_{SCN} = 0.7$ M^{-1} and $K_{ClO4} = 1.2$ M^{-1}.

1.4 Originality of the present approach

Our study provides a fresh look into the interactions between anions and lipid monolayers, bilayers and micelles in several respects. Regarding the monolayers, we examine salt effects on zwitterionic lipid monolayers in a systematic way, using a range of ion concentrations of several sodium salts of anions that cover the chaotropic side of the Hofmeister series. In addition, we apply for the first time the powerful combination of the modern methods of Brewster angle microscopy (BAM), Grazing Incidence X-ray Diffraction (GIXD) and Infrared Reflection-Absorption Spectroscopy (IRRAS) to obtain extensive structural information about the DPPC monolayers in the presence of high electrolyte concentrations. *Our strategy is to understand salt effects on DPPC monolayers by gradually reducing the length scale of the investigation*. We start from the macroscopic thermodynamic information provided by the pressure-area isotherms (cm scale), then we examine the micrometer (μm) scale using BAM, and finally examine the nanometer (nm) scale with GIXD and the bond (➡)

scale with IRRAS. A range of theoretical models based on electrostatics is also applied to the surface pressure isotherms to complement the experimental work.

The present work also provides a fresh look on salt effects on lipid bilayers. Until today no detailed studies exist on how the interactions between bilayers are influenced by the presence of anions. For the first time the osmotic stress method in combination with SAXS is used for a large number of electrolytes providing an extensive experimental database for the application of models. Also for the first time the experimental results are fitted using different theoretical models in order to compute binding constants of anions on the lipid bilayers.

Regarding micelles, the micellization properties of DPC in the presence of electrolytes have been examined for the first time. We use light scattering and concentrate on the aggregation numbers of the micelles and the area per surfactant molecule.

The unique aspect of this thesis however is that the effects of anions are examined in parallel on a range of lipid geometries and the binding constants of the anions on all these interfaces are calculated and correlated to each other for the first time.

1.5 Outline of the thesis

The thesis is divided in the following chapters:

Chapter 2 provides a general description of surfactant solutions and self-assembly including the various factors affecting the critical micelle concentration, the thermodynamics of self-assembly and the various lyotropic liquid crystalline phases that are formed in aqueous solutions.

Chapter 3 describes the principles of the experimental techniques used for the experiments in this thesis.

Chapter 4 gives a detailed description of the properties of the chemical substances (lipid molecules) used in the different experiments.

Chapter 5 provides a short description of the different fundamental intermolecular and surface forces. In this chapter we also describe the theoretical models for monolayers, bilayers and micelles that have been used to fit the experimental results.

Chapter 6 describes the monolayer experimental results of DPPC at the air-water interface in the presence of various anions in the subphase. Moreover, the fitting results using the monolayer theoretical models are presented.

Chapter 7 describes the influence of NaX salt solutions on DPPC bilayers. The chapter also contains a description of the extensive fitting attempts on the experimental data using two theoretical models.

Chapter 8 describes the experimental results of the effects of salts on the micellization of DPC. The theoretical model used and the results of its application to the experimental data are also discussed.

Chapter 9 discusses and compares the effect of anions on the three model systems.

2 CHAPTER

SURFACTANT SOLUTIONS AND SELF-ASSEMBLY

2.1 Surfactants

Surfactants are organic molecules that consist of a polar hydrophilic headgroup (water-attracting) and a non-polar hydrophobic tailgroup (water-repelling) in their structure, and are thus referred to as amphiphilic/amphipathic molecules as shown in **Figure 2-1**.

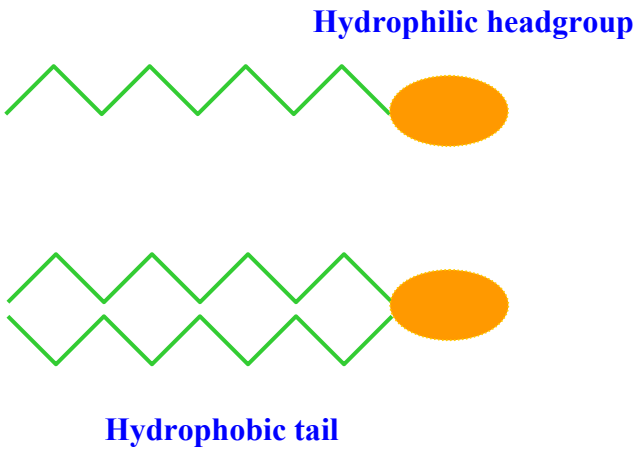

Figure 2-1. Hydrophilic – Hydrophobic parts of a single and double chain surfactant

The hydrophobic tail can be short or long, linear or branched, and it interacts weakly with the water molecules. The hydrophilic headgroup, which can be either ionic or non-ionic, interacts strongly with the aqueous environment through solvation processes involving dipole-dipole or ion-dipole interactions. In general, surfactants can be classified into four groups according to the charge present in the polar head group part of the molecule in aqueous solutions. These are: anionic (-), cationic (+), Zwitterionic (+/-) and non-ionic. Zwitterions are surfactants that contain both a positive and a negative charge simultaneously. Phospholipids are an important category of surfactant molecules, found mainly in biological membranes. A more detailed description of these molecules is given in **Chapter 4**.

2.2 Surfactant Self-Assembly

Due to their amphiphilic nature, surfactants can self-assemble into a variety of complex structures such as: monolayers at the air-water, air-oil and oil-water interfaces, micelles, bilayers, vesicles etc, as shown in **Figure 2-2**.

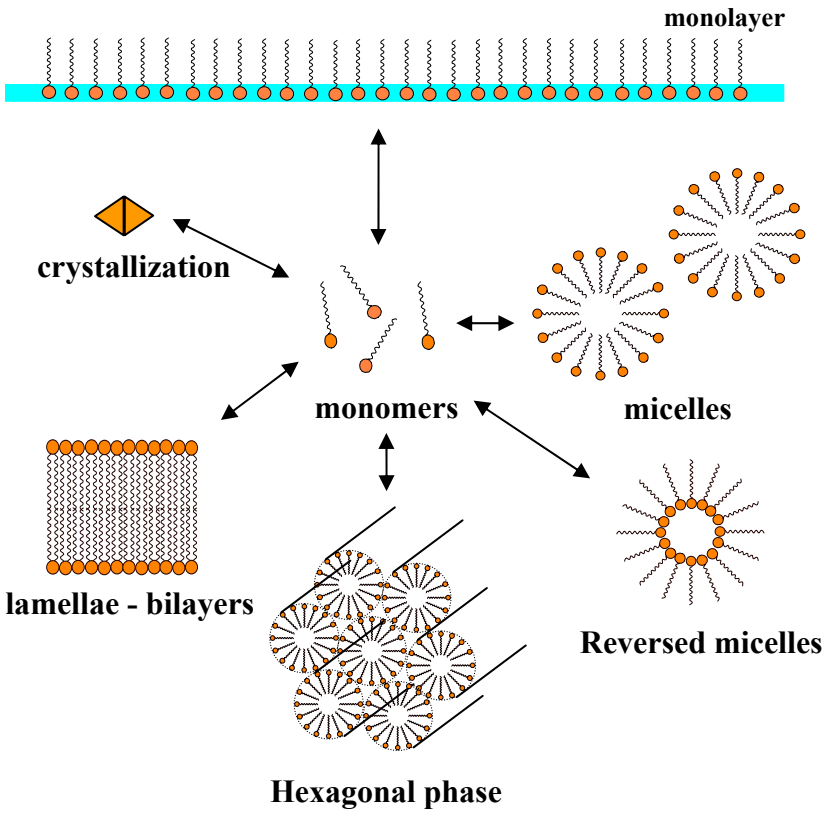

Figure 2-2. Surfactant self-assembly

In polar solvents, such as water, surfactant molecules initially migrate to the air-water interface, where they form a monolayer, in which the hydrophobic tails are oriented away from the aqueous phase while the hydrophilic heads are immersed in it. Because of their ability to accumulate at interfaces in the form of monolayers, they are called "active surface agents" and are capable of reducing the interfacial tension. As the surfactant concentration increases, the interface becomes saturated with surfactant molecules, and it consequently becomes thermodynamically favorable for these molecules to self-associate within the bulk solution into colloidal aggregates called micelles. In these aggregates, the hydrophilic heads remain exposed to water and shield the hydrophobic tails in the interior from the unfavorable contact with water (**Hiemenz et al. 1997**).

The concentration threshold at which micellization begins is known as the *critical micelle concentration* (CMC), below which surfactant molecules are predominantly dispersed as monomers and above which they form micelles. The onset of micellization at the CMC is marked by a sudden change in many physical properties of the solution including surface tension, electrical conductivity, optical turbidity and osmotic pressure, **Figure 2-3**. The thermodynamics of micellization shows that the aggregation process in water is accompanied by an **increase in the entropy** of the system which is the major contributor to the negative ΔG^o value for micellization.

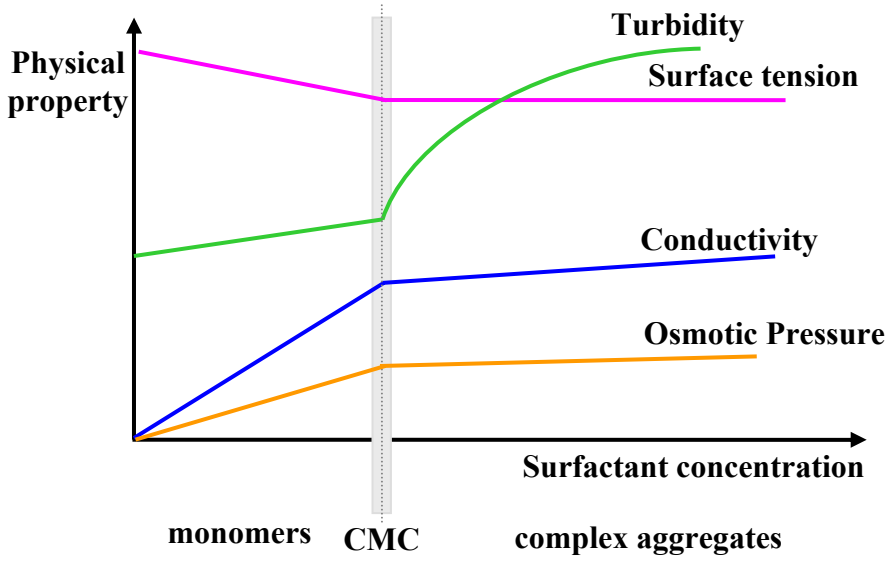

Figure 2-3. Schematic drawing of the variation of physical properties of a surfactant solution with surfactant concentration

2.3 Factors affecting CMC

2.3.1 Chemical Structure (Hydrocarbon chain length and configuration)

The CMC decreases strongly with increasing alkyl chain length of the surfactant. The dependence of CMC on the hydrocarbon chain length for surfactant molecules with a single hydrocarbon chain is related to the number of carbon atoms N_c in the hydrocarbon chain by the following expression:

$$\log (CMC) = b_0 - b_1 N_c \qquad \textbf{Equation 2.3-1}$$

where N_c is the number of carbon atoms in the hydrocarbon chain, and b_0 and b_1 are constants specific for each surfactant. The nature of the head group influences b_0 and b_1. For non-ionic surfactants b_1 is roughly equal to 0.5 while for ionic surfactants it has a value close to 0.3.
Modifications to the hydrocarbon chain such as introducing branching, double bonds or polar functional groups in the hydrocarbon generally increase the CMC (**Hunter 2001**).

2.3.2 Counter ion

In the case of ionic surfactants, the CMC is greatly affected by the counter-ion valency. In general, increasing the valence of the counter-ions (monovalent, divalent to trivalent) decreases the electrostatic repulsion between the head groups of the surfactant molecules (screened) and surfactant aggregates are formed more easily. Thus the CMC is decreased.
The CMC is also affected by the lyotropic series of counter-ions of the same valency. The lyotropic series, also known as Hofmeister series (see **Chapter 1**), is an ordering of ions of the same valency. For example, the lyotropic series for anions was constructed according to their capability to salt-in proteins and organic compounds from aqueous solutions and is as follows:

$$OH^- < F^- < Cl^- < Br^- < NO_3^- < I^- < SCN^-$$

All ions have a number of water molecules bound to them. The smaller the ions are, the more hydrated they tend to be, and thus they have larger hydrated radii than larger ions. As a result,

the **hydrated size** of the above ions decreases roughly from left to right and thus it is easier for ions on the right side of the series to neutralise the headgroup charge of the surfactant molecules (because they can approach closer to the headgroup) and minimize the CMC (**Israelachvili 1991; Hiemenz et al. 1997**). However, this argument based only on size and/or hydration, is not the whole story as it is discussed in **Chapter 1**.

2.3.3 Temperature

For ionic surfactants below a certain temperature, known as the **Krafft point**, the surfactant precipitates. Above the Krafft temperature, micelle formation becomes a dominant factor in solution and thus there is a sudden increase in solubility of the surfactant. For non-ionic surfactants, increasing the temperature causes the formation of large aggregates, which separate out as a distinct phase at the **cloud point**. This is attributed to the reduction in hydrogen bonding between head groups and water (**Hiemenz et al. 1997; Hunter 2001**).

2.3.4 Effect of added salt

The addition of an electrolyte to a surfactant solution has a major effect on the CMC especially for ionic surfactants. The presence of an electrolyte reduces the electrostatic repulsion between the headgroups of the surfactant molecules and thus the CMC decreases. On the contrary, the salt concentrations required to significantly reduce the CMC of non-ionic surfactants are much higher. Due to the high concentration of the electrolyte the surfactant molecules can be “salted – in” or “salted – out” (**Hunter 2001**).

2.3.5 Organic Molecules

Organic molecules can influence the CMC and the properties of micellar solutions greatly. The CMC is decreased in the presence of hydrocarbons such as cyclohexane, heptane, toluene, benzene etc. Also, the micellar phenomenon of **solubilization** is very important, whereby lipophiles are apparently dissolved in water by the addition of surfactants. Incorporation of a hydrophobic material within a micelle may influence the value of the CMC (**Hunter 2001**).

2.4 Thermodynamics of self-assembly – Forces between Amphiphilic molecules

The equilibrium structures (complex aggregates) formed by self-association or self-assembly of surfactants can be determined by the thermodynamics of self-assembly and the forces that act between the amphiphilic molecules within the aggregates.

2.4.1 Thermodynamic equations of self-assembly

In a system of molecules that form aggregate structures in solution the chemical potential of all identical molecules in different aggregates must be the same. The chemical potential of a surfactant molecule (monomer) **free** in solution is given by:

$$\mu = \mu_1^0 + RT\ln\alpha_1 \qquad \textbf{Equation 2.4-1}$$

where α_1 is the activity of the monomer.
The chemical potential of a molecule (monomer) in a micelle of aggregation number N may be expressed as:

$$\mu_{mic,N} = \mu_{mic,N}^0 + \frac{RT}{N}\ln\left(\frac{X_N}{N}\right) \qquad \textbf{Equation 2.4-2}$$

where μ_N^0 is the standard chemical potential in aggregates of aggregation number N, and X_N the mole fraction of monomer in micelles of aggregation number N. The term $RT\ln(X_N/N)$ is the contribution of a whole micelle to the free energy, so this term is divided by N to determine the free energy contribution of each monomer within the micelle.
Since the amphiphilic molecules equilibrate between the aqueous phase and the micelles, their chemical potentials within the two regions must be equal:

$$\mu_{mic,N}^0 - \mu_1^0 = RT\ln\alpha_1 - \frac{RT}{N}\ln\left(\frac{X_N}{N}\right) \qquad \textbf{Equation 2.4-3}$$

The standard Gibbs free energy change of formation of **one mole of micelles** is then:

$$\Delta G^0(N) = -RT\ln K$$
$$\Delta G^0(N) = -RT\ln\left(\frac{X_N}{N}\right) + NRT\ln\alpha_1 \qquad \textbf{Equation 2.4-4}$$

The free energy of formation **per mole of surfactant** (the free energy change associated with the transfer of one monomer from the solution into a micelle) is given by:

$$\frac{\Delta G_N^0}{N} = \overline{\Delta G^0} = \mu_{mic}^0 - \mu_1^0 = RT\ln\alpha_1 - \frac{RT}{N}\ln\left(\frac{X_N}{N}\right) \qquad \textbf{Equation 2.4-5}$$

If the aggregation number N is large (typically > 50) or the mole fraction of the monomers in micelles X_N is small $X_N \approx \alpha_1$, then the final term in **Equation 2.4-5** can be ignored. As a result, one can calculate the cmc when $\Delta\mu$ is known, using the following expression:

$$\frac{\Delta G_N^0}{N} = RT\ln(cmc) = RT\ln\alpha_1 \qquad \textbf{Equation 2.4-6}$$

(Israelachvili 1991; Hunter 2001)

2.4.2 Forces between amphiphilic molecules

(Israelachvili 1991; Hiemenz et al. 1997)

The self-association of surfactants into well-defined structures is initiated by the imbalance of two opposite forces, the hydrophobic-hydrophilic interactions. The hydrophobic attraction tends to help the molecules associate so that their hydrophobic chains avoid contact with water, while the repulsion between the hydrophilic headgroups, which is of solvation, steric or electrostatic origin, tends to keep the molecules in contact with water. These two interactions compete, with one tending to decrease and the other tending to increase the surface area α taken up by the headgroup of each surfactant molecule on the surface of a micelle exposed to the aqueous solution. As a result, they determine the optimal area α_0 occupied by each headgroup as shown in **Figure 2-4**.

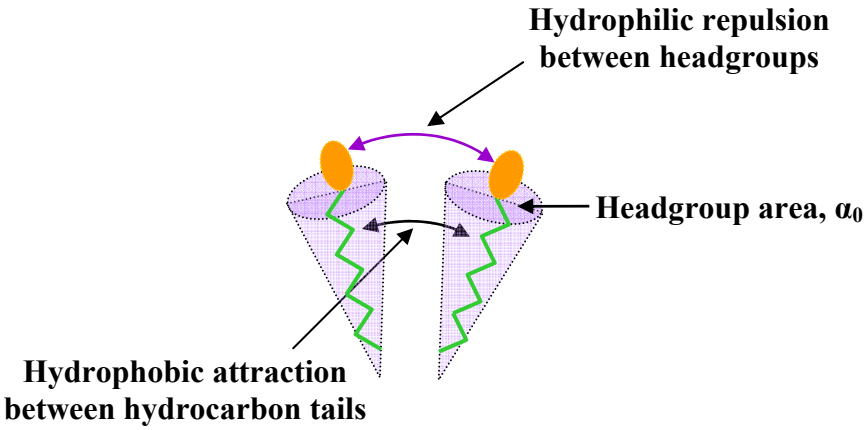

Figure 2-4. Schematic drawing of the geometric parameters of a surfactant molecule

2.5 Lyotropic Liquid Crystalline Phases of Surfactants

The self-association process is concentration dependent. As the concentration of the surfactant increases, the micellar structure (size and shape) changes significantly. More complex aggregates can then be formed, which can transform from one to another when the solution conditions (for example, ionic strength, pH, temperature, pressure, surfactant composition etc) are changed. Typically, the smaller micelles are spherical in shape while larger ones grow into one-dimensional cylindrical aggregates or into two-dimensional lamellar phases.

2.5.1 Micelles

Micelles may be represented as globular, cylindrical or ellipsoidal clusters of individual surfactant molecules in equilibrium with monomers. They have a hydrophilic exterior (polar headgroups oriented towards the aqueous phase) and a hydrophobic core (hydrocarbon tails pointing away from the aqueous phase). A typical length scale associated with micelles is about 2 nm, corresponding to the radius of spherical micelles or the diameter of cylindrical micelles, for example.

In ionic micelles, the hydrocarbon core is surrounded by a shell that resembles a concentrated electrolyte solution. This is the interfacial region between the micellar surface and the aqueous solution and contains counterions associated with the micelle. This region is called the Stern layer (**Figure 2-5**).

Besides counterions the Stern layer, which is usually 1-5 Å thick, also includes free water molecules and water of hydration. Beyond the Stern layer, the remaining counterions form the Gouy-Chapman layer which is a portion of the electrical double layer and extends up to several tens of Å into the aqueous phase.

In non-ionic micelles the micellar structure is similar to that of ionic micelles, with the notable absence of counterions in the Stern and Gouy-Chapman layer (**Hiemenz et al. 1997; Hunter 2001**). However, the ions have the possibility of binding at the *palisade layer* of non-ionic surfactants like DPC, which is zwitterionic.

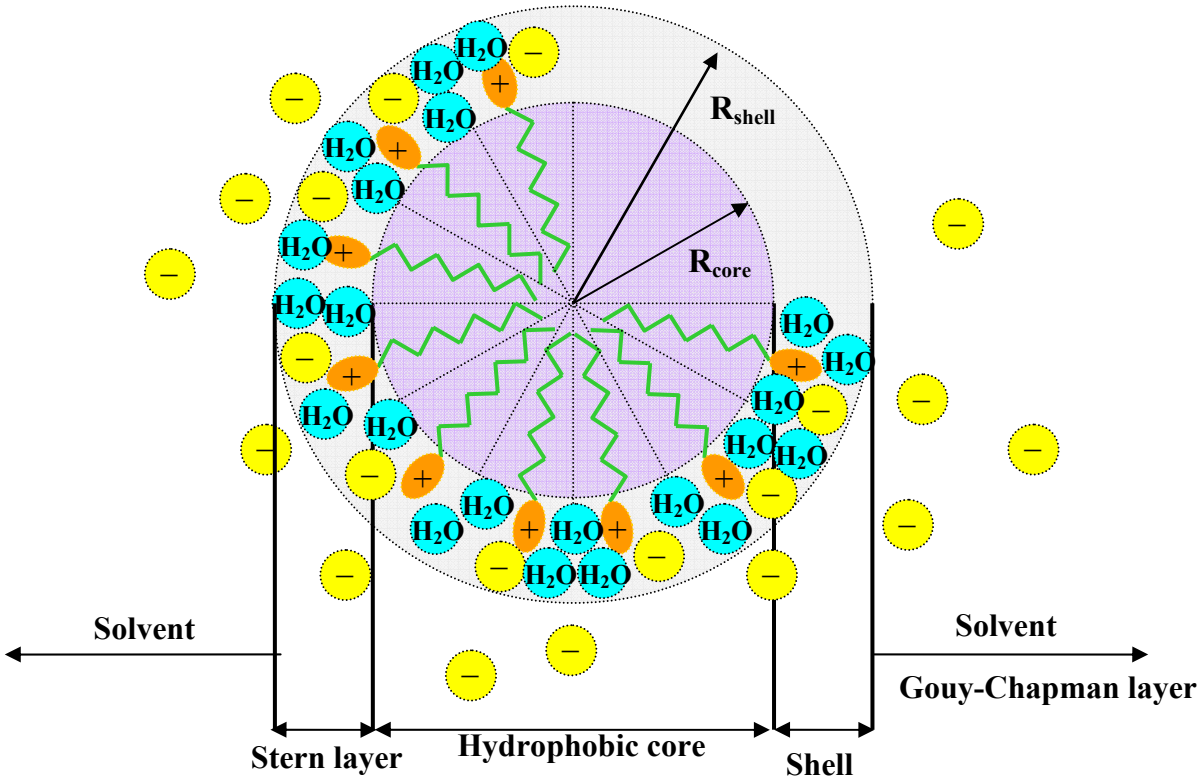

Figure 2-5. Internal structure of a micelle

2.5.2 Lamellae (Bilayers)

Within a critical range of concentrations, phospholipid molecules placed in water self-organize to form lamellar phases. Lamellar mesophases are the most frequently observed structures for double- and higher-chained amphiphiles. The most commonly observed structure is the "bilayer". A bilayer is composed of two opposing planar and parallel layers of lipid molecules arranged so that their hydrocarbon tails face one another to form the oily

bilayer core, while their electrically charged or polar heads face the watery or "aqueous" solutions on either side of the membrane as shown in **Figure 2-6**. As a result, the headgroups shield the hydrocarbon chains from the energetically unfavourable direct contact with the aqueous exterior. Because of the oily core, a pure lipid bilayer is permeable to small hydrophobic solutes but has a strong permeability barrier to inorganic ions and other hydrophilic molecules. Water itself is an exception to this rule, and crosses freely. Lamellar phases, exhibit diffraction patterns typical of a smectic lattice, and thus can be identified by equally spaced Bragg peaks (see **Chapter 3**, **Section 3.6.4**).

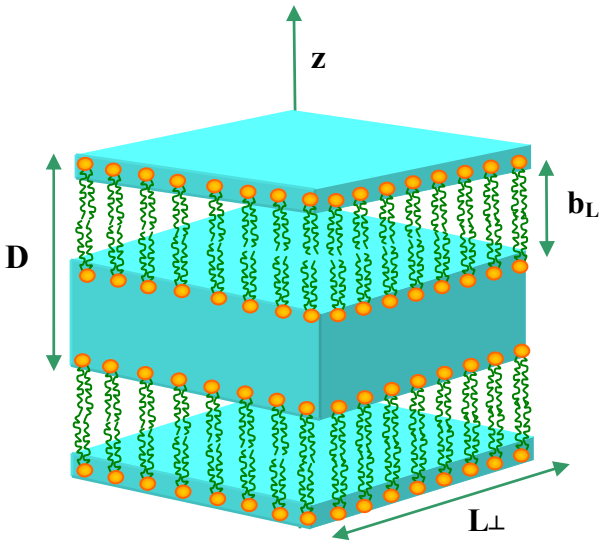

Figure 2-6. Schematic drawing of a bilayer

In general, a mesophase is called "lamellar" when it is (a) optically anisotropic, and (b) exhibits a smectic diffraction pattern (**Hyde 2001**). Phospholipid membrane structures undergo thermotropic phase transitions and as a result, they can be found as a gel ($L_\beta, L_{\beta'}$) or interdigitated lamellar phase ($L_{\beta I}$), undulated ripple phase ($P_{\beta'}$), or as a standard fluid lamellar phase (L_α), **Figure 2-7**.

2.5.2.1 Gel Lamellar Phases

Gel mesophases are characterized by a crystalline packing of the chains of the lipid molecules, evident by the long-range ordering between lamellae resulting in a large number of sharp Bragg diffraction peaks. Specifically, in the L_β gel phase the hydrocarbon chains are

extended and ordered (all-trans), arranged parallel to the layer normal, having a value of about 20Å^2 for the cross-sectional area per chain.

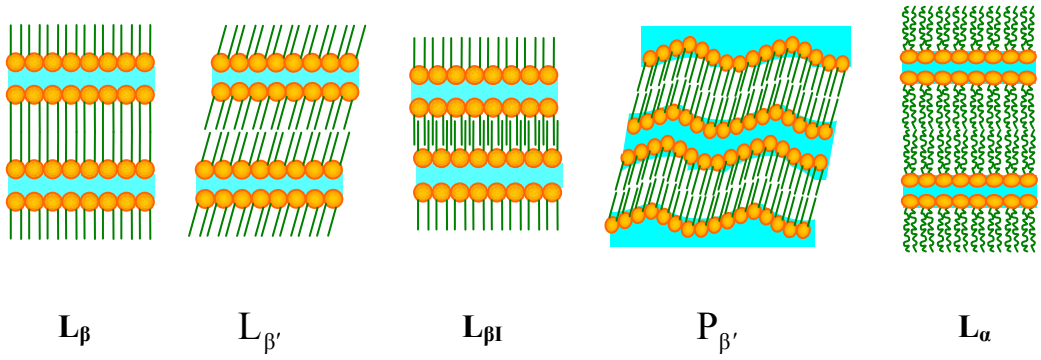

Figure 2-7. Phase transitions of lamellar mesophases

The $L_{\beta'}$ phase is similar to L_β gel phase, but with tilted hydrocarbon chains. The tilting occurs when the area available for the headgroups of the lipid molecules exceeds that of the chains. By tilting the chains the packing mismatch is corrected. The untilted interdigitated $L_{\beta I}$ lamellar phase may occur when the tilting of the hydrocarbon chains becomes too large. The $L_{\beta I}$ phase has a similar cross-sectional area per chain to L_β, but approximately twice the area available per headgroup.

In the $P_{\beta'}$ phase the hydrocarbon chains form a triangular lattice. The long axes of the chains are tilted with respect to the local plane of the membrane by about 30 degrees. The most remarkable feature of this phase is the corrugated surface profile, also called ripple structure (**Hyde 2001; Seddon et al. 1995**)

2.5.2.2 Fluid Lamellar Phases

The fluid lamellar L_α phase is observed when the gel lipid phase is heated up to a temperature specific for each lipid, called melting temperature, T_m. The $P_{\beta'} \rightarrow L_\alpha$ phase transition is associated with the transition of the hydrocarbon chains from an essentially all-trans state to a disordered liquid-like conformation, and it is therefore called chain-melting or main transition. Water can penetrate rather deeply into the hydrocarbon region of the L_α lamellar phase making it impossible to define a sharp interface between the polar and non-polar regions of the bilayer. The L_α phase swells by the addition of water between the bilayers up to

a limiting point called "equilibrium separation" (see **Chapter 3**, **Section 3.6.5**). The swelling is mainly an electrostatic effect (for charged bilayers), but it can also result from thermal undulations if the lamellar phase is quite flexible (**Hyde 2001; Seddon et al. 1995**)

2.5.3 Hexagonal phase

The hexagonal phase is a high viscous fluid phase that can be visualized as a set of close-packed cylindrical assemblies (micellar cylinders) of theoretically unlimited size in the axial direction, forming a 2-D hexagonal lattice. The micellar structures may be "normal" in water, that is, with the headgroups located at the outer surface of the cylinder, or "inverted", with the hydrophilic headgroups located internally (**Jönsson et al. 1998**).

2.5.4 Cubic phase

The cubic phase has several forms. In the bicontinuous cubic phase, for example, the aqueous and surfactant phases are both continuous and arranged in a cubic pattern. That is, they possess long range three dimensional structures. One way to visualize the cubic phase would be a three-dimensional grid of pipes. A discontinuous cubic phase may exist to either side of the hexagonal phase in the phase diagram, and exists as a three dimensional network of short rods (**Jönsson et al. 1998**).

2.6 Packing Considerations – Shape of Aggregates

The geometric packing properties of the surfactant molecules depend on their optimal area α_0, which determines the number of surfactants that can be accommodated in an aggregate of any shape, the volume v of their hydrocarbon chain or chains in the core, and the effective length, l_c, of the hydrocarbon chains in the liquid state known as the critical chain length as shown in **Figure 2-8**. A dimensionless factor known as the *packing parameter* can be defined using the above parameters, which can be used as an indicator of the preferred aggregate shape. The packing parameter is defined as:

$$\frac{v}{\alpha_0 l_c} \qquad \textbf{Equation 2.6-1}$$

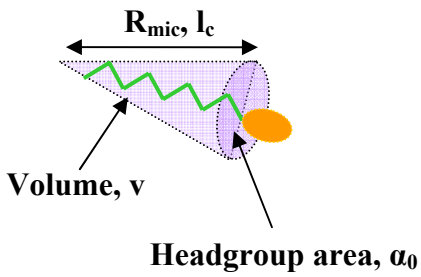

Figure 2-8. Geometric parameters of a surfactant molecule

2.6.1 Spherical micelles

For surfactant molecules that assemble into spherical micelles the packing parameter must be less or equal to 1/3:

$$\frac{v}{\alpha_0 l_c} < \frac{1}{3}$$ **Equation 2.6-2**

This occurs when the optimal surface area α_0 is sufficiently large and the hydrocarbon volume v sufficiently small, so that the radius of the micelle R does not exceed the critical chain length l_c.

2.6.2 Non spherical and cylindrical micelles

Surfactant molecules that possess small headgroup areas, for example those that are uncharged (non-ionic or zwitterionic) or possess charged headgroups in high salt, cannot pack into spherical micelles but can form cylindrical (rod-like) micelles. The packing parameter in this situation is in the range:

$$\frac{1}{3} < \frac{v}{\alpha_0 l_c} < \frac{1}{2}$$ **Equation 2.6-3**

2.6.3 Bilayers

Surfactant molecules with two hydrocarbon chains usually form bilayers and are described by a packing parameter in the range:

$$\frac{1}{2} < \frac{v}{\alpha_0 l_c} < 1 \qquad \textbf{Equation 2.6-4}$$

These molecules are characterized by a relatively small headgroup area α_0, or by hydrocarbon chains that are too bulky to fit into small aggregates, such as spherical micelles, while maintaining the surface area at its optimal value.

2.6.4 Inverted micelles

The packing parameter of surfactant molecules that have very small optimal headgroup areas or possess very bulky hydrocarbon chains exceeds unity.

$$\frac{v}{\alpha_0 l_c} > 1 \qquad \textbf{Equation 2.6-5}$$

Such surfactant molecules form "inverted" micellar structures or precipitate out of the solution (**Israelachvili 1991; Hiemenz et al. 1997**).

2.7 Factors Affecting the Aggregate Structure

The aggregate structure (size and shape) formed by various surfactant molecules depends on the molecular structure of the surfactant, nature of the solvent (temperature, pressure, ionic strength, presence of additives), and concentration of the surfactant solution.

For surfactant molecules with charged headgroups, the headgroup area α_0 can be reduced by increasing the salt concentration or lowering the pH and thus bilayers or inverted micelles can be formed ($v/\alpha_0 l_c$ increases). Changes in temperature can increase or decrease the headgroup area depending on the nature of the surfactant used to form aggregates. In general, it has been observed that with increasing temperature non – ionic spherical micelles grow in size and

become more cylindrical, while charged micelles shrink. Zwitterionic micelles appear to have an intermediate behaviour.

The critical chain length l_c decreases by introducing chain branching and unsaturated bonds to the hydrocarbon chain of the surfactant molecules. In addition, the penetration of organic molecules into the chain region increases the effective volume v of the chains and similarly decreases the critical chain length l_c. The temperature of the surfactant solution also influences the critical chain length l_c. For double-chained surfactants which are in the fluid state, the increase of temperature increases the hydrocarbon chain motion and thus reduces the l_c. Consequently, the packing parameter $v/\alpha_0 l_c$ increases. (**Israelachvili 1991; Hiemenz et al. 1997**).

3 CHAPTER

EXPERIMENTAL TECHNIQUES

3.1 Langmuir monolayers (LB)

Langmuir monolayers are formed when a solution of insoluble amphiphilic molecules is spread at the air/water interface. When the solvent evaporates, a monomolecular film is left on the water surface. These films are excellent model systems for membrane biophysics, since a biological membrane can be considered as two weakly coupled monolayers. Langmuir monolayers can also be used for studies of chemical and biological reactions in two dimensions. They are necessary for the fabrication of Langmuir-Blodgett (LB) films, which are multilayers transferred layer-by-layer from the water surface to a solid support; in this way structured materials can be constructed for optical, electronic, or sensor applications. In addition, Langmuir monolayers have important applications in technology, for example in molecular electronics.

During the last 20 years, the LB technique has undergone a revolution, mainly due to the development of novel experimental techniques for monolayer characterization. These are Fluorescence and Polarized Fluorescence Microscopy (FM and PFM, respectively), Brewster Angle Microscopy (BAM), Atomic Force Microscopy (AFM), Infrared Reflection Absortpion Spectroscopy (IRRAS) and X-ray diffraction at grazing angle (GIXD). These techniques have allowed a better understanding of Langmuir monolayers. For example, it has been possible to observe mesoscopic structures at the surface and to determine their molecular order. It has become possible to recognize a great variety of surface phases and directly observe transitions between these phases, which are two-dimensional analogues of bulk liquid crystalline phases.
A large number of molecules can form Langmuir monolayers, arguably the most important of which are phospholipids. These are amphiphilic molecules with a hydrophilic phosphorous group and one or two hydrophobic hydrocarbon tails. Phospholipids are molecules of great scientific interest, since they are major constituents of biological membranes. A better understanding of their two-dimensional physicochemical behaviour is important for a better understanding of biological systems.

3.1.1 Surface Tension at the air-water interface

The cohesive forces between liquid molecules are responsible for the property known as surface tension. Surface tension is defined as the energy required to expand the surface of a liquid by a unit area. The molecules inside a liquid (in the bulk) attract each other with forces depending on the properties of the liquid substance. Molecules in the bulk interact equally with other molecules in all directions, so that they feel a zero net force, whereas the molecules at the surface experience a net attractive force towards the liquid phase, because they are not symmetrically solvated, **Figure 3-1.** Therefore, surface molecules behave differently and try to contract to the smallest possible area. This is the origin of surface tension. Polar liquids, such as water, have strong intermolecular interactions and thus high surface tensions. Any factor which decreases the strength of the intermolecular interactions or which provides alternative surface structure will lower surface tension. Thus a presence of a monomolecular organic layer at the air-water interface lowers the surface tension (**Petty 1996; Hiemenz et al. 1997**).

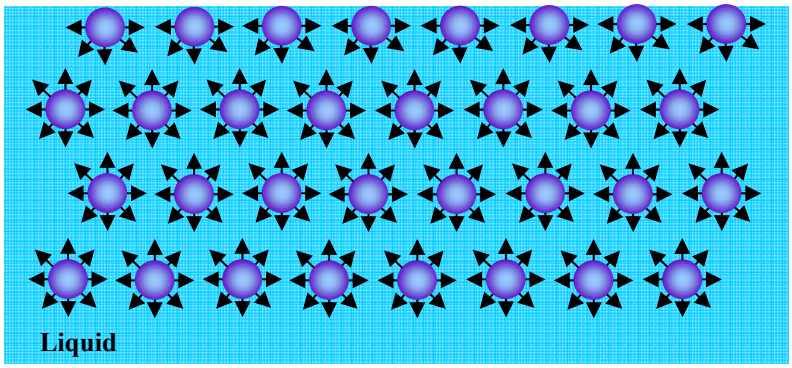

Figure 3-1. Surface tension - Forces among the molecules in bulk and at interface

3.1.2 Surface Pressure

The surface pressure of a monolayer is defined as the lowering of surface tension of the pure liquid due to the presence of the monolayer and is given by the relationship:

$$\pi = \gamma_0 - \gamma \qquad \textbf{Equation 3.1-1}$$

where γ_0 is the surface tension of the pure liquid and γ is the surface tension of the monolayer-covered surface. The surface tension and thus the surface pressure are expressed in mN/m (= dyn/cm). The variation of π with the area available to the surface active film is represented by a π – A diagram, where A ($Å^2$) is the area per molecule given by the equation:

$$A = \frac{a}{cN_{AV}V} \qquad \textbf{Equation 3.1-2}$$

a is the total film area ($Å^2$), c is the molar concentration of the spreading solution (see **Section 3.1.5**) and V(L) is the volume of the spreading solution.

The maximum value of π over aqueous solutions is 72.8mNm^{-1} at 20°C, which is the surface tension of water (**Roberts 1990; Petty 1996**).

3.1.3 Wilhelmy plate method

The Wilhelmy plate method is used to measure the surface pressure. In this method, a measurement is made by determining the force, due to surface tension, on a plate suspended so that it is partially immersed in the subphase as shown in **Figure 3-2**. This force is then converted into surface pressure (mN/m) by dividing with the dimensions of the plate, **Figure 3-2**. The plate used is very thin and usually made of platinum, but plates made of glass, quartz, mica and filter paper have also been used. The forces acting on the plate when placed on the liquid surface are gravity, downward surface tension, and upward buoyancy due to displaced water. For a rectangular plate of length l_p, width w_p, thickness t_p, and plate density ρ_p, immersed to a depth h_l in a liquid of density ρ_l, the net downward force is given by the following equation:

$$F = \rho_p g\, l_p\, w_p\, t_p + 2\gamma\,(t_p + w_p)\cos\theta - \rho_l g\, t_p\, w_p\, h_l \qquad \textbf{Equation 3.1-3}$$

where γ is the liquid surface tension, θ is the contact angle of the liquid on the solid plate and g is the gravitational force constant. The surface pressure is then determined by measuring the change in F for a stationary plate between a clean surface and the same surface with a monolayer present. If the plate is completely wetted by the liquid (i.e. $\theta = 0$, $\cos\theta = 1$) the surface pressure is obtained from the following equation:

$$\pi = \gamma_0 - \gamma = -(\gamma - \gamma_0) = -\Delta\gamma$$
$$\pi = -[\Delta F/2(t_p + w_p)] \qquad \textbf{Equation 3.1-4}$$

If the plate is so thin that, $w_p >> t_p$

$$\pi \cong -\Delta F / 2w_p \qquad \textbf{Equation 3.1-5}$$

The force is determined by measuring the change in the apparent mass of the plate, which is directly attached to a sensitive electrobalance (**Birdi 1989; Petty1996**)

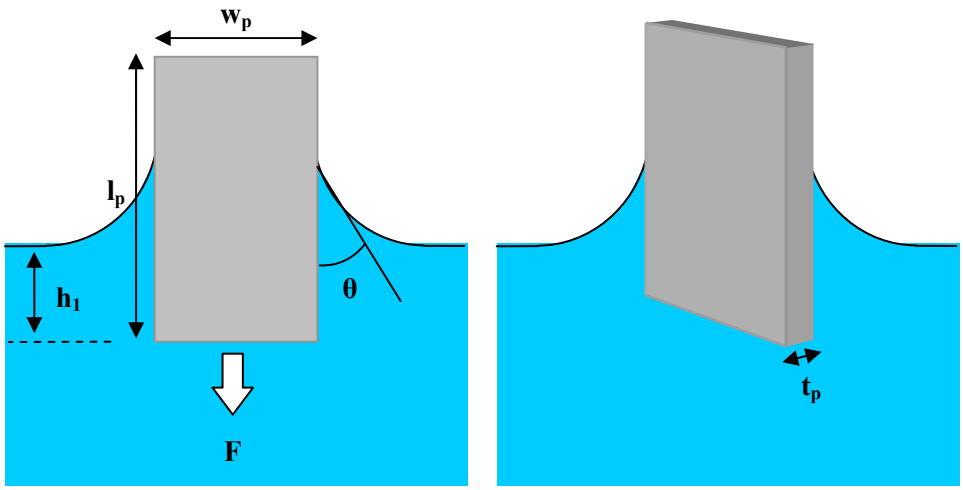

Figure 3-2. Wilhelmy plate

3.1.4 The Langmuir Balance

The basic film balance is an instrument that allows the surface area to be varied and accurately measured while changes in surface pressure are simultaneously monitored. **Figure 3-3** shows a schematic picture of a Langmuir balance. The trough that comes into direct contact with the subphase is usually made of Teflon, which has the advantage of being inert and able to withstand the organic solvents used for monolayer spreading. Also, Teflon prevents any leakage of the subphase over the edges. Temperature control of the liquid is achieved by circulating water from a thermostated bath in channels placed underneath the Teflon trough. The surface area of the trough can be varied by sweeping two hydrophobic movable barriers over the surface of the trough. The barriers are also made of Teflon and they are heavy enough to prevent any leakage of the monolayer beneath the barrier. The surface pressure and the mean molecular area are continuously monitored during the compression (**MacRitchie 1990; Petty 1996**).

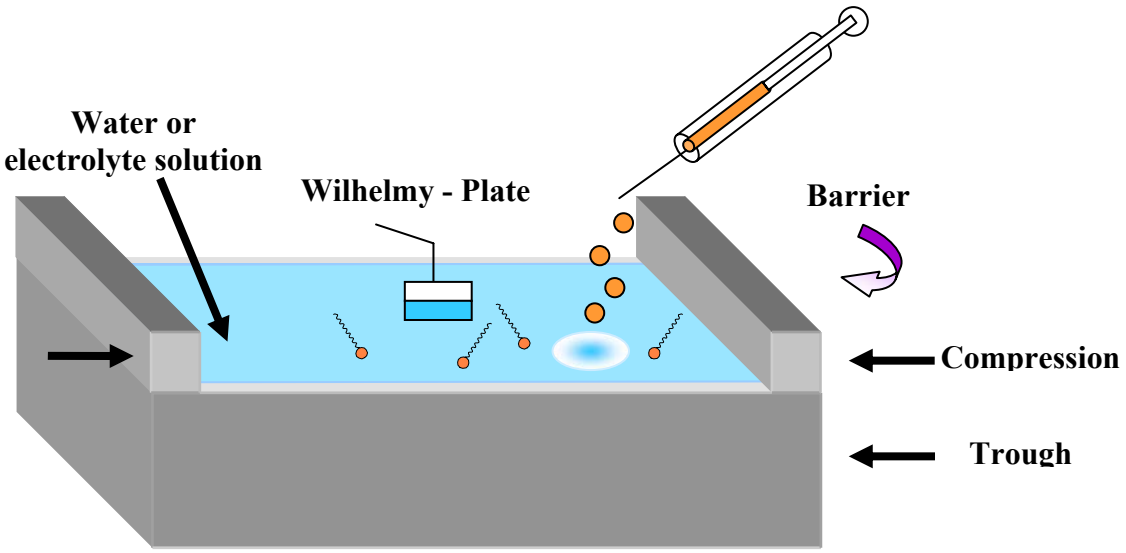

Figure 3-3. The Langmuir Balance

3.1.5 Monolayer Spreading

Monolayer forming materials are spread at the air-water interface by first dissolving them in an appropriate solvent. The solvent used must be able to dissolve an adequate quantity of the monolayer material (0.1 – 1mg/ml), must not react chemically with the material or dissolve in the subphase and also must evaporate within a reasonable period of time. Solvents which are commonly used for monolayer spreading are chloroform, n-hexane, toluene, hexadecane etc.
A microsyringe is used to dispense the spreading solution on the subphase. The application of the sample is generally accomplished by allowing drops of the spreading solution to fall near the centre of the subphase surface. The volume spread is normally on the order of 50 – 150 µl (**Roberts 1990**).

3.1.6 Formation and Stability of Monolayers

When a small quantity of an insoluble, non-volatile organic substance is placed on the water surface, one of the following results may be observed: a) The substance may remain as a compact drop leaving the rest of the liquid surface clean, or b) it may expand over the entire water surface. The stability of the formed monolayer is determined by the interaction forces

between the substance itself, the substance and the subphase, which is usually water or an aqueous solution, and between the molecules of the subphase.

A stable monolayer is formed on water when the work of adhesion between the substance and water is greater than the work of cohesion of the substance itself. Under these conditions, the substance spreads over the entire water surface and forms a monomolecular film. When the attractive forces between the molecules and the water subphase are small, the stability of the two-dimensional film is very weak and it breaks down under a very small compression. On the contrary, when strong interactions exist between the polar groups of the molecules and the hydrocarbon chains of the molecules (Van der Waals forces) forming the monolayer, then the film molecules cohere and they are not able to move freely. (**Birdi 1989**)

3.1.7 Monolayer Compounds

A wide variety of organic substances can form monolayers on the air-water interface, the simplest ones being single-chain fatty acids and alcohols. However, many more complex molecules have been proved to form monomolecular films at the air-water interface such as: dyes, porphyrins, fullerenes, vitamins, sterols, polymers, proteins and phospholipids. Most monolayer forming molecules are amphiphilic, see **Chapter 2**, **Section 2.1**. Phospholipids are the most important type of amphiphilic molecules forming monolayers; see **Chapter 4**, **Section 4.2**.

3.1.8 Surface – Pressure Isotherms and Monolayer Phases

(Davies et al. 1963; Birdi 1989; MacRitchie 1990; Roberts 1990; Petty 1996)

As the monolayer is compressed on the water surface, it will undergo several phase transformations. The phase transitions or monolayer states that are observed are analogous to the three-dimensional gas-liquid-solid states. The phase changes can be identified by measuring the surface pressure as a function of the area of water surface available to each molecule. This measurement is carried out at constant temperature and is known as a surface pressure - area isotherm or simply "isotherm". Usually an isotherm is recorded by compressing the film (reducing the area with the barriers) at a constant rate while continuously monitoring the surface pressure. The surface pressure - area isotherm is the two-dimensional equivalent of the pressure-volume isotherm in three-dimensional space. **Figure 3-4** shows a theoretical π – A plot. Not all the phases shown in **Figure 3-4** are always

observed. The presence or absence of the various phases in the π – A curve depends on various parameters as discussed in **Section 3.1.9**

3.1.8.1 Gas Phase

When the area available for each molecule on the air-water interface is many times larger than the molecular dimension, a "gaseous" phase (G) is formed, which is the simplest phase of a monolayer at the air-water interface. The film consists of molecules that are far apart on the water surface, thus the interactions between the molecules are negligible, but the attraction of the polar headgroups to the water phase and the hydrophobic effect of the apolar residues are sufficient to keep the amphiphilic molecules at the surface.
The behavior of gaseous monolayers can be modeled by **Equation 3.1-6** assuming that the molecules have an average translational kinetic energy of ½ kT for each degree of freedom.

$$\pi(A - A_0) = kT \qquad \textbf{Equation 3.1-6}$$

where A ($Å^2$) is the total surface area available to each molecule and A_0 ($Å^2$) is the excluded area per molecule, which depends on the compound used to form the monomolecular film. This relation assumes that there is no attraction but only hard-core repulsion between the molecules in the film and thus as $\pi \rightarrow 0$, $A \rightarrow \infty$ ($\pi A \rightarrow kT$) and as π increases, $A \rightarrow A_0$ (hard-core interaction). In general, ideal gas behavior is observed only when the distance between the amphiphilic molecules is very large and as a result the value of π is very small, e.g., less than 0.5 mN/m.

3.1.8.2 Liquid expanded phase

As a gaseous monolayer is compressed on the subphase surface, the surface area of the monolayer is reduced and the expanded (liquid-like) phase appears. The phase transition (G – LE) is usually accompanied by a constant pressure (horizontal) region in the isotherm (a "plateau"), in which the floating film is a mixture of the two phases. The hydrocarbon chains of the molecules in such a film are randomly oriented, with liquid-like arrangement and variable orientations. As the molecular area is progressively reduced the monolayer goes into the liquid expanded state. The interactions of the hydrocarbon chains of the molecules

(induced dipole or dispersion forces) and those between the polar headgroups (dipole or ionic interactions) become important.

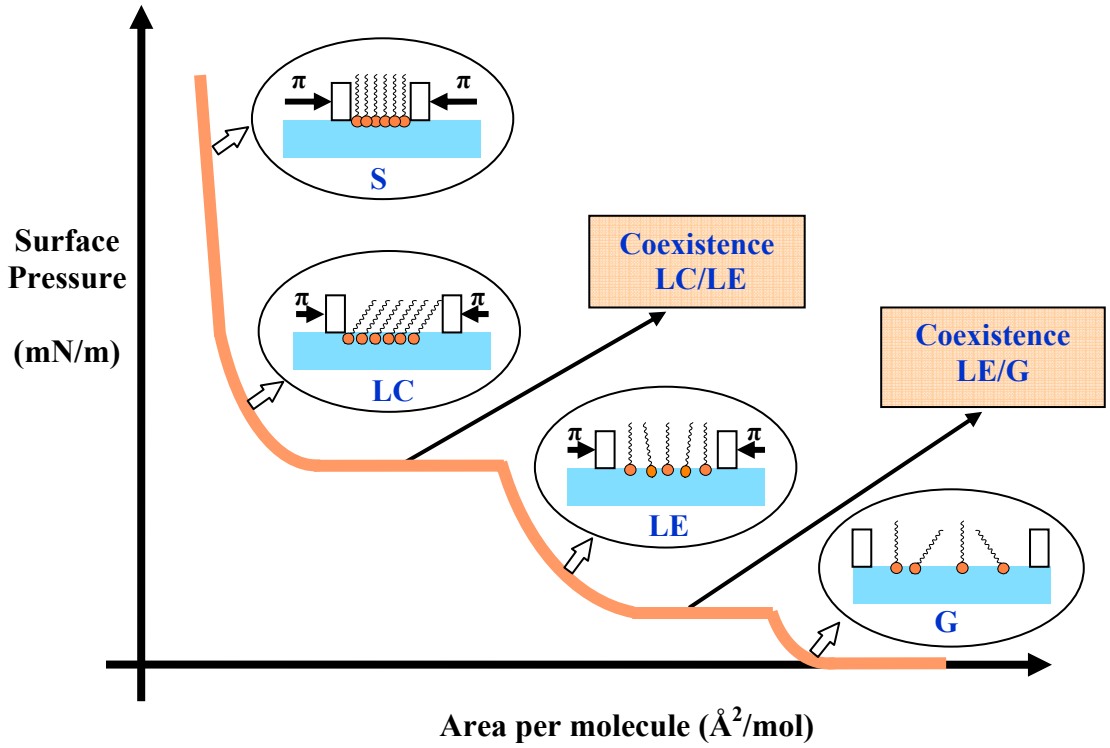

Figure 3-4. Surface Pressure – Area Isotherm

The equation of state for the liquid expanded phase is often well represented by the following relationship:

$$(\pi - \pi_a)(A - A_0) = kT \qquad \textbf{Equation 3.1-7}$$

The pressure π_a is contributed to the strong cohesion of the hydrocarbon chains, the origin of which lies in the Van der Waals forces of attraction between the hydrocarbon chains. An empirical equation for π_a (dynes/cm) is given by:

$$\pi_a = \frac{-400m}{A^{3/2}} \qquad \textbf{Equation 3.1-8}$$

where m is the number of methylene groups in the hydrocarbon chain of a molecule and A is in $Å^2$ per long-chain.

3.1.8.3 Liquid condensed phase

As the area per molecule is further decreased, the liquid condensed phase is observed. The appearance of the liquid condensed phase is accompanied by a plateau as observed in the transition from the gas phase to the liquid expanded phase. At the end of the plateau region the liquid condensed phase is formed. In this phase the molecules are closely packed and are oriented with their hydrocarbon chains pointing away from the water surface. In addition, the hydrocarbon chains are usually tilted with respect to the surface normal at a fixed direction.

3.1.8.4 Solid phase

The solid phase is observed when the molecules at the air-water interface adhere very strongly to each other through Van der Waals forces. The solid phase is found when the monolayers are compressed to very high surface pressures. The onset of the solid phase is observed by a sudden increase in the slope of the isotherm as shown in **Figure 3-4**. The film is characterized as rigid with low compressibility and high viscosity. The molecules on the surface are ordered and close-packed and create a compact 2D network. In this phase, the hydrocarbon chains of the molecules are perpendicular to the air-water interface with an all-trans (straight) chain configuration.

3.1.8.5 Collapsed phase

As the surface pressure continues to increase, with decreasing surface area, a point is reached where the surface area per molecule becomes very small, and as a result, the monomolecular film collapses. The forces acting on the monolayer at this point are very strong. The onset of collapse depends on many factors, such as the rate at which the monolayer is compressed, the nature of the substance and the interaction between the subphase and the polar headgroup of the molecule.

3.1.9 Parameters influencing the Phase Behavior of the monolayers

The phase behaviour of a monolayer is mainly determined by the physical and chemical properties of the amphiphile (architecture of the hydrophobic chains and nature of the polar group), the subphase temperature and the subphase composition (pH and counter ions). For example, various monolayer states exist depending on the length of the hydrocarbon chain and the magnitude of the attractive and repulsive forces existing between head groups. An increase in the chain length increases the attraction between molecules, condensing the π – A isotherm. On the other hand, if an ionisable amphiphile is used, the ionisation of the head groups induces repulsive forces tending to oppose phase transitions. In addition, the temperature has a great effect on the surface pressure behaviour of monolayers; the lower the temperature, the smaller the surface area per molecule adopted by the monolayer. Thus, lower temperatures induce solid compressed phases.

3.1.10 Precautions for π – A measurements

The presence of a surface-active contaminant, even in very small concentrations, can greatly influence the surface tension if the proper conditions of cleanliness are not enforced. In order to obtain reproducible and accurate π – A isotherms, many precautions must be taken into account before and during the π – A measurement:

a) Adequate cleaning of the trough, the barriers and the subphase surface, before monolayer spreading, is an essential requirement for obtaining accurate results. The trough and the barriers are thoroughly cleaned with extra pure water, absolute ethanol and acetone. The surface area is usually reduced to a minimum by compressing the barriers over the surface and then cleaned by suction with a glass capillary tube attached to a suitable pump.
b) Weighing and volumetric errors can affect the concentration of the spreading solution. The volumetric flasks and the microsyringe used to spread the monolayer at the air-water interface must be often calibrated. The concentration of the solution depends also on the purity of the compound and the temperature of the environment. The solutions must be made at the experimental temperature and maintained at this temperature when the sample is spread on the water surface.

c) Impurities in the spreading solvent as well as in the subphase solution can introduce errors. The most commonly used subphase is water which can be deionized through a reverse osmosis system that contains a final filter to remove bacteria (organic contaminants) and residual dust. Other aqueous solutions may be used as subphase solutions such as electrolyte solutions. The best method for destroying the organic impurities present in salts is to heat them in a furnace at very high temperatures (**MacRitchie 1990; Ulman 1991**).

3.1.11 Experimental Setup

Isotherm measurements were carried out with a KSV 3000 Langmuir trough (KSV Instruments, Finland) equipped with a Wilhelmy plate for the determination of the surface pressure with accuracy ± 0.01 mN/m, as shown in **Figure 3-5**. The trough surface area was 864 cm^2 and the subphase volume was 0.95 L. All experiments were performed at 22.0 ± 0.1 °C. The temperature of the subphase was maintained constant with a Julabo recirculating thermostat. The surface pressure – area isotherms were registered while compressing the monolayers with two barriers at a constant speed of 10 mm/min allowing the symmetric compression of the film.

Figure 3-5. KSV Langmuir Blodgett 3000

3.2 Brewster angle microscopy (BAM)

Brewster angle microscopy (BAM) is an increasingly important technique for the study of thin films at interfaces. The principle of the observation of monolayers at the air-water interface using BAM was introduced in 1991 by two separate groups, **Hönig – Möbius** (**Hönig et al. 1991**) and **Hènon – Meunier** (**Hènon et al. 1991**). The method is based on the minimum reflectance of light polarized parallel to the surface at the Brewster angle for a pure air-water interface. When a monolayer is present on the air-water interface it alters the optical properties of the interface, resulting in enhanced reflectivity in film-covered regions. Thus the BAM technique probes the two-dimensional organization of monolayers, including domain size and shape and heterogeneity in Langmuir films.

Compared to fluorescence microscopy BAM has several advantages. It does not need the addition of a fluorescent probe, it has greater sensitivity than the fluorescence technique, any film having a refractive index different from that of water can be observed, and the monolayer is not perturbed by the absorption of light by fluorescent probes. Moreover, BAM allows a more direct study of the optical anisotropy of monolayers than fluorescence microscopy.

3.2.1 Principles of Brewster Angle Microscopy

Brewster angle microscopy is based on the reflection of the "p-polarized light" when travelling between two dielectric media of differing refractive index.

Fresnel's equations describe the reflection and transmission of electromagnetic waves at an interface and are used to calculate the reflection coefficient R and transmission coefficient T, which are the fraction of the incident light that is reflected and refracted from an interface.

In **Figure 3-6** two media of refractive index n_1 and n_2 ($n_2 > n_1$) meet at an interface. When light moves from the medium of refractive index n_1 into the second medium of refractive index n_2, both light reflection and refraction may occur.

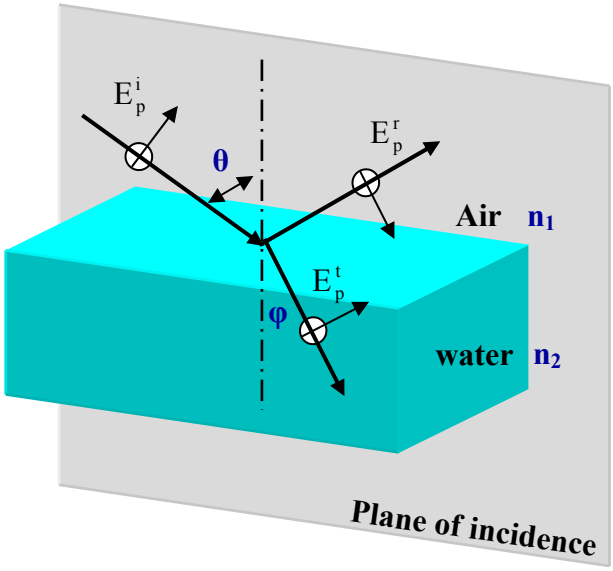

Figure 3-6. Incident, reflected and transmitted plane waves at an interface between medium 1 and 2.

The reflection coefficient R and transmission coefficient T depend on the polarization of the incident ray. If the light is polarized with the electric field of the light perpendicular to the plane of incidence in **Figure 3-6** (s-polarized), the reflection coefficient is given by (**Lyklema 2000; Hecht 1987; Feder 1997**):

$$R_s = \left\{\frac{n_1\cos\theta - n_2\cos\varphi}{n_1\cos\theta + n_2\cos\varphi}\right\}^2 = \left\{\frac{\sin(\theta-\varphi)}{\sin(\theta+\varphi)}\right\}^2 \qquad \textbf{Equation 3.2-1}$$

where φ can be derived from θ using Snell's law:

$$n_1\sin\theta = n_2\sin\varphi \qquad \textbf{Equation 3.2-2}$$

If the incident light is polarized in the plane of incidence in **Figure 3-6** (p-polarized), the reflection coefficient is given by (**Lyklema 2000; Hecht 1987; Feder 1997**):

$$R_p = \left\{\frac{n_2\cos\theta - n_1\cos\varphi}{n_2\cos\theta + n_1\cos\varphi}\right\}^2 = \left\{\frac{\tan(\theta-\varphi)}{\tan(\theta+\varphi)}\right\}^2 \qquad \textbf{Equation 3.2-3}$$

The transmission coefficient in each case is given by $T_s \equiv 1 - R_s$ and $T_p \equiv 1 - R_p$.

For a beam of p-polarized light there is an angle of incidence *theta* at which no reflection occurs, R_p goes to zero and the p-polarized incident ray is purely refracted as shown in **Figure 3-7**.

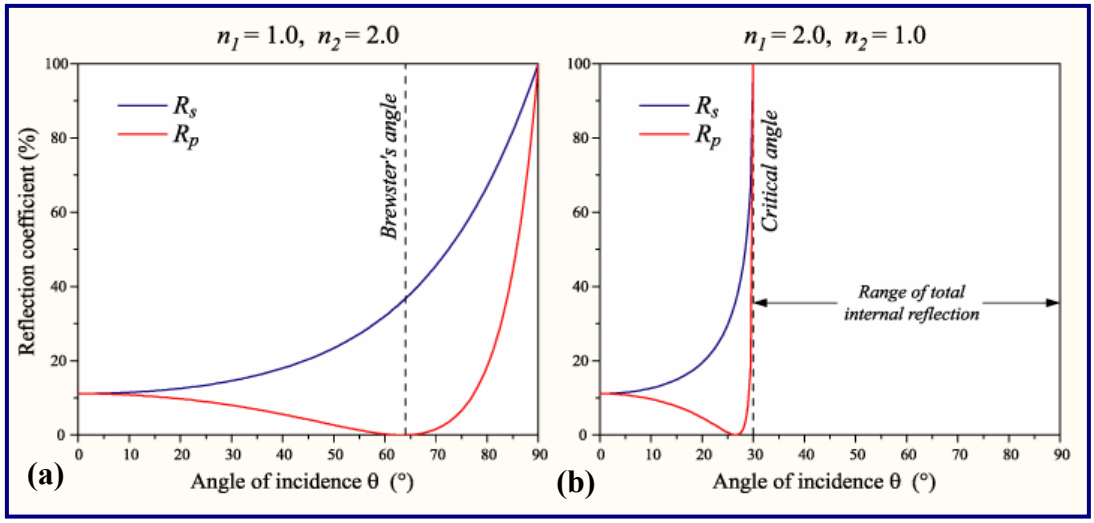

Figure 3-7. Reflectance R_p and R_s for p and s polarized light as a function of the incident angle θ for $n_1 < n_2$ (a) and $n_1 > n_2$ (b)

This angle is known as Brewster-angle and it was discovered by Sir David Brewster (1781-1868). It can be calculated by Snell's law, and is equal to:

$$\theta_{BA} = \arctan\left(\frac{n_2}{n_1}\right) \qquad \textbf{Equation 3.2-4}$$

When the incident angle of light is at the Brewster angle, θ_{BA} of an interface, the *reflectivity* R_p of the p-polarized light vanishes. For a pure water surface the Brewster angle is 53.06° according to Fresnel's equations and based on the fact that the refractive index n_1 of air is 1.0 and n_2 of pure water is 1.33. If we use p-polarized light (when R_p is zero) there is no reflection from the interface and the water surface appears as a dark phase to a CCD camera. Formation of a thin layer at the interface with a refractive index different than that of water modifies the Brewster angle condition of an interface. The reflectivity of a monolayer can be estimated by modelling the surface as a three layer system.

The model is based on the classical electromagnetic theory for a system of three parallel, optically isotropic layers; a semi-infinite layer of air with refractive index n_1, a monolayer with complex refractive index ($n_2 + ik_2$) and thickness d, and a semi-infinite layer of water, with refractive index ($n_3 + ik_3$) where n_i is the real refractive index and k_i is the absorption constant of the ith phase.

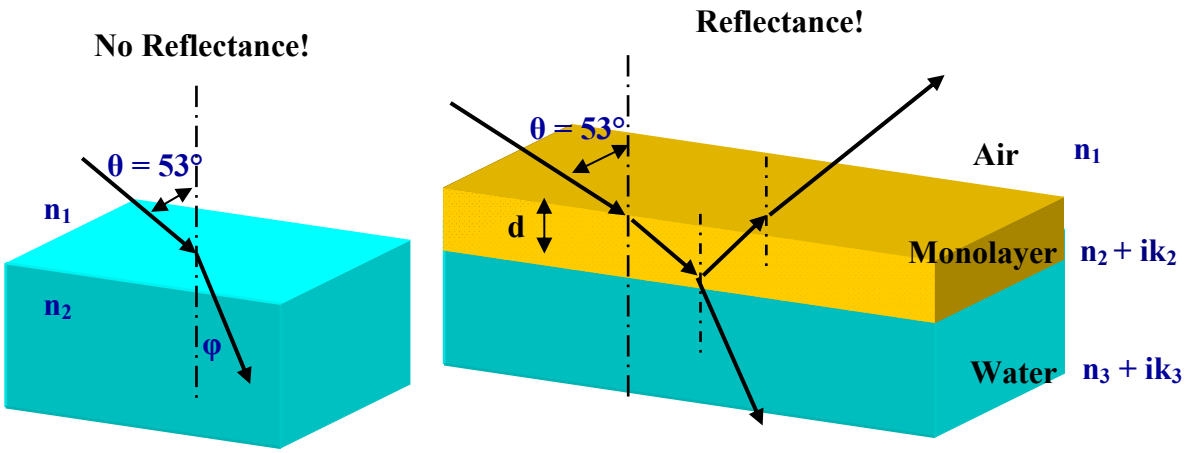

Figure 3-8. Reflection and transmission of light by a multilayer system.

The reflection coefficient in the presence of a monolayer (three-layer system), regardless of the polarization, is given by the following equation: (**Hecht 1987; Dluhy 1986**):

$$r_{123} = \frac{r_{12} + r_{23}e^{2i\beta}}{1 + r_{12}r_{23}e^{2i\beta}} \qquad \textbf{Equation 3.2-5}$$

where

$$\beta = 2 \cdot \pi \left(\frac{d}{\lambda}\right) n_2 \cos\theta \qquad \textbf{Equation 3.2-6}$$

and λ is the wavelength of the incident light, θ the angle of incidence, d and n_2 the monolayer thickness and refractive index respectively, and where

$$r_{ab} = \frac{n_b \cos\theta_a - n_a \cos\theta_b}{n_b \cos\theta_a + n_a \cos\theta_b} \qquad \textbf{Equation 3.2-7}$$

is the ratio of the reflected electric field to the incident electric field at the interface between two semi-infinite media, a and b, and θ_a is the angle that the light makes with the surface normal in medium a.

The reflectance R_{123} of the three-layer system is then found from the reflection coefficient r_{123} with:

$$R_{123} = |r_{123}|^2 \qquad \textbf{Equation 3.2-8}$$

which holds for both p- and s-polarized light.

The reflectance R depends on the monolayer thickness. In particular, the reflectance R increases as the monolayer thickness increases. Real interfaces have a nonzero thickness, roughness and anisotropy. Their coefficient of reflection R_p has a minimum at the Brewster angle but is not perfectly zero; it has a low value ($\approx 10^{-6} - 10^{-5}$), which depends strongly on the interfacial properties. The various contributions to this value are:

(i) The roughness of the interface, i.e. the variation to flatness. The roughness of liquid interfaces is due to the thermal fluctuations (capillary waves). For monolayers on the air-water interface surface tension is large, and the thermal fluctuations are of low amplitude, so one can neglect this contribution. This approximation introduces a small error in the calculated thickness of films of about 3Å, which is equal to the roughness of the pure air-water interface. (**Braslau et al. 1985**)

(ii) The thickness of the interface. The interface can be considered as an "interfacial zone" of transition between the two media rather than as a sharp dividing line. The interfacial zone is in general of molecular thickness. Moreover, when a water-air interface or a water-oil interface is covered by a monolayer, it has an additional thickness, due to the existence of the monolayer.

(iii) The optical anisotropy. The optical anisotropy of ordered monolayers at the air-water interface is due to the orientational order of the lipid molecules with respect to the water surface and its changes during the compression of the monolayer. Measurable changes in anisotropy that can be observed by BAM are produced by (a) regions of the monolayer which differ in density or orientation of the molecules with respect to the water interface, (b) transitions from a phase in which the molecules are tilted to one in which molecules are normal to the surface, (c) transitions between phases in which there are differences in the molecular tilt order, and (d) domains with different reflectance having the same molecular tilt

angle but with different orientations in the monolayer plane. It follows that the gas phase (G) and liquid expanded phase (LE), which are isotropic, cannot be visualized with Brewster angle microscopy. BAM is strictly useful for the anisotropic liquid condensed (LC) and solid phase (S).

3.2.2 Domain Nucleation and Growth – Domain Shape Morphology

Domain shape depends on the monolayer compound used to form the monolayer and the experimental conditions (temperature, pH of subphase, ionic conditions etc). Different theories have been developed in attempts to predict the shapes of lipid domains. The most successful theory for phospholipid domain growth to date, assumes a competition of molecular interactions (**McConlogue et al. 1999; Krüger et al. 2000; Kane et al**. **2000**): the line tension, λ, (analogous to a two dimensional surface tension) which favours compact circular domains and the long-range electrostatic dipolar repulsion, F_{el}, which favours domain elongation and narrowing. The shape of an individual solid domain is determined by the interplay of these forces:

$$F = \lambda p + F_{el} \qquad \textbf{Equation 3.2-9}$$

where p is the perimeter of the solid domain. The free energy is minimized with respect to the 2D-shapes of the solid domains.

In the "gaseous" state of the monolayer, the domains cover a small fraction of the area of the air-water interface and are relatively far apart therefore the electrostatic interaction is small and circular shapes result. As the monolayer is compressed on the water surface and the surface area of the monolayer is reduced, the domains grow in area; they come closer to each other and tend to thin in one dimension as a result of the long-range dipolar forces. In general, in the absence of charged headgroups, the minimum energy domain shape is determined entirely by line tension and is circular. In the other extreme, when the charge is large and the line tension is weak, the minimum energy shape is highly elongated (if the domain does not break into pieces).

Most theories for predicting domain shapes have made the approximation that the competition between electrostatic dipole-dipole interactions and line tension fully determines the actual domain shape. However, in recent studies (**Krüger et al. 2000; McConlogue et al. 1999;**

Kane et al. **2000**) it was recognized that molecular chirality of the compound used (if it is chiral) plays a significant role in determining the shape of lipid domains. For example, the stereoisomers of the lipid DPPC form domains, which are precise mirror images. While present theories can explain the domain shapes in many systems dominated by electrostatic interactions and line tension only, the actual shapes produced by such models do not exhibit the striking and specific chirality of the DPPC domains. DPPC domain shapes can be understood by molecular packing considerations or by an induced chirality in the ordering of the liquid-condensed domains.

There are many examples in the literature of the dependence of domain morphology on the chemical nature of the compound forming the monolayer and the experimental conditions. The effect of chain substitution by a hydroxyl group (OH) was demonstrated by (**Weidemann et al. 1995; Brezesinski et al. 1995; Gehlert et al. 1996; Vollhardt 2002**) by a comparison of the domain shape of 1-monostearoyl-glycerol and 1-(12 hydroxyl-stearoyl)-glycerol as shown in **Figure 3-9**. The substitution of the OH group has a dramatic effect on the domain shape morphology changing the circular domains of 1-monostearoyl-glycerol into a stripe-like domain shapes for 1-(12 hydroxyl-stearoyl)-glycerol.

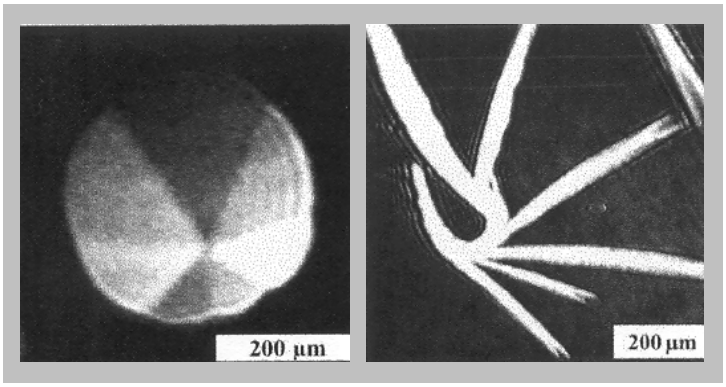

Figure 3-9. Effect of chain substitution on monostearoyl-glycerol

The effect of the hydroxyl group position (2- or 3- position) near the COOH group of hydroxypalmitic acids was studied by **Siegel et al. 2005**. The domain shapes of the two amphiphiles are similar but the domain shape for 3-hydroxypalmitic acid is more compact with irregular domain shape of fractal-like arms, **Figure 3-10**, indicating a reduced long-range orientational order.

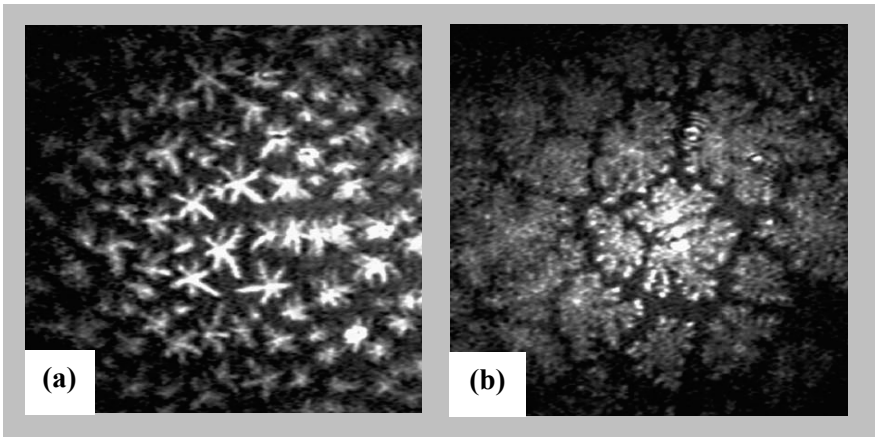

Figure 3-10. Condensed phase domains of 2- (a) and 3- (b) hydroxypalmitic acid monolayers. Image size: 750µm x 750µm (Siegel et al. 2005)

Siegel et al. 2005 also studied the domain shape morphology for 9-hydroxypalmitic acid as a function of temperature, which was found to have an important effect as shown in **Figure 3-11**. Grain-like domains are formed at low temperatures (5 °C) while as the temperature increases six-arm structures with a six-fold symmetry are formed.

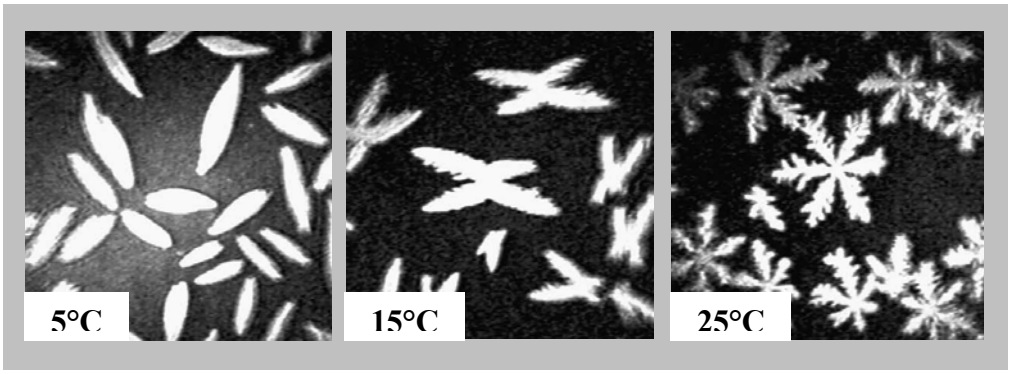

Figure 3-11. Temperature dependence of the domain shape of 9-hydroxypalmitic acid. Image size: 750µm x 750µm (Siegel et al. 2005)

A dramatic effect on the domain shape morphology was also shown by **Weidemann et al. 1996** with a small variation in the polar headgroup region of four phospholipids (DPPE, DPP(Me)E, DPP(Me)$_2$E and DPPC. The domain shape is completely different as shown in **Figure 3-12**. Following the substitution of a hydrogen by a methylene group, DPPE and DPP(Me)E form dendritic structures, DPP(Me)$_2$E forms circular domains and DPPC forms triskelion shape domains.

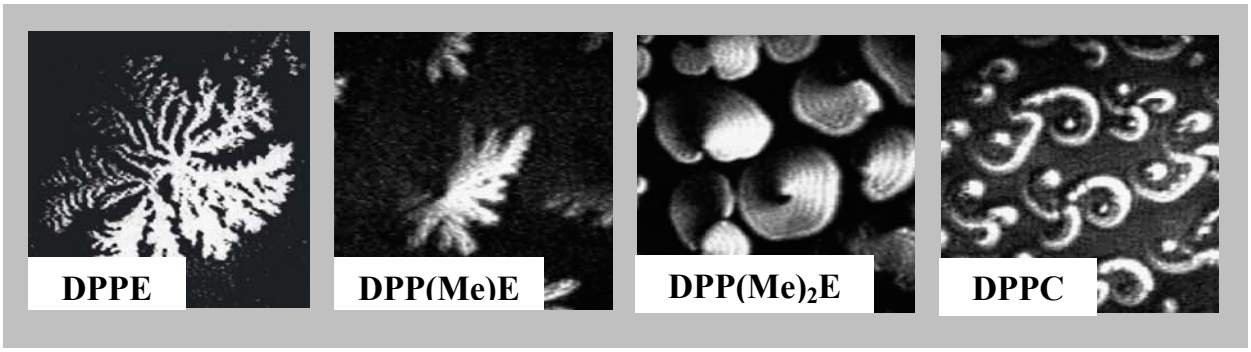

Figure 3-12. Effect of the headgroup variation on the domain shape. Image size: 500µm x 500µm (Weidemann et al. 1996)

The effect of different polar headgroups on the structural characteristics of phospholipid monolayers has been studied by **Miňones et al. 2002** who showed that by changing the headgroup of a monolayer-forming compound the domain shapes change significantly. The phospholipids used were phospatidylcholine DPPC, phospatidylglycerol DPPG and phosphatidylserine DPPS. DPPC is zwitterionic while DPPG and DPPS are negatively charged. The BAM images taken are shown in **Figure 3-13**. The domain size of the LC phase of DPPC as shown in **Figure 3-13** cannot be directly correlated with that found by **Weidemann et al. 1996** (**Figure 3-12**) because no details exist about the size of the domains in the specific reference (**Miňones et al. 2002**).

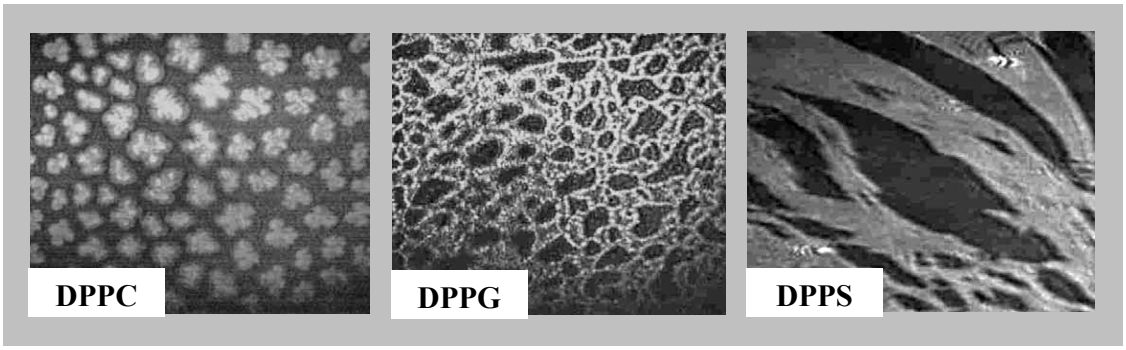

Figure 3-13. BAM images of phospholipid monolayers with different headgroup. (Miňones et al. 2002)

The molecular chirality of a compound was also found to influence the shape of domains as mentioned above. **Moy et al. 1986; Vollhardt 1996 and 2002** have shown that the equilibrium domain shapes are triskelions curved oppositely for the two enantiomeric forms (clockwise for D-DPPC and counter clockwise for L-DPPC) and non-curved for the racemic mixture, **Figure 3-14**.

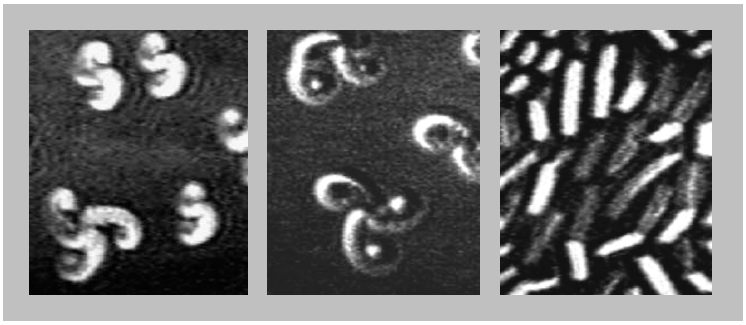

Figure 3-14. Chiral discrimination in DPPC monolayers. [Vollhardt 2002(b)]

The domain shape can also be influenced by the presence of ions in the subphase solution, especially when the monolayer forming compounds are charged. A polymerizable pyridine amphiphile [4-(10,12-Pentacosadiynamidomethyl)pyridine] forms stable monolayers at the air/water interface which are affected by the presence of Cu^{2+} ions in the subphase solutions. It was shown (**Werkman et al. 1998**) that copper ions form complexes with the pyridine amphiphile changing the shape of the domains formed, **Figure 3-15**.

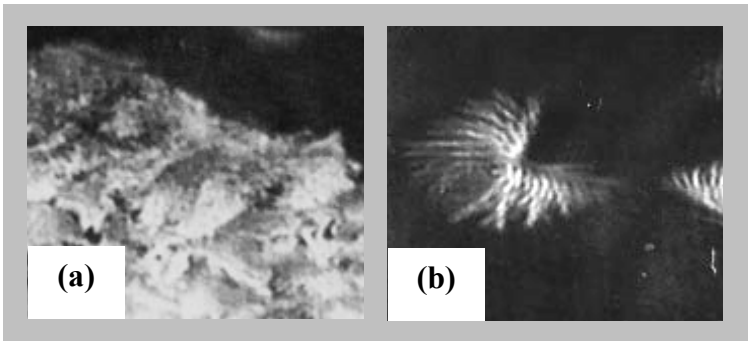

Figure 3-15. Pyridine amphiphile without (a) and with (b) Cu^{2+} ions in the subphase. (Werkman et al. 1998)

The injection of Ca^{2+} ions under a DMPA monolayer was studied by Wu et al. 1998, who showed that the domain shapes change (rather little) upon addition of Ca^{2+} at a final concentration of 1mM. The domains grow in size and have a dendritic shape, **Figure 3-16**. **Nieto-Suarez et al. 2004** have found similar results, using ethyl palmitate (EP) as a nonionic amphiphile in the presence of Ca^{2+} ions in the subphase. The presence of ions does not change greatly the domain shape of EP. The domains grow in size having a dendritic shape similar to **Figure 3-16(b)**.

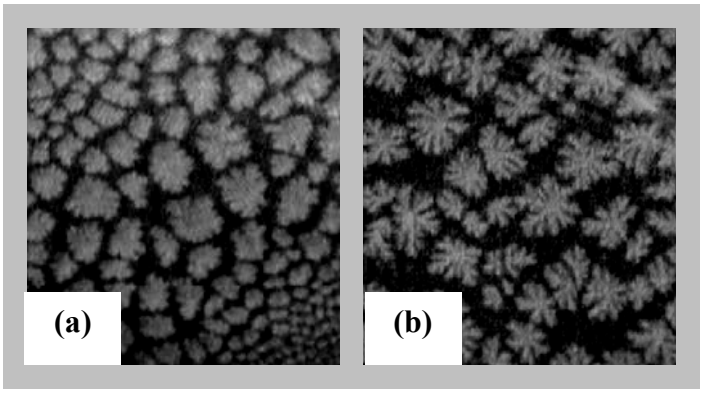

Figure 3-16. Pure DMPA (a) and DMPA in presence of Ca^{2+} ions (b). Scale 250μm (Wu et al. 1998)

3.2.3 Experimental Setup

The Brewster-angle microscope that we have used to study the morphology of the lipid monolayers was the BAM2 from NanoFilm Technology, Göttingen, Germany, shown in **Figure 3-17**. The lateral resolution of the BAM2 with a 20 mW He-Ne ion laser of wavelength equal to 514 nm is 2 μm. The reflected light is imaged using a high grade CCD camera. A general BAM setup for studying the topography of Langmuir monolayers is shown in **Figure 3-18**.

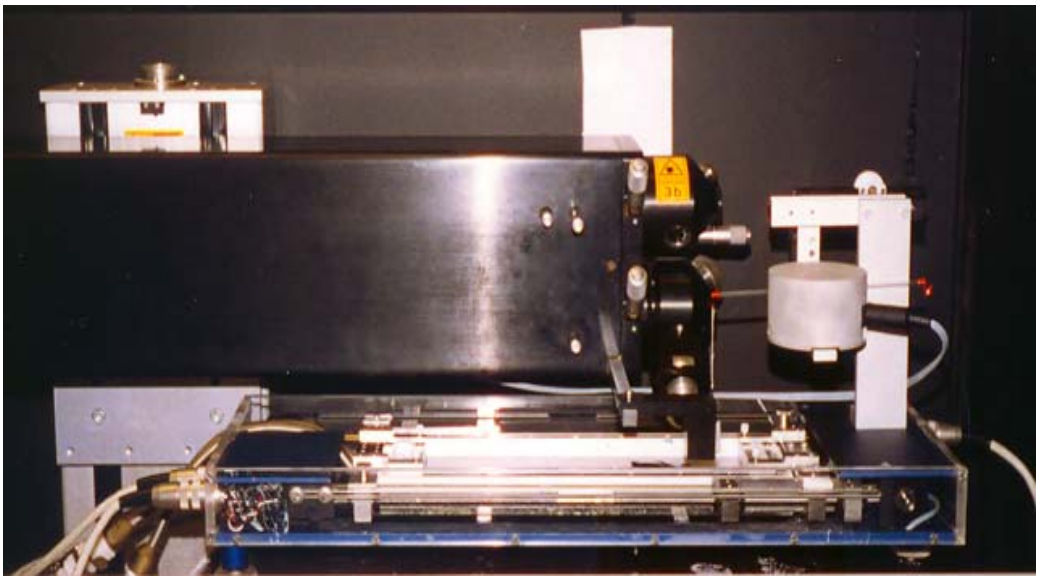

Figure 3-17. Brewster angle microscope

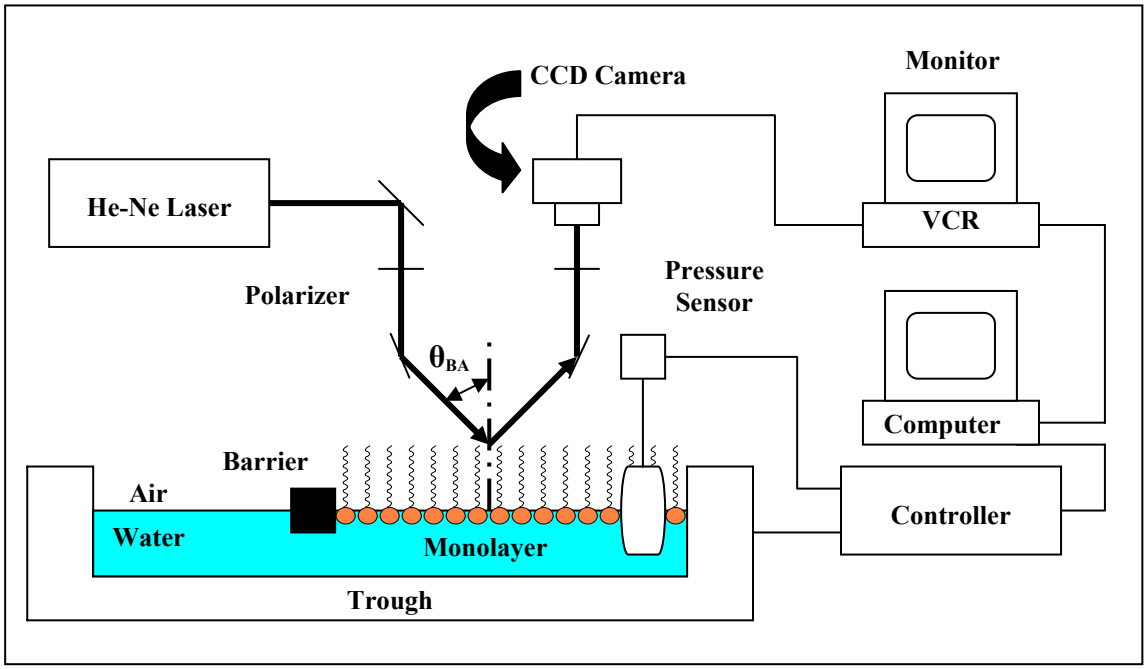

Figure 3-18. Schematic drawing of BAM for a Langmuir monolayer study

BAM images of DPPC monolayer at the air-water interface for various surface pressures are shown below. **Figure 3-19(a)** shows the liquid expanded (LE)/liquid condensed (LC) coexistence region of the monolayer of DPPC. The bright domains in the picture correspond to the denser liquid condensed (LC) phase and the dark background corresponds to the less dense liquid expanded (LE) phase. As the monolayer is compressed further the pressure rises steeply and the LC domains grow in size (**Figure 3-19(b)** to **3-19(e)**).

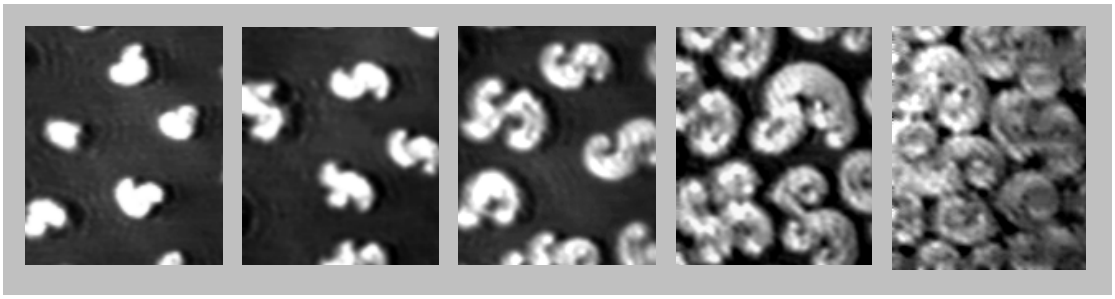

Figure 3-19. DPPC domain shapes. Coexistence of LE/LC DPPC domains (a) Growth of LC domains of DPPC (b) – (e)

3.3 Infrared Reflection Absorption Spectroscopy (IRRAS)

The in *situ* and non-invasive characterization of monomolecular films spread on the air/water interface is a fundamental issue of particular significance in the study of biological systems. IR reflection absorption spectroscopy (IRRAS), also sometimes referred to as IR external reflection spectroscopy, has been successfully used for many years as an analytical tool to study the physical properties of thin and near-monomolecular films that have been transferred to reflective metal substrates. In addition to thin films on reflective metals, another class of macromolecular films that are studied with IRRAS is insoluble Langmuir-Blodgett monolayers spread at the air-water interface. In these experiments the water surface acts as the reflective element. The usefulness of these experiments stems from the fact that a wide variety of monolayer systems (e.g. surfactants, proteins, polymers, steroids, lipids) can be studied *in situ* on their native substrate and thus artifacts associated with transfer are avoided.
The IR reflection absorption spectroscopy is based on the reflectance properties of water in the mid-infrared region of the electromagnetic spectrum. It was shown that it is possible to measure in *situ* the infrared spectrum of monomolecular films at the air-water phase boundary. IR absorptions are sensitive to changes of the permanent molecular dipole moments, which in turn depend upon changes in conformation of the acyl chains and configuration of the bonds making up the normal modes of vibration. The vibrational frequencies that are detected are thus sensitive to molecular conformation. In addition, the technique gives information on hydrogen bonding, ionic interactions in amphiphiles and secondary structure and orientation in proteins. Unlike other spectroscopic methods, which are restricted to monitoring certain molecular regions (e.g. ^{31}P NMR), or are based on the introduction of possibly perturbing probe molecules (e.g. fluorescence microscopy), vibrational spectroscopy has the advantage of noninvasively monitoring absorptions from all regions of the lipid molecule. Moreover, the time scale of the experiment ($\approx 10^{-2}$ s) ensures that the interpretation of experimental results is not complicated by time scale averaging of anisotropic motions.

3.3.1 Principles of IRRAS

The IRRAS technique is based on the selective absorption of p- and s- polarized light by a monolayer at the air-water interface. The p- and s-polarizations are defined as in Brewster

angle microscopy as being parallel and perpendicular to the plane of incidence. The IRRAS experiments consist of recording the reflectance, R(d), of the s or p-polarized light (**Equation 3.2-8**) on the thin film which is the reflective substrate and then normalizing it with respect to the reflectance of the bare water subphase, R(0). An IRRAS spectrum is then calculated either as a ratio, R(d)/R(0), or as a pseudo absorption spectrum 1- R(d)/R(0). The IR spectrum obtained by this process is a function of the wavelength, the state of polarization, the adsorbate thickness, the angle of incidence of the reflected light and the optical constants of the three phases involved (air-monolayer-water subphase). The IRRAS bands observed may be positive or negative depending on the state of polarization of the incident light, the proximity of the angle of incidence to the Brewster angle, and the direction of the change of the dipole moment during a normal mode vibration. This technique works well for relatively thick films (> 300 Å), for which the IRRAS signals are large and the surface bands appear clearly on the IRRAS spectrum. However, if the sample is an ultra-thin film such as an LB monolayer, the surface sensitivity of the IRRAS method is not sufficient and as a result the IRRAS signals are extremely weak, and long data collection times are necessary to achieve an acceptable Signal/ Noise (S/N) ratio. There is a practical limit to this data collection time, since very small changes in the atmospheric content of CO_2 or H_2O, or a drift of the spectrometer over long periods of time can drastically affect the IRRAS signals. To minimize the environmental fluctuations (water vapor compensation) and improve the S/N ratio, **Mendelson et al. 2002** have proposed a "shuttle" IRRAS approach in which two Langmuir troughs are used in tandem. The first contains the film-covered surface and the second contains only the reference subphase. The IR beam is switched alternatively into the sample trough and the reference trough after a pre-set number of scans using a computer control motor. This approach was found to minimize the effect of humidity variations during the course of the experiment and thus the S/N ratio is improved. (**Dluhy 1986; Dluhy et al. 1995; Blaudez et al. 1999; Mendelson et al. 2002; Buffeteau et al. 1990**).

3.3.2 Vibration modes and frequencies

The physical property that is measured in infrared spectroscopy is the ability of some molecules to absorb infrared radiation, through **molecular vibrations**. One type of vibration possible for a molecule produces changes in bond length; such vibrations are called **stretching vibrations**. Other vibrations result in changes in bond angles and are called

bending vibrations. Only those vibrations that result in the change of the molecular dipole moment can be observed. For each molecule, a variety of molecular vibrations is possible **Figure 3-20**.

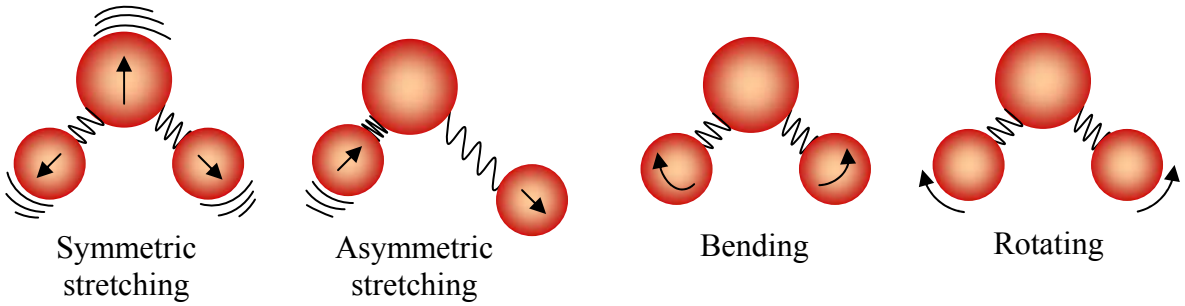

Figure 3-20. Molecular vibration modes

In the IR spectrum a number of characteristic bands are obtained that give information on the structure of the examined molecule, in our case of phospholipids. Different parts of the lipid molecule can be studied both within the hydrophobic acyl chain part, and in the polar/apolar boundary layer. The main disadvantages are the strong absorption bands of the solvent water, which by the variation of the solvent (H_2O and/or D_2O) can become balanced (eliminate the interference). The hydrocarbon chains of the phospholipids are characterized by the vibrations of the symmetric stretching $\nu_s(CH_2)$ and antisymmetric stretching $\nu_{as}(CH_2)$ of the CH_2 groups which appear in the spectral range between 3000 and 2800 cm^{-1}. The symmetrical and antisymmetric stretching oscillations are observed at 2854 and 2924 cm^{-1} respectively **Table 3-1**. The frequency of these oscillations is conformation-dependent and can be used to provide qualitative estimation *of the trans* / *gauche* bond ratio within the alkyl chains. When the conformation of the acyl chains changes from *trans* (conformational order) to *gauche* (conformational disorder) the frequency and the width of these bands increases.

In aqueous suspensions in the bulk phase, below the characteristic phase transition temperature (T_m) of the phospholipid in study, the acyl chains exist in a regular lattice structure characterized by an *all-trans* conformation as shown in **Figure 3-21**.

The symmetrical CH_2 stretching band is observed at 2849 cm^{-1}. When the temperature is increased and approaches T_m, a phase transition is observed from the gel phase to the liquid-crystalline phase, where *gauche* conformers are introduced into the rigid lattice and the regular packing is disrupted. As a result, the frequency position of the symmetrical CH_2 stretching band increases from ≈ 2848 cm^{-1} to 2853 cm^{-1}. Thus, a lipid in a conformationally

ordered state is characterized by a CH_2 stretching mode below ≈ 2850 cm^{-1}, while conformational disorder leads to an increase in frequency by 3 – 4 cm^{-1}.

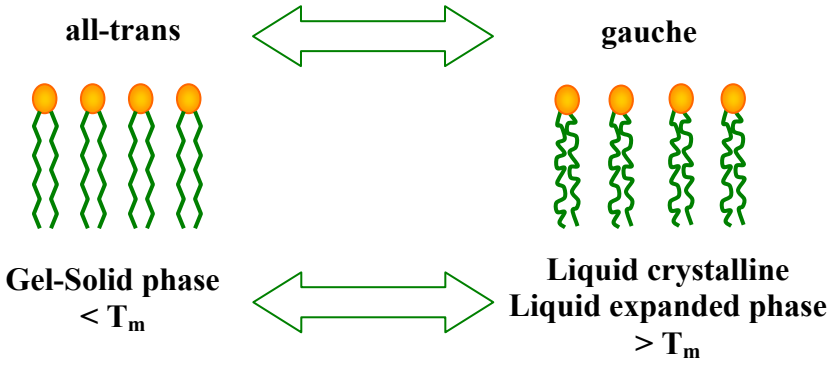

Figure 3-21. Conformation of the hydrocarbon chains below and above the transition temperature T_m

The vibration of the deformation (scissoring) CH_2 band $\delta(CH_2)$ is found at 1470 cm^{-1}. It is sensitive to the interactions between the chains (inter-chain) and to the vibrational coupling. A number of wagging bands is observed in the spectrum region of 1200 – 1400 cm^{-1}, when the hydrocarbon chains are in the all-trans conformation. The vibration bands of the phosphate stretching groups usually cover these bands.

Table 3-1. IR modes of hydrocarbon chain configuration and orientation

Mode (Hydrocarbon chains)	Frequency (cm^{-1})	Direction of the dipole moment
CH_2 symmetric stretch (ν_s)	2848 – 2854 (s)	∥ to the bisector of angle HCH
CH_2 asymmetric stretch (ν_{as})	2916 – 2924 (s)	⊥ to the bisector of angle HCH
CH_2 scissoring (δ)	1470 (m)	∥ to the bisector of angle HCH
CH_2 wagging progression	1180 – 1350 (w)	∥ to axes of the chains
CH_3 symmetric stretch (ν_s)	2090 (m)	∥ to the axis C_3 of CH_3
CH_3 asymmetric stretch (ν_{as})	2195 (m)	⊥ to the axis C_3 of CH_3
CH_3 scissoring (δ_s)	1380 (w)	∥ to the axis C_3 of CH_3
CH_3 scissoring (δ_{as})	1460 (w)	⊥ to the axis C_3 of CH_3

In the headgroup part of the lipid the most important band is the C=O stretching band of the ester carbonyl group ν(CO), which is observed at ≈ 1750 – 1720 cm^{-1}. It can be used for the

investigation of the hydration at the polar/apolar boundary layer because it depends on the hydration state of the lipid and on changes in its local environment (influence of the hydrogen bonds and interactions with other molecules).

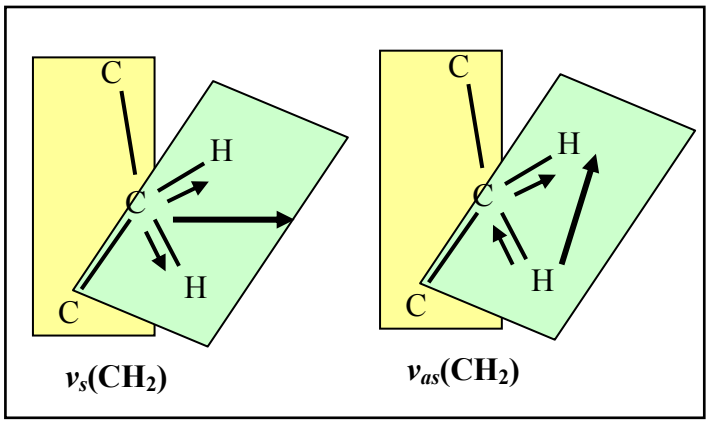

Figure 3-22. Direction of the transition dipole moments of the symmetric and antisymmetric (CH_2) IR stretching bands

The vibrations of the phosphate groups dominate the spectral region at 1300 – 1000 cm^{-1}. The position of the antisymmetric $\nu_{as}(PO_2^-)$ band is likewise an indicator for hydrogen-bond formation. This is shown by a shift of the frequency from 1250 cm^{-1} in the dry condition to 1230 cm^{-1} in the hydrated condition. In contrast, the symmetric $\nu_s(PO_2^-)$ band, which is found at 1089 cm^{-1}, is practically insensitive to hydrogen-bond formation. **Table 3-2** shows the frequencies of the most important modes in the headgroup region (**Dluhy et al. 1985; Dluhy et al. 1988; Mitchell et al. 1988; Hunt et al. 1989; Mendelson et al. 1995; Mendelson 1998; Berdysheva-Desert 2004**). The directions of the transition dipole moments for the most important vibrational modes are shown in **Figure 3-22** and **Figure 3-23**.

Table 3-2. IR modes of the polar regions of a lipid molecule

Mode (Headgroup region)	Frequency (cm^{-1})	Direction of the dipole moment
C=O stretch (esters)	1710 – 1740 (s)	∥ to C=O
PO_2^- symmetric stretch (ν_s)	1090 (m)	∥ to the axis C_2 of PO_2
PO_2^- asymmetric stretch (ν_{as})	1220 – 1250 (s)	⊥ to the axis C_2 of PO_2
$N^+(CH_3)_3$ scissoring (δ_s)	1405 (m)	
$N^+(CH_3)_3$ scissoring (δ_{as})	1485 (m)	
$CN^+(CH_3)_3$ symmetric stretch (ν_s)	920 (m)	∥ to the axis C_3 of $N(CH_3)_3$
$CN^+(CH_3)_3$ asymmetric stretch (ν_{as})	970 (m)	⊥ to the axis C_3 of $N(CH_3)_3$

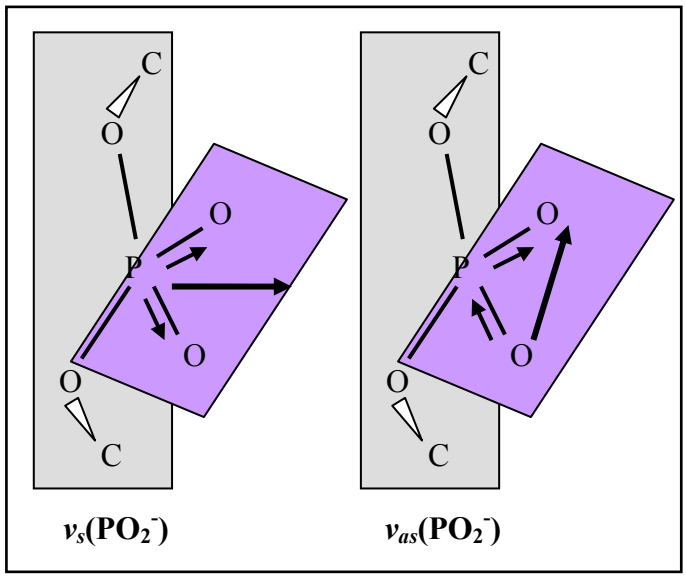

Figure 3-23. Direction of the transition dipole moments of the symmetric and asymmetric (PO_2^-) IR bands

3.3.3 Experimental Setup

IRRAS spectra were recorded using a Michelson interferometer from a Bruker IFS66 (Bruker, Karlsruhe, Germany) spectrometer equipped with a liquid-nitrogen-cooled MCT detector. The reflected beam is conducted out of the spectrometer and focused onto the water surface of a Langmuir trough as shown in **Figure 3-24.** The angle of incidence of the IR beam, polarized by a BaF_2 polarizer in the plane of incidence (p) and perpendicular to this plane (s), with

respect to the surface normal was 40° or 62°. Measurements were made by switching between two troughs at regular intervals using a trough shuttle system controlled by the acquisition computer. One trough contains the monolayer system under investigation (sample), whereas the other (reference) is filled with pure subphase. The spectra from the reference trough were subtracted from the sample spectra in order to eliminate the water vapor signal. To maintain a constant water vapor content the set-up was placed in a hermetically sealed container. Spectra were recorded with a spectral resolution of 8 cm^{-1} and collected using 200 - 400 scans.

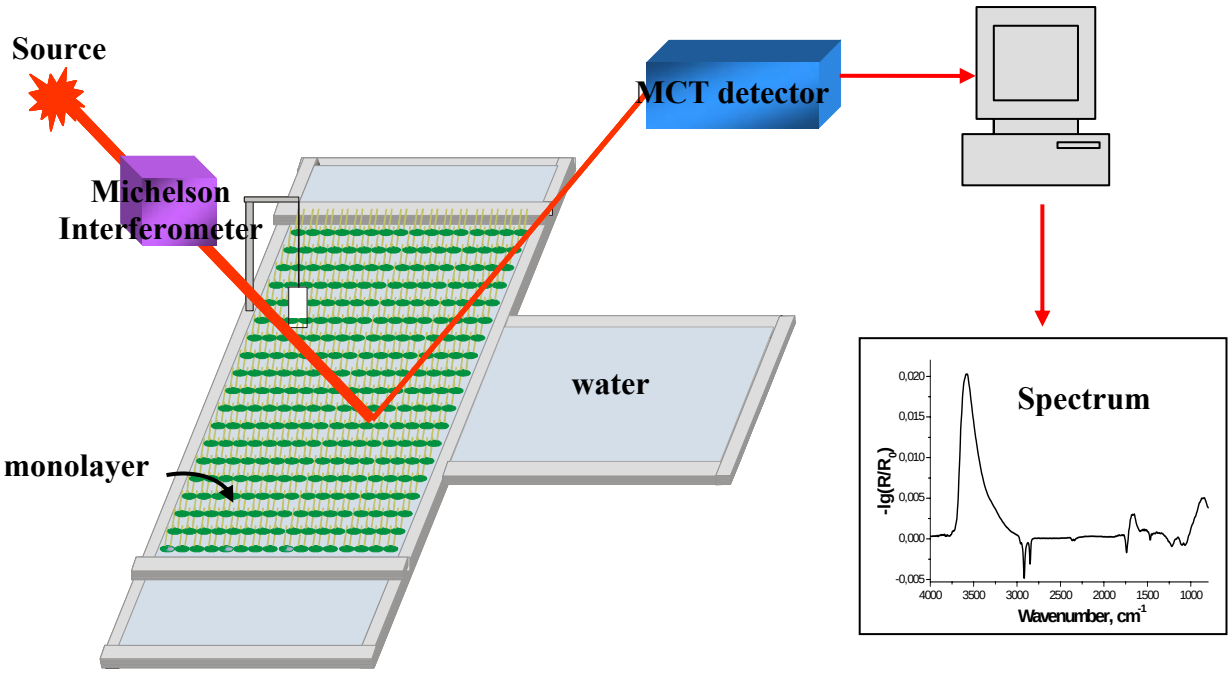

Figure 3-24. Schematic drawing of the IRRAS experiment

3.4 Grazing incidence X-ray diffraction (GIXD)

In the last decade, Grazing Incidence **Synchrotron** X-ray Diffraction (GIXD) was established as a powerful tool to study the packing of amphiphiles at the air-water interface. This technique has so far allowed the study of the phase behaviour of amphiphilic monolayers, the influence of molecular structure and chirality on the packing of the alkyl chains in phospholipid monolayers, and has made possible the determination of the two-dimensional lattice structure at the air-water interface. The technique is based on the fact that at X-ray energies, the refractive index for most materials is slightly less than 1. One can therefore easily achieve *total external reflection* from a surface if the incidence angle is small, i.e. below the critical angle. At the same time, the refracted wave becomes evanescent travelling along the surface limiting the penetration depth of the beam, and thus the X-ray intensity is highest at the surface. The advantages of this technique are: (i) higher sensitivity due to a larger interaction volume (ii) absence of strong background diffraction from the substrate material (surface selective) and (iii) capability for depth profiling of the various crystalline phases present.

3.4.1 Principles of GIXD

3.4.1.1 Evanescent wave - Refractive index

X-rays have been used for decades as an essential characterization tool to study the structure of **bulk** crystalline materials. X-rays interact weakly with matter and as a result they penetrate significant distances in a sample. For example, for X-rays of 1Å wavelength, the penetration ranges from a few micrometers (for highly absorbing materials) to a few millimetres (for weakly absorbing materials) providing microscopic structural information averaged over a large ensemble of atoms or molecules. Unfortunately, the above advantage of X-rays for bulk studies is a disadvantage when one examines surfaces and interfaces. Scattering from the top region of an air-water interface (about 100 Å deep) is so weak compared to that of the bulk that it is completely swamped. As a result, X-rays are not surface-sensitive.

In order to overcome this problem, Grazing Incidence X-ray Diffraction, (GIXD), in combination with intense collimated beams from synchrotron sources, has been developed. This technique has the advantage of restricting the penetration depth of the X-ray beam to the

surface region. This can be achieved by using grazing angles of incidence and employing the phenomenon of total external reflection from the surface, **Figure 3-25**.

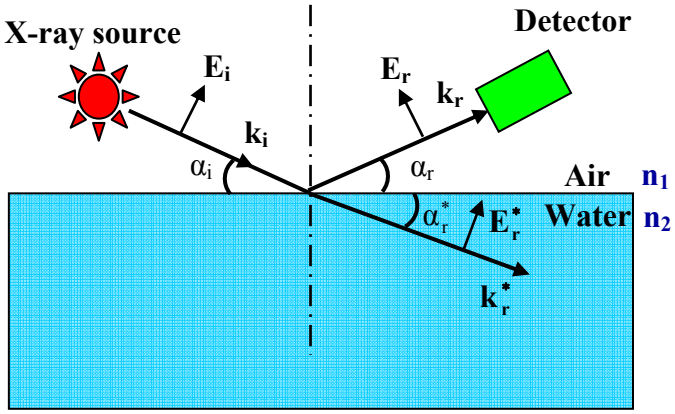

Figure 3-25. Refracted E_r^* and reflected E_r waves resulting from an incident plane wave E_i at the air-water interface

Total reflection is a process that occurs when Snell's law $n_1\cos\alpha_i = n_2\cos\alpha_r^*$ for refraction can no longer be solved for real angles. For most materials, the complex refractive index for X-rays in the 1Å wavelength range is given by

$$n = 1 - \delta - i\beta \qquad \textbf{Equation 3.4-1}$$

where $\delta = \frac{2\pi \cdot \rho \cdot r_e}{k^2}$, $k = 2\pi/\lambda$ is the X-ray wavenumber (where λ is the wavelength), ρ is the electron density of the sample and r_e is the classical electron radius equal to $r_e = 2.82 \times 10^{-13}$ cm. Typically δ is on the order of 10^{-6} to 10^{-5} in condensed matter and only 10^{-9} in air. The term β is related to photo-electric absorption and is equal to $\mu/2k$, where μ is the linear absorption coefficient.

As $n < 1$ ($\delta > 0$ and $\beta \approx 0$ for X-rays of $\lambda \approx 1$Å), and the incident X-rays are propagating in air (for which $n_1 = 1$), then by Snell's law X-rays will undergo total external reflection for angles of incidence α_i less than or equal to α_c, which is defined as $\cos\alpha_c = 1 - \delta$. Thus, $\alpha_c \approx \sqrt{2\delta} \approx 0.00173\lambda\left[\text{Å}\right]\sqrt{\rho(e/cm^3)}$. For water, $\rho = 0.334$ e/Å^3, the critical angle for total external reflection of 9.5 keV X-rays ($\lambda = 1.3$ Å) is $\alpha_c = 0.13°$. As a result, when X-rays fall on the sample at an incidence angle α_i smaller than the critical angle α_c for total external

reflection, the incident wave is totally reflected while the refracted wave becomes evanescent, travelling along the surface, and thus the penetration depth of the incident X-ray beam is only approximately 80 angstroms. The refracted beam (the evanescent wave) cannot travel further inside the medium, because its intensity decays exponentially with distance from the interface. In the grazing incidence geometry, the X-rays are said to be "surface sensitive"; that is, the evanescent wave only probes the crystalline structure in the vicinity of the surface. The undesired scattering from the bulk material, e.g. water in the case of a Langmuir monolayer, is thus efficiently eliminated, allowing an accurate measurement of the weak signals originating from the crystalline film (**Als-Nielsen et al. 1991; Kuzmenko et al. 2001; Jensen et al. 2001**).

3.4.1.2 Geometry of GIXD

The geometry of the X-ray diffraction experiment at grazing incidence is shown in **Figure 3-26**. An evanescent wave $\vec{k}_i$ is traveling along the surface and is diffracted by the two-dimensional ordered phases in the Langmuir film, resulting in a beam that makes an angle α_f with the water surface. If the ordered phase is crystalline, the evanescent wave may be Bragg scattered from a grain, which is oriented so that the *h,k* lattice "planes", with a $d_{h,k}$ spacing, make an angle $\theta_{h,k}$ with the evanescent beam fulfilling the Bragg condition $\lambda = 2d_{h,k}\sin\theta_{h,k}$. The diffracted intensity (wave $\vec{k}_f$) is recorded as a function of the horizontal angle $2\theta \neq 0$, which is the angle between incident and scattered beams in the water plane and also as a function of the vertical angle $\alpha_f \geq 0$.The directions of the incident and scattered X-rays are given by the wave vectors, $\vec{k}_i$ and $\vec{k}_f$ where:

$$\left|\vec{k}_i\right| = \left|\vec{k}_f\right| = \frac{2\pi}{\lambda} \qquad \textbf{Equation 3.4-2}$$

The scattering process is characterized by the scattering vector $\vec{Q}$ which is defined as:

$$\vec{Q} = \vec{k}_f - \vec{k}_i \qquad \textbf{Equation 3.4-3}$$

The scattering vector $\vec{Q}$ can be separated into its horizontal and vertical components, Q_{xy} (in-plane component) and Q_z (out-of-plane component), respectively as shown in **Figure 3-26**. The vertical and horizontal scattering vector components are given by **Equation 3.4-4** and **Equation 3.4-5**.

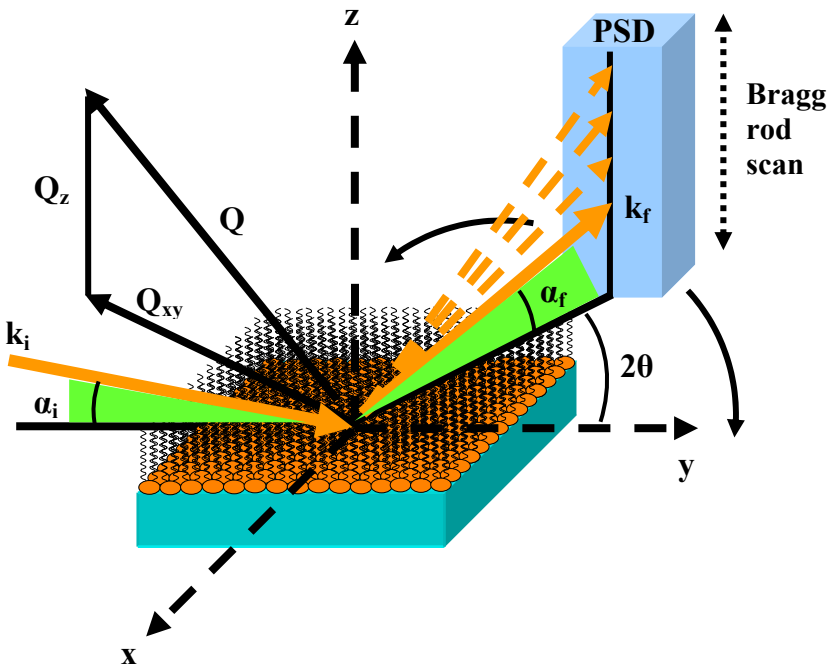

Figure 3-26. Grazing incidence X-ray diffraction geometry

$$Q_{xy} = \left(\frac{2\pi}{\lambda}\right)\left[\cos^2(\alpha_i) + \cos^2(\alpha_f) - 2\cos(\alpha_i)\cos(\alpha_f)\cos(2\theta)\right]^{1/2}$$

$$Q_{xy} \approx \left(\frac{4\pi}{\lambda}\right)\sin\left(\frac{2\theta}{2}\right)$$

Equation 3.4-4

$$Q_z = \left(\frac{2\pi}{\lambda}\right)\left[\sin(\alpha_i) + \sin(\alpha_f)\right] \approx \left(\frac{2\pi}{\lambda}\right)\sin(\alpha_f) \text{ when } \alpha_i \textbf{ is small}$$

Equation 3.4-5

It is not possible to determine the in-plane components Q_x and Q_y individually, because the crystallites on the water surface are randomly oriented, and as a result, the monolayer can be described as a "two-dimensional powder". Thus, the diffraction pattern is always averaged over all domain orientations in the monolayer plane. (**Rapaport et al. 2000; Kuzmenko et al. 2001**)

3.4.2 Diffraction data set profiles

An example of a diffraction data set is given in **Figure 3-27**, in two projections. **Figure 3-27(a)** shows a surface plot of the diffracted intensity as a function of Q_{xy} and $Q_{z,,}$ whereas **Figure 3-27(b)** is a contour plot. Projections of the measured intensity onto the Q_{xy} or the Q_z axis help visualize the data as a Bragg peak or as a Bragg rod respectively. For analysis purposes, the peaks are taken to be Lorentzian for the in-plane and Gaussian for the out-of-plane directions. Several different pieces of information may be extracted from the measured profiles. The angular 2θ positions of the Bragg peaks yield the repeat distances d of the 2-D lattice structure. The Bragg peaks may be indexed by two Miller indices *h*,*k* to yield the *a*,*b* unit cell. The full width at half-maximum (fwhm) of the Bragg peaks in Q_{xy} units yields the coherence length ξ of the crystals in the *a*,*b* plane. For chainlike molecules, precise information on the molecular chain orientation in a 2-D crystal may be obtained from the positions of the maxima of the Bragg rods, assuming the chains to be uniformly tilted.

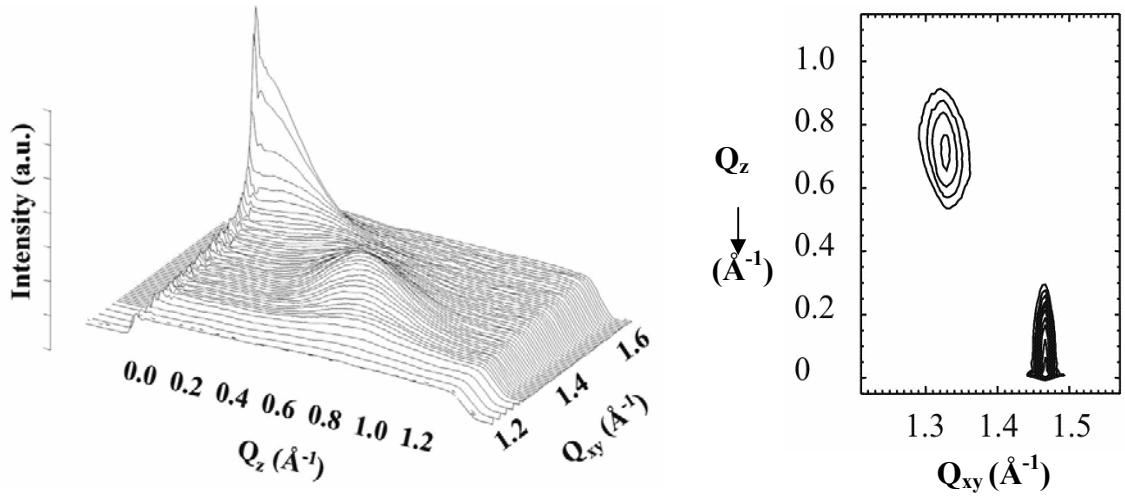

Figure 3-27. Diffraction profiles

3.4.3 Organization of the amphiphilic molecules at the air-water interface

A surfactant molecule at the air-water interface possesses two translational degrees of freedom x_1 and x_2 in the surface plane, and three rotational degrees of freedom the angles θ_t, ψ, and B (**Figure 3-28**). Different phases can be formed at the air-water interface, that can be classified according to different criteria: a) the type of the two-dimensional lattice that is

created at the air-water interface by the molecules forming the monolayer, b) the orientation of the hydrocarbon chains with respect to the surface normal (z-axis) and c) the freedom of rotation of the hydrocarbon chains around their B axis.

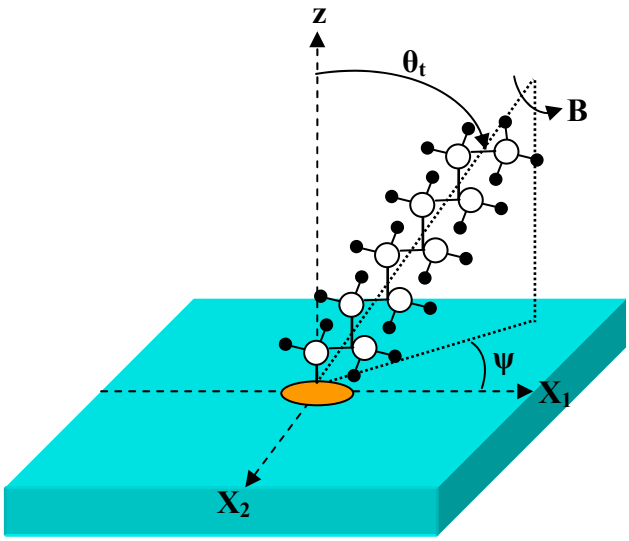

Figure 3-28. Representation of the various degrees of freedom of a surfactant molecule at the air-water interface

3.4.4 Two-dimensional lattice types

Depending on the symmetrical arrangement of the amphiphilic molecules at the air-water interface, three two-dimensional lattice types can be distinguished: oblique, centered rectangular and hexagonal.

3.4.4.1 Oblique

The oblique lattice, **Figure 3-29**, is the one with the lowest symmetry, possessing only a symmetry center in the surface plane. The unit cell formed by the vectors $\vec{\alpha}$ and $\vec{b}$ is distorted by an angle γ where $\gamma \neq 90°$. Each molecule has three nearest neighbours situated at distances l_1, l_2 and l_3. The oblique lattice is characterized by $\alpha \neq b$, $\gamma \neq 90°$, 120° and $l_1 \neq l_2 \neq l_3$.

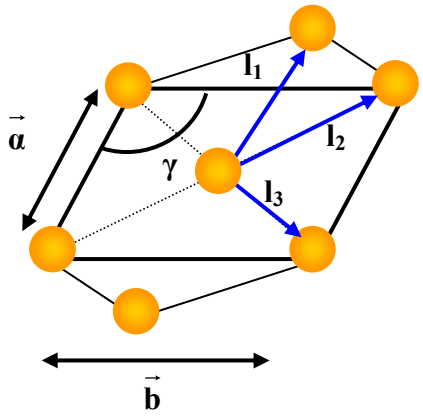

Figure 3-29. Oblique lattice formed by surfactant chains of a 2D monolayer

3.4.4.2 Centered Rectangular (Distorted Hexagonal)

The centered rectangular lattice is the most frequently observed. It possesses two axes of symmetry in the surface plane. This 2D lattice is based on a rectangular network that can be distorted in one of the two directions of the vectors $\vec{\alpha}$ and $\vec{b}$ that make up the rectangular unit cell. If the distortion is in the direction of the vector $\vec{\alpha}$, **Figure 3-30(a)**, each alkyl chain (molecule) has four nearest neighbours at distance l_1. If the distortion is in the direction of the vector $\vec{b}$, **Figure 3-30(b)**, each alkyl chain has only two nearest neighbours at distance l_1. The centered rectangular lattice is characterized by $\alpha \neq b$, $\gamma = 90°$ and $l_1 \neq l_2$.

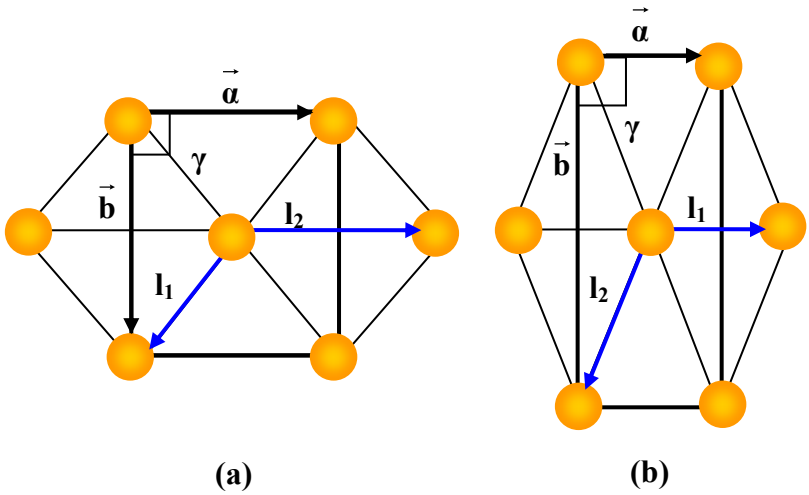

Figure 3-30. Centered Rectangular lattice formed by surfactant chains of a 2D monolayer

3.4.4.3 Hexagonal

The hexagonal lattice has the highest symmetry of all possible 2D lattices. Each molecule is surrounded by six nearest neighbours at the same distance l_1. The hexagonal lattice is characterized by $\alpha = b$, $\gamma = 120°$ as shown in **Figure 3-31**.

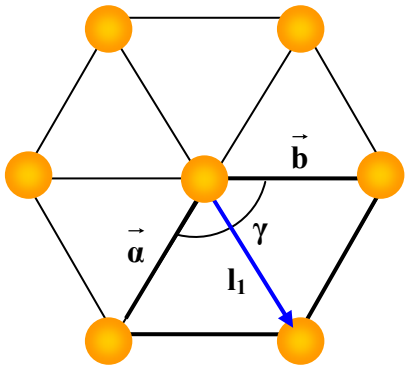

Figure 3-31. Hexagonal lattice formed by surfactant chains of a 2D monolayer

3.4.5 Orientation of hydrocarbon chains

In the different monolayer phases the orientation of each molecule can be defined by two angles, θ_t and ψ, which define the tilt angle of the molecule with respect to the surface normal and the angle of its projection on the surface, **Figure 3-28**. The alkyl chains can be vertical (untilted) or tilted with respect to the surface normal of the monolayer. If the alkyl chains of the lipid molecules are tilted, $\theta_t \neq 0$, they are inclining in a direction fixed with respect to the plane of the interface. This inclination is characterized by the azimuthal angle ψ and as a result the monolayer can display various types of orientational order which are:

a) inclination towards the nearest neighbor, tilt NN (**Figure 3-32(a)**)
b) inclination towards the next nearest neighbor, tilt NNN (**Figure 3-32(b)**)
c) inclination towards a direction different than the above (**Figure 3-32(c)**) (**Kaganer et al. 1995; Kaganer et al. 1999**)

The rotation of the hydrocarbon chains around their B axis will not be discussed here because it is not of interest in the systems examined in this thesis.

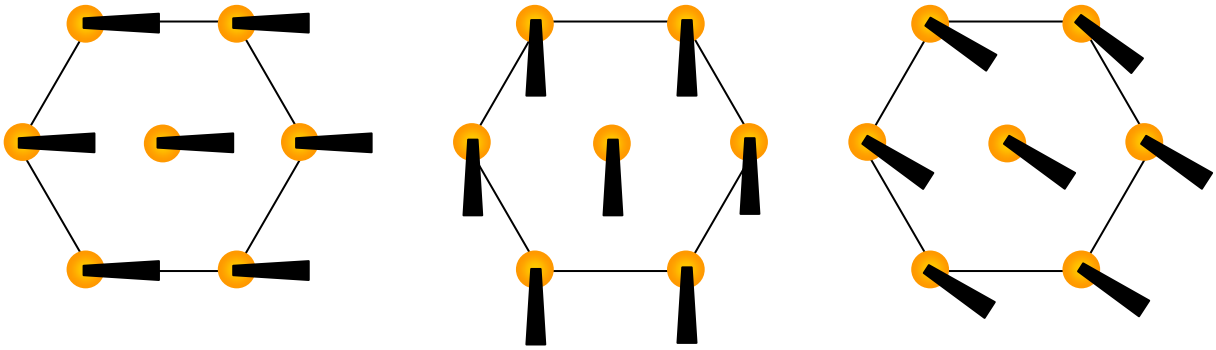

Figure 3-32. Inclination of the hydrocarbon chains at the air-water surface. NN tilt (a), NNN tilt (b) and other tilt (c)

3.4.6 Calculation of the parameters of the network lattice

Two types of information can be extracted from the measured diffraction profiles. The peak positions of the $Q_{xy}^{h,k}$ in-plane component of the scattering vector $\vec{Q}$ gives the corresponding lattice spacings a and b as well as the angle γ. The out-of-plane component $Q_{z}^{h,k}$ of the scattering vector $\vec{Q}$ yields information about the angle θ_t of the molecular tilt with respect to the surface normal and about the tilt azimuthal direction (ψ), assuming that the aliphatic tails are uniformly tilted.

The peak position of the $Q_{xy}^{h,k}$ in-plane component of the scattering vector $\vec{Q}$ gives the corresponding lattice spacings in the horizontal plane using the Bragg formula:

$$d_{h.k} = \frac{2\pi}{Q_{xy}^{h,k}} = \left[\frac{h^2}{\alpha^2} + \frac{k^2}{b^2} - 2\left(\frac{hk}{ab}\right)\cos(\gamma)\right]^{-1/2} \sin(\gamma) \qquad \textbf{Equation 3.4-6}$$

The out-of-plane component $Q_{z}^{h,k}$ of the scattering vector $\vec{Q}$ yields information about the angle θ of the molecular tilt with respect to the surface normal and about the tilt azimuthal

direction (ψ), assuming that the aliphatic tails are uniformly tilted. The $Q_z^{h,k}$ is given by the equation:

$$Q_z^{h,k} = Q_{xy}^{h,k} \cos\psi_{hk} \tan\theta \qquad \textbf{Equation 3.4-7}$$

The positional correlation length ξ which gives the magnitude of the correlation in the lattice can be estimated from the full width at half maximum (fwhm) of each in-plane peak, assuming an exponential decay of positional correlations with increasing separation within the lattice:

$$\xi = \frac{2}{\mathrm{fwhm}\left(Q_{xy}^{hk}\right)} \qquad \textbf{Equation 3.4-8}$$

Specifically, if only a single first-order peak is observed, this implies a hexagonal molecular arrangement with equal distance between the molecules. Two first-order peaks point to a centered rectangular (distorted hexagonal) unit cell, and three first-order peaks suggest an oblique packing of the molecules.

The most frequently observed molecular packing, the centered rectangular with molecular tilt to the nearest neighbor (NN), exhibits one non-degenerate in-plane peak Q_{xy}^{n} at $Q_z^n = 0$ and one 2-fold degenerate peak Q_{xy}^{d} at $Q_z^d > 0$. In this situation the tilt angle θ_t is given by the relationship:

$$\theta_t = \arctan\left(\frac{Q_z^d}{\sqrt{\left(Q_{xy}^d\right)^2 - \left(Q_{xy}^n/2\right)^2}}\right) \qquad \textbf{Equation 3.4-9}$$

For a tilted centered rectangular phase whose molecules point toward next-nearest neighbor (NNN) both Q_{xy}^{n} and Q_{xy}^{d} are located at nonzero Q_z values having a ratio $Q_z^n / Q_z^d = 2:1$. In this case, the tilt angle can be calculated from the equation:

$$\theta_t = \arctan\frac{Q_z^n}{Q_{xy}^d} \qquad \textbf{Equation 3.4-10}$$

The area per molecule in the horizontal plane A_{xy} (in-plane unit cell area) can be calculated by the following equation:

$$A_{xy} = \alpha \times b\sin\gamma \qquad \textbf{Equation 3.4-11}$$

The area per molecule A_0 in the plane perpendicular to the hydrocarbon chains (chain cross-sectional area) is:

$$A_0 = A_{xy}\cos\theta_t \qquad \textbf{Equation 3.4-12}$$

The behavior for each molecular arrangement and the relation between the scattering vectors Q_{xy} and Q_z are given in **Table 3-3** (**Kenn et al. 1991; Weiderman et al. 1998; Petrov et al. 2001**).

Table 3-3. Relation between the Q_{xy} and Q_z scattering vectors

Lattice	Azimuthal direction (ψ)	Peaks	Q_{xy}	Q_z	Relation between Q_{xy} and Q_z
Oblique	Intermediate between NN and NNN	3	> 0	> 0	$Q_{z3} = Q_{z1} + Q_{z2}$
Hexagonal	Untilted chains	1	> 0	= 0	---------
Centered Rectangular	Tilt NN	2	> 0	> 0 = 0	$Q^n_{xy} \neq Q^d_{xy}$ $Q^n_z = 0$ $Q^d_z \neq 0$
	Tilt NNN	2	> 0 > 0	> 0 > 0	$Q^n_z/Q^d_z = 2:1$
	Untilted chains	2	> 0 > 0	= 0	$Q^n_{xy} \neq Q^d_{xy}$ $Q^n_z = Q^d_z$

3.4.7 Experimental setup

The GIXD experiments were performed using the liquid-surface diffractometer on the undulator beamline BW1 at HASYLAB, DESY, Hamburg (Germany) as shown in **Figure 3-33**. The Synchrotron beam was made monochromatic by Bragg reflection on a beryllium (002) crystal and was adjusted to strike the monolayer on the water surface at an angle of incidence $\alpha_i = 0.85\alpha_c$, where $\alpha_c \approx 0.13°$ is the critical angle of total external reflection. The wavelength was 1.304 Å. The intensity of the diffracted radiation is detected by a linear position - sensitive detector (PSD) (OED-100-M, Braun, Garching, Germany) as a function of the vertical scattering angle α_f. The resolution of the horizontal scattering angle 2θ is given by a Soller collimator located in front of the PSD.

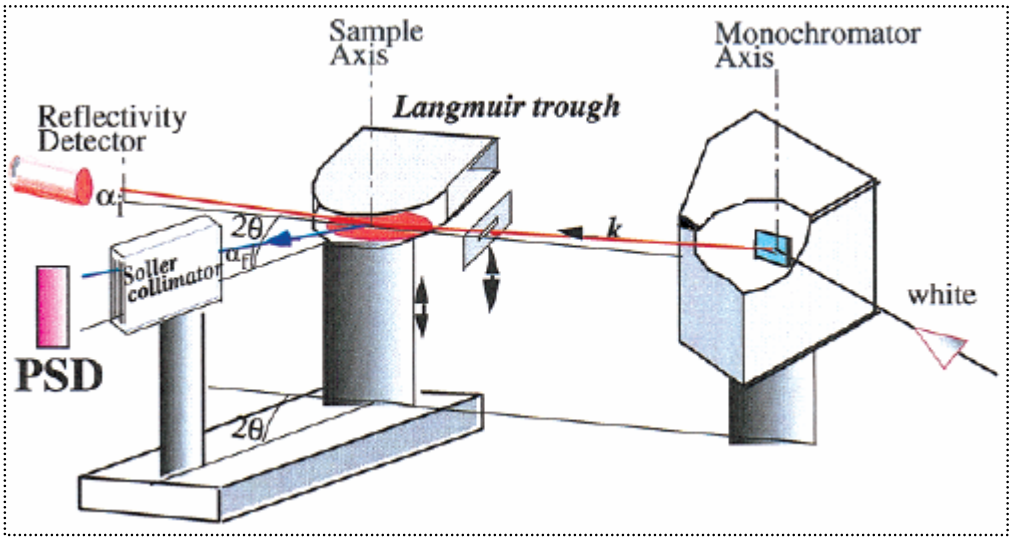

Figure 3-33. Experimental setup of the diffractometer at beamline BW1. Hasylab-Hamburg (Rapaport et al. 2000)

The collection of the diffracted radiation by means of a position-sensitive detector (PSD) is made by scanning the detector over a range along the horizontal scattering vector Q_{xy} and integrating over the whole Q_z window of the PSD, to yield the Bragg peaks. Simultaneously, the scattered intensity, recorded in channels along the PSD, but integrated over the scattering vector Q_{xy} in the horizontal plane across a Bragg peak, produces Q_z - resolved scans called Bragg-rods.

3.5 Osmotic stress (OS)

In order to study the interbilayer forces in multilamellar systems as well as the forces between macromolecular aggregates in ordered assemblies, the technique of the osmotic stress is used (**Parsegian et al. 1986; Rand et al. 1988**) in association with X-ray diffraction. This method can be applied to a wide variety of systems, such as neutral or electrically charged membranes, proteins, and DNA. The basis of the method is to let the system of interest come to thermodynamic equilibrium with a polymer solution of known osmotic pressure. The method permits the precise definition of the thermodynamic sample parameters (chemical potential or work of condensing the sample), and is usually coupled to methods that detect the structural consequences of solvent removal from the sample.

3.5.1 Principles of Osmotic stress. Osmosis – Osmotic Pressure

Osmosis is the diffusion of a solvent through a semipermeable membrane from a region of low solute concentration to a region of high solute concentration. The semipermeable membrane is permeable to the solvent, but not to the solute, resulting in a chemical potential difference across the membrane which drives the diffusion. The solvent flows from the region (side of the membrane) of high chemical potential to the region of low chemical potential, until the chemical potential is equal on both sides. Osmosis can be opposed by increasing the pressure in the region of high solute concentration with respect to that in the low solute concentration region. The force per unit area required to prevent the passage of water through a semi-permeable membrane and into a solution of greater concentration is called osmotic pressure. Three different ways exist to exert a precise osmotic pressure on a sample (**Parsegian et al. 1986; Safran et al. 1987; Rand et al. 1989**):

a) The sample is put in contact with a polymer solution of known osmotic pressure often using a semipermeable membrane. The polymer molecules cannot penetrate the phase under study, because of their large size. As a result the polymer solution exerts osmotic pressure.
b) For pressures higher than 10 – 100 atm a hydraulic pump piston is used to apply a physical pressure on the sample squeezing out the aqueous solution through a strong, semipermeable membrane.

c) The sample is exposed to known vapour pressures using saturated salt solutions. With this method osmotic pressures up to 10^4 atm can be applied to the sample.

In our experiments, we have used polymer solutions to apply osmotic pressure to our samples. The solvent (usually water) exchanges freely between the sample and the polymer solution, **Figure 3-34**. As the polymer concentration is increased, the osmotic pressure difference between the polymer solution and the sample becomes greater. In a chemical sense, the "thirsty" polymer solution competes with the sample for water.

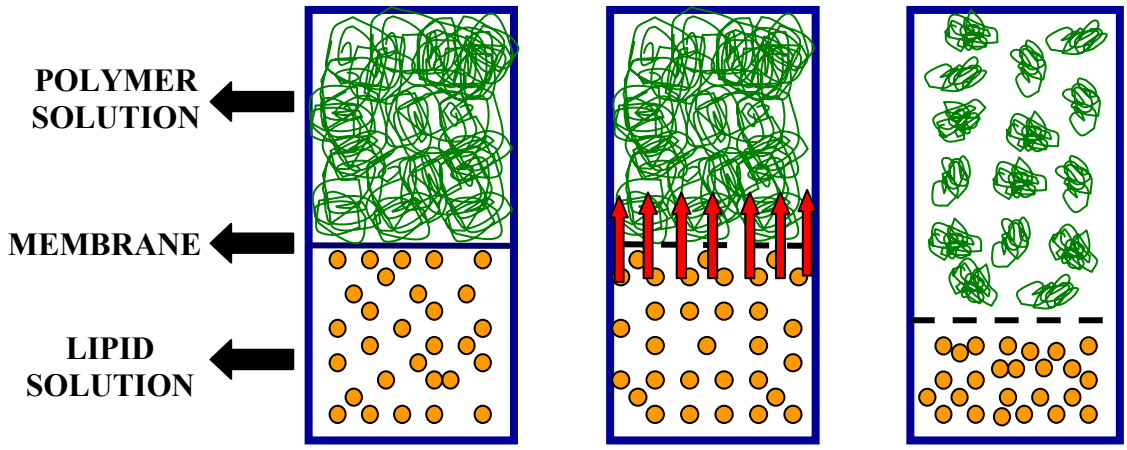

Figure 3-34. Applying osmotic stress with polymer solutions

When the system is in equilibrium, the chemical potential of the pure solvent will be equal to the chemical potential of water in the sample which is under osmotic pressure, in other words equilibrium is reached when the force per unit area applied to the sample is the same as the osmotic pressure in the polymer solution (**Parsegian et al. 1986; Hiemenz et al. 1997**). This condition is expressed as follows:

$$\mu_A^0(\text{pure solvent}) = \mu_A^{\Pi}(\text{sample under pressure } \Pi) \qquad \textbf{Equation 3.5-1}$$

For the pure solvent, at constant temperature we can write:

$$\int_{\mu_A^0}^{\mu_A^{\Pi}} d\mu_A = \int_{P_A}^{P_A+\Pi} \overline{V} dP \qquad \textbf{Equation 3.5-2}$$

which, assuming the solvent to be incompressible, leads to:

$$\mu_A^{\Pi} - \mu_A^0 = -\Pi\overline{V} \qquad \textbf{Equation 3.5-3}$$

where $\overline{V}$ is the molar volume of the solvent.
Since

$$\mu_A^{\Pi} = \mu_A^0 + RT\ell n\alpha_A \qquad \textbf{Equation 3.5-4}$$

combining **Equations 3.5-3** and **3.5-4** we obtain:

$$\ell n\alpha_A = -\frac{\Pi\overline{V}}{RT} \qquad \textbf{Equation 3.5-5}$$

In practice, the stressing polymer solution is in vast excess compared to the system of interest, so that the water activity of this "reservoir" can be regarded as fixed during the transfer of matter between the two phases.

3.5.2 Osmotic Stress and Intermolecular Forces

Direct measurement of forces between amphiphilic membranes can be achieved using the osmotic stress technique in combination with X-ray diffraction, which provides the interbilayer spacing. As a result, pressure – distance curves can be constructed that give information on the interactions (forces) that occur between bilayers. These are hydration forces, Van der Waals forces, electrostatic forces and steric interactions e.g. thermal undulations (Helfrich force). At equilibrium, the total osmotic pressure applied by the polymer solution is equal to the sum of the individual forces acting between the lipid bilayers:

$$\Pi_{TOT} = \Pi_{VDW} + \Pi_{ELEC} + \Pi_{HYD} + \Pi_{UND} \qquad \textbf{Equation 3.5-6}$$

A detailed description on these forces is given in **Chapter 5**. In **Figure 3-35** the influence of each force on a general pressure – distance curve for bilayers is shown.

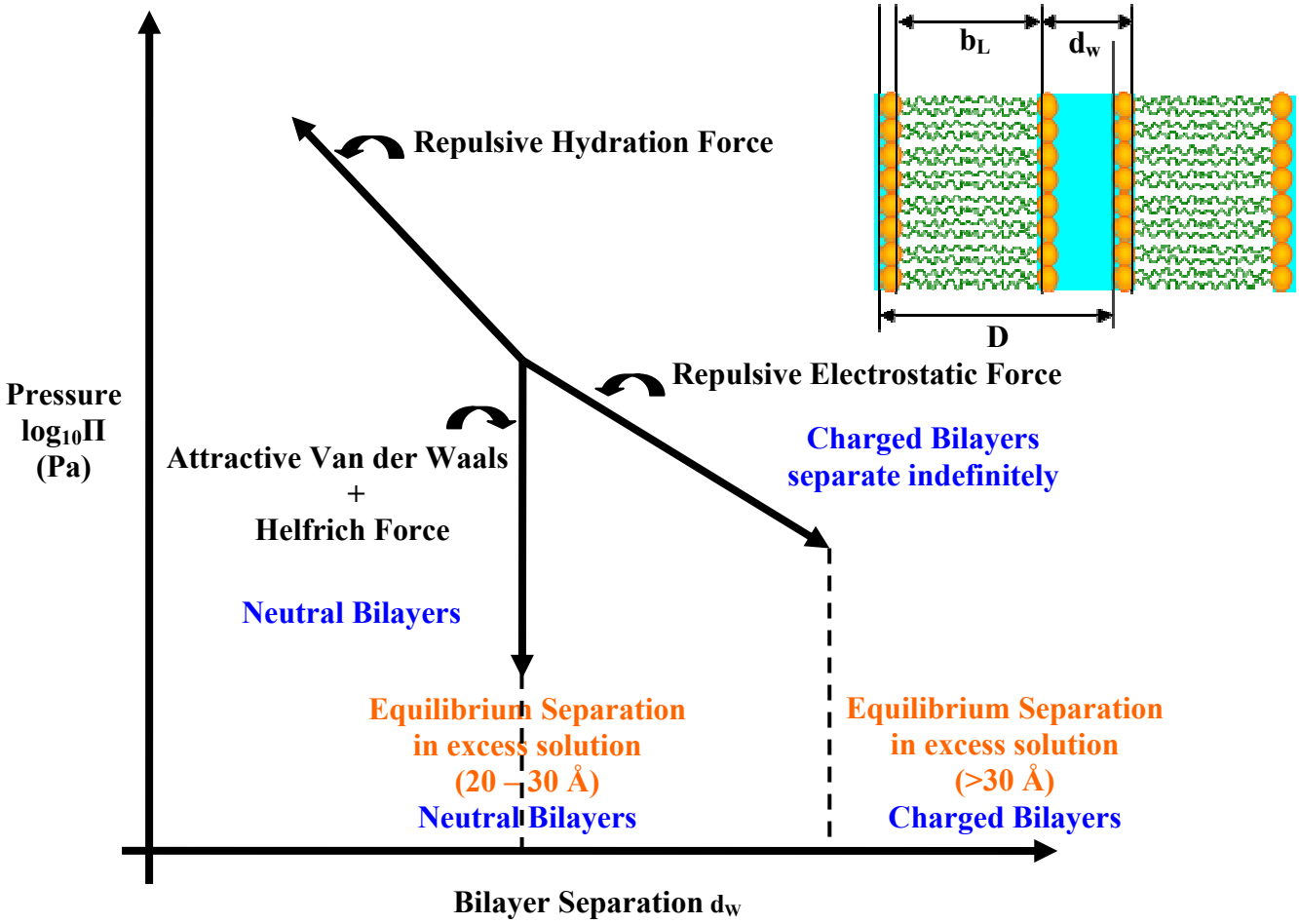

Figure 3-35. logΠ – d_w schematic diagram

3.5.3 Properties of PEG

Poly(ethylene glycol) (PEG) is a widely used polymer in biology and biochemistry. It is used to precipitate molecules, to stabilize or to aggregate particles, and as a vehicle for drug delivery. The chemical structure of this linear polymer, H-(O-CH_2CH_2)n-OH, includes a long chain of poly(ethylene oxide) and two terminal groups, H and OH. PEG is water-soluble at moderate temperatures in all proportions over a wide range of molecular weights. Solutions of PEG are highly viscous. The high affinity of PEG for water is responsible for the elevation of osmotic pressure of PEG solutions, and has been utilized to regulate the amount of water between macromolecules and between lipid bilayers.

3.5.4 Osmotic Pressure of PEG in salt solutions

The osmotic pressure, Π_{mix}, due to the mixing of polymer and solvent molecules (e.g. salt solution) can be expressed by the Flory-Huggins equation for the free energy change upon mixing which is given by the following equation (for low values of the polymer volume fraction φ_2) (**Hiemenz et al. 1997**):

$$\mu_1 - \mu_1^0 = RT\ln\varphi_1 + RT\left(1 - \frac{1}{n}\right)\varphi_2 + RT\chi \cdot \varphi_2^2 \qquad \textbf{Equation 3.5-7}$$

where φ_1 is the volume fraction of the solvent, φ_2 is the volume fraction of the polymer, n is the number of segments in the polymer chains (proportional to the molecular weight) and χ is the Flory-Huggins interaction parameter, which characterizes the interaction between the polymer segments and the solvent molecules.
The osmotic pressure is then given by the following equation:

$$-\pi\overline{V} = RT\ln\varphi_1 + RT\left(1 - \frac{1}{n}\right)\varphi_2 + RT\chi \cdot \varphi_2^2 \qquad \textbf{Equation 3.5-8}$$

Equation 3.5-8 shows that the osmotic pressure of the PEG polymer can be affected by the presence of electrolyte which may influence the Flory-Huggins interaction parameter. However, the effect of an electrolyte solution on the osmotic pressure of a PEG solution is small, according to **Parsegian et al. 1986**, and does not depend strongly on the ionic strength for small electrolyte concentrations. The strongest effect of a salt solution on the osmotic pressure of PEG was reported for the chaotropic salt $NaClO_4$, which lowers the osmotic pressure exerted by PEG20000 in 1M solutions by up to 40% (**Parsegian et al. 1986**).
If we accept that the effect of any salt solution on the osmotic pressure of PEG is the maximum found for $NaClO_4$ (40%), then according to **Equation 3.5-9** the change in the osmotic pressure of PEG for two limiting concentrations e.g. G = 0.015 and G = 0.79 is as shown in **Table 3-4**.

Table 3-4. **Osmotic pressure variation of PEG solutions in the presence of salt**

G	Π (dyn/cm^2)	Π(40%) (dyn/cm^2)	logΠ (dyn/cm^2)
0.015	77918	77918 ± 31167	4.89 ± 0.2
0.79	50300335	50300335 ± 20120134	7.70 ± 0.2

From **Table 3-4** we see that even if the effect of a salt solution on the osmotic pressure is considerable, the error in the logΠ scale used in the representation of the experimental results is significantly compressed.

3.5.5 Experimental Setup

A known amount of poly(ethylene glycol) polymer, (PEG), was mixed with NaX solutions of various concentrations and then added to dry DPPC in weighing bottles, without using a semipermeable membrane, as shown in **Figure 3-36**, since the PEG 20000 mixes very poorly with the sample solution. The samples were allowed to equilibrate at room temperature for 48 to 72h and then were transferred to an oven that was thermostated at T = 50 ± 1°C for 18 to 20h prior to X-ray measurements. After reaching equilibration, the samples were transferred to aluminium X-ray sample holders, sealed with Kapton and mounted immediately to a thermostated **aluminium** cell at T = 50 ± 1°C. Repeat spacings were determined by X-ray diffraction as described in **Section 3.6.4**. The time allowed to the samples for equilibration was established by a reference experiment using DPPC in pure water reproducing the results found in the literature (**Rand et al. 1989**). Moreover, various researchers in order to characterize lipid lamellar phases used the same procedure.

The osmotic pressure applied by the PEG solution is related to PEG concentration and temperature as follows:

$$\Pi\ (\mathrm{dyn/cm^2}) = -1.31 \times 10^6 G^2 T + 141.8 \times 10^6 G^2 + 4.05 \times 10^6 G \qquad \textbf{Equation 3.5-9}$$

where G = w/(100-w) with w the weight percentage of the polymer in the solution, and T = 50 ± 1°C.

This calibration expression has been established by **Michel et al. 1973**; **Michel 1983**, and is strictly valid in the range 5° ≤ T ≤ 40°C and up to G = 0.8 for PEG 8000. We have used this expression with PEG 20000 because, according to **Michel et al. 1973**, the osmotic pressure depends on polymer concentration and is roughly independent of MW in the range 8000 –

20000 Da. Moreover, **Equation 3.5-9** has been used at temperatures exceeding 40°C without further verification because, according to **Dubois et al. 1998**, PEG is not subject to hydrolysis or fragmentation that might modify the applied osmotic pressure under these conditions.

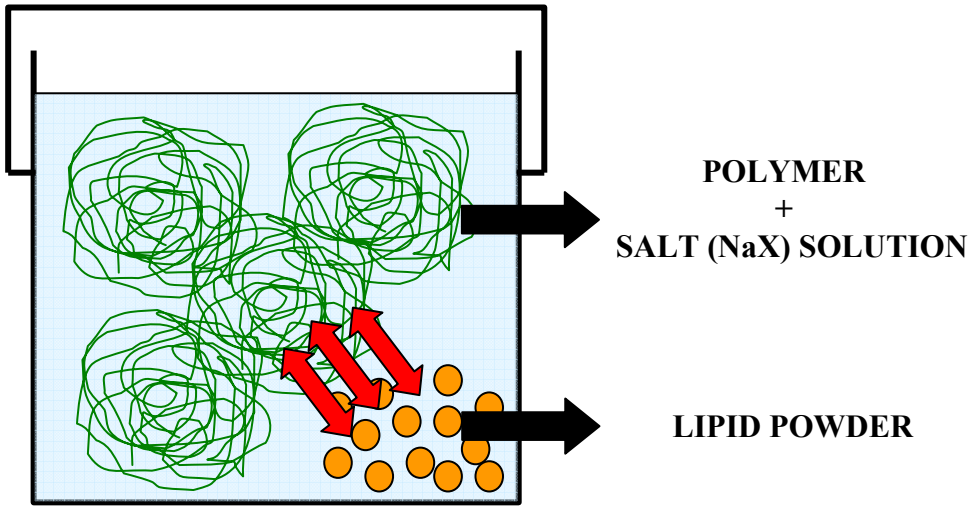

Figure 3-36. Osmotic stress experiment performed without a semipermeable membrane in the presence of PEG

3.6 Small angle X-ray scattering (SAXS)

Small angle X-ray scattering (SAXS) is a well-established measurement technique first developed about 70 years ago. It is commonly used for the investigation of large length scale structures (not necessarily periodic) with "colloidal" dimensions, from 1 up to several hundreds of nm. These structures can be high molecular weight polymers, biological macromolecules (phospholipids, proteins, nucleic acids), and self-assembled superstructures. Small angle X-ray scattering has various advantages compared to other methods that can be used to study the structure of colloidal and macromolecular systems, such as light scattering, electron microscopy and X-ray diffraction: (a) SAXS offers the possibility of studying macromolecules in their natural environment e.g. in aqueous solutions. (b) It is suitable for the study of bulk materials which are opaque to visible light. (c) It is practically a non-destructive method, in contrast to electron microscopy. (d) Crystallinity is not a requirement for SAXS.

3.6.1 Properties and Production methods of X-Rays

X-rays are electromagnetic radiation with typical photon energies in the range of 100eV – 100keV. They exist in the region of the electromagnetic spectrum lying between gamma rays and extreme ultraviolet corresponding to a wavelength of the order of 0.1 - 100Å. X-rays being electromagnetic radiation travel in straight lines at the same speed (c) in vacuum. They can be reflected, refracted, scattered, absorbed, polarized etc. They also show interference and diffraction effects.

X-rays are produced generally by either X-ray tubes or synchrotron radiation. The primary source used in laboratory X-ray instruments is the X-ray tube. The apparatus for production of X-rays is shown in **Figure 3-37**. X-rays are generated when a focused electron beam accelerated across a high voltage field, bombards a stationary or rotating metal target. There are two different atomic processes that can produce X-ray photons. One is called Bremsstrahlung which means "braking radiation". The other is called K-Shell emission or characteristic X-rays.

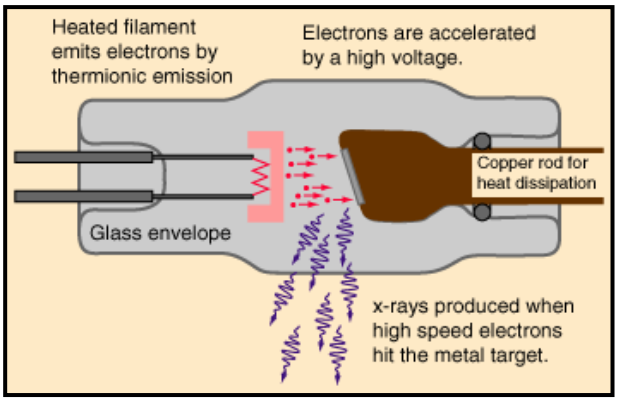

Figure 3-37. **X-ray tube, Production of X-rays**

In the Bremsstrahlung process, accelerated charges (electrons), collide with atoms in the target and give off electromagnetic radiation. In the quantum picture, many photons of different wavelengths are produced, but none of the photons can have more energy than the original photon-producing electron. As a result, a continuous spectrum of X-rays are emitted which are termed Bremsstrahlung radiation or "white" radiation. After giving rise to the spectrum of X-ray radiation, the original electron is slowed down or stopped.

In the K-shell method, the bombarding electrons can eject (knock out) inner shell electrons in atoms through an ionization process. A free electron of higher energy (from the outer shells) can then fall into the empty position in the K-shell. The energy lost by the falling electron shows up as an emitted X-ray photon that is characteristic of the target material as shown in **Figure 3-38**.

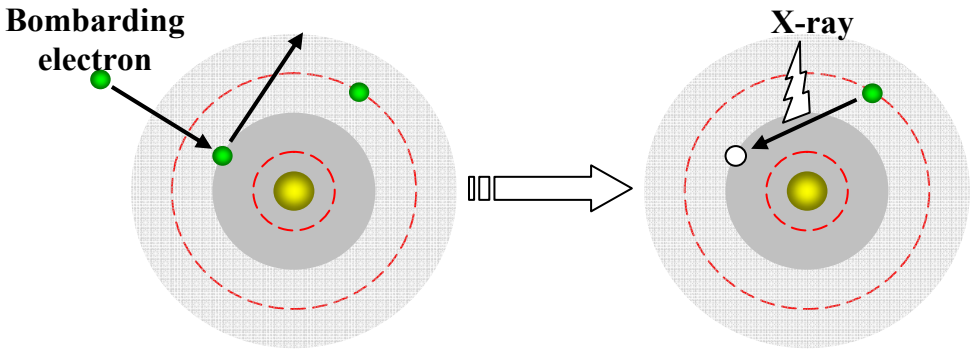

Figure 3-38. K-shell emission of x-rays

Meanwhile, higher energy electrons fall into the vacated energy states in the outer shells, and so on. All transitions into the K shell generate the characteristic K lines of the material. **Figure 3-39** shows that the K_a line is radiated when the electrons from the L shell cascade down into the K-shell and the K_b line results from the M shell. *K-shell emission produces higher intensity X-rays than Bremsstrahlung and the X-ray photon is emitted at a single wavelength.*

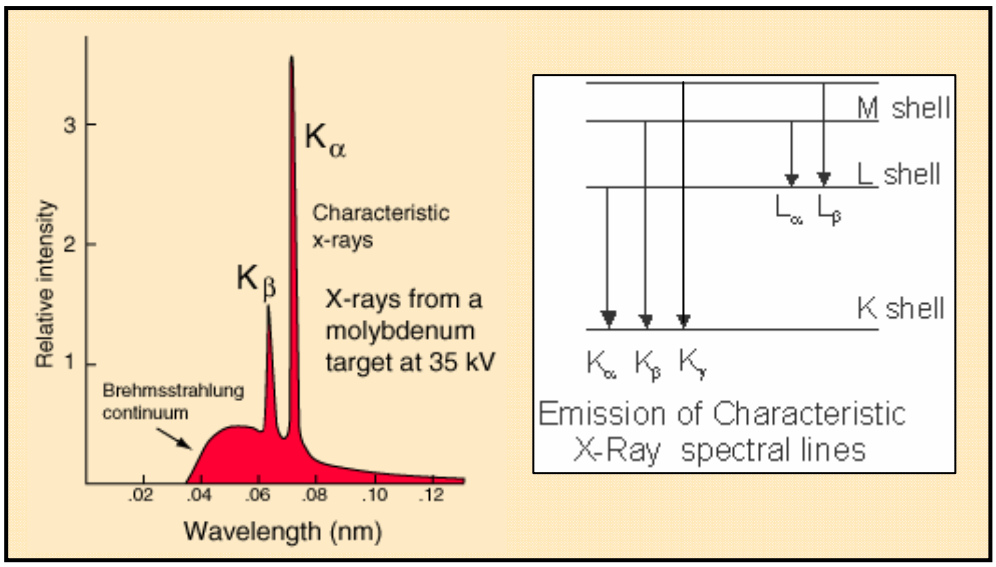

Figure 3-39. Characteristic K lines in K-shell emission

Copper is often chosen as the target metal because of its high electrical and thermal conductivity, its low cost and because the K_a line has a wavelength of 1.5418 Å. For copper, the excitation potential (V) for ionization through the K-shell is 8.98 kV. The intensity of the K_a line is maximized at $4V \approx 36$ kV.

3.6.2 Bragg's Law on a crystal lattice

X-rays primarily interact with electrons in atoms. When X-ray photons collide with electrons, some photons from the incident beam will be deflected away from their original path. If no energy is transferred to the atom and the wavelength of these X-rays is unchanged, the process is called ***elastic scattering***. Elastic scattering dominates diffraction effects. These are the X-rays that we measure in diffraction experiments, as the scattered X-rays carry information about the electron distribution in materials. In the inelastic scattering process that

is known as ***Compton scattering***, a small fraction of the energy of an incident photon (X-rays) is transferred to an electron with which it collides. The wavelength of the scattered X-rays increases (loss of energy) and there is no phase relationship between incident and scattered waves. Diffracted waves from different atoms can interfere with each other and the resulting intensity distribution is strongly modulated by this interaction. If the atoms are arranged in a periodic manner, the diffracted waves will consist of sharp interference maxima (peaks). Measuring the diffraction pattern, we can deduce the distribution of atoms in a material.

The peaks in an X-ray diffraction pattern are directly related to the atomic distances. When X-rays are scattered from a crystal lattice, peaks of scattered intensity are observed which correspond to the following conditions:

1. The angle of incidence = angle of scattering.
2. The pathlength difference is equal to an integer number of wavelengths.

For a given set of lattice planes with an inter-plane distance of d as shown in **Figure 3-40**, ***Bragg's law*** gives the condition for a diffraction peak to occur:

$$n\lambda = 2d\sin\theta \qquad \textbf{Equation 3.6-1}$$

where n is an integral number describing the order of the reflection, λ is the wavelength of the X-rays, d is the spacing between lattice planes and θ is the Bragg angle at which a maximum in the diffracted intensity occurs.

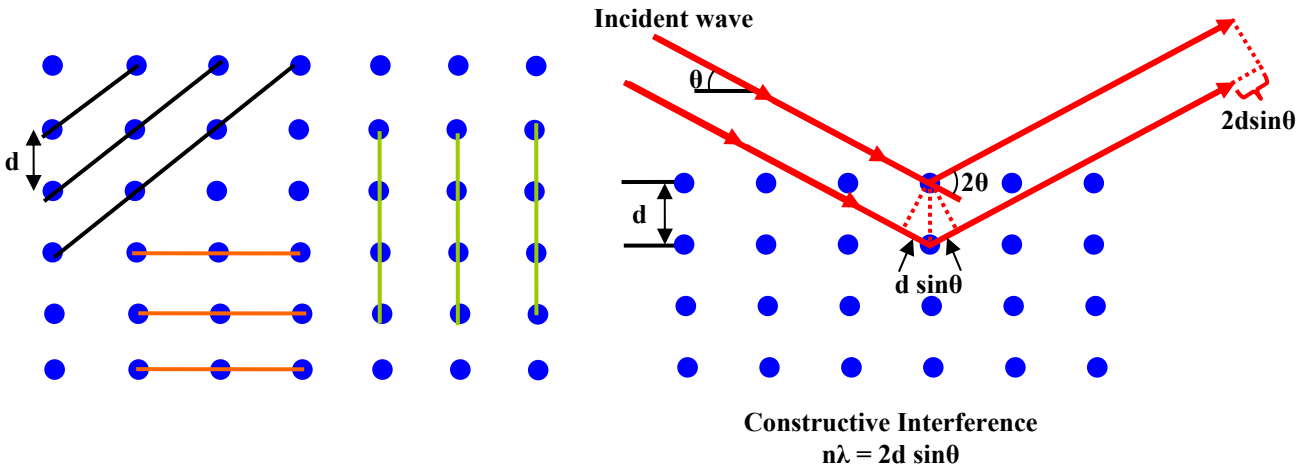

Figure 3-40. Bragg's Law – Diffraction of X-rays

At other angles there is little or no diffracted intensity because of negative interferences. From Bragg's Law we have the relations:

$$\sin\theta = \frac{n\lambda}{2d} \leq 1 \qquad \textbf{Equation 3.6-2}$$

$$\lambda \leq 2d \quad \text{for } n = 1 \qquad \textbf{Equation 3.6-3}$$

From the equations above the first order diffraction can occur only for wavelength $\lambda \leq 2d$. Since the lattice spacing d is on the order of Angstroms, visible light cannot be used but X-rays are suitable for diffraction studies. Bragg's Law is applied to scattering centers consisting of any periodic distribution of electron density. The law holds for molecules or collections of molecules such as colloids, polymers, proteins, therefore it is one of the most important laws used for interpreting X-ray diffraction data.

3.6.3 Principle of X-Ray Scattering Experiment

Figure 3-41 shows a typical experimental set-up with the essential parts of a small-angle scattering instrument. A monochromatic x-ray beam of incident wave vector $\vec{k}_i$ is selected by a collimator and strikes the sample. A fraction of this beam is deviated, e.g. scattered, and travels in other directions after leaving the sample. The detector usually records the scattered beam after passing through slits, which define a precise solid angle.

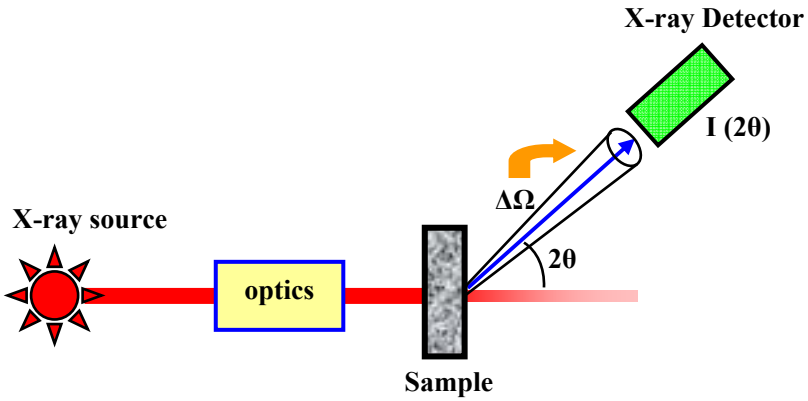

Figure 3-41. Schematic drawing of a typical X-ray scattering instrument

The scattered intensity is collected as a function of the scattering angle 2θ. Elastic interactions are characterised by zero energy transfer, so that the final wave vector k_f is equal in modulus to k_i. The relevant parameter to analyse the interaction is the momentum transfer or scattering vector, **Figure 3-42**, given by the following expression:

$$\vec{q} = \overrightarrow{k_i} - \overrightarrow{k_f} \qquad \textbf{Equation 3.6-4}$$

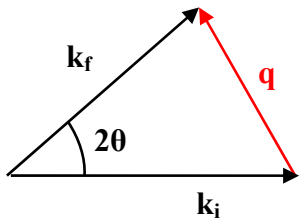

Figure 3-42. The scattering vector q

The scattering vector amplitude is defined as:

$$q = \frac{4\pi \cdot \sin\theta}{\lambda} \qquad \textbf{Equation 3.6-5}$$

Since λ is usually equal to a few Angstroms for x-rays in the small angle region, qD (no units - the standard unit for q is $Å^{-1}$) is almost always small compared to 1 for distances d of the order of the diameters of atoms or small molecules. Consequently, the rays scattered from different parts of an atom or small molecule arrive at the detector almost completely in phase. A general property of scattering is that the scattering process cannot resolve and give information about structure characterized by a length d when the condition:

$$qD = \frac{4\pi \cdot \sin\theta}{\lambda} D << 1 \qquad \textbf{Equation 3.6-6}$$

is fulfilled. That means that small angle x-ray scattering is mostly sensitive to structure in the range of about $D = 2\pi/q$. Information about the structure of the sample can be obtained from analysis of measurements of the scattering intensity. The scattered intensity I(q) is the Fourier transform of g(r), the correlation function of the electronic density ρ(r), which corresponds to

the probability to find a scatterer at position *r* in the sample, if another scatterer is located at position 0: elastic x-ray scattering experiments reveal the spatial correlations in the sample. Small angle scattering experiments are designed to measure I(q) at very small scattering vectors, with 2θ ranging from a few micro-radians to a tenth of a radian, in order to investigate systems with characteristic sizes ranging from crystallographic distances (a few Å) to colloidal sizes (up to a few microns). The number of photons scattered by a sample is proportional to its total volume V and to its electronic contrast. In the case of a binary system, such as objects of density ρ_1 embedded in a solvent of density ρ_2, the electronic contrast is $\Delta\rho = \rho_1 - \rho_2$ ($eÅ^{-3}$ or cm^{-3}). The higher the contrast between particles and solvent, the more intense the scattered signal. The experimental intensity is usually fitted in order to determine the density ρ(r), the size, the shape and the internal structure of one elementary scatterer, as well as the structure and the interactions between scatterers. The determination of physical quantities, such as molecular weight, particle volume or specific surface is feasible only if I(q) is measured on an absolute scale. The material absorbs part of the incident beam as shown in **Figure 3-41**. The number of photons scattered in the solid angle ΔΩ in the direction 2θ must be normalised with respect to the number of photons transmitted through the sample. For this purpose, several parameters should be controlled: the sample thickness *e* (cm) and transmittance T, the incident flux of photons φ_o (photons/s) and the solid angle of one pixel of the experiment ΔΩ. The absolute intensity can then be obtained in absolute units (cm^{-1}):

$$I(q) = \frac{C(q)}{\varphi_o \cdot e \cdot t \cdot T \cdot \Delta\Omega}\left(cm^{-1}\right) \qquad \textbf{Equation 3.6-7}$$

where C(q) is the number of photons detected at position q, t is the time of measurement and ΔΩ is the solid angle, equal to $\Delta\Omega = m^2/d^2$, with m the size of a pixel and d the distance of the sample from the detector.

3.6.4 Phase Identification

X-ray scattering is the most reliable method of carrying out lipid phase identification. The characterization of lipid mesophases by diffraction is based on symmetry. Two basic regions of the diffraction pattern are used to identify the phase. The small angle region identifies the symmetry and long-range organization of the phase, whereas the wide angle region gives

information on the molecular packing, or the short range organization of the phase. Aggregation of amphiphilic molecules into micelles leads to diffuse scattering in the small angle region. If the positions of the aggregates are completely independent of each other (dilute micellar solutions), then the observed scattering is the sum of the scattering from each individual aggregate. With increasing concentration, interactions arise between the micelles e.g. electrostatic forces or hydration forces. This causes the diffuse scattering to be modulated, so that as the interactions become stronger the scattering becomes more sharply peaked. At some point the repulsive interactions are strong enough to lead to an ordering of aggregates onto a lattice, forming ordered liquid crystalline phases. The "signature" for the observation of an ordered mesophase is the appearance of one or more sharp Bragg peaks in the small angle region. The long range ordering of the lipid-water aggregates (bilayers, cylinders or micelles) onto one-, two-, or three-dimensional lattices gives rise to Bragg reflections. While the positions of the diffraction peaks are related to periodic distances within the lyotropic lipid mesophase, their sharpness or width reflects the extent of this periodicity over large distances. The measured reciprocal spacings are given by:

$$s = \frac{2}{\lambda}\sin\theta \qquad \textbf{Equation 3.6-8}$$

where $q = 2\pi \cdot s$, 2θ is the scattering angle, and λ the radiation wavelength.

The one-dimensional periodic structure of lamellar lipid-water mesophases exhibits diffraction patterns in the small-angle regime that are described by the equation:

$$s_n = n\frac{1}{D} \qquad \textbf{Equation 3.6-9}$$

where n = 1, 2, 3, 4, … and D is the lamellar repeat unit, which consists of the sum of the water and lipid layer thickness.

3.6.5 Phase Dimensions and Peak Position analysis (Swelling Law)

Structural information can be deduced from the positions of the diffraction lines, in conjunction with chemical parameters such as the lipid molecular weight MW, the water and

lipid partial specific volumes, $\bar{v}_w$ and $\bar{v}_L$ respectively, and the lipid weight concentration c. The lipid volume fraction is given by the equation:

$$\varphi_L = \left[1 + \frac{(1-c)\bar{v}_w}{c\bar{v}_L}\right]^{-1} \qquad \textbf{Equation 3.6-10}$$

and the volume fraction of water is $\varphi_W = 1 - \varphi_L$. The lipid volume fraction is also related to the membrane (bilayer) thickness, b_L, as shown in **Figure 3-43**. If the membranes are perfectly flat and the area per lipid head is A, with n_s the number of lipid molecules in a unit cell, the total membrane area S is $S = n_s A$, the volume of the unit cell being $V = (D \times S)/2$. The lipid volume fraction is then given by:

$$\varphi_L = \frac{n_s u_s}{V} = \frac{2u_s}{AD} = \frac{b_L}{D} \qquad \textbf{Equation 3.6-11}$$

where u_s is the molecular volume of the lipid and D the repeat distance between the bilayers (**Figure 3-43**).

The peak position, q, from x-ray measurements is related to the repeat distance D as follows:

$$q = \frac{2\pi}{D} \qquad \textbf{Equation 3.6-12}$$

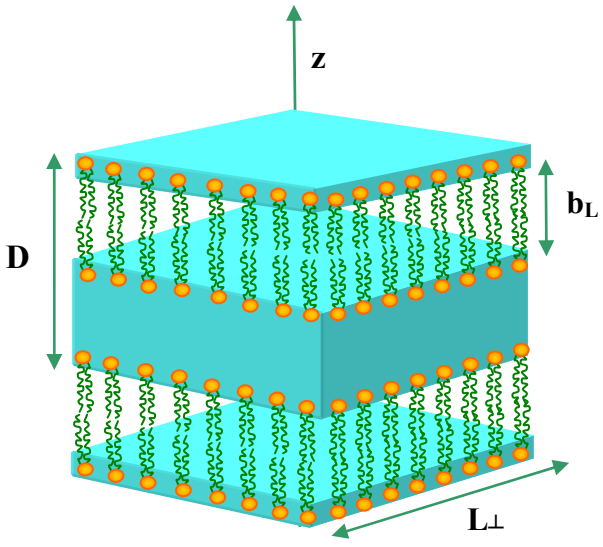

Figure 3-43. Geometric model of a lyotropic lamellar phase

Using **Equation 3.6-11** and **Equation 3.6-12** one can study the dilution law or maximum swelling law of bilayers through a graph of D vs $(\varphi_L)^{-1}$ as shown in **Figure 3-44**. According to **Equation 3.6-11** this graph should be a straight line with slope b_L. Lamellar phases spontaneously take up water and swell (the lipid volume fraction decreases and D increases) up to a limiting point, which defines the equilibrium separation of the bilayers. At that point, the lamellae cannot accommodate more water therefore this is called maximum swelling. The maximum swelling law offers the opportunity to test lamellar flexibility and interactions between the lamellae.

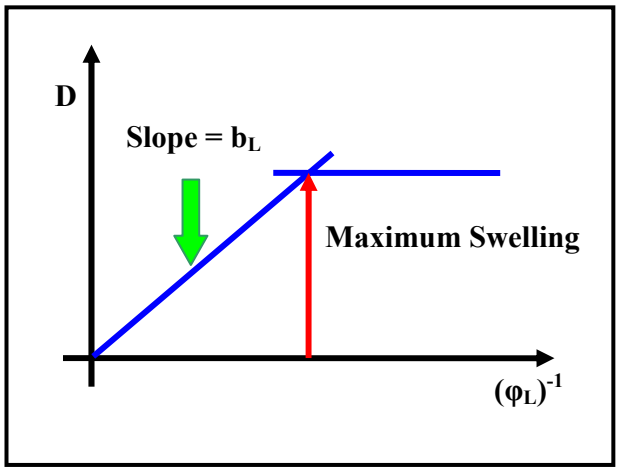

Figure 3-44. The maximum swelling law

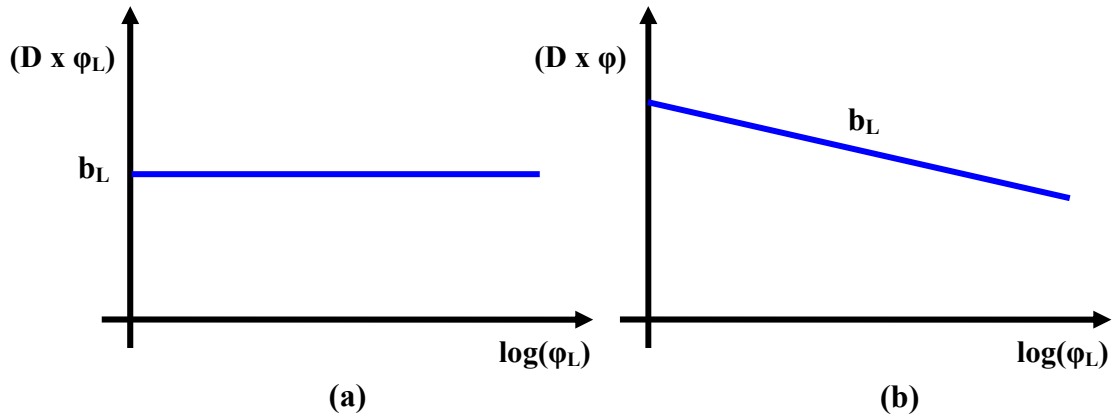

Figure 3-45. Dilution behaviour of the repeat distance

For a flat, electrostatically stabilized membrane, one expects a constant thickness of the bilayers, as shown in **Figure 3-45**, while this does not hold for lamellae with undulation

interactions. The strength of the undulations can be assessed using a plot of (D x φ_L) against log(φ_L): in the case of strongly undulating lammelae D x φ_L decreases linearly with log(φ_L).

3.6.6 Experimental Setup

The X-ray Diffraction method was used to determine the structural parameters of DPPC bilayers in the presence of sodium salt solutions of concentrations 0.05M, 0.1M and 0.5M. The experiments were performed using a Huxley-Holmes High Flux camera at the Service de Chimie Moléculaire, CEA-Saclay (France), as shown in **Figure 3-46**.

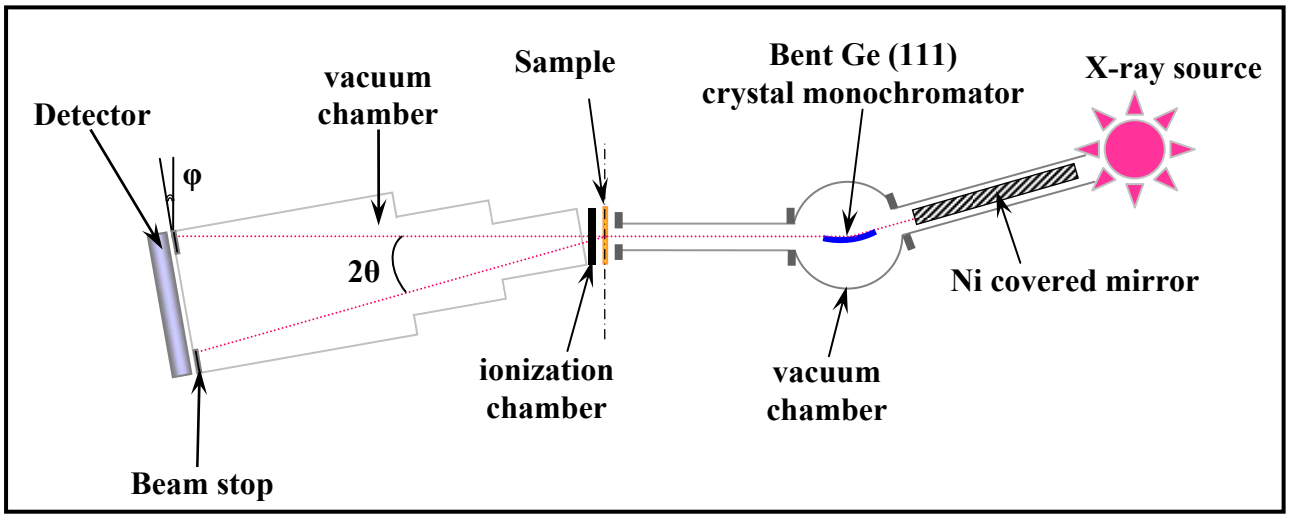

Figure 3-46. General layout of the x-ray experimental setup

The X-ray source is a copper rotating anode operating at 15kW. By the combination of a nickel-covered mirror and a bent, asymmetrically cut germanium ‹111› monochromator, the Kα_1 of the copper radiation (λ = 1.54Å) is selected and separated from high-energy radiations to reduce the background signal. A two-dimensional gas-filled detector with a diameter equal to 0.3 m is used to record the experimental spectra. The effective q-range of this detector is from 0.02 to 0.4 $Å^{-1}$. The exposure time for each sample was 30 min. All experiments have been performed at a temperature T = 50 ± 1°C, at which the L_a lamellar phase of the DPPC molecule is formed.

The lamellar repeat spacing D was obtained experimentally by the Bragg diffraction law, and can be divided into the bilayer thickness, b_L and the water layer thickness or bilayer separation d_w:

$$b_L = \varphi_L D \qquad \textbf{Equation 3.6-13}$$

$$d_w = D - b_L \qquad \textbf{Equation 3.6-14}$$

φ_L is the volume concentration of the lipid in the sample, obtained by the weight concentration (see **Equation 3.6-10**). $\bar{v}_w$ was taken as 1.00 ml/g and $\bar{v}_L$ as 1.0091 ml/g for DPPC with melted hydrocarbon chains. In addition, through the lipid bilayer thickness, b_L, one can estimate the headgroup area, A, of the DPPC molecules using the following relationship:

$$A = \frac{2x10^{24} \cdot MW \cdot \overline{v_L}}{b_L \cdot N_{AV}} \qquad \textbf{Equation 3.6-15}$$

where MW is the lipid molecular weight, $\bar{v}_L$ the lipid partial specific volumes, N_{AV} Avogadro's number and b_L the lipid bilayer thickness.

3.7 Dynamic Light Scattering (DLS)

Scattering experiments can provide a wealth of detailed information about the structural and dynamical properties of matter. Light Scattering is an established technique that has been used for many years for the determination of the average size and the size distribution of particles in a suspension. Two fundamentally different experimental approaches can be performed depending on how the scattered intensity is measured. a) Time averaged experiments where the scattered intensity is averaged over long observation times and collected as a function of the scattering angle θ. This method is called Static Light Scattering. b) Time resolved experiments where at one or several scattering angles the temporal variations of the scattered intensity are registered and analyzed. This method is called Dynamic Light Scattering (DLS) or Quasi – Elastic Light Scattering (QELS). Several parameters of interest can be deduced by these techniques such as molecular weight, radius of gyration, diffusion coefficient, hydrodynamic radius, second virial coefficient or interparticle structure factor, form factor etc. The techniques have also the advantages of being relatively fast, noninvasive, and require minimal sample preparation.

3.7.1 Principles of Light Scattering

According to the light scattering theory, when light impinges on matter the electric field of the light induces an oscillating motion of the electrons in the molecules of the sample. The molecules then serve as a secondary source of light and subsequently radiate (scatter) light. The frequency change, the angular distribution, the polarization and the intensity of the scattered light are determined by the size, shape and molecular interactions in the scattering material.

A schematic of a Light Scattering experiment is shown in **Figure 3-47**. A dispersion of particles is illuminated with a collimated laser beam. The direction of propagation of this beam is described by an incident wave vector $\vec{k}_i$ which is defined as:

$$\left|\vec{k}_i\right| = \frac{2\pi}{\lambda_0} n \qquad \textbf{Equation 3.7-1}$$

where λ_0 and n are the wavelength of light in vacuum and the refractive index of the medium respectively.

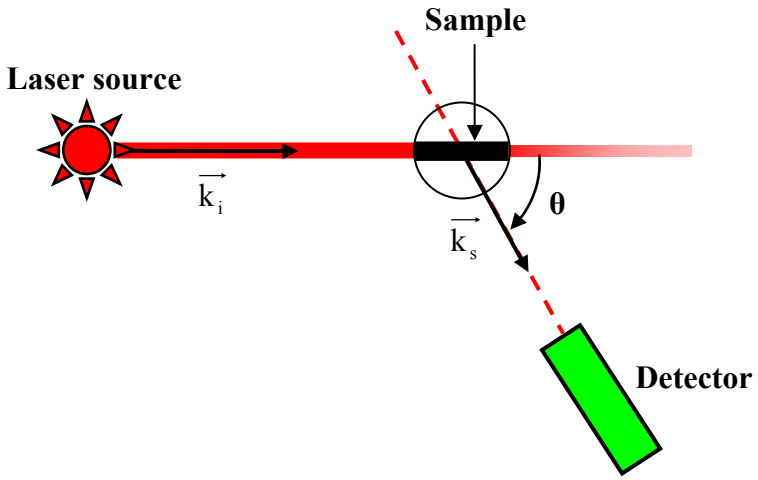

Figure 3-47. Schematic representation of a light scattering instrument

The radiation scattered at an angle θ with respect to the incident beam is characterized by a scattered wave vector $\vec{k}_s$ in the direction of propagation of this beam. Part of the radiation scattered at an angle θ, is registered with a very sensitive detector. The scattering vector $\vec{q}$ characterizes the properties of the scattered light (just as for SAXS) which is defined as the difference between the incident and the scattered wave vector:

$$\vec{q} = \vec{k}_i - \vec{k}_s \qquad \textbf{Equation 3.7-2}$$

The magnitude of the scattering vector $\vec{q}$, taking into account that $\left|\vec{k}_i\right| = \left|\vec{k}_s\right|$ is given by:

$$q = \frac{4\pi \cdot n}{\lambda_0} \sin\left(\frac{\theta}{2}\right) \qquad \textbf{Equation 3.7-3}$$

The inverse scattering vector q^{-1} has the dimension of a length. In order to obtain useful information from a scattering experiment, the length scale of the investigated sample must be comparable to the value of q^{-1}. Typical values of q^{-1} are in the range of 10 to 1000nm thus the light scattering technique is suitable for studying colloidal systems and for the characterization of colloidal dispersions of particles (**Johnson et al. 1994; Hallet 1999**).

3.7.2 Theory of Dynamic Light Scattering

DLS, also known as Photon Correlation Spectroscopy (PCS), uses the time dependence of the intensity of the scattered light to determine the translational diffusion coefficient of small particles. The scattered radiation is collected over a small solid angle, which exhibits intensity fluctuations on a time scale of microseconds to milliseconds. This happens because, in a colloidal dispersion, the particles continuously collide with the molecules of the liquid phase performing a random thermal motion called Brownian motion (the particles change often their direction and speed). This motion causes the intensity of the scattered light at any point in space to fluctuate with time. As a result, the radiation frequency is shifted to higher or lower values depending on the particle velocity and direction relative to the detector (Doppler Effect). The average displacements of a Brownian motion of the electrons can be quantified by the diffusion coefficient D, which in turn is related to the size of the particles.

The diffusion coefficient of the particles can be measured by means of an autocorrelation function (ACF) $g_2(t_d)$, which is used to study the correlation, or similarity between the value of scattered intensity I(t) at a given time t and the value of intensity $I(t + t_d)$ at a later time with time delay t_d. The time t_d is known as the *delay time*, since it represents the delay in time between two discrete time intervals Δt as illustrated in **Figure 3-48**. Thus, the ACF is used to analyze the time dependence of the intensity fluctuations. The comparison of I(t) and $I(t + t_d)$ is made for many different values of t in order to obtain a good statistical average for $g_2(t_d)$. The autocorrelation function is given by the following expression:

$$g_2(t_d) = \langle I(t) \cdot I(t + t_d) \rangle \qquad \textbf{Equation 3.7-4}$$

The brackets denote an average which is performed for a large number of times t. For short time delays, t_d, the positions and hence the scattered intensities of a particle are highly correlated, so that the $g_2(t_d)$ function has a big value. For long time delays, the positions of a particle in random motion are no longer correlated and thus the autocorrelation function has a small value.

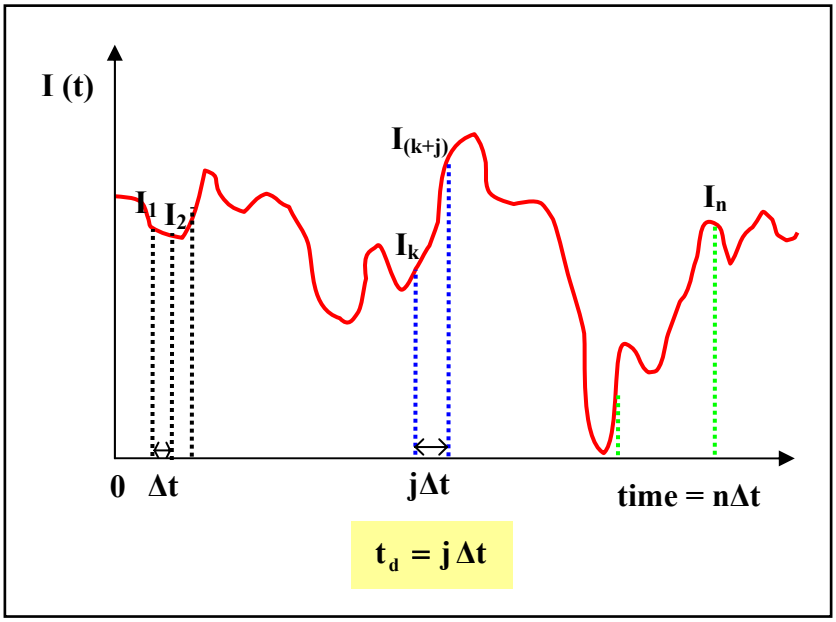

Figure 3-48. Autocorrelation function dependence on time

At the two limiting cases, $t_d \rightarrow 0$ and $t_d \rightarrow \infty$, the autocorrelation function equals:

$$\lim_{t_d \rightarrow 0} g_2(t_d) = \langle I_t^2 \rangle \qquad \textbf{Equation 3.7-5}$$

$$\lim_{t_d \rightarrow \infty} g_2(t_d) = \langle I_t \rangle^2 \qquad \textbf{Equation 3.7-6}$$

It is known for any fluctuating quantity that the average of the square of that quantity is always larger than the square of the average:

$$\langle I_t^2 \rangle > \langle I_t \rangle^2 \qquad \textbf{Equation 3.7-7}$$

The quantity of the right hand side of **Equation 3.7-7** is the lowest value possible for the autocorrelation function and thus for diffusing particles the value of $g_2(t_d)$ is found between the two limiting cases. In general, the autocorrelation function $g_2(t_d)$ of the fluctuation scattered light intensity I(t) is an exponentially decaying function of time t_d, as shown in **Figure 3-49**.

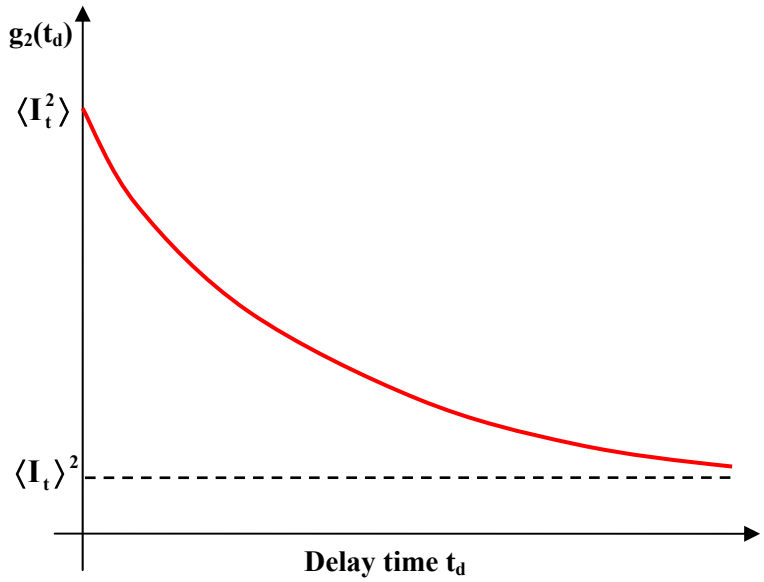

Figure 3-49. Exponetial decay of autocorrelation function with time

The function $g_2(t_d)$ can be described by the expression:

$$g_2(t_d) = A[g_1(t_d)]^2 + B \qquad \textbf{Equation 3.7-8}$$

where A is an instrumental factor, B is the long-time value for $g_2(t_d)$, commonly referred to as the baseline, and $g_1(t_d)$ is the electric field autocorrelation function. The electric field ACF is equal to:

$$g_1(t_d) = e^{-\Gamma t_d} \qquad \textbf{Equation 3.7-9}$$

where Γ is the decay rate that is related to the diffusion coefficient D and the characteristic decay time constant of the exponential function τ by the following equations:

$$\Gamma = Dq^2 \qquad \textbf{Equation 3.7-10}$$

$$D = \frac{1}{2q^2\tau} \qquad \textbf{Equation 3.7-11}$$

q is the scattering vector defined in **Equation 3.7-3**. The characteristic decay time constant characterizes quantitatively the speed with which the autocorrelation function $g_2(t_d)$ decays towards the long t_d limiting value of a fluctuation in the scattered intensity I(t). Thus, small

particles will "jitter" about in solution relatively rapidly, resulting in a rapidly fluctuating intensity signal; by contrast, larger ones will diffuse more slowly, resulting in slower intensity fluctuations and longer characteristic decay time τ.

The diffusion coefficient D that is determined by the analysis of the ACF is used to determine the size of the particles, specifically the hydrodynamic radius R_h, using the Stokes – Einstein relationship:

$$D = \frac{kT}{6\pi \cdot \eta R_h} \qquad \textbf{Equation 3.7-12}$$

where k is Boltzmann's constant, T the absolute temperature and η the viscosity of the dispersing liquid. The above equation is valid only for monodispersed, non-interacting, spherically shaped particles of any size. (**Santos et al. 1996; Corti 1983; Hiemenz et al. 1997**) Other equations exist for ellipsoidal or cylindrical particles or for polymeric random coils.

3.7.3 Cumulants

In the case of polydisperse samples the autocorrelation function $g_1(t_d)$ is no longer a simple exponential, i.e. having a single, well-defined decay time constant τ. The existence of more than one rate of diffusion inevitably gives rise to a mixture of decaying exponential functions, each of which has a different time decay constant τ_i corresponding to a particular diffusivity D_i and, hence, to a particle radius R_i. Thus, it is necessary to analyze precisely the deviations of the autocorrelation function $g_2(t_d)$ from single-exponential behavior, in order to extract the distribution of D values (and hence of particle diameters) from the detailed shape of $g_2(t_d)$. For polydisperse samples the $g_1(t_d)$ is given by the following expression:

$$g_1(t_d) = \int_0^\infty G(\Gamma)\exp(-\Gamma\tau)d\Gamma \qquad \textbf{Equation 3.7-13}$$

where $G(\Gamma)$ is normalized so that:

$$\int_0^\infty G(\Gamma)d\Gamma = 1 \qquad \textbf{Equation 3.7-14}$$

To find the precise functional form for the distribution of decay rates G(Γ), efficient mathematical methods of analysis have been developed, one of the simplest ones being the method of CUMULANTS proposed by **Koppel 1972**. The generating function $g_x(t_d)$ in the cumulants method is defined as $g_x(t_d) = \ln[g_x(t_d)]$. If the constant baseline is substracted from $g_2(t_d)$, the plot of $\ln[g_2(t_d)]$ versus t_d is linear because the time-dependent part of $g_2(t_d)$ is a single exponential for a monodispersed system. Deviation from linearity indicates polydispersity. The $g_1(t_d)$ ACF for polydisperse systems is given by a series expansion using the method of cumulants:

$$\ln[g_1(t_d)] \equiv K_1 t_d + \frac{K_2 t_d^2}{2!} - \frac{K_3 t_d^3}{3!} + \ldots \qquad \textbf{Equation 3.7-15}$$

where

$$\begin{aligned} K_1 &= \langle\Gamma\rangle \\ K_2 &= \langle(\Gamma - \langle\Gamma\rangle)^2\rangle \\ K_3 &= \langle(\Gamma - \langle\Gamma\rangle)^3\rangle \\ K_4 &= \langle(\Gamma - \langle\Gamma\rangle)^4\rangle - 3K_2^2 \\ K_n &= \left\{(-1)^n \frac{d^n}{dt_d^n}\ln[g_1(t_d)]\right\}_{t_d=0} \end{aligned} \qquad \textbf{Equation 3.7-16}$$

K_n is the nth cumulant of $g_1(t_d)$. K_1 is the mean of Γ and defines an effective (average) diffusion coefficient, **Equation 3.7-17**; K_2 is the variance of the distribution that provides information about the spread of the particle size distribution. The higher cumulants give information on asymmetry and other properties of the distribution with increasing uncertainty (**Frisken 2001; Santos et al. 1996; Koppel 1972; Corti 1983**).

$$D = \frac{K_1}{q^2} \qquad \textbf{Equation 3.7-17}$$

3.7.4 Experimental Setup

The *Brookhaven BI-9000AT* Digital correlator with combination of the *Brookhaven BI-200SM* goniometer has been used in the DLS experiments reported in this thesis. The experimental setup is shown in **Figure 3-50**.

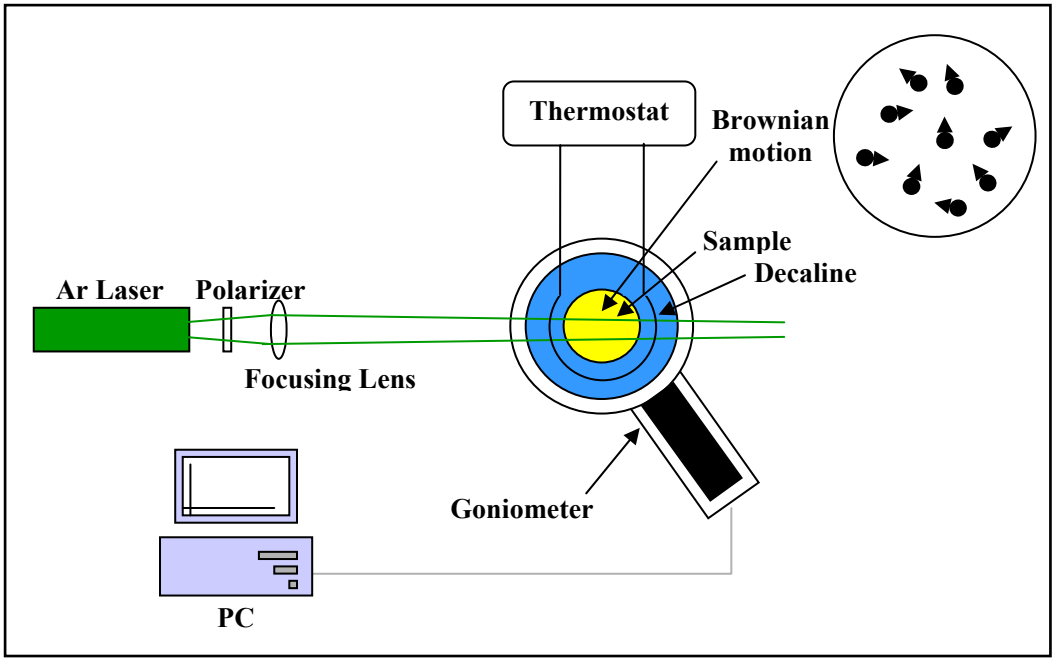

Figure 3-50. Schematic drawing of the DLS experiment

The two instruments form a powerful and versatile suite for studying particulate systems. The BI-200SM goniometer is generally used for particle size analysis, the investigation of the structure of complex fluids, micelles, microemulsions and colloids. It allows the use of multi-angle measurements yielding more information on particles and molecules than a single-angle system. The BI-9000AT correlator is equally versatile, allowing sampling times as low as 25ns and as high as 40ms, with delays ranging from 25ns to 1310s. It can process two different signals simultaneously, for example to cross-correlate two signals from different positions in a liquid or from two detector angles. The light source is a *Stabilite 2017 Argon Ion Laser* from Spectra Physics. It delivers a power of 2W at 514.5 nm.

The sample to be analysed, is placed in the cell of the BI-200SM goniometer where a beam of monochromatic light from the Stabilite Laser passes through it. Some of the incident light is scattered in all directions by the particles within the sample and the intensity ACF is recorded.

Then we use one of several different approaches, as described above, to numerically fit the data with calculated size distributions using the BI-9000AT correlator software.

3.7.5 DLS – SLS

The experimental size of DPC micelles obtained by the cumulants numerical fit of the software, is compared with that found using the standard Static Light Scattering (SLS) equations which apply for spherical micelles in solution. These are:

$$R = \sqrt[3]{\frac{3NV_{mol}}{4\pi}} \qquad \textbf{Equation 3.7-18}$$

where R is the average radius of a micelle, V_{mol} is the molecular volume of a DPC molecule and N is the aggregation number of a globular micelle given by the following equation:

$$N = \frac{M}{(MM)_{mon}} \qquad \textbf{Equation 3.7-19}$$

where M is the micellar mass and $(MM)_{mon}$ is the mass of a surfactant DPC molecule.
Also, the area per molecule, α, can be calculated using the following expression:

$$\alpha = \frac{4\pi \cdot R^2}{N} \qquad \textbf{Equation 3.7-20}$$

3.8 Freeze-fracture microscopy

3.8.1 Principles of Freeze-fracture microscopy

The Freeze-fracture technique used in combination with both scanning electron microscopy (SEM) and transmission electron microscopy (TEM) was originally developed in order to obtain information (structural details) about the internal contents of cell membranes. Now it is widely used not only for cell membranes but also for viewing samples that form lipid bilayers. The freeze-fracturing make it possible to examine the specimen without altering it chemically or physically (dehydration, impregnation with a resin, drying). In general, the sample is rapidly frozen in liquid nitrogen or freon, and then it is freeze-fractured at a temperature below -110°C. The fractured plane is replicated with a heavy metal, usually platinum, and then coated with a thin layer of carbon, thus providing a metal-carbon template. The sample is thawed and the replica is separated from the sample, cleaned from residues, and then examined with electron microscopy.

When a sample is fractured, the fracture plane follows *the path of least resistance*. As a result, the lipid bilayers most likely split along the middle of the two layers, or through the hydrophobic region of the membrane exposing the lipid bilayers interior. Specifically for cell membranes, cellular organelles remain embedded in one layer, causing changes in the fracture plane such as elevations, depressions, and ridges, representing the many surfaces of the cell. In this way information about their particular size and distributions are revealed.

The Freeze-fracture technique is very useful but it has some disadvantages. One disadvantage is that this technique has no use outside of obtaining structural descriptions. No functional information is obtained about a cell using this technique. Second, the fracturing proceeds at its own will, scientists cannot choose a particular path for the fracture plane to follow.

3.8.2 Experimental Setup

Small pieces of the lipid sample prepared in a mixture of glycerol and salt solution of known concentration were mounted and forced into contact with a copper sample holder and quickly frozen using Freon – 22 that has a boiling point of -145 °C. Next, the sample is fractured with a microtome knife. The lipid bilayers split along the paths of least resistance, forming the fractured plane. The fractured-exposed sample is then coated with a heavy metal (platinum)

which is deposited on the fracture surface in order to produce shadows on the surface; Next, the fractured surface is covered with a solid, uniform layer of carbon over the top of the metal, producing a template of the solution constituents. Shadowing is carried out using an appropriate current which passes (using external knobs) into the platinum and carbon rods through circuits. The current causes the rods to evaporate and coat the fractured-exposed sample. The rate of evaporation can be controlled to vary the thickness of deposition of platinum and carbon. The sample is no longer needed and can thus be thrown away. The remaining metal-carbon replica is viewed with electron microscopy. The experimental procedure is shown in **Figure 3-51**.

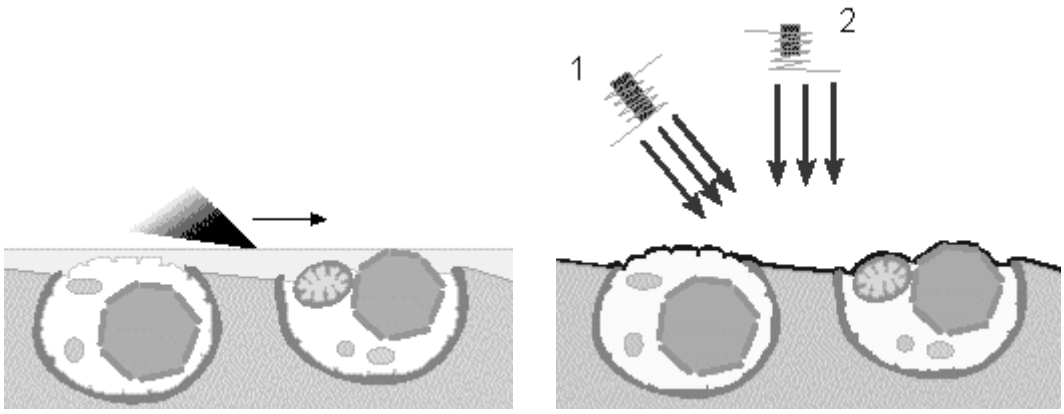

Figure 3-51. Freeze-fracture and metal-carbon templating

.

3.9 Karl Fischer titrations

3.9.1 Karl Fischer titrations

The Karl Fischer titration is a moisture determination method specific for water. It is a chemical analysis procedure which is based on the oxidation of sulphur dioxide by iodine in an alkaline methanolic solution. In principle, the following chemical reaction takes place:

$$H_2O + I_2 + SO_2 + 3Base \rightarrow 2Base \cdot HI + Base \cdot HSO_4R$$

The Karl Fischer titration is a two stage process. The first stage involves the reaction of sulphur dioxide with methanol to form an ester, which is neutralised by a nitrogen base (RN). The second stage is a rapid oxidation of the alkyl sulphite anion to alkyl sulphate by iodine - a reaction that consumes water.

The titration can be performed volumetrically or coulometrically for samples with high moisture content (titrimetry) and for those with water contents in the ppm range (coulometry) respectively. In the volumetric method, a Karl Fischer solution containing iodine is added until the first trace of excess iodine is visible. The amount of iodine converted is determined from the burette volume of the iodine-containing Karl Fischer solution.

In the coulometric procedure, the iodine participating in the reaction is generated directly in the titration cell by electrochemical oxidation of iodide until again a trace of unreacted iodine is detected. The iodine reacts with the water that is present. According to Faraday's Law the amount of water titrated is proportional to the total current used in generating the iodine necessary to react with the water present. One mole of iodine reacts quantitatively with one mole of water. As a result, one milligram of water is equivalent to 10.71 coulombs. Based on this principle, the water content of the sample can be determined by the quantity of electricity required for electrolysis.

As shown in **Figure 3-52**, two types of coulometric reagents are required: an anolyte, which is placed in the anode chamber of the electrolysis cell, and a catholyte, which is placed in the cathode chamber.

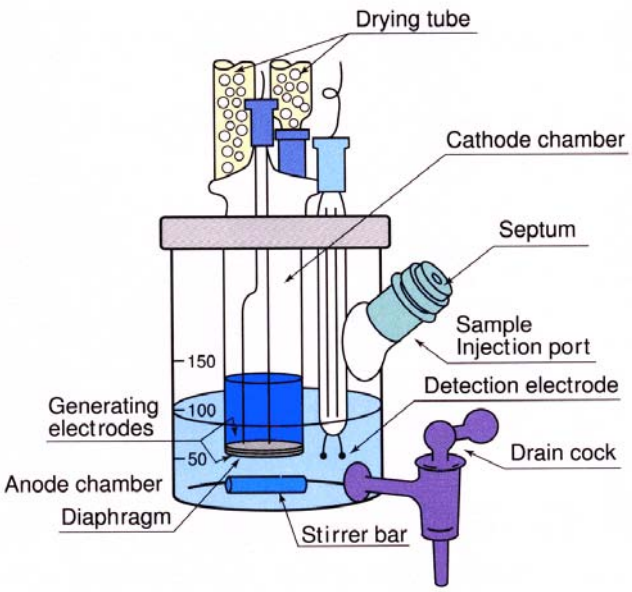

Figure 3-52. Coulometric titration

3.9.2 Experimental Setup

The experimental apparatus consists of an automatic burette, a backtitration flask, a stirrer, and equipment for amperometric titration at constant voltage or potentiometric titration at constant current.

4 CHAPTER

LIPIDS USED IN THIS THESIS

4.1 Chemical Substances

The lipid molecules used in this study were 1,2-dipalmitoyl-sn-glycerol-3-phosphocholine (DPPC) and the synthetic molecule dodecylphosphocholine (DPC). A detailed description of the two molecules is given below.

4.2 Lipid molecules and Biological membranes

Biological membranes are organized assemblies consisting mainly of lipids and proteins. All membranes constituents are held together by noncovalent interactions; as a result membranes are fluid structures. Lipid molecules and proteins diffuse rapidly in the plane of the membrane. In contrast, they rotate across the membranes at much slower rates. Therefore, membranes can be regarded as two-dimensional solutions of oriented proteins and lipids.

Among the different lipids found in biomembranes, phospholipids play an important role because they represent the main constituents of cellular membranes. Phospholipids are fatty acid derivatives. Each molecule is made up of one glycerol moiety attached to two fatty acids

and a phosphate group. Phospholipids are structurally similar to triglycerides with the difference that a phosphate group and one of several nitrogen-containing molecules replace one of the fatty acids. The hydrocarbon chains constitute the hydrophobic part and the phosphate and amino groups make the hydrophilic part of the molecule, **Figure 4-1**.

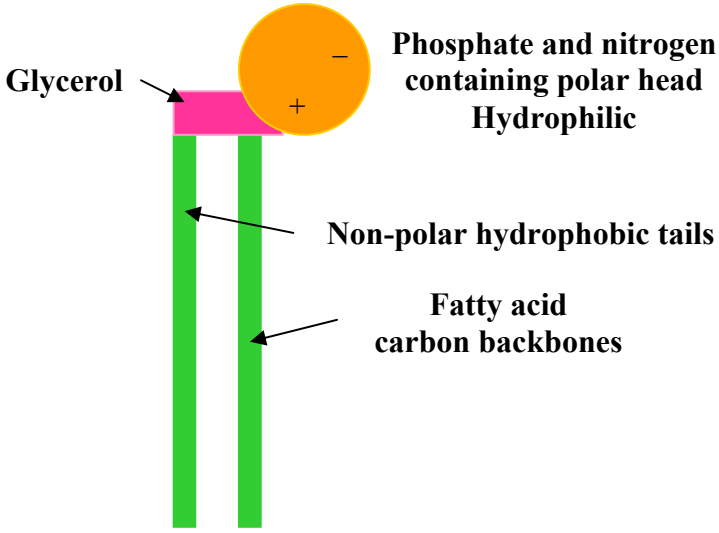

Figure 4-1. Basic Lipid Structure

4.3 Phospholipid DPPC

1,2-dipalmitoyl-sn-glycerol-3-phosphocholine (DPPC) shown in **Figure 4-2** is one of the most common phospholipids present in biological and model membranes. It is a zwitterionic molecule with two hydrocarbon chains containing 16 carbon atoms each. The hydrocarbon chain bonded through an ester linkage to the chiral carbon of the glycerol is given the name sn2, while the other chain is given the name sn1. The DPPC molecule, being a double-chain amphiphile, can form stable monolayers at the air-water interface but also lamellar phases in aqueous solutions.

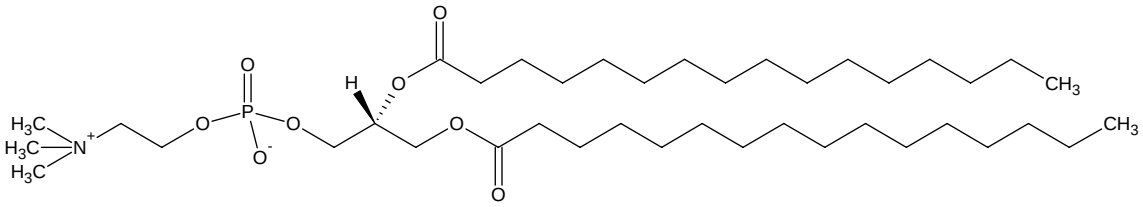

Figure 4-2. Chemical structure of DPPC molecule

An approximate phase diagram of the system DPPC/water is shown in **Figure 4-3**. The phase diagram reveals the existence of a limiting transition temperature T_m called melting temperature, which is the lowest temperature at which water can penetrate between the layers of the lipid molecules and form the fluid lamellar phase. Dipalmitoylphosphatidylcholine bilayers undergo two major phase transitions (gel-fluid transitions) in aqueous solutions: a pretransition $L_\beta \rightarrow P_{\beta'}$ and a main transition $P_{\beta'} \rightarrow L_\alpha$. The driving forces for the gel-fluid transition are (a) the increase in entropy of the system with the lipid chain rotational disorder and (b) the increase in lipid headgroup hydration. DPPC bilayers adopt the liquid lamellar L_α phase at temperatures higher than 41°C. The hydrocarbon chains are in a fluid state and the hydrophilic groups occupy the surface separating the lipid and water layers. **Figure 4-4** shows pictures of the fully hydrated DPPC bilayers in the L_α, L_β and $L_{\beta'}$ phase generated by computer simulations. The pretransition to the ripple $P_{\beta'}$ phase is observed at a temperature about 35°C.

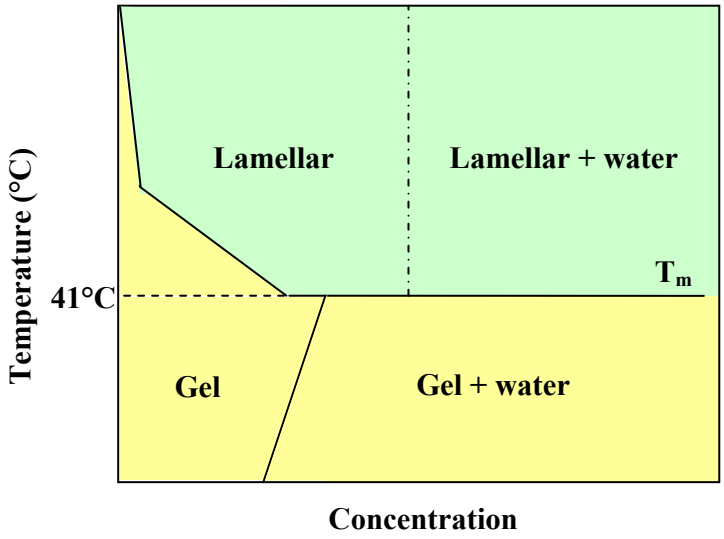

Figure 4-3. Phase behaviour of DPPC (Chapman et al. 1967)

Compared to the fluid phase, the gel phase exists at lower hydration and temperature, with mostly straight hydrocarbon chains and closer packing of the lipids, **Figure 4-4**.
The lamellar repeat distance D increases from ≈ 63Å in the gel phase to ≈ 72Å in the ripple phase. However, the repeat distance D of the fluid lamellar phase decreases to about 66Å due to the highly disordered chains of the lipid molecules. At 25°C (gel phase) the repeat distance

D between the bilayers increases with water content, up to a limiting point corresponding to lipid volume concentration $\varphi_L \approx 74\%$.

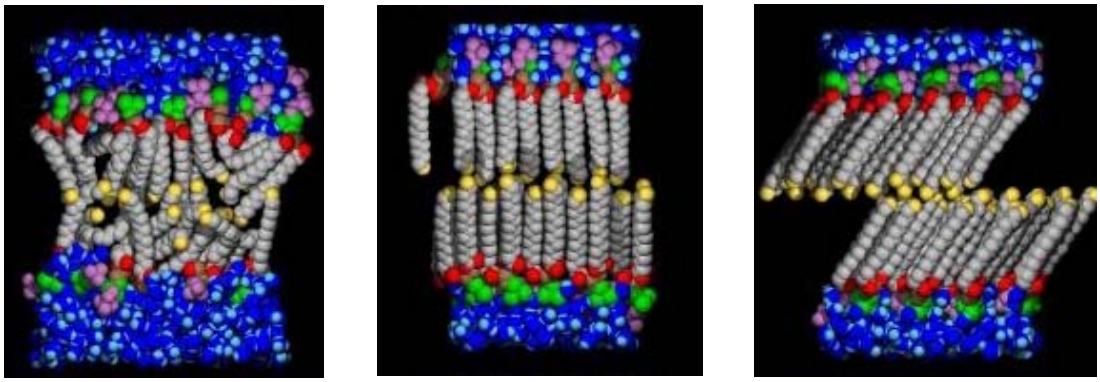

L_α L_β $L_{\beta'}$

Figure 4-4. Pictures of DPPC lamellar phases generated by computer simulations (Feller et al. 1997)

On the contrary, at 50°C (fluid phase) the limiting equilibrium point appears at $\varphi_L \approx 53\%$. The equilibrium bilayer parameters of the DPPC molecule at the two temperatures 25°C and 50°C are given in **Table 4-1**, as determined by various groups. Other important physical parameters of the DPPC molecule are given in **Table 4-2**.

Table 4-1. Bilayer Parameters of the DPPC molecule for the gel and fluid phase

Bilayer Parameters (Angstroms)	**DPPC 25°C**	**DPPC 50°C**
Repeat spacing, **D**	63.8[a] , 63.8[b] , 62.0[c],	67.0[a] , 67.0[b], 66.3[d]
Equilibrium lipid concentration, φ_L	0.74[a] , 0.69[b] , 0.70[c]	0.54[a] , 0.51[b], 0.53[d]
Lipid bilayer thickness, b_L	47.1[a] , 44.2[b] , 43.6[c]	35.9[a] , 34.2[b] , 34.9[d]
Water layer thickness, d_w	16.7[a] , 19.6[b] , 18.4[c]	31.1[a] , 32.8[b] , 31.4[d]
Headgroup area, **A**	48.6[a] , 52.3[b] , -----	68.1[a] , 71.2[b] , 70.0[d]

a Values taken from **Rand et al. 1989**
b Values taken from **Lis et al. 1982**
c Values taken from **Cunningham et al. 1986**
d Values obtained in the present thesis

Table 4-2. Physical Parameters of the DPPC molecule

Physical Parameters	**DPPC 20°C**	**DPPC 50°C**
Density (g/ml)	1.068, 1.065, 1.064	0.9910, 0.9890, 0.9921
Specific partial volume (ml/g)	0.937, 0.939, 0.940	1.0091, 1.011, 1.008
Total lipid volume ($Å^3$/ molecule)	1142, 1144, 1145	1230, 1232, 1228

All values are taken from **Nagle et al. 2004**

4.4 Phospholipid DPC

Dodecylphosphocholine (DPC) is a synthetic lysophospholipid which is currently the most frequently used and one of the best characterized "membrane mimetic" models for the study of peptide-lipid and protein-lipid interactions. DPC forms small, spherical, freely-rotating micelles in aqueous solutions, making it an excellent tool to mimic the anisotropic environment of lipid membranes. Its chemical structure contains a hydrophilic and a hydrophobic part as shown in **Figure 4-5**. The phosphoric acid group is connected through P-O-C bonds to a choline group, $(CH_3)_3N(CH_2)_2OH$, and an aliphatic dodecyl chain. The choline, which contains a quaternary amine with a positive charge, and the phosphate is ionic and polar.

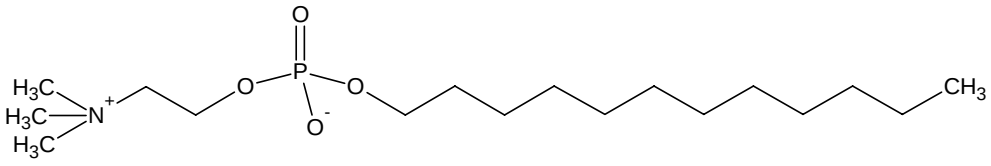

Figure 4-5. Chemical Structure of DPC

DPC micelles are considered to be a better mimic for lipid bilayers than SDS micelles because they contain a phosphatidylcholine headgroup which is structurally similar to the headgroup of many phospholipids, in particular DPPC. Some physical parameters of the DPC molecule and of DPC micelles are given in **Table 4-3** and **Table 4-4**.

Table 4-3. Physical Parameters of the DPC molecule

Physical Parameters	DPC molecule
Density (g/ml)	1.067[a], 1.084[c]
Specific partial volume (ml/g)	0.937[a], 0.922[c]
Total lipid volume ($Å^3$/ molecule)	538[c]

a Values taken from **Lauterwein et al. 1979**
c Values obtained in the present thesis

Table 4-4. Physical Parameters of the DPC micelles

Physical Parameters	DPC micelles
CMC (mM)	1.1[a], 1.16[c]
Diameter of DPC micelles (Å)	47[a], 55[a], 43[b], 57[c]
Aggregation number	56[a], 50[b], 56[c]

a Values taken from **Lauterwein et al. 1979**
b Values taken from **Kallick et al. 1995**
c Values obtained in the present thesis

5 CHAPTER

THEORETICAL MODELS AND INTERMOLECULAR – SURFACE FORCES

5.1 Introduction

In order to clarify and understand the mechanism of action of Hofmeister anions, "binding" constants of the anions on the headgroups of DPPC and DPC molecules will be calculated in this thesis using two theoretical models, one considering local binding of anions on the headgroups of the lipid molecules and one assuming a partitioning of anions in a diffuse layer created by the lipid molecules. Both models are based on the idea that the presence of anions near the lipid headgroups (through either binding or partitioning) generates an electrostatic surface potential due to the ion distribution in the solution and thus a diffuse electrical double layer is created. Therefore, before we describe the two theoretical models we discuss the basic equations that describe the theory of the electrical double layer.

5.2 Electrostatic Forces

5.2.1 Diffuse Electrical Double Layer and Poisson – Boltzmann Equation

Electrostatic repulsive interactions arise when two similarly **charged** surfaces approach each other in a liquid solution, in order to prevent the diffuse electric layers of the surfaces to overlap. The charging of a surface in a liquid can be achieved in the following ways:

a) by the ionization or dissociation of surface groups e.g. surface carboxylic groups
b) by the adsorption of ions from solution onto uncharged or oppositely charged surfaces.

Whatever the charging mechanism, the actual charge is determined by an equilibrium process involving exchange of charged species between the bulk solution and the interface. Thus, the final surface charge is balanced by an equal but oppositely charged region of counterions, some of which are bound to the surface while others form a distirbution of ions in rapid thermal motion close to the surface known as the diffuse electrical double layer, **Figure 5-1**. The charged surfaces are characterized by a surface charge density σ and a potential Φ_0 as shown in **Figure 5-1**. The adjacent solution contains electrolyte and is characterized by the bulk concentration c_{i0}, ion valency z_i and solvent dielectric constant ε_r.

The properties of a charged *planar* interface can be described by the **Gouy - Chapman** theory. The **Gouy - Chapman** theory relates the surface charge density and the surface potential using the Poisson – Boltzmann equations (PBE), with which the ion distribution in a solution can be calculated. The Poisson equation is given by the following expression:

$$\varepsilon_0 \varepsilon_r \vec{\nabla}^2 \Phi = -\rho(\text{free ions}) = -e\sum_i z_i c_i\left(\vec{r}\right) \qquad \textbf{Equation 5.2-1}$$

where ρ(free ions) is the solution's charge distribution and $c_i\left(\vec{r}\right)$ represents the local concentration of ionic species i in the solution.

The Boltzmann ion distribution (the change in concentration of the counterions near the charged surface) is given by the following equation:

$$c_i\left(\vec{r}\right) = c_{i0}\exp\left(\frac{-z_i e\Phi}{kT}\right) \qquad \textbf{Equation 5.2-2}$$

where c_{i0} is the bulk electrolyte concentration of the ion species i at a position where $\Phi = 0$.

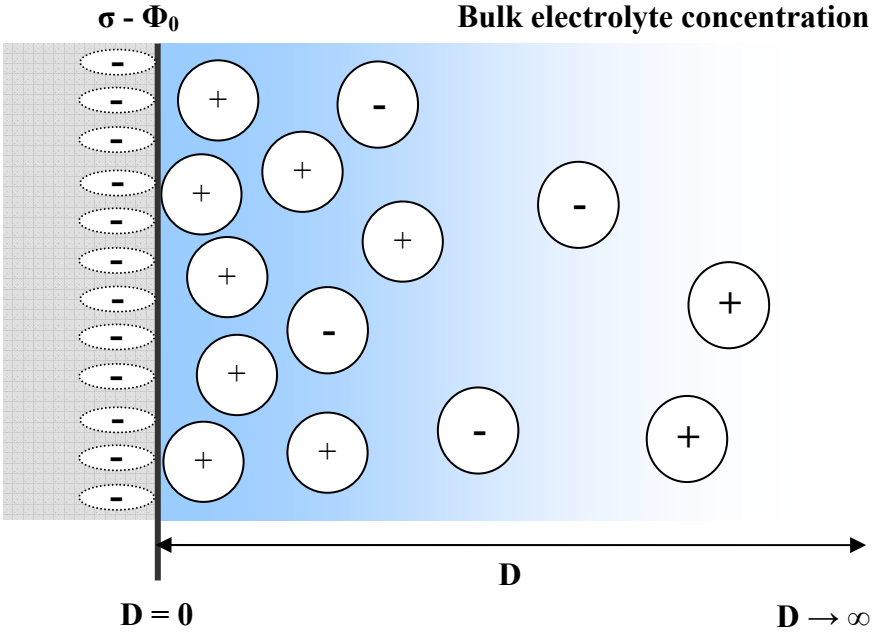

Figure 5-1. Diffuse Electrical Double Layer

By combining **Equations 5.2-1** and **5.2-2** one obtains the Poisson-Botzmann equation (PBE) which is written as follows in one dimension:

$$\frac{d^2\Phi}{dx^2} = -\frac{e}{\varepsilon_0\varepsilon_r}\sum_i z_i c_{i0}\exp\left(\frac{-z_i e\Phi}{kT}\right) \qquad \textbf{Equation 5.2-3}$$

For the solution of the PBE two boundary conditions are used: (i) The potential and electric field at large distances from the surface are zero $\Phi_{(\infty)} = 0$, $\left.\frac{d\Phi}{dx}\right|_{x\to\infty} = 0$, (ii) The potential on the surface is related to the surface density charge, σ, through the Gauss theorem $\left.\frac{d\Phi}{dx}\right|_{x=0} = \frac{-\sigma}{\varepsilon_0\varepsilon_r}$. Taking into account these boundary conditions one can derive the profile of the potential with distance from the charged surface. For a symmetrical z:z electrolyte:

$$\Phi(D) = \frac{2kT}{ze}\ln\left\{\frac{1+\Gamma_0\exp(-\kappa D)}{1-\Gamma_0\exp(-\kappa D)}\right\} \approx \frac{4kT}{ze}\Gamma_0\exp(-\kappa D) \qquad \textbf{Equation 5.2-4}$$

Γ_0 is related to the surface potential Φ_0 and is equal to:

$$\Gamma_0 = \frac{\exp(ze\Phi_0/2kT)-1}{\exp(ze\Phi_0/2kT)+1} = \tanh\left(\frac{ze\Phi_0}{4kT}\right) \qquad \textbf{Equation 5.2-5}$$

and $1/\kappa$ (m) is the **Debye screening length** (taken as the effective thickness of the diffuse electrical double layer) given by:

$$\frac{1}{\kappa} = \left(\frac{\varepsilon_0\varepsilon_r kT}{\sum_i (z_i e)^2 c_{i0}}\right)^{1/2} \qquad \textbf{Equation 5.2-6}$$

The magnitude of the Debye screening length depends only on the properties of the solution. It measures how the combination of valency, concentration, and dielectric constant of the electrolyte solution contribute to the screening of interactions between charges in solutions.
The surface charge density σ is related to the surface potential Φ_0 by the following expression:

$$\sigma = (8kTc_{i0}\varepsilon_0\varepsilon_r)^{1/2}\sinh\left(\frac{ze\Phi_0}{2kT}\right) \qquad \textbf{Equation 5.2-7}$$

It can be seen that as $|\sigma|$ increases, $|\Phi_0|$ increases.

The total ion surface concentration (counter-ions and co-ions) is given by the Grahame equation:

$$\sum_i c_i(\text{total}) = \frac{\sigma^2}{2kT\varepsilon_0\varepsilon_r} + \frac{P_{osm}}{kT} \qquad \textbf{Equation 5.2-8}$$

In the limit of low potentials (large ionic strength, small Debye length, and small surface charge density) the PBE reduces to the **linear** PBE, leading to the Debye – Hückel theory. The potential distribution and the surface charge density (for a symmetrical 1:1 electrolyte in this linearized theory) are given by:

$$\Phi(D) = \Phi_0 \exp(-\kappa D) \qquad \textbf{Equation 5.2-9}$$

$$\sigma = \varepsilon_0 \varepsilon_r \kappa \Phi_0 \qquad \textbf{Equation 5.2-10}$$

5.2.2 Model of local binding

Anion binding to the headgroups of the lipid molecules DPPC and DPC, which form monolayers, bilayers and micelles as shown in **Figures 5-2** to **5-4** for the three different geometries, can be modelled as a chemical reaction of anion X^- that binds to a neutral lipid L^0 (e.g DPPC, DPC) to form a charged lipid, L^-:

$$L^0 + X^- \leftrightarrow (LX)^-$$

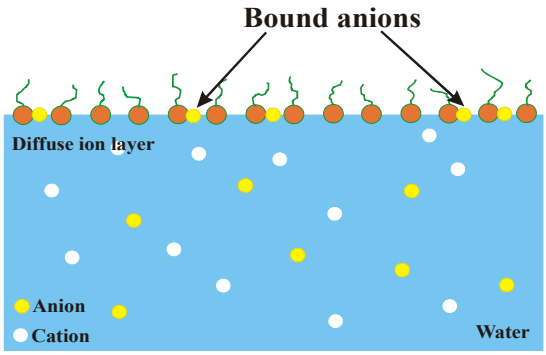

Figure 5-2. Local binding of anions on the headgroups of lipid molecules at the air-water interface

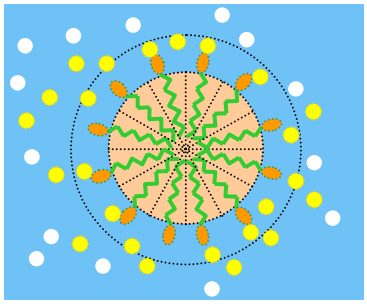

Figure 5-3. Local binding of anions on the headgroups of lipid molecules at the micellar surface

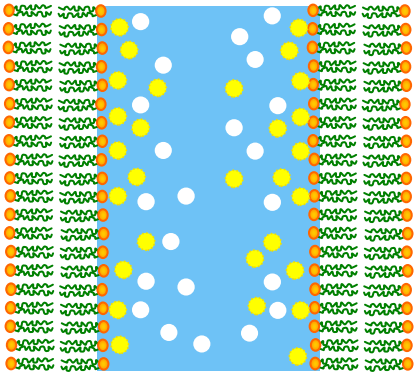

Figure 5-4. Local binding of anions on the headgroups of lipid molecules forming bilayers

The association constant K of the above reaction is defined as:

$$K = \frac{\left[(LX)^{-}\right]}{\left[L^{0}\right]\left[X^{-}\right]} = \frac{x_b}{(1-x_b)c_{i,surf}} = \frac{x_b}{(1-x_b)c_{i0}\exp(-ze\Phi_0/kT)} \qquad \textbf{Equation 5.2-11}$$

where x_b is the percentage of lipid molecules that have acquired a charge due to anion binding, $c_{i,surf}$ is the local anion concentration at the binding plane given by Boltzmann's distribution, c_{i0} is the electrolyte concentration in the subphase, k is Boltmann's constant, and Φ_0 the electrostatic potential at the binding plane that is created due to anion adsorption on the lipid headgroups.

The surface charge density σ which is given by **Equation 5.2-7** is related to the fraction of lipids on which anions are bound:

$$|\sigma| = \frac{ex_b}{A} \qquad \textbf{Equation 5.2-12}$$

where A is the surface area of the lipid molecule. Knowing x_b and using the chemical equilibrium expression (**Equation 5.2-11**) one can compute the binding constant K.

5.2.3 Model of diffuse lipid layer

This model is based on the concept of an active diffuse interface, as explained by **Zemb et al. 2004** and shown in **Figure 5-5** for monolayers at the air-water interface. The concept of the active diffuse interface can be applied also to the bilayer and micelle geometries. The model is explained below for the monolayer geometry but is similar for the other two geometries. In this model, the interface is divided in two regions. The top region ($0 < x < \delta$), of layer thickness δ, is playing an *active* role in the process of ion adsorption, and is responsible for the ionic "selectivity" of the interface with respect to the bulk ($\delta < x \leq \infty$).

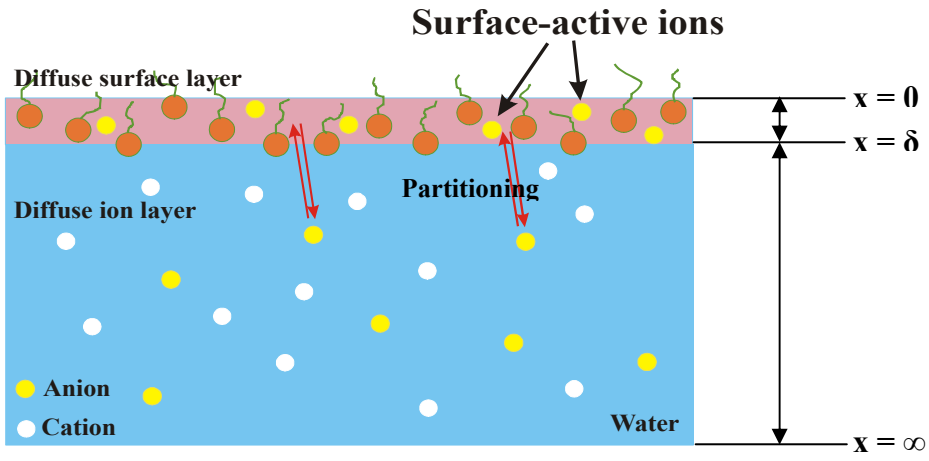

Figure 5-5. Partitioning of the anions between the diffuse lipid layer and the bulk water

The cations are assumed not to enter this layer while the anions can penetrate the headgroup plane of the lipid molecules. This "partitioning" is driven by a constant attraction potential $U_{..}$ The active interface "repels" hydrophilic ions and "attracts" hydrophobic anions reducing the free energy of the system by liberating water molecules (from the solvation shells of the hydrophobic anions) that are returned to bulk water. The active interface must have the following properties: (a) it must have a considerable degree of disorder, and (b) solvent structure near and within it must differ considerably from bulk solvent.

Figure 5-6 shows the expected concentration profiles of anions and cations in the active interface and the diffuse double layer beyond.

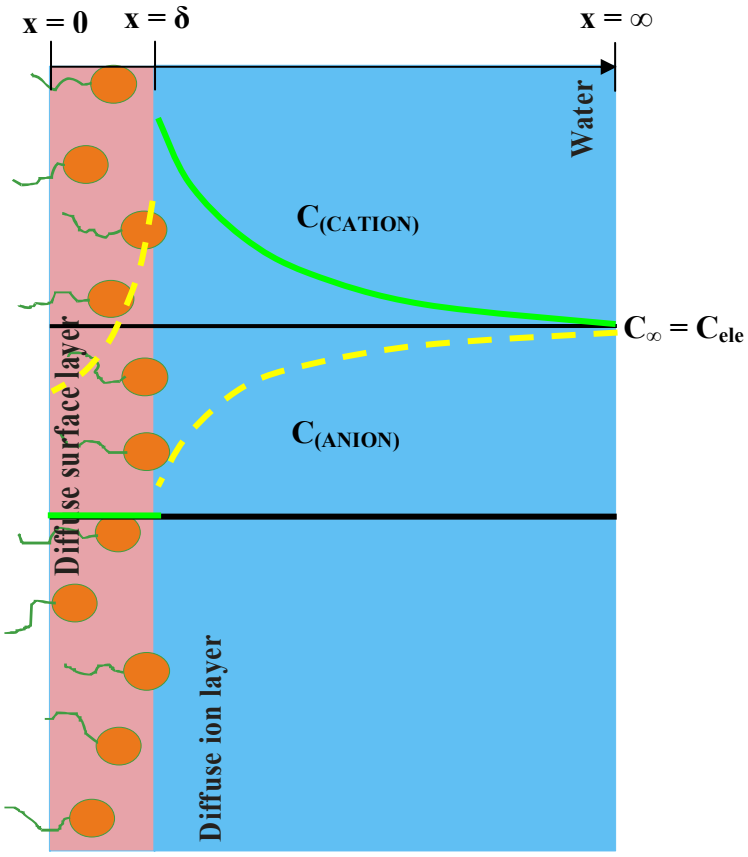

Figure 5-6. Charge distribution (ionic profile) in the diffuse lipid layer and beyond

The analysis of this two-layer model is quite complicated and is based on the solution of the Poisson-Boltzmann equation in the two regions.

For x > δ the PBE given by **Equation 5.2-3** contains in this case the contribution from both the cations and anions through appropriate local Boltzmann factors:

$$\varepsilon_0\varepsilon_r \frac{d^2\Phi}{dx^2} = -\left(z_+ q_e C_{\infty,+} e^{-\left(\frac{z_+ q_e \Phi}{kT}\right)} + z_- q_e C_{\infty,-} e^{-\left(\frac{z_- q_e \Phi}{kT}\right)} \right) \qquad \textbf{Equation 5.2-13}$$

where $z_+ = +1$, $z_- = -1$, and $C_{\infty,+} = C_{\infty,-} = C_\infty$. Although complex, this differential equation for the electrostatic potential has an analytical solution for symmetric electrolytes that can be found in several colloid and surface chemistry textbooks:

$$\tanh\frac{ze\Phi(x)}{4kT} = \tanh\frac{ze\Phi_\delta}{4kT} e^{-\kappa(x-\delta)} \qquad \textbf{Equation 5.2-14}$$

where κ is the inverse Debye's screening length and Φ_δ is the electrostatic potential at x = δ.

For $0 \le x < \delta$ the PBE is transformed into **Equation 5.2-15**, where $\beta = {}^{1}\!/_{kT}$ and U_i is defined as the difference of chemical potential for ion i between the two regions and is taken here as a constant characteristic for each ion.

$$\frac{d^2\Phi}{dx^2} = -\frac{\rho}{\varepsilon_0\varepsilon_r} = -\frac{1}{\varepsilon_0\varepsilon_r}\left(z_+ q_e C_{\infty,+} e^{-\left(\frac{z_+ q_e \Phi}{kT} + \beta U_+\right)} - z_- q_e C_{\infty,-} e^{-\left(\frac{z_- q_e \Phi}{kT} + \beta U_-\right)} \right) \quad \textbf{Equation 5.2-15}$$

By setting $U_+ \approx \infty$ for $0 \le x < \delta$, we exclude the cations from the active interface. The resulting equation has an analytical solution in this case ($z_- = -1$), given by:

$$C(x) = \frac{C_0}{\cos^2\left(\frac{Yx}{\delta}\right)} \quad \textbf{Equation 5.2-16}$$

where Y is defined as $Y = \sqrt{2\pi \cdot L_B C_0 \delta^2}$, and $C_0 = C_\infty \exp\left(\frac{q_e \Phi_0}{kT} - \beta U_-\right)$ is the anion concentration at x = 0. L_B is the Bjerrum length which is the length at which two elementary charges interact in a given solvent with energy equal to the thermal energy kT (measures the characteristic distance in the solvent where the electrostatic energy is compensated by the thermal energy kT) and is given by:

$$L_B = \frac{e^2}{4\pi \cdot \varepsilon_r \varepsilon_0 kT} \quad \textbf{Equation 5.2-17}$$

where e is a unit charge and ε_r, ε_0 are the permittivity of the solvent and vacuum.

If **x = δ**, the concentration of the anions at the boundary between the two phases is given as:

$$C_{(0 \le x < \delta)} = \frac{C_0}{\cos^2 Y} \quad \textbf{Equation 5.2-18}$$

In addition, at x = δ the electrostatic potential and the electric field $E = -\nabla\Phi$ calculated in the two regions must be equal. Thus one obtains three equations with three unknown parameters:

$$\beta q_e \Phi_\delta = \beta U_- + \ln\left(\frac{C_0}{C_\infty \cos^2 Y}\right) \qquad \textbf{Equation 5.2-19}$$

$$Y = \sqrt{2\pi \cdot L_B C_0 \delta^2} \qquad \textbf{Equation 5.2-20}$$

$$Y \tan Y = -\kappa\delta \sinh\frac{\Phi_\delta}{2} \qquad \textbf{Equation 5.2-21}$$

For a given U_- we can compute Φ_δ, C_0 and Y and we use those values to evaluate the electrostatic contribution due to the presence of the anions at the three different geometries.

5.3 Monolayer theoretical models

The main goal of the monolayer models is to relate the increase of surface pressure at constant area per molecule to the concentration of electrolyte present in the subphase in order to obtain thermodynamic "binding" constants of anions. This can only be done at low surface pressures, for which the monolayer is in the liquid-expanded (LE) phase. It is impossible to create models for the case of phase coexistence. The pure LC phase could be modeled as well but the increase of the experimental surface pressure at high pressures is very difficult to measure precisely.

The total surface pressure of a monolayer at the air-electrolyte interface can be written as follows:

$$\pi_{tot} = \pi_{water} + \pi_{el} \qquad \textbf{Equation 5.3-1}$$

π_{el} is calculated by subtracting π_{water} from π_{tot} that is $\Delta\pi_{el} = \pi_{tot} - \pi_{water}$. $\Delta\pi_{el}$ is a measurable quantity. It is the difference between the surface pressure over pure water and that over an electrolyte solution at the same area per molecule. The electrostatic contribution, $\Delta\pi_{ele}$, can be defined as follows:

$$\Delta\pi_{ele} = -\frac{d\Omega}{dA} \qquad \textbf{Equation 5.3-2}$$

where Ω is the interfacial free energy (grand potential) which is defined as:

$$\Omega = U - TS - \sum_i \mu_i N_i \qquad \textbf{Equation 5.3-3}$$

where:

$$U = \frac{1}{2}\int \varepsilon_0 \varepsilon_r E^2(r)dr \qquad \textbf{Equation 5.3-4}$$

$$-TS = kT\sum_i \int C_i\left(\beta\mu_i^0 + \ln C_i - 1\right)dr \qquad \textbf{Equation 5.3-5}$$

$$\mu_i N_i = kT\left(\beta\mu_i^0 + \ln C_{i,0}\right)\int C_i dr \qquad \textbf{Equation 5.3-6}$$

U can be defined as the internal energy of electric field, -TS is the entropic contribution associated with the distribution of ions, μ_i is the chemical potential of ionic species i, N_i is the total number of ions of species i, dr = Adx, A is the total area (of the monolayer) and all the other parameters have their usual meaning as defined above.

5.3.1 Model of local binding adjusted for the monolayer geometry

In this model, the anions in the subphase solution of a Langmuir monolayer are assumed to bind to the headgroups of DPPC molecules that form the lipid monolayer at the air - water interface as shown in **Figure 5-2**. In the simplest version of this model, it is assumed that the cations do not bind to the headgroups of DPPC. The bound anions form a charge plane, beyond which a diffuse double layer extends into the solution.

In order to estimate the association constant, K, of the anions on the headgroups of DPPC using **Equation 5.2-11** the following procedure is used: the electrostatic contribution to the surface pressure, $\Delta\pi_{ele}$, measured for a Langmuir monolayer as explained above, is modelled using the grand potential definition for $\Delta\pi_{ele}$ (*in the case of local binding*). After a thorough mathematical analysis, Ω is found equal to:

$$\beta\Omega = \int\left[\frac{\left|\nabla\overline{\Phi}\right|^2}{8\pi\cdot L_B} + 2C_{i,0}\left(\overline{\Phi}\sinh\overline{\Phi} - \cosh\overline{\Phi} + 1\right)\right]dr + \frac{1}{S}\iint\left(x_b\ln x_b + (1-x_b)\ln(1-x_b) - x_b\ln\left(KC_{i,0}\right) + \beta\mu_{site}^0 - \ln S - 1\right)dA \qquad \textbf{Equation 5.3-7}$$

where $\overline{\Phi}$ is equal to $\frac{q_e\Phi}{kT}$, x_b is the fraction of charged sites due to anion adsorption, and S is the surface area per molecule of the uncharged DPPC headgroups. By introducing the solution of the PBE for $\overline{\Phi}$ and $\nabla\overline{\Phi}$ and combining **Equations 5.3-2** and **5.3-7** we obtain a very compact analytical expression for $\Delta\pi_{ele:}$

$$\beta\Delta\pi_{ele} = \frac{1}{S} + 2\sigma\cdot\gamma \qquad \textbf{Equation 5.3-8}$$

where σ is the surface charge density given by **Equation 5.2-7** and $\gamma \equiv \tanh\left(\frac{ze\Phi_0}{4kT}\right)$.

As a result, for a given value of the binding constant of anions and combining **Equations 5.2-11** and **5.2-7** one can obtain the electrical potential at the charge plane which is related to the charge density, σ, and thus $\Delta\pi_{ele}$ can be evaluated at different salt concentrations and compared with the experimental values.

5.3.2 Model of diffuse lipid layer adjusted for the monolayer geometry

In this model, the anions in the subphase solution are assumed to penetrate the headgroup plane of DPPC molecules without specifically binding to the headgroups of the lipid. Cations are assumed not to enter this layer as shown in **Figure 5-5**.

In the case of the diffuse lipid layer an extra term must be added to the internal energy U (**Equation 5.3-4**):

$$U = \frac{1}{2}\int\varepsilon_0\varepsilon_r E^2(r)dr + \sum_i\int C_i U_i dr \qquad \textbf{Equation 5.3-9}$$

and the interfacial free energy for a 1:1 electrolyte can be shown to be:

$$\Omega = \int \left\{ \frac{\left|\nabla \overline{\Phi}\right|^2}{8\pi \cdot L_B} + C_{i,0}\left[-\left(\overline{\Phi}+1\right)e^{-\left(\overline{\Phi}+\beta U_+\right)} + \left(\Phi-1\right)e^{-\left(\overline{\Phi}+\beta U_-\right)}\right]\right\} dr \qquad \textbf{Equation 5.3-10}$$

where $\overline{\Phi}$ is equal to $\frac{q_e \Phi}{kT}$. After introducing the solution for Φ in the two regions and carrying out the integration we find the following expression for $\Delta\pi_{ele}$:

$$\beta\Delta\pi_{ele} = -\beta\frac{\Omega}{A} = -2\frac{\sigma}{q_e}\cdot\gamma_\delta - \frac{Y}{2\pi \cdot L_B \cdot \delta}\left(2\tanh Y - Y\right) \qquad \textbf{Equation 5.3-11}$$

σ is the surface charge density given by **Equation 5.2-7**, Y is given by **Equation 5.2-20** γ_δ is given by **Equation 5.2-14**. For a given value of the constant attraction potential U_-, Φ_δ, C_0 and Y are computed as explained in **Section 5.2.3** and the interfacial free energy Ω and the electrostatic contribution $\Delta\pi_{ele}$ can be evaluated.

5.4 Bilayer theoretical models

The main goal of the bilayer models is to obtain "binding" constants of anions by calculating the change of the total osmotic pressure, Π_{tot}, with the water bilayer distance d_w as the concentration of the salt solutions present between the bilayers increases. Before continuing with the theoretical models for bilayers, it is necessary to provide a description of the forces acting between the lipid bilayers.

5.4.1 Interactions between lipid membranes (bilayers)

When two lipid bilayers, **Figure 5-7**, approach one another they experience many different kinds of interaction. These interactions include both long-range attractive and repulsive forces and short-range interactions close to molecular contact.

The free energy of interaction between flat bilayers (with structure parameters D, the repeat distance between the bilayers, $b_{L,}$ the bilayer thickness, and d_w, the water bilayer separation) is given by the sum of the following interactions:

$$W_{TOT} = W_{VDW} + W_{ELEC} + W_{HYD} + W_{UND} \qquad \textbf{Equation 5.4-1}$$

The corresponding total osmotic pressure between the bilayers is given by:

$$\Pi_{TOT} = \Pi_{VDW} + \Pi_{ELEC} + \Pi_{HYD} + \Pi_{UND} \qquad \textbf{Equation 5.4-2}$$

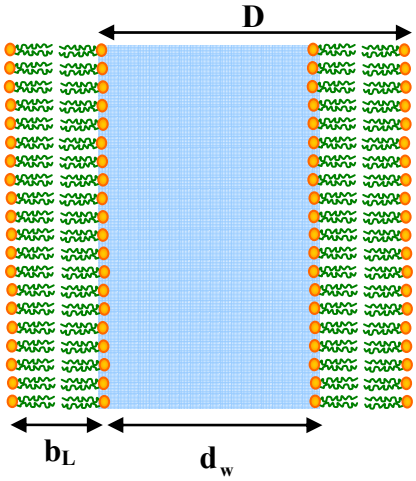

Figure 5-7. Two flat membrane layers (bilayers)

The first term in **Equation 5.4-1** describes the Van der Waals interaction, the existence of which was first described by Van der Waals to explain the observed deviation of real gas behaviour from the ideal gas law. It was soon found that Van der Waals forces play a central role in all phenomena involving intermolecular forces, even though they are not often as strong as Coulombic or H bonding interactions. These intermolecular forces originate from: a) randomly orienting dipole-dipole (or orientation) interactions, first described by Keesom b) randomly orienting dipole-induced dipole (or induction) interactions, first described by Debye c) fluctuating dipole-induced dipole (or dispersion) interactions, first described by London.
The Van der Waals interaction for two flat surfaces at separation D, or d_w for bilayers, is given by the expression:

$$W_{VDW} = \frac{A}{12\pi \cdot (d_w)^2} \qquad \textbf{Equation 5.4-3}$$

where A is the non-retarded Hamaker constant, which is equal to:

$$A_{131} = A_{\nu=0} + A_{\nu>0} = \frac{3}{4}kT\left(\frac{\varepsilon_1 - \varepsilon_3}{\varepsilon_1 + \varepsilon_3}\right)^2 + \frac{3h\nu_e}{16\sqrt{2}}\frac{\left(n_1^2 - n_3^2\right)^2}{\left(n_1^2 + n_3^2\right)^{3/2}} \qquad \textbf{Equation 5.4-4}$$

where ε_1 and ε_3 are the dielectric constants of lipids (1) and solvent (3) and n_1 and n_3 are the refractive indices of the same. In the above Equation, the first term $A_{\nu=0}$ gives the zero-frequency part of the Van der Waals energy (which includes the Keesom and Debye interaction energies), while the latter term represents the dispersion energy which includes the London energy contribution. ν_e (s^{-1}) is the absorption frequency in the UV region. (**Israelachvili 1991; Hunter 2001**). It is important to notice that when the solvent medium is an electrolyte solution, the Van der Waals forces become screened due to the change of the polarization of the free ions. As a result the zero-frequency part of the Hamaker constant is reduced by a factor proportional to $e^{-2\kappa D}$ where κ^{-1} is the Debye length of the solution. Thus across an electrolyte solution the screened non-retarded Hamaker constant is given by:

$$A = A_{\nu=0}(2\kappa \cdot D)e^{-2\kappa \cdot D} + A_{\nu>0} \qquad \textbf{Equation 5.4-5}$$

Equation 5.4-3 applies for $d_w << b_L$. As a result, the two bilayers can be replaced by two identical surfaces separated by the solvent. In contrast, if the separation d_w is much larger than the bilayer thickness, $d_w >> b_L$, the bilayers act as two-dimensional sheets. Thus, the Van der Waals interaction energy between lipid bilayers of thickness b_L separated by a water distance d_w is given by:

$$W_{VDW} = \frac{A}{12\pi}\left[\frac{1}{(d_w)^2} + \frac{1}{\left(d_w + 2b_L\right)^2} - \frac{2}{\left(d_w + b_L\right)^2}\right] \qquad \textbf{Equation 5.4-6}$$

The Van der Waals attraction force is given by the following expression respectively:

$$\Pi_{VDW} = -\frac{dW_{VDW}}{dd_w}$$

$$\Pi_{VDW} = -\frac{A}{6\pi}\left[\frac{1}{(d_w)^3} + \frac{1}{\left(d_w + 2b_L\right)^3} - \frac{2}{\left(d_w + b_L\right)^3}\right] \qquad \textbf{Equation 5.4-7}$$

$$\Pi_{VDW} = -\frac{A}{6\pi}\left[\frac{1}{(d_w)^3} + \frac{1}{\left(D + b_L\right)^3} - \frac{2}{(D)^3}\right]$$

where A < 0 (**Equation 5.4-4**). **Equations 5.4-6** and **5.4-7** are applied when the Debye length is sufficiently small and the zero – frequency contribution to the Hamaker constant is screened.

The Van der Waals forces between amphiphilic structures (bilayers) are generally small for the following reasons:

1. The Hamaker constant between hydrocarbon phases in water is relatively small, lying in the range 4 - $7x10^{-21}$J.
2. **Equation 5.4-6** is valid at separations d_w smaller than 3nm. Above 3nm the Hamaker constant diminishes progressively as d_w increases due to retardation effects.
3. In the presence of an electrolyte there is an additional reduction of the Hamaker constant due to the ionic screening of the zero-frequency contribution $A_{v=0,}$ as it was explained before. (**Israelachvili 1991; Lipowsky 1995; Tadmor 2001; Ninham 1970**).

The second term in **Equation 5.4-1** comes from electrostatic repulsion and is relevant only for charged membranes in polar solvents. The apparent stability of colloids with an electrical double layer at their surfaces is due to the repulsive potential energy generated when the double layers overlap as shown in **Figure 5-8**. As the two charged surfaces approach each other, the ion concentration between the surfaces increases due to the requirement to maintain electrical neutrality and so a repulsive force of electrostatic origin is generated.

The electrostatic interaction can be easily calculated for two limiting cases, the case when no electrolyte is present, and that of salt excess. When there are no other ions in water apart from the counter-ions (absence of salt and $\boldsymbol{\kappa d_w << 1}$), this is considered to be the case of weak screening and the electrostatic interaction energy is given by:

$$W_{ELEC} = \frac{\pi kT}{2L_B d_w} \qquad \textbf{Equation 5.4-8}$$

where L_B is the Bjerrum length of the solvent.

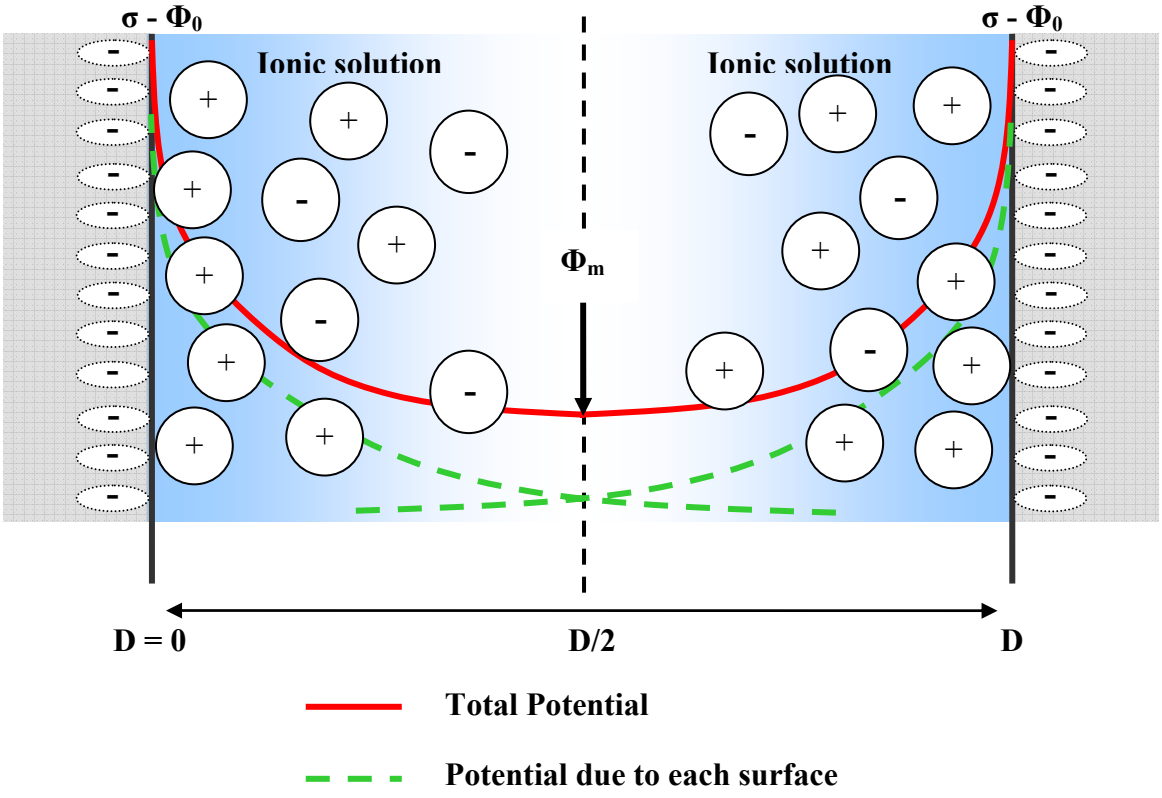

Figure 5-8. Two parallel, negatively charged surfaces interacting through an electrolyte solution

The repulsive electrostatic pressure in this case is known as Langmuir Equation and is given by:

$$\Pi_{ELEC} = \frac{\pi kT}{2L_B (d_w)^2} \qquad \textbf{Equation 5.4-9}$$

In the opposite case (strongly screened regime, salt excess and $\boldsymbol{\kappa d_w >> 1}$), the repulsive force (osmotic pressure) between two identically charged surfaces in an electrolyte solution is given by:

$$\frac{F}{area} = P_{osm}(midplane) - P_{osm}(bulk)$$
$$\frac{F}{area} = kT\left\{\sum_i c_i(midplane) - \sum_i c_{i0}\right\} \qquad \textbf{Equation 5.4-10}$$

Through Boltzmann's distribution (**Equation 5.2-2**), the ion concentration at the midplane is related to the bulk concentration:

$$c_i(\text{midplane}) = c_{i0}\exp\left(\frac{-z_i e\Phi_m}{kT}\right) \qquad \textbf{Equation 5.4-11}$$

where Φ_m is the potential at the midplane between bilayers relative to $\Phi = 0$ in the reservoir.
As a result, the general expression for the electrostatic contributions between two planar surfaces is given by the following expression:

$$\Pi_{ELEC} = \frac{F}{\text{area}} = kT\left\{\sum_i c_{i0}\left[\exp\left(\frac{-z_i e\Phi_m}{kT}\right) - 1\right]\right\} \qquad \textbf{Equation 5.4-12}$$

For moderate surface charge densities, the midplane potential is assumed to be small and equal to the sum of the Gouy-Chapman potentials from each surface at x = D/2 which is given by **Equation 5.2-4**. Thus, for a symmetrical z:z electrolyte the potential at the midplane is given by :

$$\Phi_m = \Phi_1\left(\frac{D}{2}\right) + \Phi_2\left(\frac{D}{2}\right) \approx \frac{8kT}{ze}\Gamma_0\exp\left(\frac{-\kappa D}{2}\right) \qquad \textbf{Equation 5.4-13}$$

The combination of **Equations 5.4-11**, **5.4-12**, and **5.4-13** yields the repulsive pressure between two planar surfaces:

$$P_{ELEC} = 64kTc_{i0}\Gamma_0^2\exp(-\kappa D) \qquad \textbf{Equation 5.4-14}$$

where c_{i0} represents the bulk electrolyte concentration and Γ_0 is given by **Equation 5.2-4**.
The repulsive potential energy per unit area due to the overlap of the flat electrical double layers, W_{ELEC}, is the work done when the two electrical double layers are brought closer to each other from an infinite separation. It is given by the following expression:

$$W_{ELEC} = \frac{64kTc_{i0}\Gamma_0^2}{\kappa}\exp(-\kappa D) \qquad \textbf{Equation 5.4-15}$$

Equations 5.4-14 and **5.4-15** show that the double layer repulsion decays roughly exponentially with surface separation. The rate of exponential decay is governed by the Debye constant, κ, which varies with the square root of the ionic strength of the solution. Unlike Van der Waals attraction, the electrostatic repulsion depends strongly on the type and concentration of electrolyte present, the pH, and the surface charge density or potential. (**Evans et al. 1999; Israelachvili 1991; Hiemenz et al. 1997**). The electrostatic double-layer repulsion generally diminishes in the presence of high electrolyte concentrations, but it exceeds the weak Van der Waals attraction (between lipid bilayers) remaining strong enough to keep the surfaces apart. (**Evans et al. 1999; Gelbart et al. 1994; Israelachvili 1991**)

The third term in **Equation 5.4-2** describes the very short-range repulsion known as hydration force. If only the DLVO forces existed between two surfaces or colloidal particles, then in the absence of a strong electrostatic repulsive force, as happens for neutral molecules or high concentrations of salt, the surfaces or particles would be expected to come into direct contact in a primary energy minimum. This does not happen because of the existence of an additional monotonic short-range force, which is strongly repulsive at distances smaller than 3nm and dominates over the Van der Waals and electrostatic double layer forces at short distances (<25Å) . This force is known as structural force or hydration force.

Hydration forces were originally proposed by Langmuir to account for the repulsion and swelling of amphiphilic and colloidal surfaces in water, observed even when there is no electrostatic repulsion between them. The origin and nature of this monotonically repulsive hydration force is still not clear. These forces are believed to arise whenever surfaces have a strong affinity for water which is in turn related to the way surfaces induce order in or alter the structure of the adjacent water molecules. However, an alternative explanation has been proposed, in which these forces arise from the protrusions of the lipid molecules. Today it is generally believed that both hydration and protrusion contribute to the short-range repulsive force between the bilayers. Specifically the hydration force is believed to occur due to:

a) Hydrophilic surface groups. When two surfaces approach each other, the water of hydration that is strongly bound is removed to the main solution (bulk). This is not favourable energetically and creates a repulsive force of hydration or more correctly a force of dehydration between the surfaces.

b) Thermal motion of "surface" molecules. As a result they influence the structure of water. The hydration force developes because of the molecular fluctuations of aliphatic chains and other parts of the molecules that comprise the interface
c) Changes of the orientation of water molecules. It is believed that near the surface the water molecules are strongly oriented and as the distance from the surface is increased the orientation of the water molecules is decreased. As two surfaces come closer the orientation of interfacial water is reduced giving rise to a repulsive force. (**Israelachvili 1991; Rand et al. 1989; Leikin et al. 1993**)

Measurements of these forces between bilayers in aqueous solutions have shown that at distances d_w below 1 – 3 nm they decay exponentially with distance. They may be represented empirically by:

$$W_{HYD} = C\exp\left(-d_w/\lambda\right) \qquad \textbf{Equation 5.4-16}$$

or by:

$$\Pi_{HYD} = P_0\exp\left(-d_w/\lambda\right) \qquad \textbf{Equation 5.4-17}$$

Equation 5.4-16 gives the hydration interaction energy and **Equation 5.4-17** the repulsive force per unit area (pressure) between two flat surfaces. P_0 is the hydration coefficient; λ is the "characteristic" hydration decay length ranging between 1 – 3 Å and d_w the water bilayer separation. It was found that the degree of hydration in lipid bilayers is affected by:

1. The methylation of the lipid headgroups. As the methylation increases the hydration force increases.
2. The chain melting and heterogeneity.
3. The addition of nonpolar lipids to bilayers. (**Rand et al. 1989; Leikin et al. 1993; McIntosh et al. 1994 ; Lipowsky 1995**)

The last term in **Equation 5.4-2** refers to the undulation interaction energy that appears only when bilayers are found in the fluid-like phase. Fluid-like structures undergo thermaly – excitable fluctuations at the macroscopic level. For example, fluid membranes or bilayers, can be considered as elastic sheets which have two characteristic types of wave-like motions: undulatory and peristaltic (squeezing). The undulation of the membrane bilayers is shown in

Figure 5-9. Membrane undulations, as sterically stabilizing interactions, were first reported by Helfrich. These undulations produce a pressure that originates from the confinement of the membrane in a volume limited by its neighbours, that is, flexible bilayers left free in unlimited solvent will bend to occupy space far greater than their actual volume.

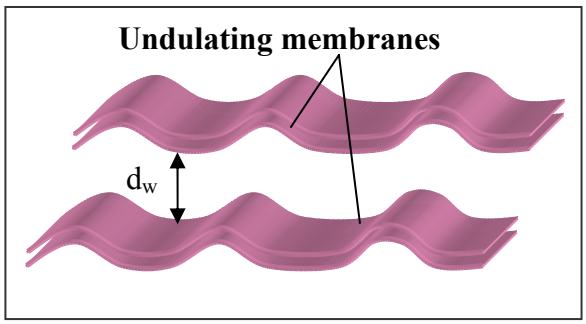

Figure 5-9. Undulation Forces

As a result, the membrane loses configurational entropy leading to an effective long-range repulsive force, which must be taken into account in the force balance of the system. On the contrary, the undulation interaction is neglected in the force balance of lipids that form stiff membrane stacks, that is, when they form the gel-crystalline phase (**Israelachvili 1991; Gelbart et al. 1994**).

The undulation interaction energy is given by:

$$W_{UND} = \frac{3\pi^2 (kT)^2}{256\kappa_c} \frac{1}{(d_w)^2} \qquad \textbf{Equation 5.4-18}$$

where κ_c is the bending rigidity modulus. The corresponding pressure induced by these undulations may be calculated according to:

$$\Pi_{UND} = \frac{3\pi^2 (kT)^2}{128\kappa_c} \frac{1}{(d_w)^3} = \frac{3\pi^2 (kT)^2}{128 (b_L)^3 \kappa_c} \left(\frac{\varphi_L}{1-\varphi_L} \right)^3 \qquad \textbf{Equation 5.4-19}$$

where b_L the bilayer thickness and φ_L the volume fraction of the lipid. (**Israelachvili 1991; Gelbart et al. 1994; Lipowsky 1995**)

5.4.2 Forces Between Neutral Phospholipid Bilayers

Lamellar phases formed by neutral (zwitterionic) phospholipids spontaneously take up water and swell in two dimensions up to a limiting bilayer separation called equilibrium separation. At the equilibrium separation the repulsive and attractive forces balance. The nature of the lipid used to form the lamellar phase influences the equilibrium separation (point of balance), as well as the forces encountered as bilayers are pushed together.

In the absence of electrostatic repulsion (neutral bilayers), the repulsive force is considered to be the hydration repulsive force given by **Equation 5.4-17**. The attractive force is assumed to be the Van der Waals force given by **Equation 5.4-7**. The parameters for the hydration force (P_0, λ) and the strength of the Van der Waals force, through the Hamaker constant, may be obtained by setting:

$$\Pi_{TOT} = \Pi_{HYD} + \Pi_{UND} + \Pi_{VDW} \qquad \textbf{Equation 5.4-20}$$

where Π_{TOT} is the observed osmotic pressure (the pressure applied by a polymer solution) versus the water bilayer separation d_w. The magnitude of the Van der Waals force can be determined also from the osmotic pressure curve when swelling is no longer occurring, that is when the equilibrium separation is reached. At that point the net repulsive force is taken to be equal to the Van der Waals attractive force. Π_{UND} is usually taken into account when the lipid bilayers are in the fluid state.

5.4.3 Forces Between Neutral Phospholipid Bilayers Charged by Ion Adsorption

Bilayers that are electrically charged, either by the adsorption of ions or by the presence of ionizable groups, show an additional electrostatic, double-layer repulsion with the expected force dependence on lipid charge and electrolyte concentration only at separations larger than 20 – 30Å. At closer distances, the electrostatic force is overwhelmed by the hydration repulsive force, which is similar to the hydration force that appears in neutral lipids. In this situation the net pressure applied to the bilayers is equal to the sum of hydration, undulation and electrostatic repulsive force and Van der Waals attraction:

$$\Pi_{TOT} = \Pi_{HYD} + \Pi_{UND} + \Pi_{ELEC} + \Pi_{VDW} \qquad \textbf{Equation 5.4-21}$$

The electrostatic double-layer force, $\Pi_{ELEC,}$ is given by **Equation 5.4-12**. Π_{UND} is taken into account when the lipid bilayers are in the fluid state.

5.4.4 Model of local binding adjusted for the bilayer geometry

The total force is given by **Equation 5.4-21** above. In this model, the electrostatic contribution Π_{ELEC} must be calculated for the whole range of salt concentrations between the lipid bilayers and not only for the two limiting of no salt and of excess salt.
The general expression for the electrostatic contributions between two planar surfaces is given by **Equation 5.4-12**. In order to calculate Φ_m, the non-linear Poisson Boltzmann equation is used (**Equation 5.2-3**) in combination with the surface charge density and the chemical equilibrium (association constant) as explained in **Section 5.2**
As a result, for different values of water bilayer separation, d_w, the electrostatic potential $\Phi(x)$ between x = 0 and x = $(d_w/2)$ is obtained according to the PBE and the two limiting conditions (with σ and K). With $\Phi(x)$ calculated, the electrostatic contribution to the osmotic pressure is obtained using **Equation 5.4-12**.

5.4.5 Model of diffuse lipid layer adjusted for the bilayer geometry

The same principles as for the monolayer geometry apply to the diffuse lipid layer model for the bilayer geometry. In order to calculate the electrostatic contribution to the total osmotic pressure exerted between the lipid bilayers, **Equation 5.4-12** is used. The electrostatic potential Φ_m at the midplane, the concentration distribution, and other necessary quantites are obtained by numerically solving the PBE equation for the diffuse double layer and the surface lipid layer (**Equation 5.2-15**).

5.5 Micellar theoretical model

The micellar model evaluates the change of the free energy of micellization, F_m, of DPC micelles in the absence and in the presence of salt solution in order to obtain (again)

"binding" constants of anions and compare them to those found using the other two geometries (monolayers and bilayers).

5.5.1 Model of local binding adjusted for the micellar geometry

The general relation between headgroup surface area, α, of a surfactant molecule in a micelle and free energy of micellization, F_m, can be written as the sum of three terms: (i) A hydrophobic term proportional to the surface tension between the hydrocarbon tails constituting the hydrophobic core and the aqueous solution. This term tends to minimize the hydrocarbon-water contact, hence α. (ii) A term which describes the lateral non-electrostatic repulsion which tends to maximize the average area per molecule, α, at the hydrocarbon-water interface. (iii) For ionic surfactants there is a purely electrostatic term, due to the formation of a double layer surrounding a micelle. The free energy F per mole of surfactant in the micelle is then given as the sum of these three terms (**Ben-Shaul et al. 1985; Szleifer et al. 1987; Israelachvili 1992**):

$$F_m = \gamma(\alpha-\alpha_0) + \frac{C(\mu_{H_2O})}{\alpha-\alpha_0} + F_{el} \qquad \textbf{Equation 5.5-1}$$

α_0 is the incompressible area of chains or charged groups at the interface (20Å^2 for the DPC molecule). The micelle/water surface tension γ is not precisely known (**Israelachvili 1992**). It must be below that of the air/water interface. In the following, we have chosen the value γ =25 mN/m. The constant C is adjusted so that the area per headgroup coincides with the observed value for a "reference" salt. The electrostatic term F_{el} is obtained by DLVO theory, where the surface charge density is determined by ionic adsorption and described by the charge regulation model (see **Section 5.2.2**) of **Ninham et al. 1971**. According to this model, the surface potential of the micelle, Φ_0, is given by **Equation 5.2-11** where Φ_0 and x_b (fraction of surface sites covered with a bound anion) are calculated within the Poisson-Boltzmann (PB) model.

At high salinity c_{i0}, the micellar radius is much larger than the Debye length κ^{-1}, $\kappa R \gg 1$, and it is sufficient to use the analytical PB solution for the planar geometry. The standard Grahame equation relates the surface charge and potential (**Equation 5.2-7**) while the electrostatic free energy per surfactant in the charge regulation condition becomes:

$$\frac{F_{el}}{RT} = -2x_b \cdot \tanh\left(\frac{ze\Phi_0}{4kT}\right) + \ln(1 - x_b) \qquad \textbf{Equation 5.5-2}$$

Minimising the total free energy, **Equation 5.5-1**, with respect to α gives the area per head group at equilibrium. In the absence of electrostatics (no adsorption, K = 0, $F_{el} = 0$), $\alpha \equiv \alpha_{neutral} = \alpha_0 + (C/\gamma)^{1/2}$.

6 CHAPTER

MONOLAYER EXPERIMENTAL RESULTS

6.1 Introduction

The effect of sodium salts of different monovalent anions belonging to the Hofmeister series was studied on DPPC monolayers at the air-electrolyte interface. The monolayer phase behavior and the morphology and structure of the lipid phases were studied by Surface Pressure – Area isotherms, Brewster Angle Microscopy (BAM), Grazing Incidence X-ray Diffraction (GIXD) and Infrared Reflection-Absorption Spectroscopy (IRRAS).

The goal of this investigation is to obtain structural information showing the precise effects of the anions on the lipid interfacial structures, and eventually to obtain meaningful and reproducible "binding constants" of anions on lipid monolayers. The simplicity of the planar monolayer in addition to the coexistence of various two-dimensional phases on the water surface provides a unique model to study ion-lipid interactions under very well-defined conditions dictated by the surface pressure. Various interfacial models of ion binding can be tested against experiment in order to obtain thermodynamic "binding" constants for each anion studied. These binding constants can be subsequently correlated to analogous binding constants of ions at other interfaces or to potential local interactions (hydration, dispersion, electrostatics etc) to identify interaction mechanisms.

6.2 Pressure – Area Isotherm results of Langmuir Monolayers of DPPC in the presence of NaX salts

In order to study the effect of various electrolytes on the monolayers of DPPC, different sodium salt solutions with concentrations between 0.1 and 0.5 M (and sometimes up to 1.5 M) were used as subphases. Specifically, the salts used were NaCl, NaBr, $NaNO_3$, NaI, $NaBF_4$, $NaClO_4$ and NaSCN. The experimental procedure that was followed for the formation of DPPC monolayers at the air - water (electrolyte) interface was described in **Chapter 3**. Briefly, DPPC monolayers were obtained by spreading 90 - 100 μl of a 1 mM chloroform solution of DPPC. After 10 min of evaporation time for the spreading solvent, the surface pressure – area isotherms were registered while compressing the monolayers at a constant speed of 10 mm/min. Different solvent evaporation times (10-30 min) and different compression speeds (2-10 mm/min) were used as well, and were found to have little effect on the isotherms. DPPC isotherms were recorded at least three times or as many times as necessary to obtain an accurate average isotherm for each concentration of the salt used. The phospholipid DPPC was obtained from Avanti Polar Lipids, and used without further purification. Chloroform (p.a. grade, Merck, Germany) was used as a solvent to prepare 1 mM solutions of DPPC. All sodium salts were purchased from Sigma-Aldrich or Merck with purity > 99%, with the exception of the salts $NaBF_4$ and NaSCN, the purity of which was > 98%. All salts were baked in an oven at 300 °C for 2 hours prior to solution preparation. Salt solutions were prepared using ultrapure water (specific resistance of 18.2 MΩ cm) produced by a Millipore reverse osmosis unit.

Figure 6-1(a) shows the pressure-area isotherm of the monolayer of DPPC on pure water at T = 22°C. As is known from previous studies (**Albrecht et al. 1978; Jyoti et al. 1996**), a plateau region exists at a surface pressure of about 6.5 mN/m indicating the coexistence of two phases formed on compression, the liquid-expanded (LE) and the liquid-condensed (LC) phase. At smaller surface pressures (< 1 mN/m) the gaseous phase exists while at higher surface pressures (>10 mN/m) the solid phase occurs. **Figure 6-1(b)** illustrates the very good reproducibility of DPPC isotherms at a particular range of areas per molecule between 80 and 90 $Å^2$/molecule. The reason this range of A values was chosen is explained below.

The DPPC isotherm shown in **Figure 6-1** is used as a reference isotherm for all our subsequent experiments with NaX salt solutions in the subphase.

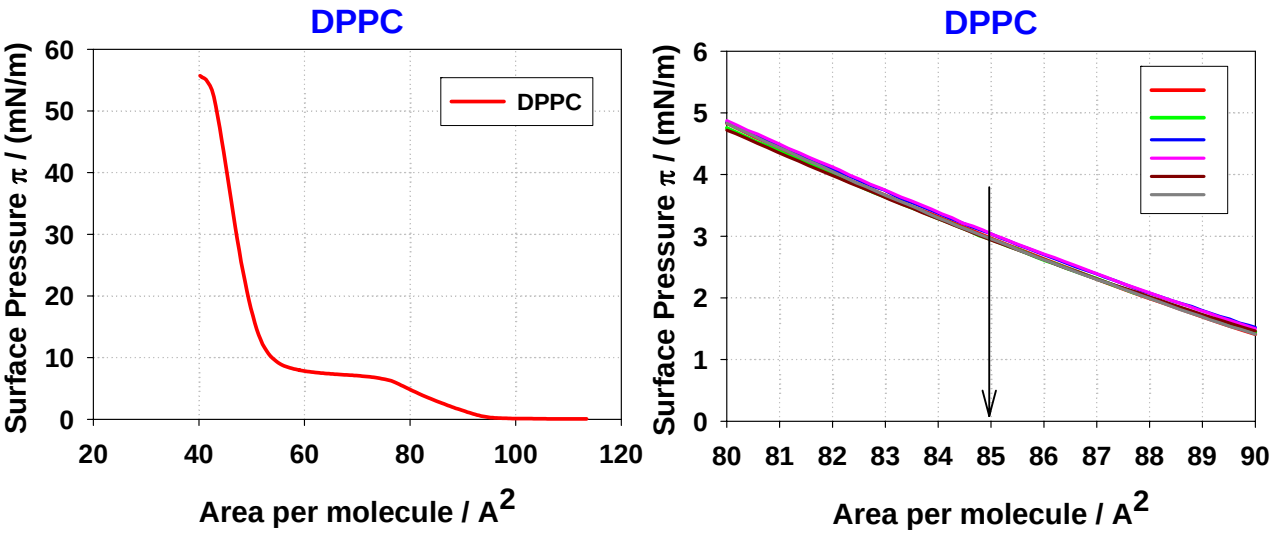

Figure 6-1. Surface pressure vs molecular area isotherms of DPPC at the air – water interface at T = 22.0 ± 0.1°C (a). Reproducibility of DPPC isotherms at the air – water interface T = 22.0 ± 0.1°C (b)

The influence of two anions of the Hofmeister series, Br^- and I^-, (Br^- is less chaotropic than I^-) on the DPPC isotherm is shown below.

Figure 6-2 and **Figure 6-3** show how the change in concentration of NaBr and NaI salt solutions affects a DPPC monolayer respectively. As a general observation, the presence of salt in the subphase increases the surface pressure at a fixed area per molecule, the effect being more pronounced at higher areas per molecule (LE phase) and less so at high surface pressures where the LC phase predominates. For this reason, we chose the region of high areas per molecule (LE phase) to carry out comparisons of the effects of different salt concentrations or different electrolytes. An area of 85 $Å^2$/molecule generally falls in the center of this region. Surface areas between 80 and 55 $Å^2$/molecule were avoided since they coincide with the plateau region of DPPC, i.e. with two-phase coexistence.

The transition from the liquid expanded (LE) to the liquid condensed (LC) phase of DPPC monolayers is shifted to higher surface pressures and smaller molecular areas and the plateau becomes shorter as the salt concentration increases. In addition, comparing **Figure 6-2** and **Figure 6-3** it is clearly seen that the DPPC monolayers are not only affected by the concentration of the salt solution used but also by the type of the anion used in the subphase solutions.

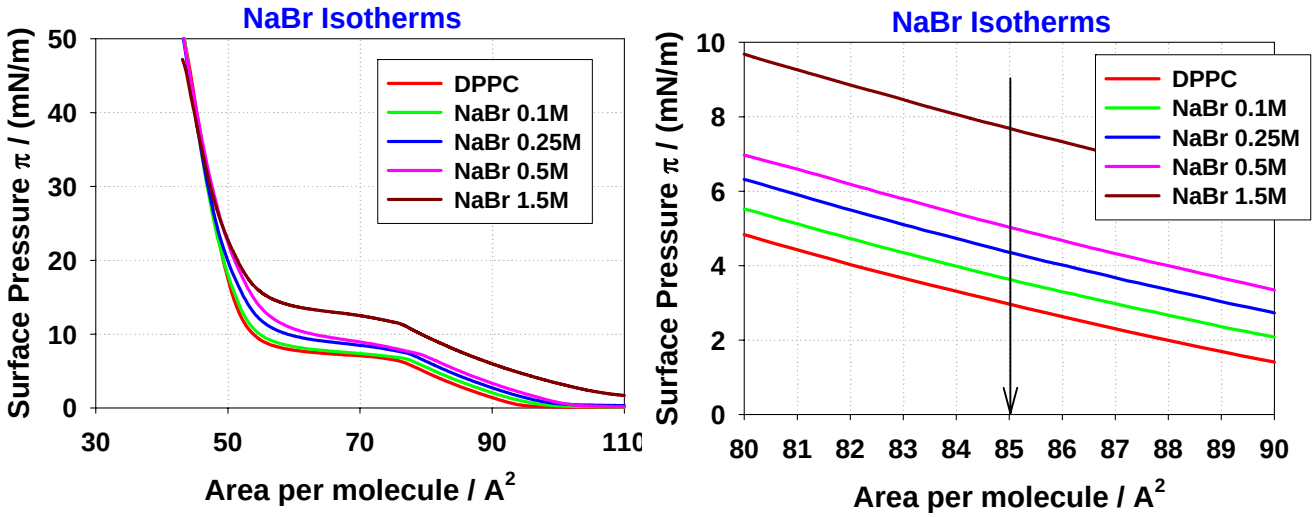

Figure 6-2. Surface pressure vs molecular area isotherms of DPPC on NaBr salt solutions of various concentrations at T = 22.0 ± 0.1°C

Comparing the results found in the presence of Br^- with those found in the presence of I^-, we observe that the effect of I^- on the DPPC monolayer is greater since it leads to a larger surface pressure increase at the same (fixed) area per molecule. Additional π - A isotherms of DPPC on NaCl, $NaNO_3$, $NaBF_4$, $NaClO_4$ and NaSCN solutions of various concentrations were obtained and are given in **Appendix I**.

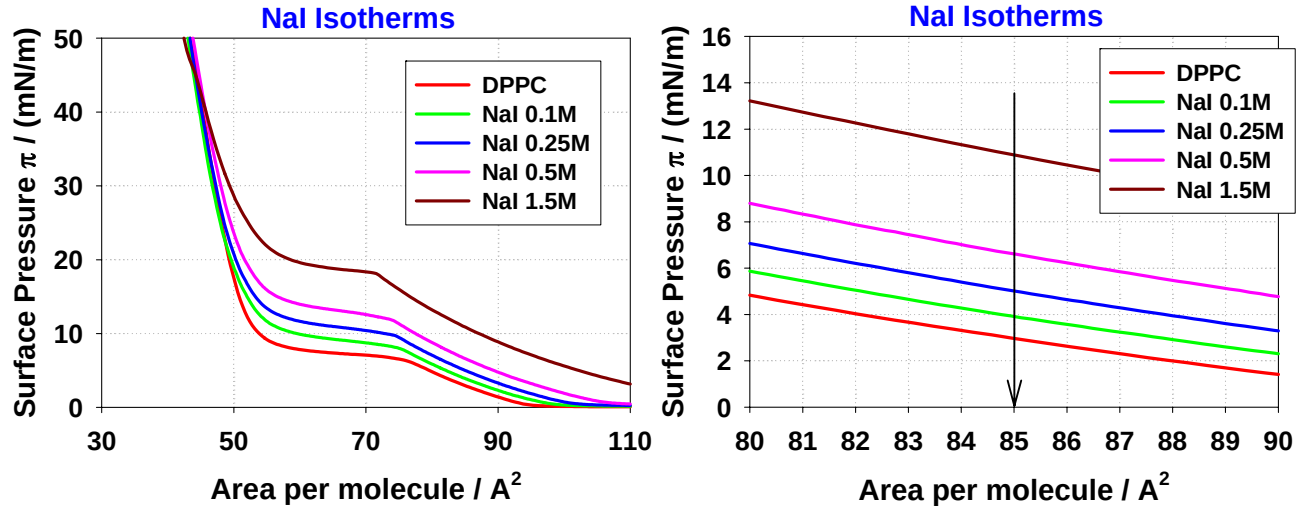

Figure 6-3. Surface pressure vs molecular area isotherms of DPPC on NaI salt solutions of various concentrations at T = 22.0 ± 0.1°C

The 80 – 90 Å^2/ per molecule regions of the π - A isotherms of DPPC on pure water and on 0.1 M solutions of various sodium salts are presented in **Figure 6-4**. It can be seen that the increase in surface pressure is different for different anions and the magnitude of the increase follows the order: $Cl^- < Br^- < NO_3^- < I^- < BF_4^- < ClO_4^- < SCN^-$. The effect of anions follows the order of the Hofmeister series with ClO_4^- appearing in front of SCN^-. Similar results were obtained with 0.25M and 0.5M salt concentration in the subphase and are not shown here.

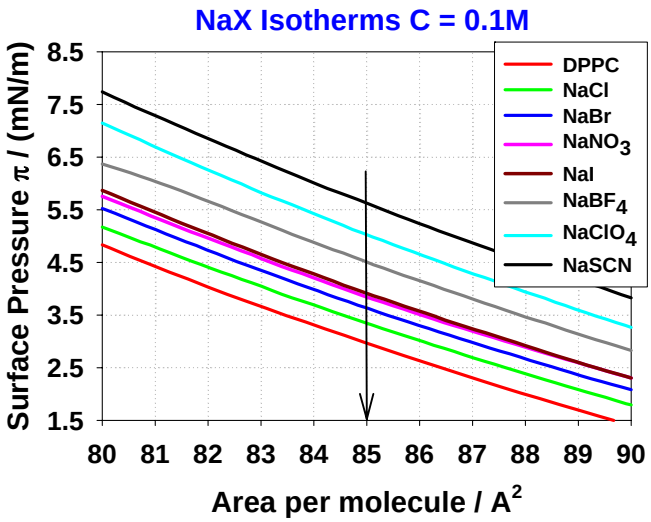

Figure 6-4. Surface pressure vs molecular area isotherms of DPPC on 0.1M NaX salt at T = 22.0 ± 0.1°C

As an illustration of the Hofmeister effect of salts on DPPC, we plot in **Figure 6-5** the surface pressure as a function of the square root of salt concentration for a lipid area of 85 Å^2 per molecule. Approximate straight lines are obtained, the slopes of which follow the Hofmeister series. From **Figures 6-1** to **6-5** we conclude that the effect of anions on the DPPC isotherms is significant. The increase of surface pressure, π, at a fixed area per molecule, A, in presence of NaX solutions in the subphase indicates that the LE phase is favored over the LC phase; that is the LE phase is stabilized in the presence of high concentrations of salts. The increase of surface pressure and the stabilization of the LE phase could be due to adsorption of anions on the headgroups of DPPC molecules, which would thus create an additional electrostatic repulsion between the DPPC molecules. However, it is not clear from the π – A isotherms to what extent the LC phase is affected by the presence of ions in the subphase. To fully understand the mechanism of action of the various anions on the DPPC monolayers we must

examine the effect of NaX salt solutions on the LC phase and this is done below with methods that can yield information at much shorter length scales.

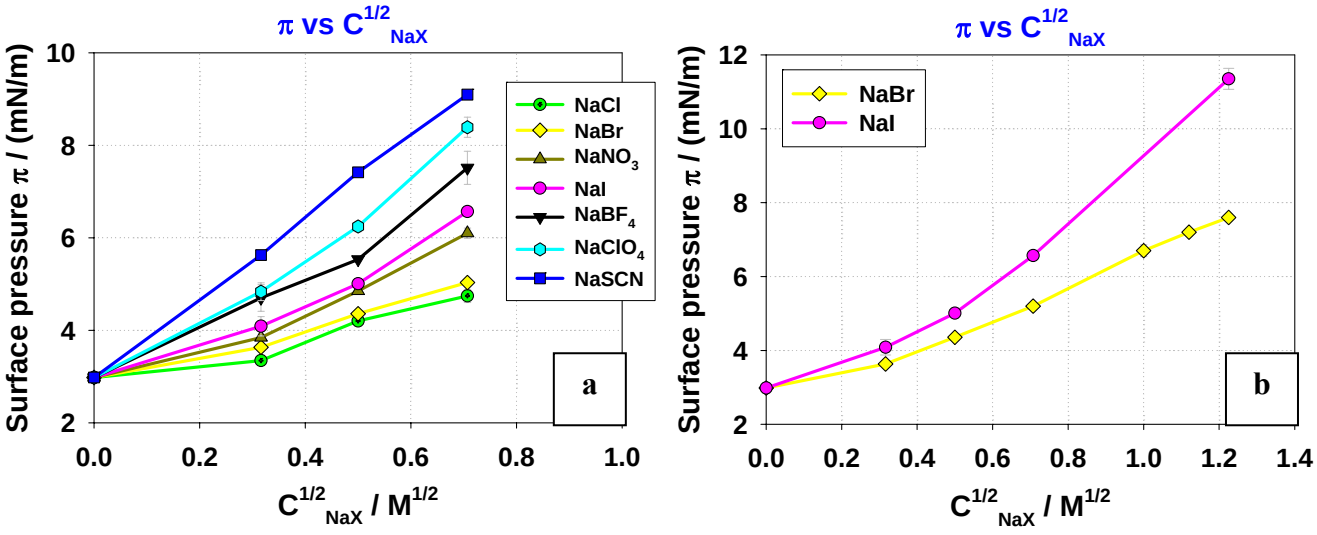

Figure 6-5. Surface pressure as a function of the square root of salt concentration in the subphase (a). Surface pressure as a function of the square root of salt concentration of NaBr and NaI (b). Both figures are at A = 85 Å^2 / molecule and T = 22.0 ± 0.1°C

6.3 Brewster Angle Microscopy – Domain Morphology results

In order to investigate the effect of NaX salt solutions on the LC phase of DPPC monolayers, we have used the Brewster angle microscope, which allows direct observation (on a μm scale) of the nucleation and growth of the structure of the condensed-phase (LC) domains of lipid monolayers (as explained in **Chapter 3**). The morphology (size and shape) of DPPC monolayer domains has been thoroughly studied over the past 10 years with fluorescence and Brewster angle microscopy (**Wiedemann et al. 1995 and 1996; McConlogue et al. 1997 and 1999; Li et al. 1998**). **Figure 6-6** shows the LC phase domains of DPPC at different areas per molecule, as they have been observed by us on pure water.

Figure 6-7 to **6-12** show the BAM images of DPPC monolayers that have been obtained on subphases of NaX salt solutions of concentrations ranging between 0.1 and 1.5 M. **Figure 6-7** shows the shape and size of LC phase domains of DPPC on NaCl salt solutions of concentration 1M and 1.5M respectively.

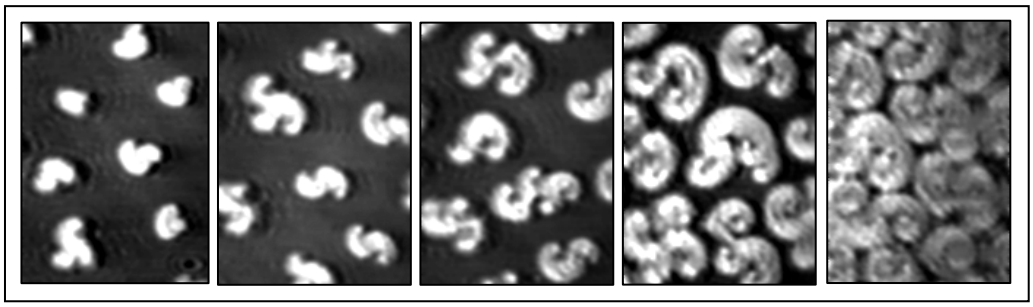

Figure 6-6. BAM images of LC phase domains of DPPC at the air – water interface. The area per molecule from left to right is 59.0 ± 0.5 Å^2, 56.5 ± 0.5 Å^2, 54.5 ± 0.5 Å^2, 53.0 ± 0.5 Å^2 and 50.5 ± 0.5 Å^2. Scale 100 μm.

If we compare the BAM images of the DPPC domains on pure water (**Figure 6-6**) and on NaCl solutions (**Figure 6-7**) it can be observed that the presence of Cl^- ions in the subphase does not affect the domain morphology of DPPC monolayers significantly, even when a very high salt concentration is used in the subphase.

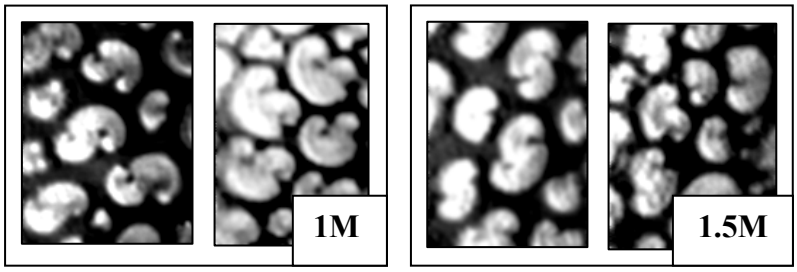

Figure 6-7. BAM images of LC phase domains of DPPC on NaCl solutions of concentrations 1.0M and 1.5M. For both concentrations the area per molecule is equal to 56.5 ± 0.5 Å^2 and 54.0 ± 0.5 Å^2 (left to right). Scale 100 μm.

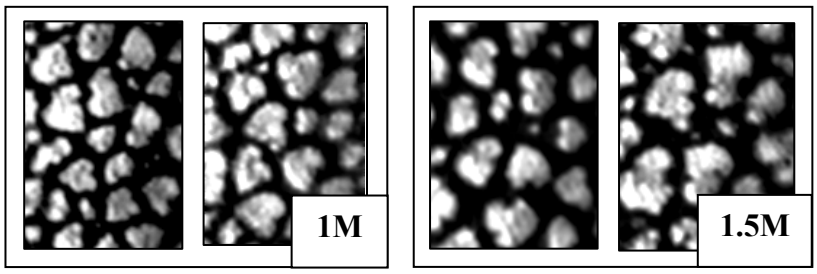

Figure 6-8. BAM images of LC phase domains of DPPC on NaBr solutions of concentrations 1.0M and 1.5M. For both concentrations the area per molecule is equal to 57.0 ± 0.5 Å^2 and 55.0 ± 0.5 Å^2 (left to right). Scale 100 μm.

Comparing the BAM images obtained for the ions Br^-, NO_3^- and I^- (**Figures 6-8** to **6-10**) we can see that the LC domains become more rounded as the concentration of the salt solution increases in the subphase. As the concentration of the NaX solutions increases, the shape of the domains loses its characteristic "triskelion" geometry and becomes more rounded (but still not isotropic) while for concentrations lower than 0.5 M the different anions mainly change the density of LC domains on the surface and not their size and shape.

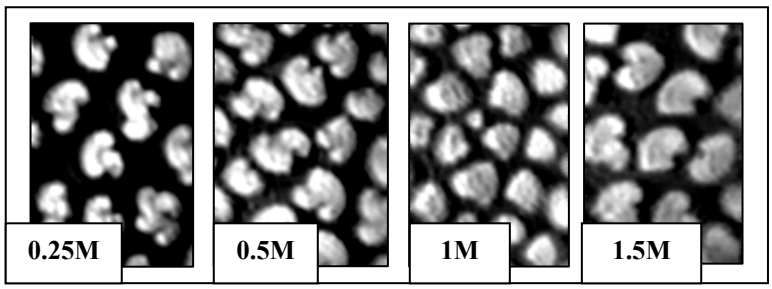

Figure 6-9. BAM images of LC phase domains of DPPC on $NaNO_3$ solutions of concentrations from 0.25M to 1.5M. The area per molecule is equal to 56 ± 1 Å^2. Scale 100 μm.

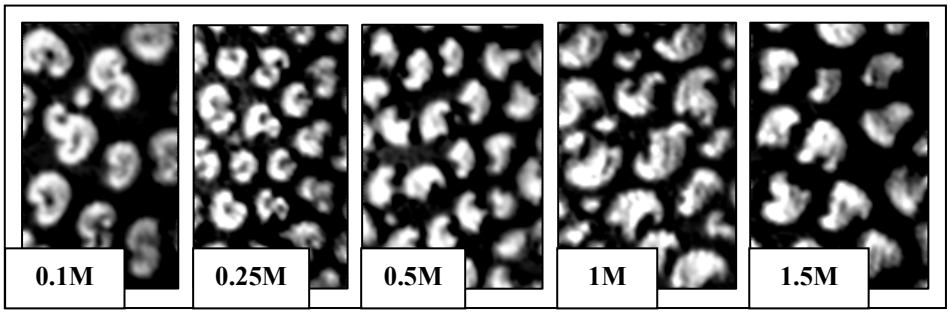

Figure 6-10. BAM images of LC phase domains of DPPC on NaI solutions of concentrations from 0.1M to 1.5M. The area per molecule is equal to 56 ± 1 Å^2. Scale 100 μm.

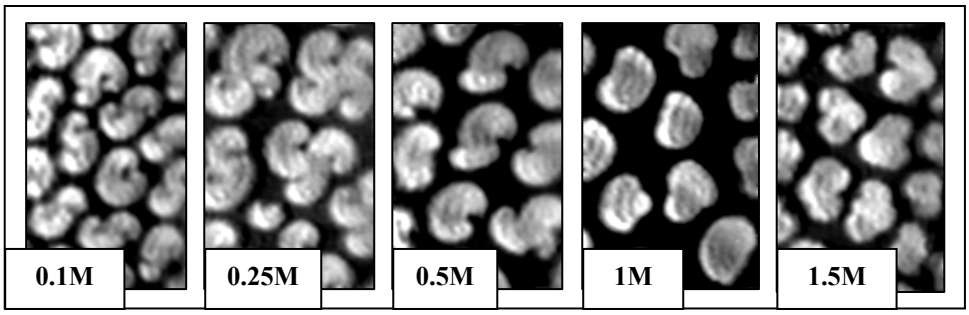

Figure 6-11. BAM images of LC phase domains of DPPC on $NaBF_4$ solutions of concentrations from 0.1M to 1.5M. The area per molecule is equal to 56 ± 1 Å^2. Scale 100 μm.

The anions BF_4^- and SCN^- have a stronger effect on the size and shape of DPPC domains as is shown in **Figures 6-11** and **6-12**. The domain shape becomes more rounded compared to the DPPC domain morphology in the presence of the anions Br^-, NO_3^- and I^- (**Figures 6-8 to 6-10**) at the same concentration. Moreover, the most chaotropic ion SCN^- reduces the size of the LC domains drastically, at the same area per molecule, as the concentration of the salt increases.

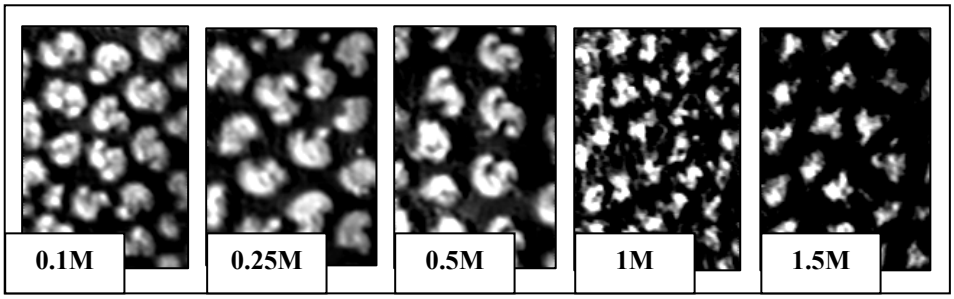

Figure 6-12. BAM images of LC phase domains of DPPC on NaSCN solutions of concentrations from 0.1M to 1.5M. The area per molecule is equal to 56 ± 1 Å^2. Scale 100 μm.

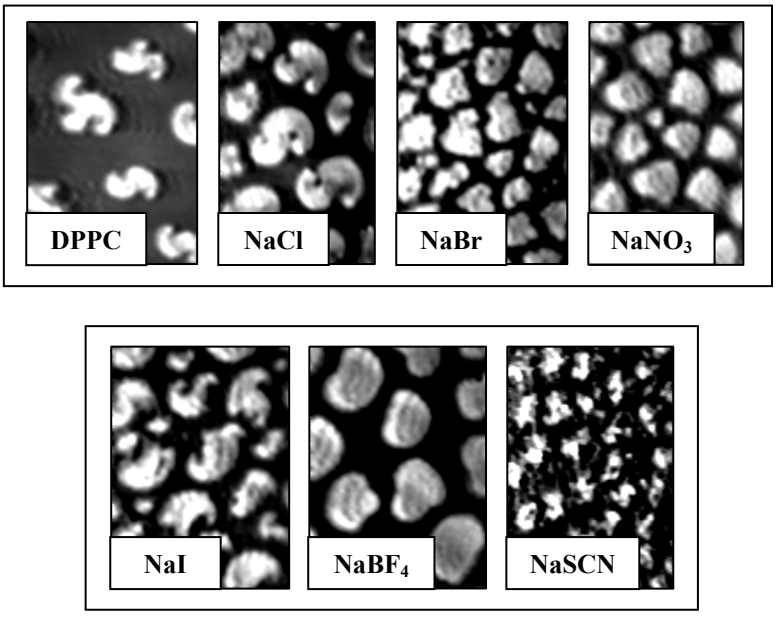

Figure 6-13. BAM images of LC phase domains of DPPC for a surface area of 56 ± 1 Å^2 per molecule in the presence of 1M solutions of NaCl, NaBr, $NaNO_3$, NaI, $NaBF_4$ and NaSCN. A picture of DPPC domains on pure water at the same area per molecule is also included for comparison. Scale 100 μm.

Figure 6-13 compares BAM images obtained for DPPC monolayers in the presence of all the NaX salt solutions used in this study at a concentration of 1 M. In general, although some differences of the DPPC LC domain morphology can be distinguished in the presence of the various electrolytes, the overall impression from **Figure 6-13** is that the LC domain shapes are not very sensitive to the specific salt in the subphase.

Current theory for predicting the shapes of lipid domains at the air – water interface (see **Chapter 3**, **Section 3.2.3**) assumes that the shape of an individual solid domain is determined by the competition between line tension and electrostatic interactions, the former favoring rounded domains and the latter more elongated domains. In general, in the absence of charged headgroups, the line tension is stronger than the electrostatic interaction, and thus the domain shape is circular. The opposite occurs when the lipid headgroups are charged and the line tension is weak. The experimental results obtained here (**Figures 6-7** to **6-13**) clearly show that the domain shape becomes more rounded as the anion in the subphase is changed from Cl^- to SCN^- and also as the concentration of the NaX salts in the subphase increases. These observations indicate that the line tension overwhelms the electrostatic interaction. These experimental results can be interpreted by the following way: Anions in the subphase gradually screen the dipole potentials of the DPPC headgroups, leading to weakened electrostatic forces and rounding of the domain shape. *The various anions do not appear to bind (adsorb) on the DPPC headgroups of the LC phase because then the DPPC molecules would have become charged and as a result electrostatics would then dominate and the LC domains should get more elongated*. This is clearly not observed in our experiments.

6.4 Grazing Incidence X-ray Diffraction results

Grazing incidence X-ray diffraction experiments were performed as explained in **Chapter 3**. GIXD was used to obtain information (at the nanometer scale, nm) about the two-dimensional packing and the chain tilt of DPPC molecules at the air-water interface in the presence of NaBr or NaI in the subphase. Measurements were made at 22 °C at surface pressures of 15, 25, 35, and 45 mN m^{-1} and for salt concentrations of 0.5 and 1.5 M. Br^- and I^- were chosen as the investigated anions since they influence the pressure-area isotherms to a different extent as was revealed from π – A measurements described before (**Figure 6-5**). Br^- affects the DPPC monolayers less than I^-, which is more chaotropic. Two Bragg peaks (non-degenerate and degenerate) indicating an orthorhombic in-plane lattice describe the measured

scattering curves and thus a rectangular unit cell was assumed to calculate the lattice parameters and chain tilt angle. The non-degenerate in-plane (Q^{n}_{xy} at $Q^{n}_{z} = 0$) and the 2-fold degenerate out-of-plane (Q^{d}_{xy} at $Q^{d}_{z} > 0$) scattering vectors for DPPC monolayer on pure water are listed in **Table 6-1** as they were calculated by a Lorentzian and a Gaussian fitting analysis respectively. An example of the fitting analysis is shown below (**Figure 6-14** and **Figure** 6-15) for DPPC on pure water at a surface pressure π = 15 mN/m.

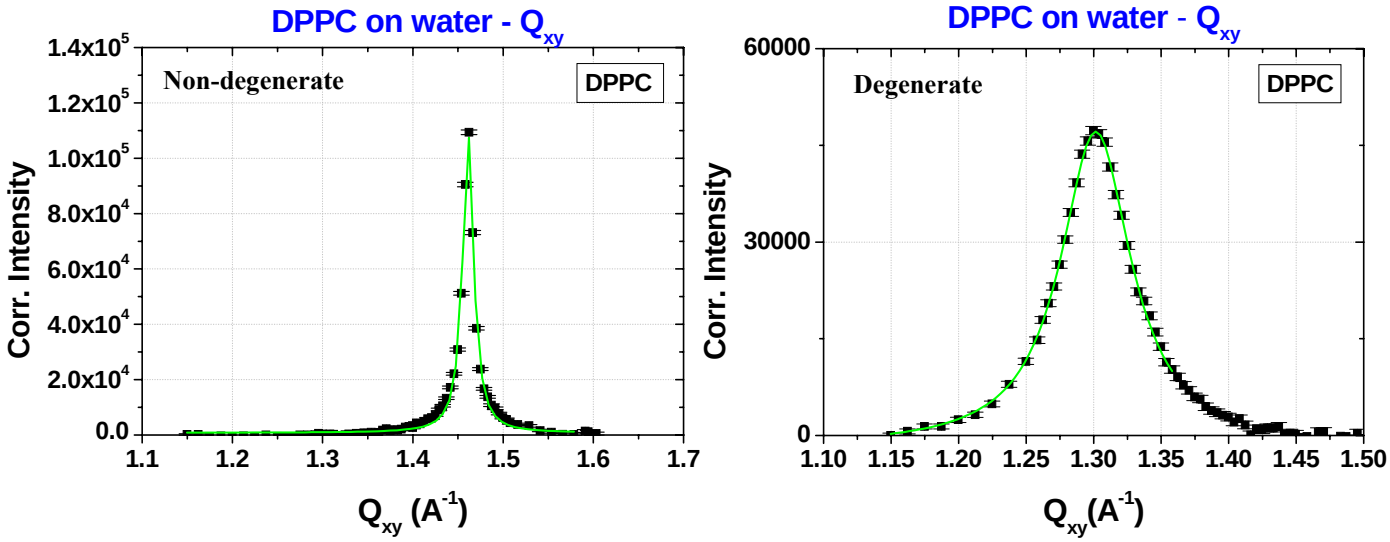

Figure 6-14. Corrected X-ray Intensities vs the in-plane Q_{xy} scattering vector component for DPPC at the air-water interface. Determination of the positions of the two Bragg peaks (non-degenerate and degenerate) using a Lorentzian fit of the experimental results

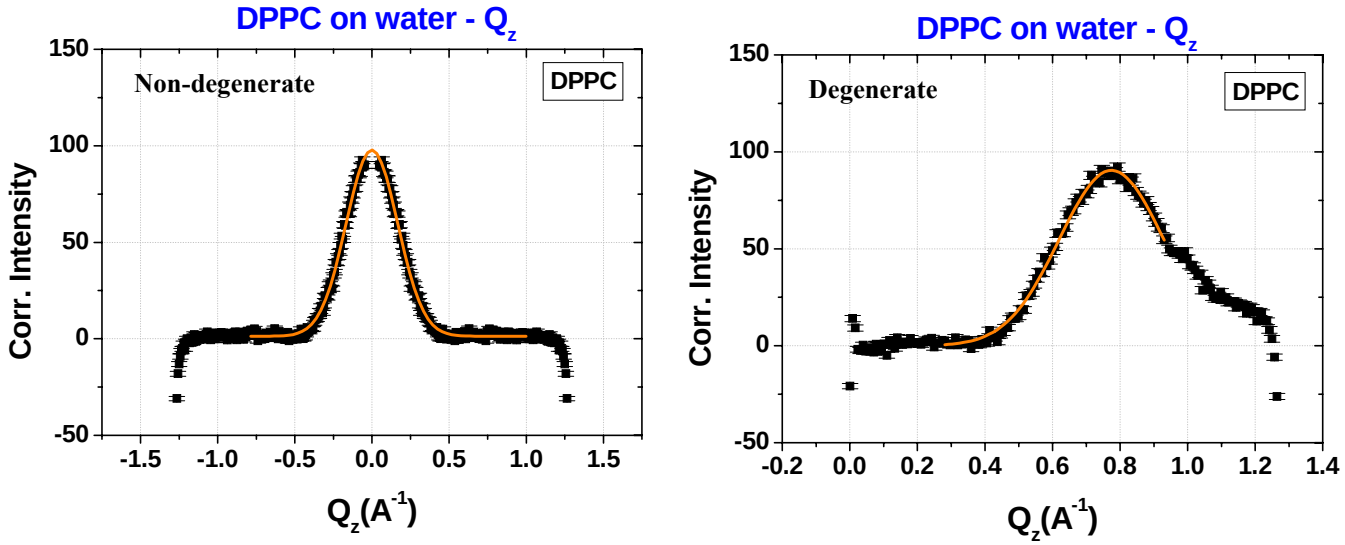

Figure 6-15. Corrected X-ray Intensities vs the out-of-plane Q_z scattering vector component for DPPC at the air-water interface. Determination of the positions of the two Bragg peaks (non-degenerate and degenerate) using a Gaussian fit of the experimental results

The calculated lattice parameters *a, b* and *γ* of the DPPC chain lattice and the tilt angles for DPPC monolayers on pure water are given in **Table 6-2**.

Table 6-1. In-plane and Out-of-plane scattering vectors of DPPC at the air-water interface

DPPC on	π (mN/m)	Q_{xy} (Å^{-1})	Q_z (Å^{-1})
H_2O	15	1.461 1.301	0 0.771
	25	1.466 1.327	0 0.737
	35	1.470 1.354	0 0.680
	45	1.474 1.393	0 0.607

Table 6-2. Lattice parameters, *a*, *b*, and *γ*, tilt angle t with respect to the normal, in-plane unit cell area A_{xy} and chain cross-sectional area A_o at different surface pressures

DPPC on	π (mN/m)	*a* (Å)	*b* (Å)	*γ* (°)	T (deg)	A_{xy} (Å^2)	A_o (Å^2)
H_2O	15	5.84	5.20	124.2	35.6	25.1	20.4
	25	5.68	5.14	123.5	33.7	24.4	20.3
	35	5.52	5.09	122.9	30.9	23.6	20.3
	45	5.32	5.02	121.9	27.2	22.6	20.1

Tables 6-3 to **6-6** contain the horizontal and vertical scattering vector components and the lattice parameters for a DPPC monolayer spread on 0.5 and 1.5 M NaBr and NaI salt solutions. If we compare the results (lattice parameters, tilt angle) for DPPC on pure water (**Table 6-2**) and for DPPC in the presence of Br^- anions (**Table 6-4)** it can be concluded that the DPPC LC phase is very little affected by the presence of Br^- anions, even when very high concentrations of the salt solution are used in the subphase. The chain tilt-angles for DPPC on pure water and on 0.5 and 1.5 M NaBr are compared in **Figure 6-16**, where it is observed that the tilt angle is not influenced by the presence of Br^- anions. In general, the cell parameters, the chain tilt-angle and the unit cell distortion are very similar in the presence and the absence of NaBr. This can also be seen in **Figure 6-17**, which is a contour plot of the in-plane component of the scattered intensity Q_{xy} vs the out-of-plane component Q_z for DPPC monolayers at 25 and 45 mN/m on pure water, on 0.5 M and 1.5 M NaBr solution.

Table 6-3. In-plane and Out-of-plane scattering vectors of DPPC in the presence of NaBr salt solutions of concentrations 0.5 M and 1.5 M respectively

DPPC on	π (mN/m)	Q_{xy} (Å^{-1})	Q_z (Å^{-1})	DPPC on	π (mN/m)	Q_{xy} (Å^{-1})	Q_z (Å^{-1})
NaBr 0.5M	15	1.461 1.300	0 0.774	NaBr 1.5M	15	1.460 1.302	0 0.764
	25	1.465 1.330	0 0.726		25	1.465 1.321	0 0.730
	35	1.470 1.360	0 0.692		35	1.469 1.353	0 0.677
	45	1.474 1.396	0 0.588		45	1.474 1.385	0 0.609

Table 6-4. Lattice parameters, *a*, *b*, and *γ*, tilt angle t with respect to the normal, in-plane unit cell area A_{xy} and chain cross-sectional area A_o at different surface pressures in the presence of NaBr salt solutions of concentrations 0.5 M and 1.5 M respectively

DPPC on	π (mN/m)	*a* (Å)	*b* (Å)	*γ* (°)	t (deg)	A_{xy} (Å^2)	A_o (Å^2)
NaBr 0.5 M	15	5.84	5.20	124.2	35.8	25.1	20.4
	25	5.66	5.14	123.4	33.2	24.3	20.3
	35	5.49	5.08	122.7	31.2	23.5	20.1
	45	5.30	5.02	121.9	26.4	22.6	20.2
NaBr 1.5 M	15	5.83	5.20	124.1	35.3	25.1	20.4
	25	5.72	5.15	123.7	33.6	24.5	20.4
	35	5.53	5.09	122.9	30.8	23.6	20.3
	45	5.36	5.03	122.2	27.4	22.8	20.3

The GIXD results imply that Br^- ions do not penetrate into or bind to the LC phase, because in that case we should observe significant changes of the unit cell parameters. Interestingly, in all cases the diffraction pattern with distinct peaks at low surface pressure changes to a pattern with the scattering intensity more distributed along an arc. The reason for such a change could be that at low pressure the molecules are able to pack in a lattice with defined tilt angle and tilt direction. Pressure increase leads obviously to packing problems, and such an intensity distribution can be described by assuming a fixed tilt angle but a variable tilt direction.

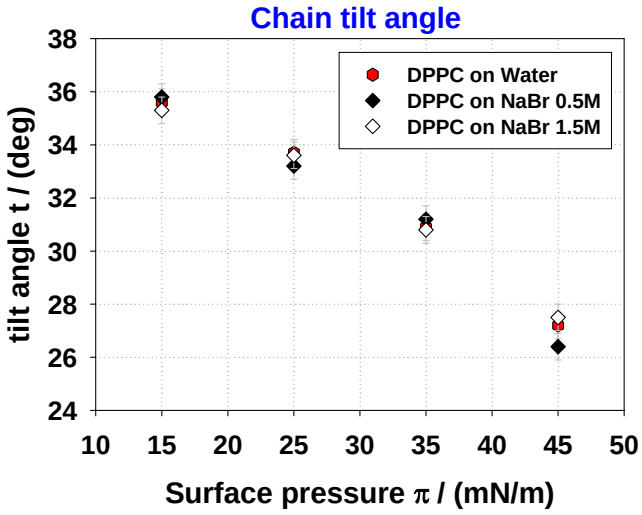

Figure 6-16. Chain tilt-angle for DPPC monolayers on pure water and in the presence of NaBr salt solutions of concentrations 0.5 M and 1.5 M

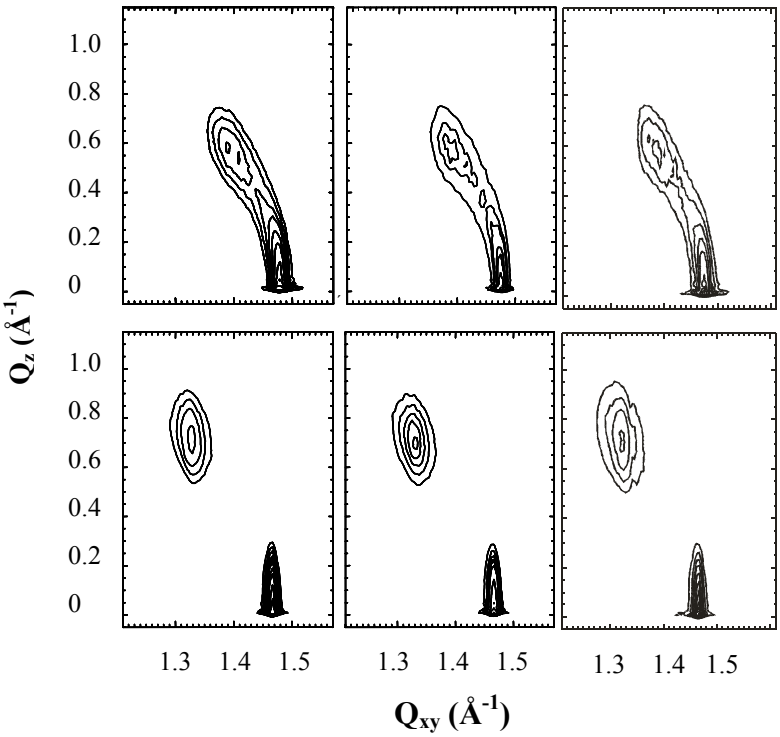

Figure 6-17. Contour plots of the corrected X-ray intensities as a function of in-plane Q_{xy} and out-of-plane Q_z scattering vector components for DPPC on water (left) and on 0.5 M (middle) and 1.5 M (right) NaBr respectively at π = 25 mN/m (bottom) and 45 mN/m (top)

Table 6-5. In-plane and Out-of-plane scattering vectors of DPPC in the presence of NaI salt solutions of concentration 0.5 M and 1.5 M respectively

DPPC on	π (mN/m)	Q_{xy} (Å^{-1})	Q_z (Å^{-1})
NaI 0.5M	15	no peaks	no peaks
	25	too weak	too weak
	35	1.456 1.364	0 0.623
	45	1.473 1.398	0 0.548
NaI 1.5M	all pressures	Weak broad peak	Weak broad peak

Table 6-6. Lattice parameters, *a*, *b*, and *γ*, tilt angle t with respect to the normal, in-plane unit cell area A_{xy} and chain cross-sectional area A_o at different surface pressures in the presence of NaI salt solutions of concentrations 0.5 M and 1.5 M respectively

DPPC on	π (mN/m)	*a* (Å)	*b* (Å)	*γ* (°)	t (deg)	A_{xy} (Å^2)	A_o (Å^2)
NaI 0.5 M	15	No peaks	----	----	----	----	----
	25	Too weak	----	----	----	----	----
	35	5.45	5.08	122.4	28.4	23.4	20.5
	45	5.29	5.02	121.8	24.8	22.6	20.5
NaI 1.5 M	all pressures	weak/broad peak	----	----	----	----	----

Similar measurements have been made with NaI salt solutions of concentrations 0.5 M and 1.5 M in the subphase. The experimental results reveal some additional special features. On a 0.5 M NaI solution, there are no diffraction peaks at 15 mN/m. At 25 mN/m the scattering intensity is still much less compared to that in the other experiments. Only the (02) Bragg peak close to the horizon can be clearly seen. Therefore, **Table 6-5** shows only the data at surface pressures 35 mN/m and 45 mN/m for the in-plane Q_{xy} and out-of-plane Q_z scattering components. **Table 6-6** gives the corresponding lattice parameters and chain tilt-angle for DPPC on NaI salt solutions. The experimental results show that the tilt angle of the chains is smaller compared to that of DPPC on water or on NaBr. The smaller tilt angle of DPPC molecules on NaI salt solutions of concentration 0.5 M could be an indication for a changed head group conformation or hydration. If the head group needs less space, the tilt of the chains is reduced. This could be the result of interactions of the head group with the I^- ions. However, the results obtained at higher NaI concentrations in the subphase support another explanation for the experimental results obtained. Much less scattering is observed using 1.5 M NaI even at the highest surface pressure examined (45 mN/m) as it is shown in **Figure**

6-18 where the contour plots of the corrected X-ray intensities for a DPPC monolayer on water and in the presence of NaI concentrations 0.5M and 1.5M are compared respectively.

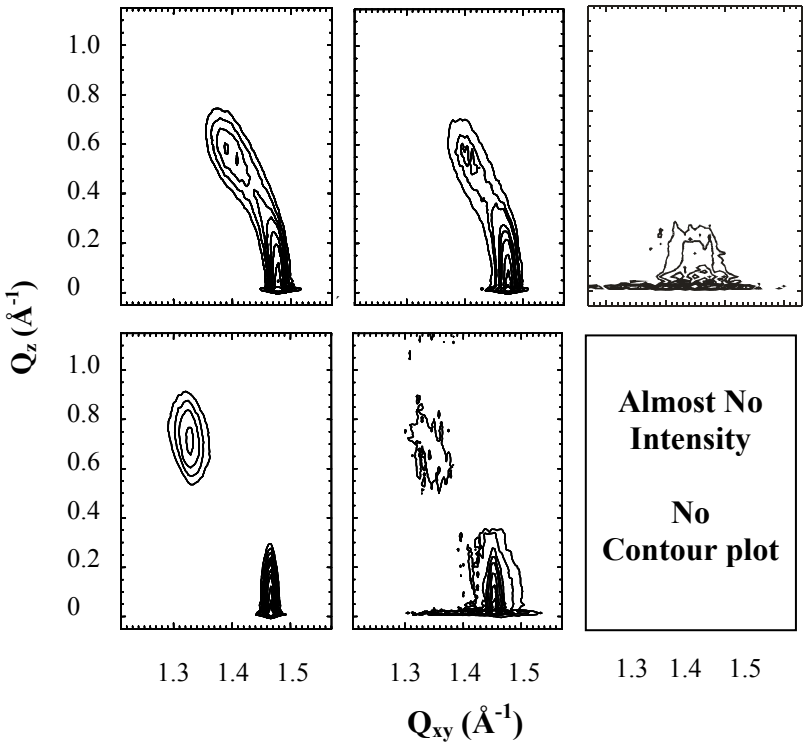

Figure 6-18. Contour plots of the corrected X-ray intensities as a function of in-plane Q_{xy} and out-of-plane Q_z scattering vector components for DPPC on water (left) and on 0.5 M (middle) and 1.5 M (right) NaI respectively at π = 25 mN/m (bottom) and 45 mN/m (top)

Only one broad peak close to zero Q_z is observed in **Figure 6-18** in the presence of 1.5 M NaI at 45 mN/m which is more clearly seen in **Figure 6-19**. **Figure 6-19** is a 3D-plot of the corrected X-Ray intensity as a function of the scattering components at surface pressure π = 35 mN/m. This shows that the LC phase is strongly disturbed. One reasonable explanation is that radicals produced by the high energy X-ray beam lead to an oxidation reaction producing iodine (I). Iodine itself can penetrate into the hydrophobic region of the DPPC monolayer and disturbs the chain packing to a large extent. *Consequently, the change of the tilt angle of DPPC molecules in the presence of NaI may not be due to adsorption (binding) of the I^- ions on the headgroups of DPPC molecules but rather to the formation of iodine in the subphase.*

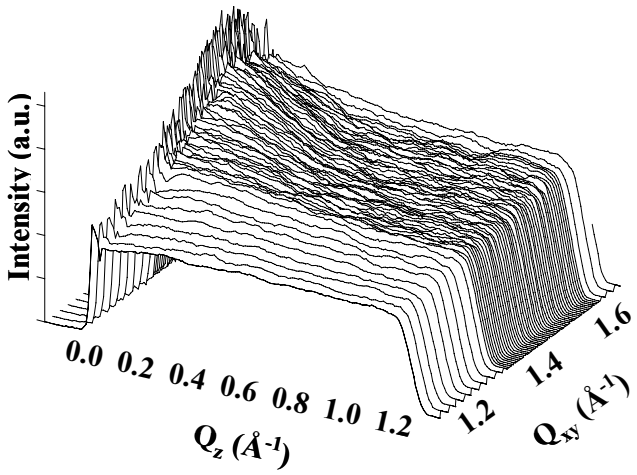

Figure 6-19. 3D-plot of the corrected X-ray intensities as a function of in-plane Q_{xy} and out-of-plane Q_z scattering vector components for a DPPC monolayers on 1.5 M NaI at π = 35 mN/m at T = 22 °C

6.5 Infrared Reflection – Absorption Spectroscopy results

Infrared Reflection-Absorption Spectroscopy (IRRAS) was used to provide additional information about the influence of high concentrations of the chaotropic anion I^- on DPPC monolayers. Previous FT-IR studies have shown that changes in the wavenumbers and intensities of specific bands provide valuable information on chain conformation ($\nu_{as}CH_2$, ν_sCH_2), H-bonding, hydration and ion binding on the headgroup of the lipid (νCO, $\nu_{as}PO_2^-$) (**Mendelson et al. 1995, 2002**). Particularly interesting are the C–H stretching bands of the saturated hydrocarbon chains between 3000 and 2800 cm^{-1}, and the region between 1250 and 1000 cm^{-1}, which gives information about the vibrations of the phosphate headgroup. The IR spectra of a DPPC monolayer at the air-water interface for a surface pressure π = 6 mN/m is shown in **Figure 6-20(a)**. The spectrum is plotted in absorbance units [$-\log(R/R_0)$], where R is the single beam reflectance spectrum of the DPPC monolayer on water and R_0 is the single beam reflectance spectrum of the water subphase. The spectra were recorded with s or p-polarized light under an angle of incidence of 40° normal to the surface. The most important bands are shown in **Figure 6-20(b)**. These are the symmetric stretching $\nu_s(CH_2)$ and antisymmetric stretching $\nu_{as}(CH_2)$ bands of the CH_2 group. In addition, the vibration band of the phosphate stretching group is observed $\nu_{as}(PO_2^-)$ between 1220 – 1250 cm^{-1}. It has been observed that during the main phase transition in DPPC monolayers the symmetric CH_2 stretching frequency decreases from 2855 to 2851 cm^{-1} and the antisymmetric CH_2 decreases

from 2924 to 2919 cm^{-1} indicating an increase of trans over gauche conformations and a higher degree of order. For DPPC on pure water at π = 6 mN/m, the vibration band $v_s(CH_2)$ is found at 2851.6 cm^{-1} and the vibration band $v_{as}(CH_2)$ is found at 2920.4 cm^{-1} signifying thus a change in the chain conformation form gauche to trans. The phosphate stretching groups $v_{as}(PO_2^-)$ is found at 1230.4 cm^{-1}.

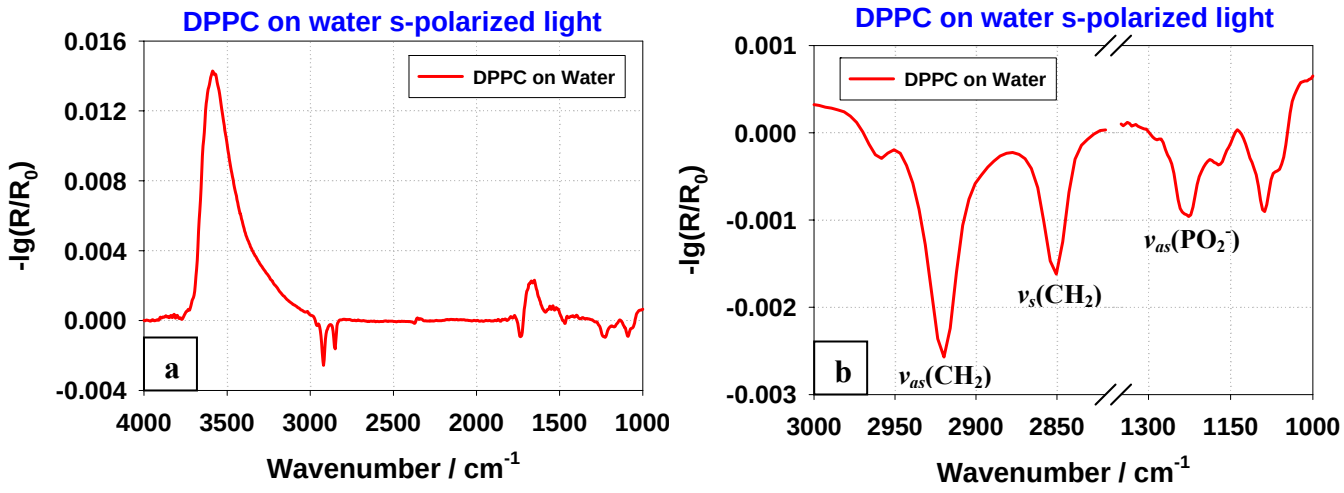

Figure 6-20. IRRAS refelction spectrum of a DPPC monolayer at the air-water interface (a) IRRAS reflection spectrum of the 1000 – 3000 cm^{-1} region of DPPC monolayer at the air-water interface (b). The spectrum was recorded at surface pressure π = 6 mN/m at T = 20 °C. s-polarized light at an angle 40° normal to the surface was used

The characteristic frequencies of the IR spectra of a DPPC monolayer on pure water at various surface pressures at 20 °C are given in **Table 6-7**.

Table 6-7. DPPC monolayer stretching vibrations on pure water at T = 20 °C

DPPC on water			
Vibration	**$v_{as}CH_2$ / cm^{-1}**	**v_sCH_2 / cm^{-1}**	**$v_{as}PO_2^-$ / cm^{-1}**
π (mN/m)			
0	2924.7 ± 0.2	2855.6 ± 0.3	1228.3 ± 0.5
2	2924.6 ± 0.2	2855.3 ± 0.3	1228.8 ± 0.5
3	2924.2 ± 0.2	2855.3 ± 0.3	1228.6 ± 0.5
4	2923.9 ± 0.2	2854.4 ± 0.3	1228.8 ± 0.5
4.5	2922.2 ± 0.2	2853.3 ± 0.3	1229.0 ± 0.5
5	2921.1 ± 0.2	2852.2 ± 0.3	1229.3 ± 0.5
5.5	2920.7 ± 0.2	2851.8 ± 0.3	1230.2 ± 0.5
6	2920.4 ± 0.2	2851.6 ± 0.3	1230.4 ± 0.5
8	2920.0 ± 0.2	2851.4 ± 0.3	1230.3 ± 0.5

15	2919.8 ± 0.2	2851.1 ± 0.3	1229.7 ± 0.5
25	2919.5 ± 0.2	2851.0 ± 0.3	1231.5 ± 0.5
35	2919.4 ± 0.2	2851.1 ± 0.3	1231.1 ± 0.5
45	2919.1 ± 0.2	2851.1 ± 0.3	1230.2 ± 0.5

It is clearly seen from the results represented in **Table 6-7** that the values of the symmetric and antisymmetric CH_2 stretching groups are decreasing upon increasing the surface pressure indicating a *decrease* of the lattice distortion and thus an *increase* of the conformational order. IR spectra have also been recorded for DPPC on a 1.5 M NaI solution at selected surface pressures and are given in **Table 6-8**.

Table 6-8. DPPC monolayer stretching vibrations on NaI solutions of concentration of 1.5 M at T = 20 °C

DPPC on NaI 1.5 M			
Vibration	**$\nu_{as}CH_2$ / cm^{-1}**	**$\nu_{s}CH_2$ / cm^{-1}**	**$\nu_{as}PO_2^-$ / cm^{-1}**
π (mN/m)			
6	2924.2 ± 0.2	2854.7 ± 0.3	1225.9 ± 0.5
8	2924.0 ± 0.2	2854.5 ± 0.3	1225.5 ± 0.3
10	2923.5 ± 0.2	2854.4 ± 0.3	1225.8 ± 0.3
12	2923.1 ± 0.2	2853.8 ± 0.3	1225.8 ± 0.3
12.5	2923.0 ± 0.2	2853.7 ± 0.3	1225.7 ± 0.3
14	2922.8 ± 0.2	2853.6 ± 0.3	1226.5 ± 0.3
14.5	2922.3 ± 0.2	2853.5 ± 0.3	1226.1 ± 0.3
15	2921.8 ± 0.2	2853.0 ± 0.3	1226.6 ± 0.5
18	2921.6 ± 0.2	2852.8 ± 0.3	1227.1 ± 0.2
19	2921.4 ± 0.2	2852.5 ± 0.3	1227.3 ± 0.3
20	2921.2 ± 0.2	2852.2 ± 0.3	1227.1 ± 0.3
25	2920.0± 0.2	2851.6 ± 0.3	1228.0 ± 0.5
35	2919.2 ± 0.2	2851.0 ± 0.3	1230.6 ± 0.5

If we compare the frequencies observed for DPPC on a 1.5 M NaI solution (**Table 6-8**) and those observed for DPPC on pure water (**Table 6-7**) we notice that the stretching vibrations of the symmetric and antisymmetric CH_2 bands are increased up to 25 mN/m in the presence of I^-, indicating that the order of the hydrocarbon chains is decreased with respect to that of DPPC molecules on pure water. As a result, a higher content of gauche conformations are formed at the air-electrolyte interface. This is a further proof that I^- ions in the subphase enhance the stability of the disordered LE phase of DPPC monolayers and as a result the LE/LC phase transition pressure in the DPPC monolayer increases with increasing concentration of I^- ions. This is also shown in **Figure 6-21** where at high salt concentration

the transition observed between LE/LC phase is smeared over a larger pressure range. At higher lateral pressures e.g. π = 35 – 45 mN/m, the same stretching frequencies (hence the same conformation of the alkyl chains) as on pure water (all-trans conformation) are observed. *This observation suggests that I⁻ anions do not affect the LC phase, which is recovered unchanged at high pressures.*

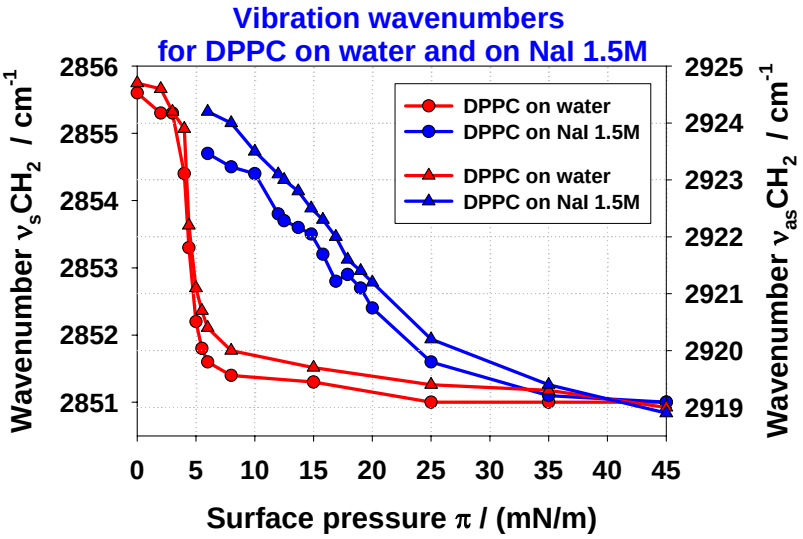

Figure 6-21. Surface pressure versus frequency of the CH_2 symmetrical (left axis, circles) and asymmetrical (right axis, triangles) stretching vibrations of DPPC monolayer on water and on NaI salt solution of concentration 1.5 M. The lines are drawn to guide the eye; s-polarized light at 40° normal to the surface was used

The above observations are supported not only by the change of the stretching vibrations but also by the change of the intensity of the vibrational bands which is decreased in presence of NaI salt solution compared to that of DPPC on pure water at the same surface pressure (e.g. π = 15 mN/m) as shown in **Figure 6-22**. Both the CH_2 and PO_2 vibrational bands weaken in intensity for 1.5 M NaI as the subphase. The decrease of the reflectance-absorbance intensity and the broadening of the peaks indicate a disordered configurational state of the chains and thus the peak maxima are shifted to higher frequency values. The same behaviour is observed at all the surface pressures studied.

An additional observation is that the asymmetric $\nu_{as}PO_2^-$ stretching frequency at ca. 1230 cm^{-1} decreases slightly in the presence of I^- indicating an increase in the average hydration of the phosphate group. Similar results were obtained by **Hunt et al. 1989** for DPPC monolayers in

the presence of Ca^{2+} and Pr^{3+} cations in the subphase where the frequency shift of the phosphate stretching band was explained as cation – induced hydrogen bond disruption.

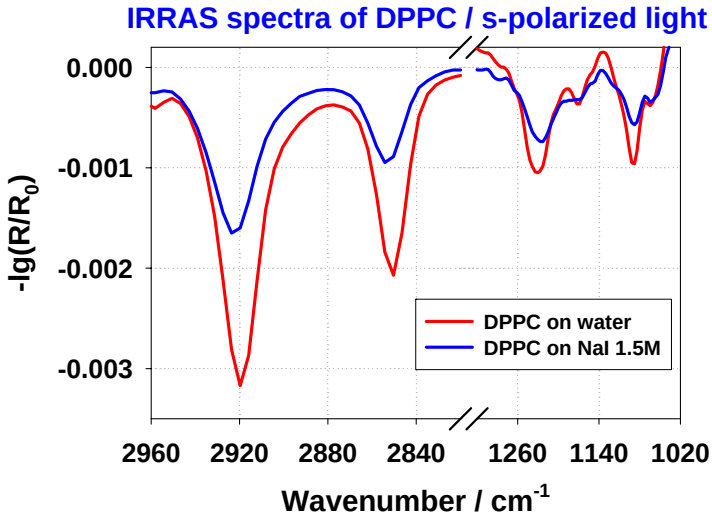

Figure 6-22. IRRAS spectra of the 1000 – 3000 cm^{-1} region of DPPC monolayers on pure water and on NaI salt solution of concentration 1.5M at π = 15 mN/m and T = 20 °C. s-polarized light at 40 ° normal to the surface was used

6.6 Conclusions on the monolayer results

The presence of electrolytes in the subphase was found to increase the surface pressure at a fixed area per molecule, indicating a stabilization of the liquid-expanded phase of the monolayer. This increase is different for different anions and different electrolyte concentrations following the Hofmeister anion series. Brewster angle microscopy has shown that the shape of the LC phase domains is not strongly affected by the electrolytes. The domains become rather more rounded than elongated, implying that the electrostatic component, which determines their shape, decreases in the presence of salt. This can be understood as a screening effect, and it suggests that anions do not bind to the LC domains. X-Ray diffraction and Infrared Spectroscopy experiments show that moderate concentrations of the anions Br^- and I^-, with increasing chaotropic behavior (Br^- is less chaotropic than I^-), do not significantly change the conformation and packing properties of the hydrocarbon chains. The lattice parameters and the ordering of the lipid molecules in the liquid-condensed phase remain essentially unaffected even at quite high electrolyte concentrations. The alteration of the chain packing found for high concentrations of NaI (1.5 M) can be explained by the

formation of iodine in the subphase through a radical-mediated oxidation reaction and is not the result of electrostatic interactions between I^- and the PC. The above observations are supported by the fact that on a highly concentrated NaI subphase the proportion of gauche conformers in the alkyl chains is much enhanced at low pressure, but as the surface pressure increases the effect is reduced reaching the behavior of the LC phase of DPPC on pure water. These findings suggest that anions partition into or bind to the looser liquid-expanded phase, thus providing entropic stabilization of that phase, but do not penetrate into or bind to the domains of the liquid-condensed phase. This intriguing result is discussed below in terms of the possible modes of interaction of anions with lipid interfaces.

6.7 Fitting the surface pressure isotherms

6.7.1 Local binding model results

The difference between the surface pressure over an electrolyte solution, π_{tot}, and that over pure water, π_{water}, at the same area per molecule, is a measurable quantity and provides the pure electrostatic contribution, $\Delta\pi_{el}$, to the surface pressure due to the presence of an electrolyte in the subphase. These $\Delta\pi_{el}$ for various concentrations of several electrolytes at 85 $Å^2$ per molecule are summarized in **Table 6-9**. **Figure 6-23** also presents the tabulated results in a graphical way.

Table 6-9. $\Delta\pi_{el}$ of various ions at different concentrations

$\Delta\pi_{el}$ / (mN/m)							
Concentration / M	**NaCl**	**NaBr**	**$NaNO_3$**	**NaI**	**$NaBF_4$**	**$NaClO_4$**	**NaSCN**
0.1	0.58	0.62	0.86	1.1	1.50	1.85	2.73
0.25	1.20	1.34	1.87	2.0	2.75	3.26	4.40
0.5	1.90	2.3	3.10	3.6	4.40	5.4	6.20
0.75	----	3.1	----	----	----	----	----
1.0	----	3.7	----	----	----	----	----
1.25	----	4.2	----	----	----	----	----
1.5	----	4.6	----	8.3	----	----	----

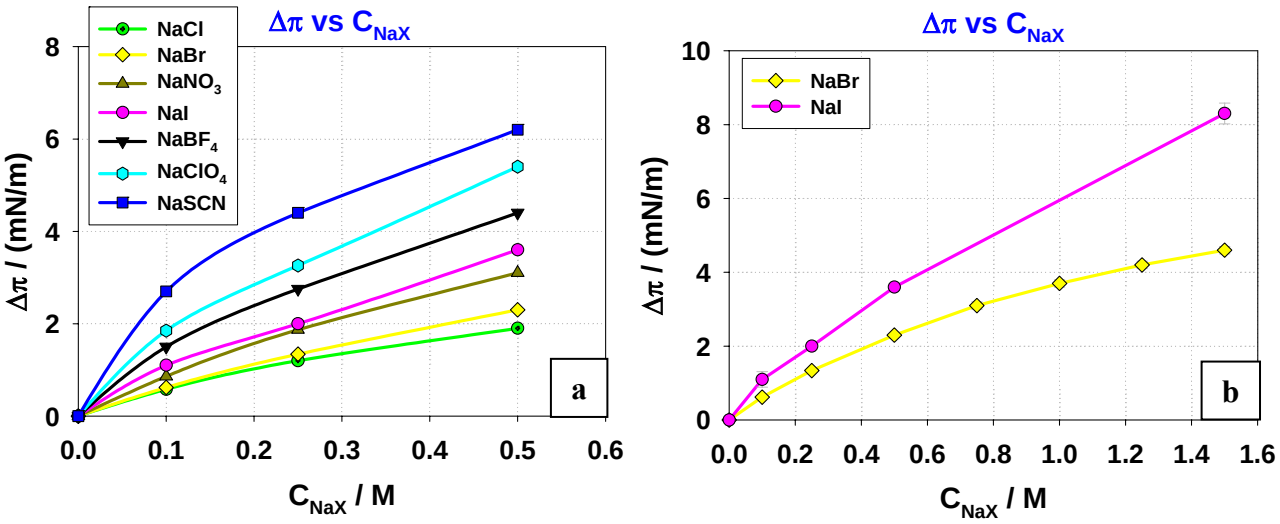

Figure 6-23. $\Delta\pi_{ele}$ as a function of the salt concentration in the subphase (a). $\Delta\pi_{ele}$ as a function of the salt concentration of NaBr and NaI (b). Both figures are at A = 85 Å^2 / molecule and T = 22.0 ± 0.1°C

The plots of $\Delta\pi_{ele}$ vs anion concentration can be modeled using a binding model, which assumes that the anions bind to the headgroups of DPPC molecules that form the lipid monolayer at the air - water interface through a chemical reaction. An association constant, K, of the anions on the headgroups of DPPC can be deduced from such a model (see **Chapter 5**). The cations are assumed not to bind to the headgroups of DPPC.

Figures 6-24 to **6-30** show the fitting results on the Δπ – Concentration diagrams for NaCl, NaBr, $NaNO_3$, NaI, $NaBF_4$, $NaClO_4$, and NaSCN. From these figures it can be seen that a simple binding model of the anions on the headgroups of the DPPC molecules cannot explain the increase of surface pressure observed in the presence of NaX salt solutions in the subphase. The general observation is that for any value of K the fitting curves deviate from the experimental points, especially at high salt concentration where the electrostatic contribution is rapidly screened. In some cases the fitting curves may exhibit broad maxima. In contrast, experimental $\Delta\pi_{el}$ appears to increase steadily with concentration, indicating that a saturation of the headgroup plane (interface) with ions is not achieved even at very high concentrations.

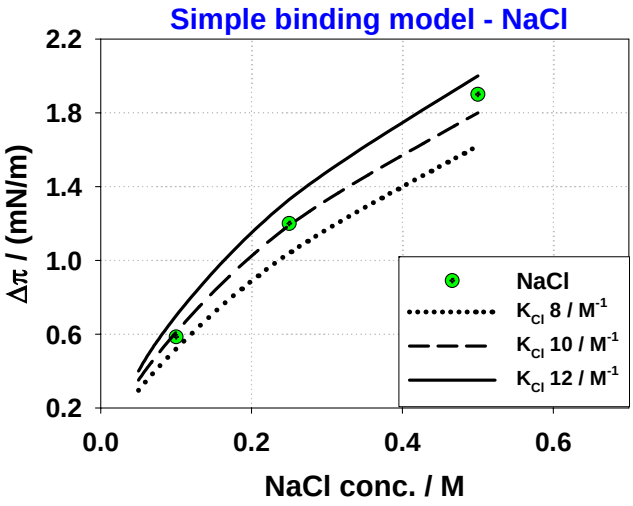

Figure 6-24. Fitting curves – Binding model for Cl^- anions on the headgroups of DPPC molecules at the air – water interface. Theoretical curves for three different binding constants are presented

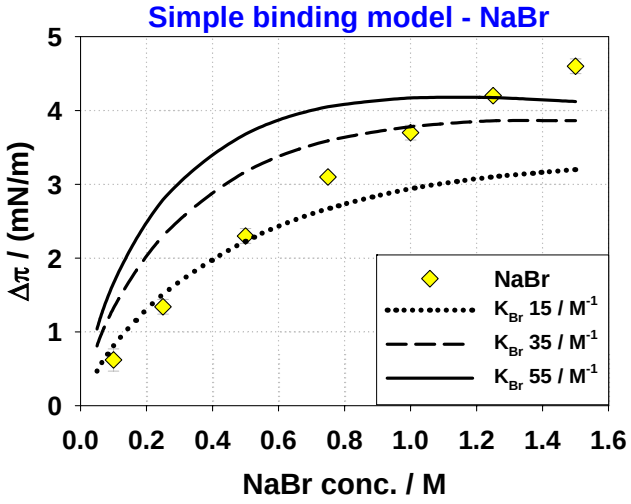

Figure 6-25. Fitting curves – Binding model for Br^- anions on the headgroups of DPPC molecules at the air – water interface. Theoretical curves for three different binding constants are presented

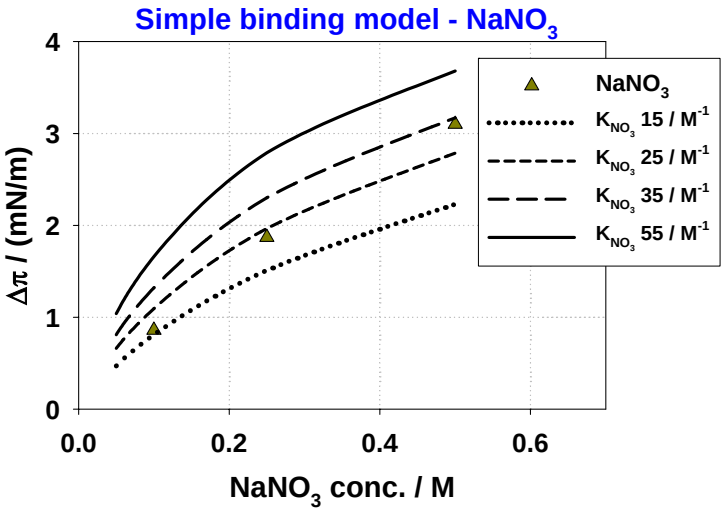

Figure 6-26. Fitting curves – Binding model for NO_3^- anions on the headgroups of DPPC molecules at the air – water interface. Theoretical curves for four different binding constants are presented

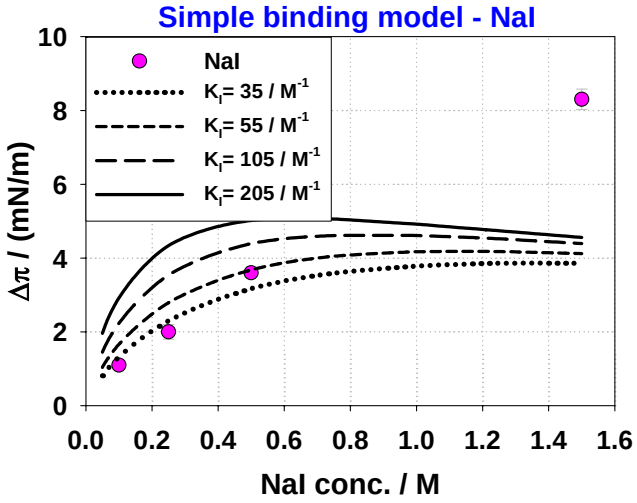

Figure 6-27. Fitting curves – Binding model for I^- anions on the headgroups of DPPC molecules at the air – water interface. Theoretical curves for large binding constants have a weak maximum

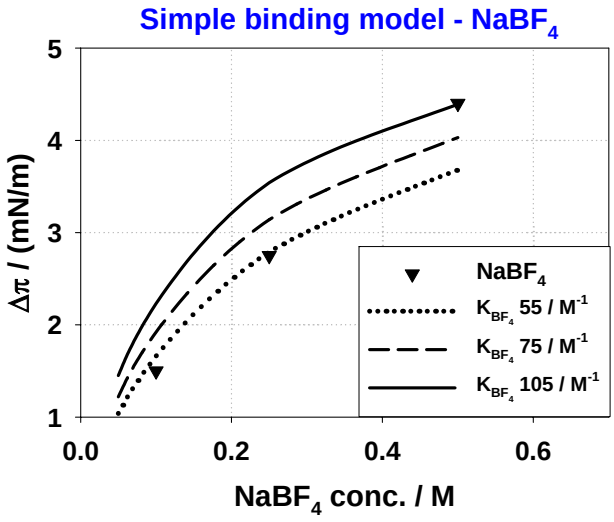

Figure 6-28. Fitting curves – Binding model for BF_4^- anions on the headgroups of DPPC molecules at the air – water interface. Theoretical curves for three different binding constants are presented

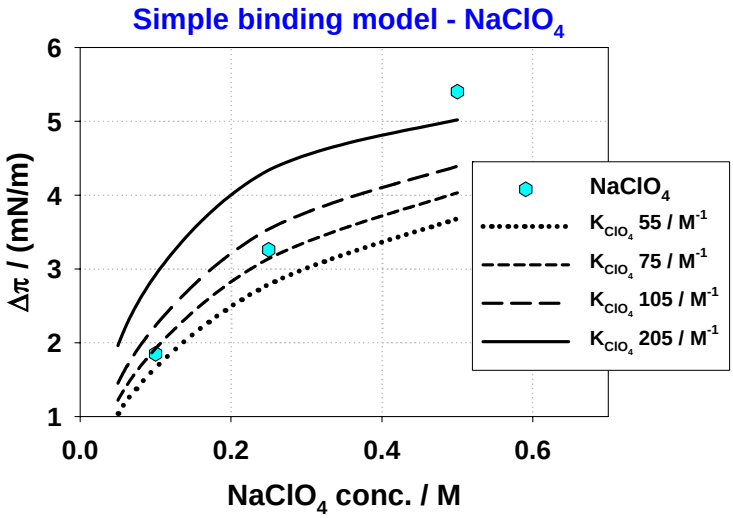

Figure 6-29. Fitting curves – Binding model for ClO_4^- anions on the headgroups of DPPC molecules at the air – water interface. High values of the binding constant cannot fit the data

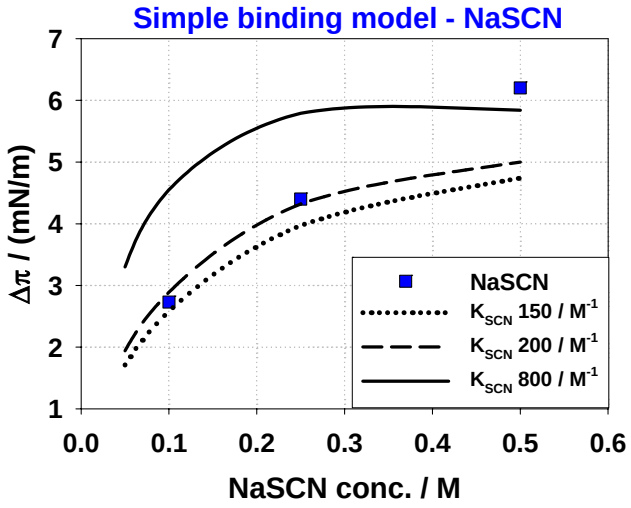

Figure 6-30. Fitting curves – Binding model for SCN^- anions on the headgroups of DPPC molecules at the air – water interface. Even extremely high values of the binding constant cannot fit the data

6.7.2 Diffuse layer model results

In this model, the anions in the subphase solution are assumed to penetrate the headgroup plane of DPPC molecules without specifically binding to the headgroups of the lipid. Cations are assumed not to enter this layer. The anions feel a unifrom attractive potential, U_-, within the lipid layer, and the surface pressure increment in the presence of salt is calculated as explained in **Chapter 5**, **Section 5.3.2**.

Figures 6-31 to **6-37** show the attempts that have been made to fit the $\Delta\pi$ – Concentration diagrams for NaCl, NaBr, $NaNO_3$, NaI, $NaBF_4$, $NaClO_4$, and NaSCN in the subphase using various values of the interaction potential U_-.

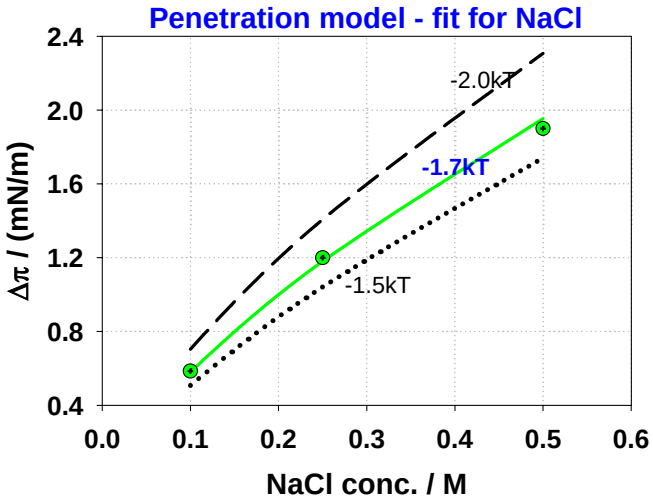

Figure 6-31. Fitting curves – Diffuse layer model for Cl^- anions on the headgroups of DPPC molecules at the air – water interface

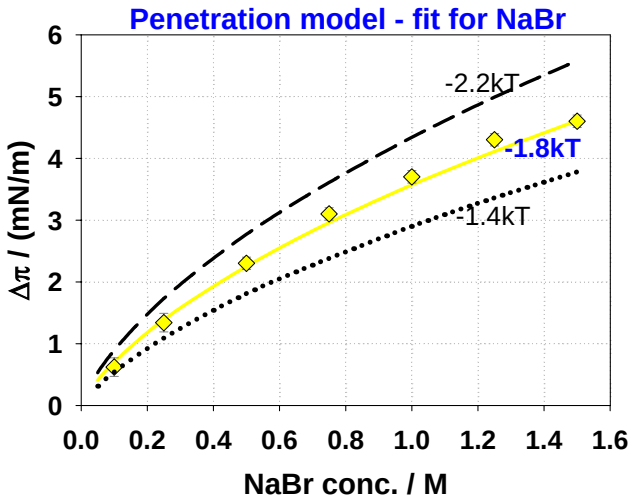

Figure 6-32. Fitting curves – Diffuse layer model for Br^- anions on the headgroups of DPPC molecules at the air – water interface

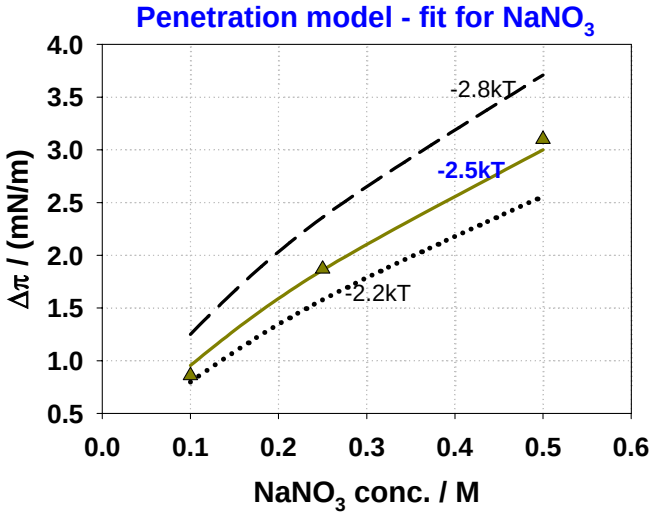

Figure 6-33. Fitting curves – Diffuse layer model for NO_3^- anions on the headgroups of DPPC molecules at the air – water interface

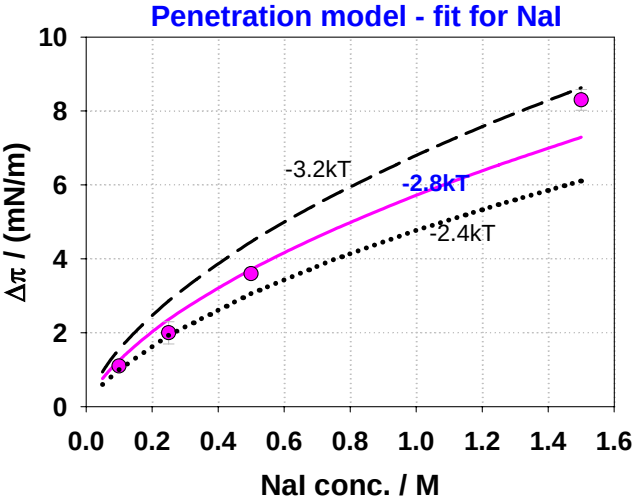

Figure 6-34. Fitting curves – Diffuse layer model for I^- anions on the headgroups of DPPC molecules at the air – water interface

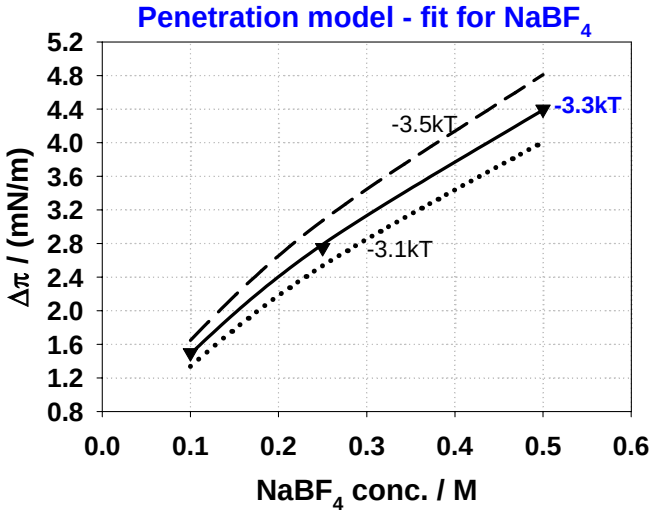

Figure 6-35. Fitting curves – Diffuse layer model for BF_4^- anions on the headgroups of DPPC molecules at the air – water interface

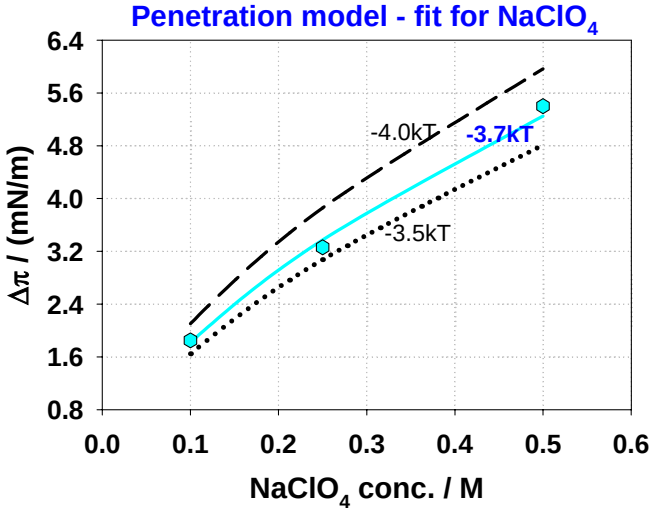

Figure 6-36. Fitting curves – Diffuse layer model for ClO_4^- anions on the headgroups of DPPC molecules at the air – water interface

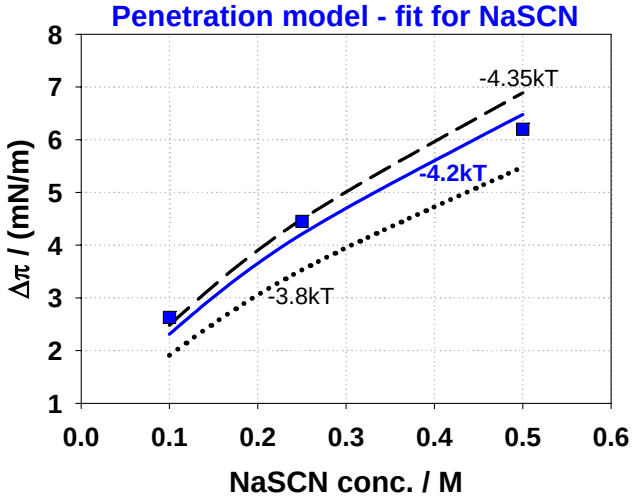

Figure 6-37. Fitting curves – Diffuse layer model for SCN^- anions on the headgroups of DPPC molecules at the air – water interface

Figures 6-31 to **6-37** demonstrate that a unique interaction potential U_- can be estimated for each anion with which the experimental data can be fitted quite well, even at high salt concentrations, in contrast to the binding model. Specifically, the $\Delta\pi$ – Concentration plot of DPPC in the presence of NaBr solution in the subphase for which experimental points at high salt concentration exist, can be fitted extremely well with an interaction potential of $U_- = -1.80 \pm 0.05$ kT. Likewise, the $\Delta\pi$ – Concentration plots of DPPC in the presence of NaCl, $NaNO_3$, NaI, $NaBF_4$, $NaClO_4$, and NaSCN can be fitted very well with the corresponding U_- given in **Table 6-10**.

Table 6-10. Interaction potentials of anions X^- partinioning in the DPPC lipid layer at the air-water interface

Interaction Potential / kT	
NaX Salt	**U_{X^-}**
NaCl	-1.70 ± 0.05
NaBr	-1.80 ± 0.05
$NaNO_3$	-2.50 ± 0.05
NaI	-2.80 ± 0.10
$NaBF_4$	-3.30 ± 0.05
$NaClO_4$	-3.70 ± 0.05
NaSCN	-4.20 ± 0.10

From **Figures 6-31** to **6-37** it is seen that data at high salt concentrations are crucial for the proper determination of binding parameters. Therefore in order to obtain more accurate results, experimental points at higher salt concentrations must be obtained for all the salts used.

In general, it can be concluded that the diffuse layer model is able to fit the experimental data in contrast to the binding model. This indicates that the X^- ions affect the properties of the DPPC monolayers at the air-water interface in ways that do not involve binding on the headgroups of the DPPC molecules. Our results imply rather that the LE phase is entropically stabilized through ionic partitioning in the interfacial lipid layer. The interaction potentials U_- obtained by the fitting analysis through the diffuse layer model can be correlated with other ion properties such as the size, R_P, the volume, V, the polarizability, α_p, the hydration free energy, ΔG_{hyd} or even with the coordination properties of the ions such as the ion softness as

it is shown in **Figures 6-38** to **6-42**. The values of the ionic properties are taken from **Table 1-1**.

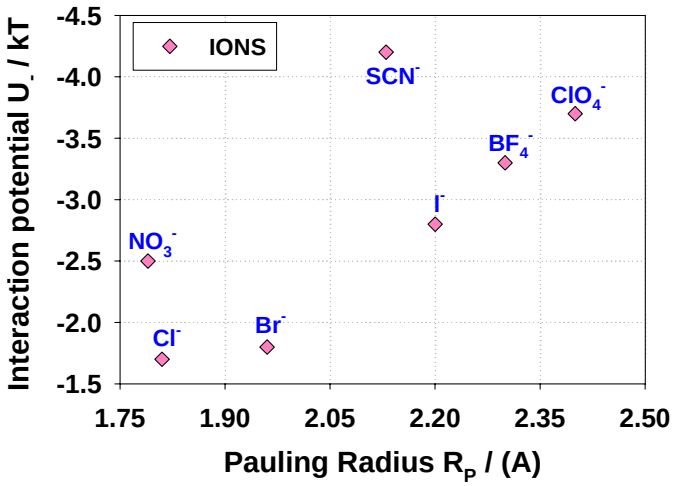

Figure 6-38. Correlation between the interaction potential, U_-, and the Pauling radius, R_P, of anions

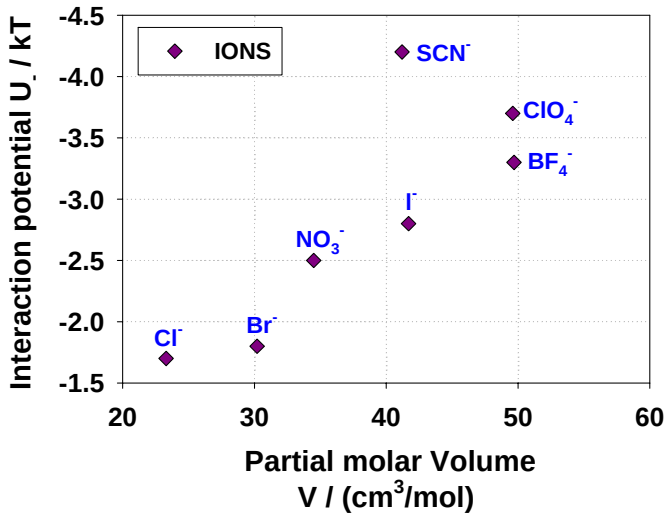

Figure 6-39. Correlation between the interaction potential, U_-, and the Partial molar volume, V, of anions

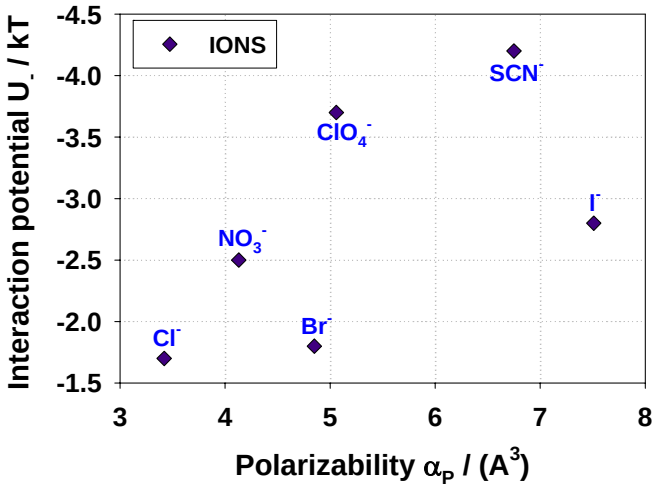

Figure 6-40. Correlation between the interaction potential, U-, and the Polarizability, α_p, of anions

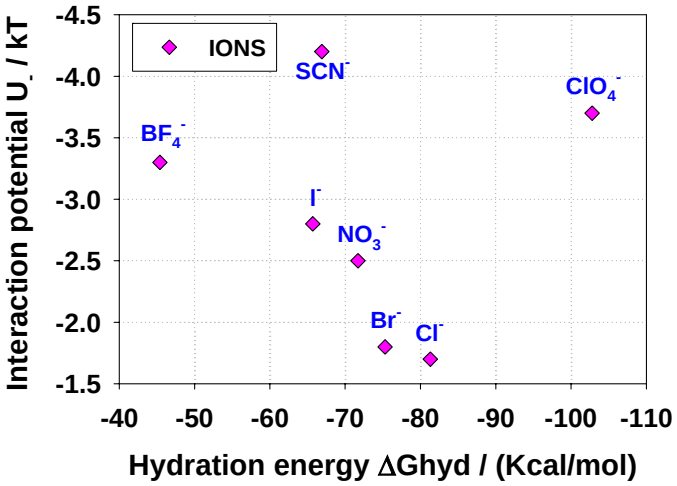

Figure 6-41. Correlation between the interaction potential, U-, and the Hydration free energy, ΔG_{hyd}, of anions

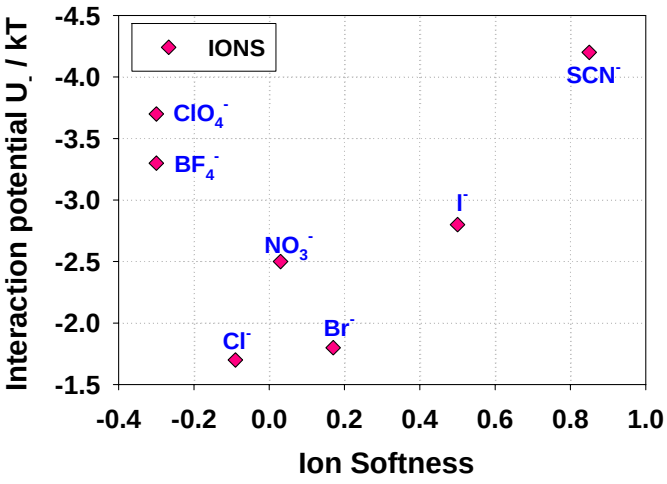

Figure 6-42. Correlation between the interaction potential, U-, and the softness of anions

From these figures it is seen that there is no good correlation between the interaction potential U_- and any of the important ionic physical properties. This indicates that the mechanism of the Hofmeister effect does not depend on a particular ionic property, but is more complex.

7 CHAPTER

BILAYER EXPERIMENTAL RESULTS

7.1 Introduction - Interactions between lipid bilayers

In order to analyze the logΠ – d_w curves, one must take into consideration the four different kinds of interactions that occur between lipid bilayers. These are: the hydration force, the Van der Waals attraction force, the electrostatic repulsion force and the steric repulsion force due to the thermal undulations of the bilayers. The aim is to estimate the relative contribution of each force to the total logΠ – d_w force curve. Fitting models are developed, with which it is attempted to fit the experimental results with a minimum of parameters. The efforts to fit the experimental curves of DPPC in water in the absence and in the presence of NaX salts are described in **Section 7.3.**

7.2 logΠ – d_w plots and Data Analysis

The data obtained by the combination of osmotic stress and small angle X-ray scattering are used to generate logΠ – d_w curves (see **Appendix II**). As an example, the results obtained for DPPC bilayers in water are shown in **Table 7-1** and **Table 7-2**. The maximum swelling of DPPC in water is shown in **Figure 7-1**.

Table 7-1. DPPC bilayer parameters in water at different osmotic pressures

Parameters							
LogΠ (Pa)	**3.85** ± 0.10	**4.20** ± 0.10	**4.63** ± 0.10	**5.29** ± 0.10	**5.55** ± 0.10	**6.05** ± 0.10	**6.70** ± 0.10
D (Å)	63.3 ± 0.5	62.4 ± 0.5	60.85 ± 0.5	57.1 ± 0.5	56.7 ± 0.5	54.7 ± 0.5	53.0 ± 0.5
φ_L%	51.6 ± 1.6	55.2 ± 1.0	61.0 ± 1.0	62.5 ± 0.8	65.7 ± 0.6	69.5 ± 0.7	74.3 ± 0.5
b_L^* (Å)	35.0 ± 1.0	35.2 ± 0.7	35.9 ± 0.7	36.2 ± 0.5	37.1 ± 0.4	38.1 ± 0.5	39.3 ± 0.4
d_w (Å)	28.3 ± 1.2	27.2 ± 0.8	24.95 ± 0.85	20.8 ± 0.7	19.6 ± 0.7	16.6 ± 0.7	13.7 ± 0.7
A (Å^2)	70.3 ± 2.0	70.0 ± 1.4	68.5 ± 1.3	67.8 ± 1.0	66.3 ± 0.8	64.6 ± 0.9	62.3 ± 0.7

b_L^* bilayer thickness corrected

Table 7-2. DPPC bilayer parameters at maximum swelling

Parameters	DPPC
Dmax (Å)	**66.3**
φmax%	**52.6**
$d_{w(max)}$ (Å)	**31.4**

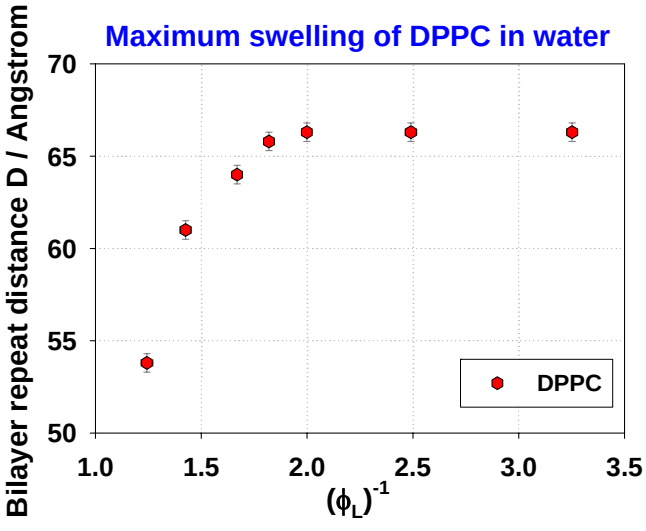

Figure 7-1. Maximum swelling of DPPC in water

The logΠ – d_w curve for DPPC in water is given in **Figure 7-2**. The experimental point at logΠ = 0 is the equilibrium separation at maximum swelling of DPPC bilayers in water, $d_{w(max)}$ = 31.4 Å (see **Appendix II**).

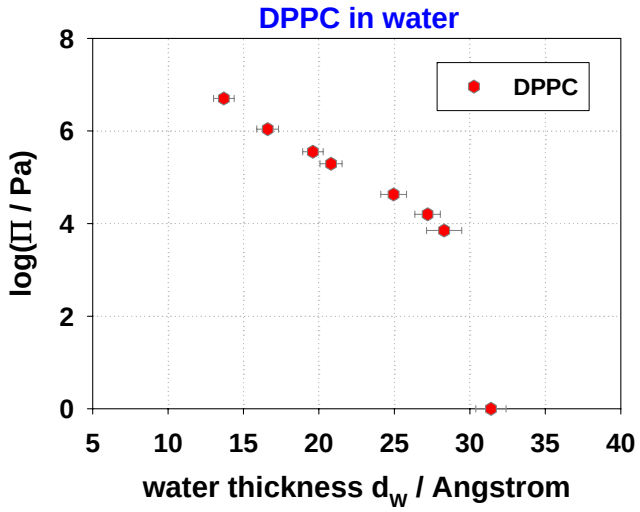

Figure 7-2. logΠ – d_w curve for DPPC in water

The corresponding maximum swelling curves for DPPC bilayers in NaX salt solutions, which are used to find $d_{w(max)}$ at logΠ = 0 (the equilibrium separation), are presented in **Figure 7-3** to **7-6**. The electrolytes used are NaBr, $NaNO_3$, NaI, NaSCN at concentrations 0.05M, 0.1M, and 0.5M. **Figure 7-3** and **Figure 7-4**, show that the experimental results are insensitive to the concentration of NaBr and $NaNO_3$, even at concentrations as high as 0.5M. Thus the maximum swelling of DPPC in the presence of NaBr and $NaNO_3$ is not influenced by salt concentration. Moreover, the maximum swelling of DPPC in the presence of NaBr and $NaNO_3$ is about the same as that of DPPC in pure water as shown in **Figure 7-7**. On the contrary, the maximum swelling of DPPC is greatly influenced by the presence of NaI and NaSCN as shown in **Figure 7-5** and **Figure 7-6**.

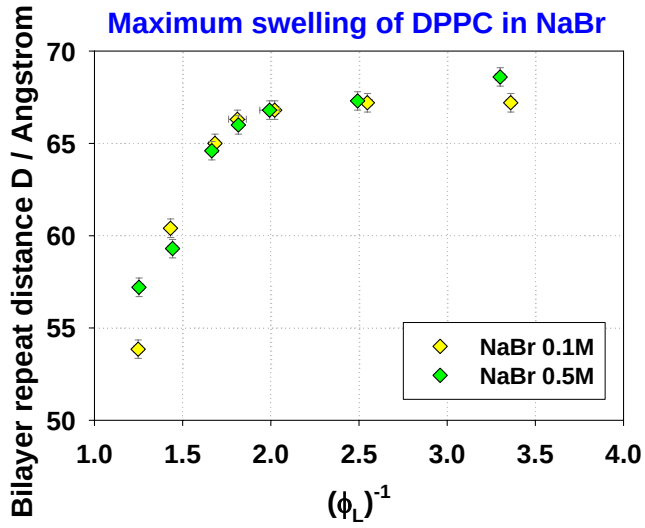

Figure 7-3. Maximum swelling of DPPC in the presence of NaBr at concentrations 0.1M and 0.5M

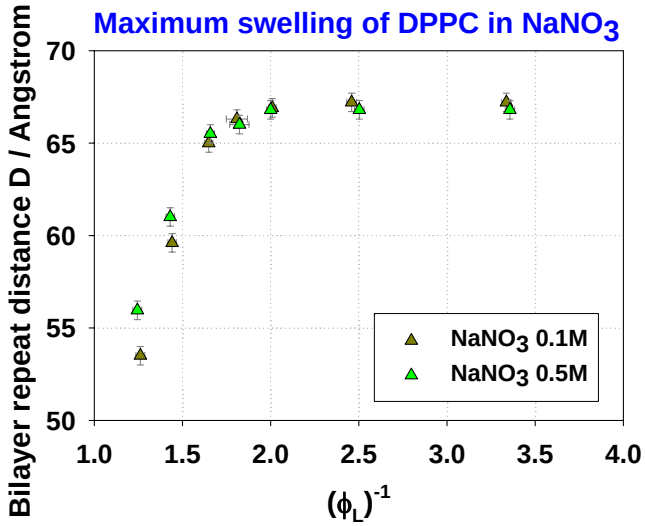

Figure 7-4. Maximum swelling of DPPC in the presence of $NaNO_3$ at concentrations 0.1M and 0.5M

In **Figure 7-5**, it is clearly seen that the concentration of the NaI salt solution affects the maximum swelling of DPPC bilayers. At 0.1M NaI appears to have the strongest effect on the maximum swelling of DPPC bilayers, which is found equal to φ_{max} = 39.2% for 0.1M NaI, while it is φ_{max} = 48.8% and φ_{max} = 46.5% for NaI concentrations of 0.05M and 0.5M respectively.

The NaSCN salt solution appears to have a similar effect on DPPC bilayers, as shown in **Figure 7-6**. In this case the maximum swelling (φ_{max}) increases and thus the equilibrium separation $d_{w(max)}$ decreases steadily with the concentration of NaSCN.

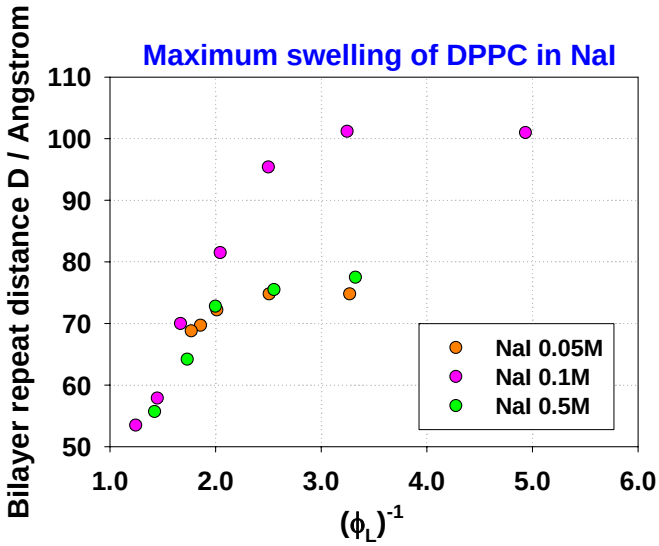

Figure 7-5. Maximum swelling of DPPC in the presence of NaI at concentrations 0.05M, 0.1M and 0.5M

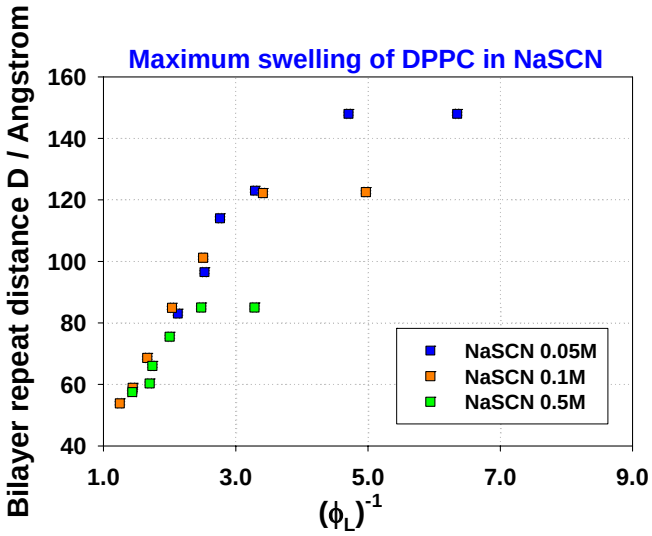

Figure 7-6. Maximum swelling of DPPC in the presence of NaSCN at concentrations 0.05M, 0.1M and 0.5M

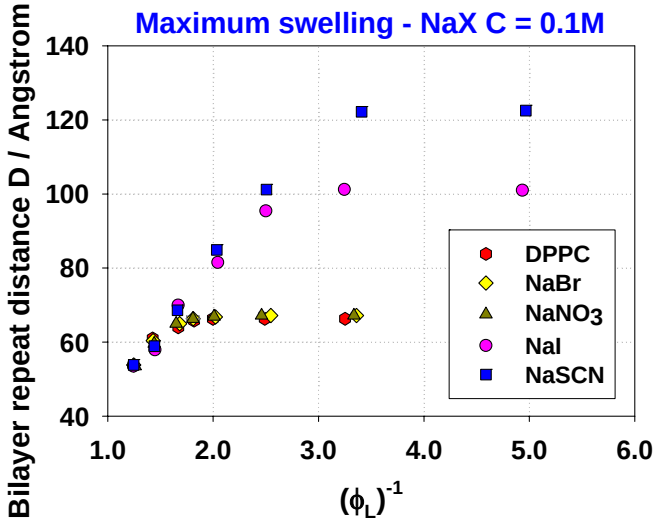

Figure 7-7. Maximum swelling of DPPC in the presence of NaX salt solutions of concentration C = 0.1M

The dissimilar effect of NaSCN and NaI on DPPC bilayers is discussed below. In general, the previous experimental results show that the maximum swelling is influenced both by the type of the anion and the concentration of the sodium salt solutions. The anion used influences the maximum swelling in the following order:

$$Br^- < NO_3^- < I^- < SCN^-$$

which is a direct Hofmeister series with the SCN^- having the largest effect on the equilibrium separation. This is shown more clearly in **Figure 7-7** for NaX solutions of concentration C = 0.1M. Similar results are obtained with NaX concentrations of 0.5M and are not shown here.

The influence of the concentration is more complex and depends on the type of the anion used. The effect of the concentration is discussed below.

Table 7-3 summarizes the main results for the maximum swelling of DPPC in the presence of the sodium salt solutions at various concentrations.

Table 7-3. Maximum swelling in NaX solutions

Concentration	Parameters	NaI	NaSCN		
C = 0.05M	Dmax (Å)	74.8	148.0		
	Φmax%	48.8	26.3		
	$d_{w(max)}$ (Å)	**38.3**	**109.05**		
C = 0.1M		**NaBr**	**$NaNO_3$**	**NaI**	**NaSCN**
	Dmax (Å)	67.2	67.2	101	122.5
	Φmax%	52.2	52.2	39.2	33.3
	$d_{w(max)}$ (Å)	**32.1**	**32.1**	**61.5**	**81.7**
C = 0.5M		**NaBr**	**$NaNO_3$**	**NaI**	**NaSCN**
	Dmax (Å)	68.0	66.8	77.5	85.6
	Φmax%	52.5	52.1	46.5	42.7
	$d_{w(max)}$ (Å)	**32.3**	**32.0**	**41.5**	**49.0**

The headgroup area, A, of DPPC in the presence of various NaX salt solutions was also calculated using the data obtained by the combination of osmotic stress and small angle X-ray scattering (see **Appendix II**). **Figures 7-8** to **7-10** show the dependence of the headgroup area of DPPC on the osmotic pressure exerted on the lipid bilayers for different electrolyte concentrations.

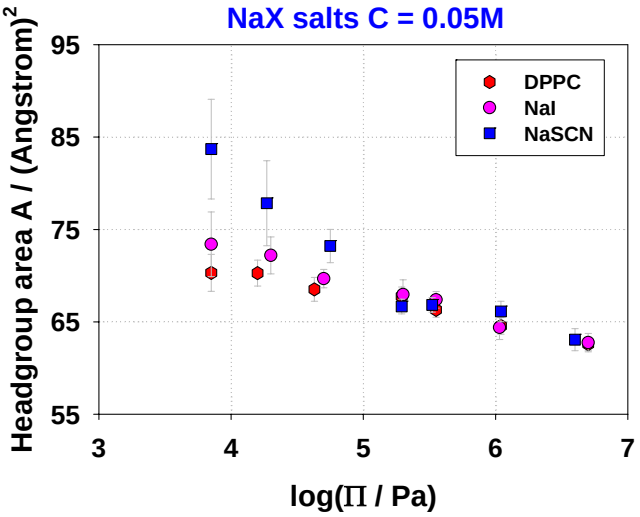

Figure 7-8. Headgroup area, A, vs the osmotic pressure, Π, exerted on DPPC bilayers in the presence of NaX solutions of concentration 0.05 M

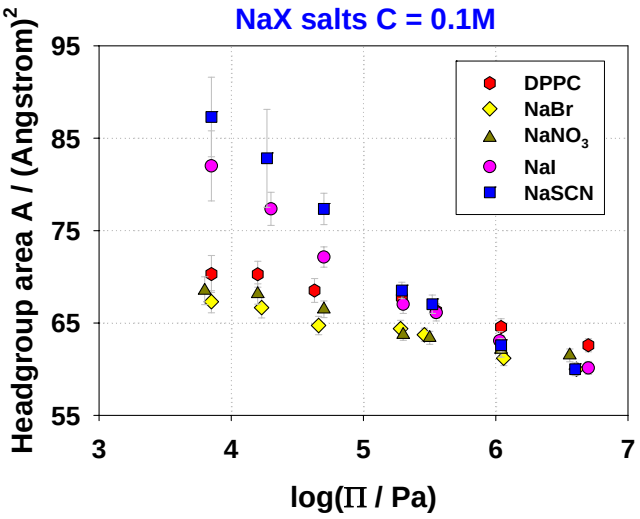

Figure 7-9. Headgroup area, A, vs the osmotic pressure, Π, exerted on DPPC bilayers in the presence of NaX solutions of concentration 0.1 M

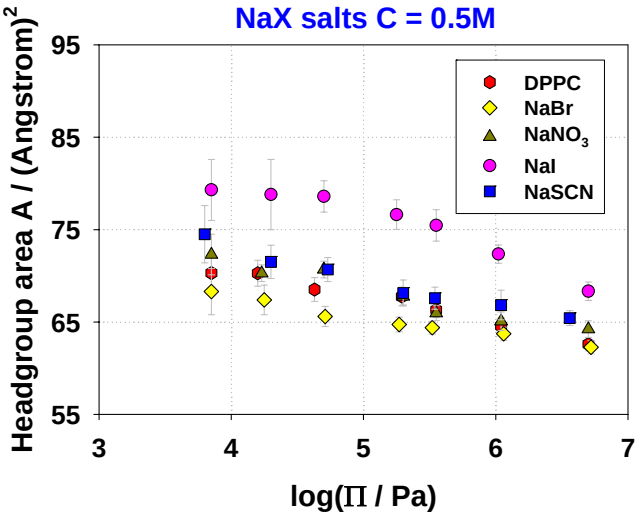

Figure 7-10. Headgroup area, A, vs the osmotic pressure, Π, exerted on DPPC bilayers in the presence of NaX solutions of concentration 0.5 M

From **Figures 7-8** to **7-10** it is seen that the headgroup area of DPPC molecules is affected by the type and concentration of anions used. The chaotropic anions I^- and SCN^- are those that have the strongest effect on the headgroup area, A, of DPPC while the ions Br^- and NO_3^- do not seem to have a great influence on A. The effect of the anions is more pronounced at small osmotic pressures. In addition, the headgroup area of DPPC appears to decrease as the

concentration of the electrolyte solution is increased. An exception to this observation is the change of the headgroup area of DPPC in the presence of NaI solution of concentration 0.5M.

Tables 7-4 to **7-7** contain the full osmotic stress – X-ray experimental results as they have been calculated (**Appendix II**) for DPPC in the presence of sodium salt solutions at various concentrations. The experimental point at logΠ = 0 corresponding to maximum swelling of the DPPC bilayers in salt solutions is given in **Table 7-3**.

Table 7-4. Bilayer parameters for DPPC in NaBr salt solutions at different osmotic pressures

Concentration	Parameters						
C = 0.1M	log(Π / Pa)	3.85 ± 0.10	4.23 ± 0.10	4.66 ± 0.10	5.28 ± 0.10	5.46 ± 0.10	6.06 ± 0.10	6.61 ± 0.10
	D (Å)	66.5 ± 0.5	65.3 ± 0.5	64.0 ± 0.5	59.2 ± 0.5	58.5 ± 0.5	56.5 ± 0.5	55.0 ± 0.5
	φ_L%	52.0 ± 0.8	56.55 ± 0.80	61.5 ± 0.7	62.9 ± 0.5	63.9 ± 0.6	71.2 ± 0.4	74.5 ± 0.4
	b_L^* (Å)	36.5 ± 0.6	36.9 ± 0.6	38.0 ± 0.5	38.2 ± 0.4	38.6 ± 0.5	40.2 ± 0.4	41.0 ± 0.4
	d_w (Å)	30.0 ± 0.8	28.4 ± 0.8	26.0 ± 0.7	21.0 ± 0.7	19.9 ± 0.7	16.3 ± 0.6	14.0 ± 0.6
	A (Å^2)	67.3 ± 1.2	66.7 ± 1.1	64.8 ± 1.0	64.4 ± 0.9	63.7 ± 0.7	61.2 ± 0.8	60.0 ± 0.6
C = 0.5M	log(Π / Pa)	3.85 ± 0.10	4.25 ± 0.10	4.71 ± 0.10	5.27 ± 0.10	5.52 ± 0.10	6.06 ± 0.10	6.72 ± 0.10
	D (Å)	65.9 ± 0.5	64.8 ± 0.5	62.7 ± 0.5	60.1 ± 0.5	58.5 ± 0.5	50.6 ± 0.5	53.4 ± 0.5
	φ_L%	51.6 ± 3.0	56.3 ± 1.2	62.3 ± 0.9	65.5 ± 0.5	66.8 ± 0.5	69.2 ± 0.4	74.2 ± 0.4
	b_L^* (Å)	36.0 ± 2.0	36.5 ± 0.8	37.5 ± 0.6	38.0 ± 0.4	38.2 ± 0.4	38.6 ± 0.4	39.5 ± 0.4
	d_w (Å)	29.9 ± 1.5	28.3 ± 1.0	25.2 ± 0.8	22.1 ± 0.6	20.3 ± 0.7	17.0 ± 0.6	13.9 ± 0.7
	A (Å^2)	68.3 ± 2.5	67.4 ± 1.6	65.6 ± 1.1	64.7 ± 0.8	64.4 ± 0.7	63.7 ± 0.7	62.3 ± 0.7

Table 7-5. Bilayer parameters for DPPC in $NaNO_3$ salt solutions at different osmotic pressures

Concentration	Parameters						
	log(Π / Pa)	3.80 ± 0.10	4.20 ± 0.10	4.70 ± 0.10	5.30 ± 0.10	5.50 ± 0.10	6.04 ± 0.10	6.56 ± 0.10
	D (Å)	66.5 ± 0.5	65.8 ± 0.5	64.0 ± 0.5	61.0 ± 0.5	58.6 ± 0.5	55.8 ± 0.5	54.8 ± 0.5

C = 0.1M	**φ_L%**	49.9 ± 1.1	54.4 ± 0.7	58.2 ± 0.6	66.1 ± 0.3	66.8 ± 0.5	70.9 ± 0.6	72.3 ± 0.5
	b_L^* (Å)	36.0 ± 0.8	36.1 ± 0.6	37.0 ± 0.5	38.6 ± 0.4	38.8 ± 0.4	39.6 ± 0.5	40.0 ± 0.4
	d_w (Å)	30.5 ± 0.9	29.7 ± 0.7	27.0 ± 0.7	22.4 ± 0.6	19.8 ± 0.7	16.2 ± 0.7	14.8 ± 0.7
	A (Å^2)	68.5 ± 1.5	68.1 ± 1.1	66.5 ± 0.9	63.7 ± 0.6	63.4 ± 0.7	62.2 ± 0.8	61.5 ± 0.7
C = 0.5M	**log(Π / Pa)**	3.85 ± 0.10	4.23 ± 0.10	4.70 ± 0.10	5.30 ± 0.10	5.55 ± 0.10	6.04 ± 0.10	6.70 ± 0.10
	D (Å)	65.0 ± 0.5	64.0 ± 0.5	61.1 ± 0.5	58.9 ± 0.5	56.0 ± 0.5	54.9 ± 0.5	53.1 ± 0.5
	φ_L%	50.2 ± 1.5	53.4 ± 0.5	56.2 ± 0.6	62.6 ± 0.6	67.0 ± 0.5	69.2 ± 0.8	71.1 ± 0.7
	b_L^* (Å)	34.0 ± 1.0	34.2 ± 0.4	34.8 ± 0.5	36.3 ± 0.5	37.3 ± 0.4	37.8 ± 0.5	38.3 ± 0.5
	d_w (Å)	31.0 ± 1.1	29.8 ± 0.7	26.3 ± 0.7	22.6 ± 0.7	18.7 ± 0.6	17.1 ± 0.7	14.8 ± 0.7
	A (Å^2)	72.3 ± 2.2	71.9 ± 0.9	70.6 ± 0.9	67.8 ± 0.9	66.0 ± 0.8	65.1 ± 1.0	64.3 ± 0.9

Table 7-6. Bilayer parameters for DPPC in NaI salt solutions at different osmotic pressures

Concentration	**Parameters**							
C = 0.05M	**log(Π / Pa)**	3.85 ± 0.10	4.30 ± 0.10	4.70 ± 0.10	5.30 ± 0.10	5.55 ± 0.10	6.03 ± 0.10	6.70 ± 0.10
	D (Å)	69.3 ± 0.5	66.3 ± 0.5	62.3 ± 0.5	58.3 ± 0.5	57.3 ± 0.5	54.0 ± 0.5	53.6 ± 0.5
	φ_L%	49.9 ± 1.1	54.4 ± 0.7	58.2 ± 0.6	66.1 ± 0.3	66.8 ± 0.5	70.9 ± 0.6	72.3 ± 0.5
	b_L^* (Å)	33.5 ± 1.4	34.0 ± 0.9	35.3 ± 0.5	36.2 ± 0.8	36.5 ± 0.5	38.2 ± 0.8	39.2 ± 0.6
	d_w (Å)	35.8 ± 1.5	32.3 ± 1.0	27.0 ± 0.7	22.1 ± 1.0	20.8 ± 0.7	15.8 ± 0.9	14.4 ± 0.8
	A (Å^2)	73.4 ± 3.5	72.2 ± 2.0	69.7 ± 1.0	68.0 ± 1.6	67.4 ± 0.9	64.4 ± 1.3	62.8 ± 1.0
C = 0.1M	**log(Π / Pa)**	3.85 ± 0.10	4.30 ± 0.10	4.60 ± 0.10	5.30 ± 0.10	5.55 ± 0.10	6.03 ± 0.10	6.70 ± 0.10
	D (Å)	72.0 ± 0.5	68.0 ± 0.5	66.0 ± 0.5	59.1 ± 0.5	57.1 ± 0.5	55.4 ± 0.5	54.5 ± 0.5
	φ_L%	36.7 ± 2.9	45.9 ± 1.0	53.3 ± 0.6	61.9 ± 0.8	63.6 ± 0.6	69.4 ± 0.9	75.5 ± 0.5
	b_L^* (Å)	30.0 ± 1.4	31.8 ± 0.7	34.1 ± 0.5	36.7 ± 0.6	37.2 ± 0.5	39.0 ± 0.6	40.9 ± 0.5
	d_w (Å)	42.0 ± 1.5	36.2 ± 0.9	31.9 ± 0.7	22.4 ± 0.7	19.9 ± 0.7	16.4 ± 0.8	13.6 ± 0.7

	A (Å^2)	82.0 ± 3.8	77.3 ± 1.8	72.1 ± 1.1	67.0 ± 1.0	66.1 ± 0.9	63.1 ± 1.0	60.2 ± 0.7
C = 0.5M	**log(Π / Pa)**	3.85 ± 0.10	4.30 ± 0.10	4.70 ± 0.10	5.25 ± 0.10	5.55 ± 0.10	6.02 ± 0.10	6.70 ± 0.10
	D (Å)	70.2 ± 0.5	64.8 ± 0.5	62.2 ± 0.5	57.5 ± 0.5	54.0 ± 0.5	52.5 ± 0.5	51.3 ± 0.5
	φ_L%	45.2 ± 1.5	46.2 ± 0.5	50.7 ± 0.6	55.3 ± 0.6	57.45 ± 0.5	62.8 ± 0.8	69.4 ± 0.7
	b_L^* (Å)	31.0 ± 1.3	31.2 ± 1.4	31.5 ± 0.7	32.1 ± 0.7	32.6 ± 0.7	34.0 ± 0.5	36.0 ± 0.5
	d_w (Å)	39.2 ± 1.4	33.6 ± 1.5	30.7 ± 0.8	25.4 ± 0.8	21.4 ± 0.9	18.5 ± 0.7	15.3 ± 0.7
	A (Å^2)	79.3 ± 3.3	78.8 ± 3.8	78.6 ± 1.7	76.6 ± 1.6	75.4 ± 1.7	72.3 ± 1.0	68.3 ± 1.0

Table 7-7. Bilayer parameters for DPPC in NaSCN salt solutions at different osmotic pressures

Concentration	**Parameters**							
C = 0.05M	**log(Π / Pa)**	3.85 ± 0.10	4.27 ± 0.10	4.75 ± 0.10	5.29 ± 0.10	5.52 ± 0.10	6.04 ± 0.10	6.60 ± 0.10
	D (Å)	92.0 ± 0.5	76.5 ± 0.5	63.5 ± 0.5	60.5 ± 0.5	59.0 ± 0.5	55.0 ± 0.5	53.2 ± 0.5
	φ_L%	32.0 ± 1.1	41.2 ± 0.7	49.8 ± 0.6	63.9 ± 0.3	63.3 ± 0.5	65.3 ± 0.6	72.9 ± 0.5
	b_L^* (Å)	29.4 ± 1.9	31.6 ± 1.9	33.6 ± 0.8	36.9 ± 0.5	36.8 ± 0.5	37.2 ± 0.6	39.0 ± 0.7
	d_w (Å)	62.6 ± 2.0	44.9 ± 2.0	29.9 ± 0.9	23.6 ± 0.7	22.2 ± 0.7	17.8 ± 0.8	14.2 ± 0.9
	A (Å^2)	83.7 ± 5.4	77.8 ± 4.6	73.2 ± 1.8	66.7 ± 0.8	66.8 ± 0.8	66.1 ± 1.1	63.1 ± 1.2
C = 0.1M	**log(Π / Pa)**	3.85 ± 0.10	4.27 ± 0.10	4.70 ± 0.10	5.29 ± 0.10	5.52 ± 0.10	6.04 ± 0.10	6.60 ± 0.10
	D (Å)	81.5 ± 0.5	72.5 ± 0.5	66.3 ± 0.5	61.2 ± 0.5	58.8 ± 0.5	56.5 ± 0.5	54.5 ± 0.5
	φ_L%	36.8 ± 2.9	41.1 ± 2.1	47.5 ± 1.0	59.9.9 ± 0.6	62.2 ± 0.7	70.0 ± 0.4	75.1 ± 0.5
	b_L^* (Å)	28.2 ± 1.4	29.7 ± 1.9	31.8 ± 0.7	35.9 ± 0.5	36.7 ± 0.5	39.3 ± 0.4	41.0 ± 0.5
	d_w (Å)	53.3 ± 1.5	42.8 ± 2.0	34.5 ± 0.8	25.3 ± 0.7	22.1 ± 0.7	17.2 ± 0.6	13.5 ± 0.7
	A (Å^2)	87.3 ± 4.3	82.8 ± 5.3	77.3 ± 1.7	68.5 ± 0.9	67.1 ± 1.0	62.6 ± 0.7	60.0 ± 0.7
	log(Π / Pa)	3.80 ± 0.10	4.30 ± 0.10	4.72 ± 0.10	5.29 ± 0.10	5.54 ± 0.10	6.03 ± 0.10	6.56 ± 0.10
	D (Å)	73.0 ± 0.5	69.5 ± 0.5	65.2 ± 0.5	60.5 ± 0.5	57.9 ± 0.5	54.5 ± 0.5	52.8 ± 0.5

C = 0.5M	**φ_L%**	37.55 ± 1.5	50.3 ± 0.5	53.1 ± 0.6	61.35 ± 0.6	63.5 ± 0.5	66.0 ± 0.8	70.9 ± 0.7
	b_L^* (Å)	33.0 ± 1.4	34.4 ± 0.9	34.8 ± 0.6	36.1 ± 0.7	36.4 ± 0.7	36.8 ± 0.9	37.6 ± 0.5
	d_w (Å)	40.0 ± 1.5	35.1 ± 1.0	30.4 ± 0.8	24.4 ± 0.9	21.5 ± 0.8	17.7 ± 1.0	15.2 ± 0.7
	A (Å^2)	74.5 ± 3.1	71.5 ± 1.8	70.7 ± 1.3	68.2 ± 1.4	67.6 ± 1.2	66.8 ± 1.6	65.4 ± 0.8

Using the experimental results from the above tables, we generate the logΠ – d_w curves for DPPC (**Figures 7-11** to **7-13**). **Figure 7-11** shows the experimental results of DPPC in NaI and NaSCN salt solutions of concentration C = 0.05M compared to DPPC in water. Likewise, **Figure 7-12** and **Figure 7-13** show the experimental results of DPPC in NaBr, $NaNO_3$, NaI and NaSCN of concentration C = 0.1M and C = 0.5M respectively. Each figure is plotted twice, once with and once without the experimental point at equilibrium separation (logΠ = 0) for better reading of the results.

Generally, we observe that the water bilayer separation (d_w) (for the same osmotic pressure) increases when salts are present (at all salt concentrations). The change of d_w is more pronounced at small osmotic pressures and diminishes as the osmotic pressure applied to the bilayers increases. This implies that the hydration force between DPPC bilayers in pure water and in the presence of salts is similar. The increase of the water bilayer separation appears to depend on the type of anion that is used in the sodium salts. SCN^- has the strongest effect on d_w, while Br^- has the smallest effect at all concentrations. *The effect of the anions on d_w follows the Hofmeister series*.

Furthermore, the increase of the water bilayer separation (d_w) depends on the concentration of the sodium salt solutions as is shown more clearly in **Figure 7-14** to **7-16** and **Figure 7-17**.

In the presence of NaBr and $NaNO_3$, salt solutions (**Figure 7-14** and **Figure 7-15**) the water bilayer separation (d_w) does not seem to change by varying the salt concentration. d_w increases in the presence of NaBr and $NaNO_3$ in comparison with that in water, but it is not influenced by the concentration of these salts. **Figure 7-16** shows the influence of NaI on d_w at three concentrations, 0.05M, 0.1M and 0.5M. Interestingly, NaI is more effective at a concentration of 0.1M while 0.05M provides the smallest effect and 0.5M gives intermediate results. This apparent inconsistency is discussed below.

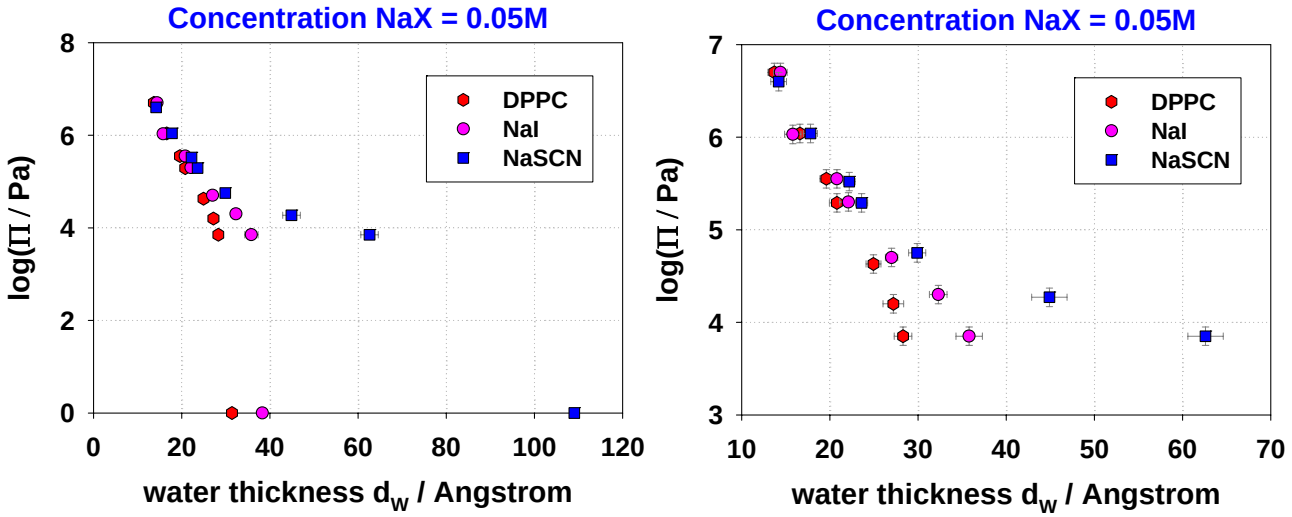

Figure 7-11. logΠ – d_w curves of DPPC in the presence of NaI and NaSCN at concentration C = 0.05M

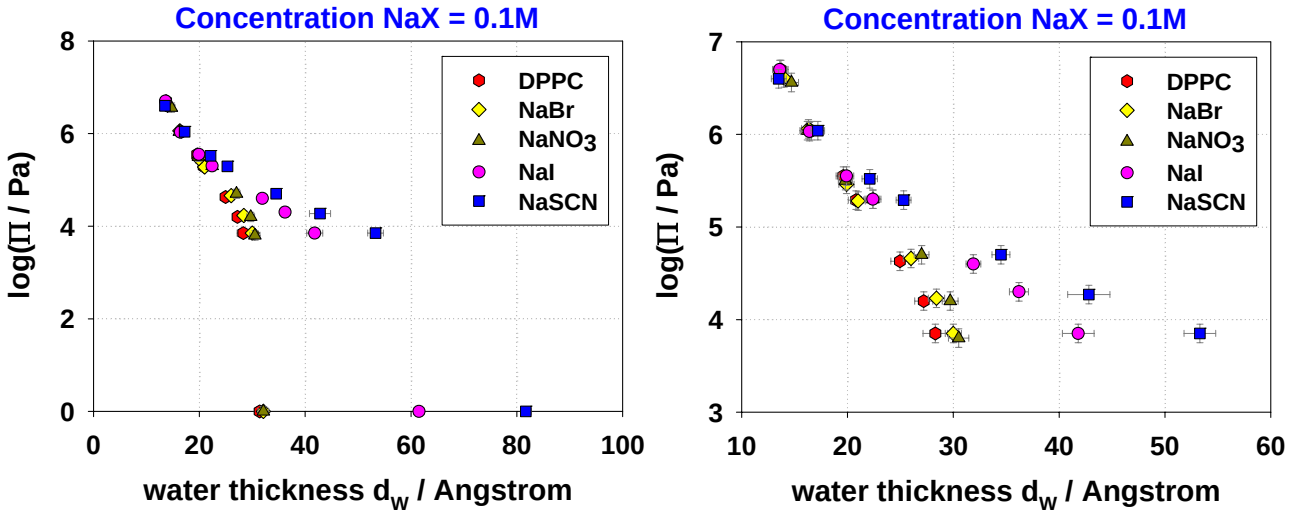

Figure 7-12. logΠ – d_w curves of DPPC in the presence of NaBr, $NaNO_3$, NaI and NaSCN at concentration C = 0.1M

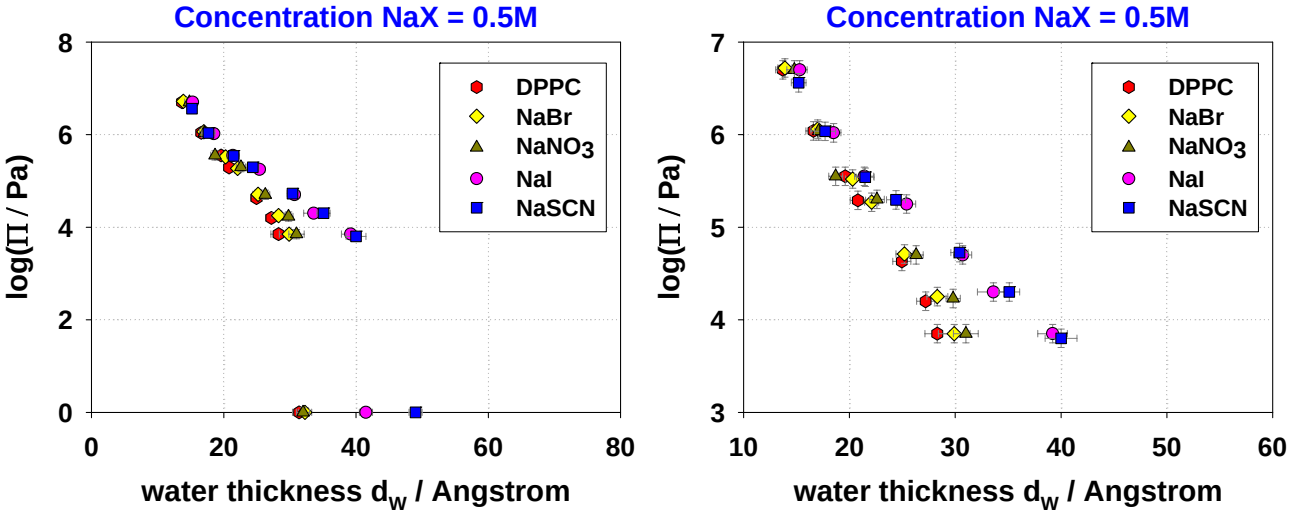

Figure 7-13. logΠ – d_w curves of DPPC in the presence of NaBr, $NaNO_3$, NaI and NaSCN at concentration C = 0.5M

Similar results are obtained in the presence of NaSCN. The influence of NaSCN concentration on d_w is shown in **Figure 7-17**. The concentrations used were 0.05M, 0.1M and 0.5M. The situation is a little different for NaSCN, since the influence of the salt on d_w *decreases* upon *increasing* the concentration from 0.05M to 0.5M. In Chapter 3, Section 3.5.2, a schematic diagram of $\log\Pi - d_w$ was presented, which gives information on the forces existing between the bilayers. It was shown there that the difference between the force curve ($\log\Pi - d_w$) for a neutral bilayer and that for a charged bilayer is due to the presence of an electrostatic, double-layer repulsion, which stems either from the adsorption of ions on the lipid headgroups or from the presence of ionizable groups. We believe that the difference between the force curves of DPPC in water and in the presence of NaX solutions, especially in the cases of NaI and NaSCN, is largely due to an electrostatic repulsive force created by the adsorption of Br^-, NO_3^-, I^-, and SCN^- on the DPPC headgroups. *The strength of this electrostatic repulsive force*, that is the difference between the $\log\Pi - d_w$ curves of DPPC in water and in the presence of NaX solutions, *depends on the electrolyte concentration*.

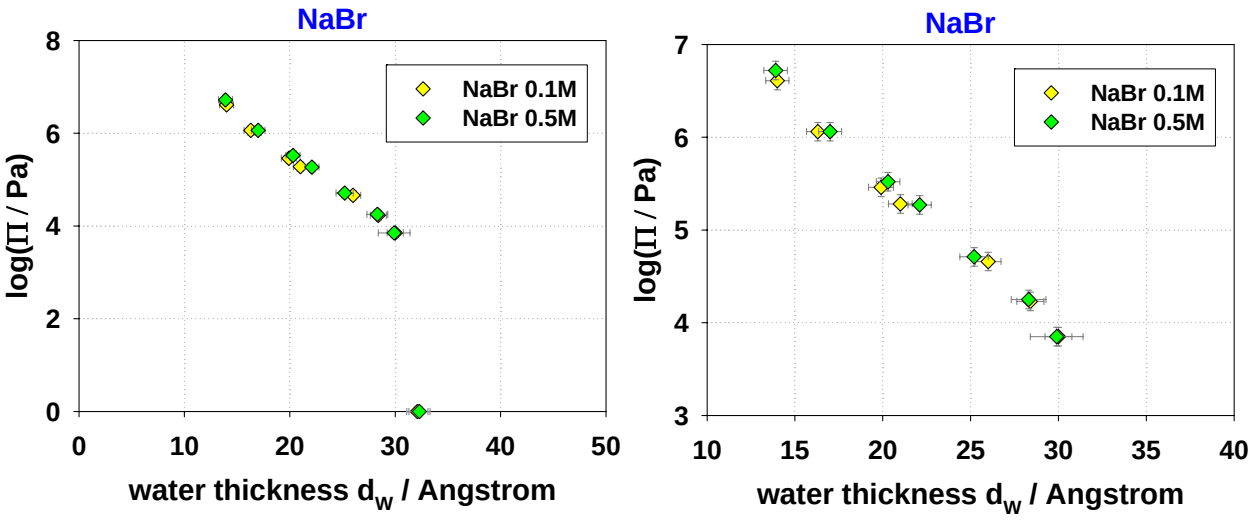

Figure 7-14. $\log\Pi - d_w$ of DPPC in the presence of NaBr at concentration 0.1M and 0.5M

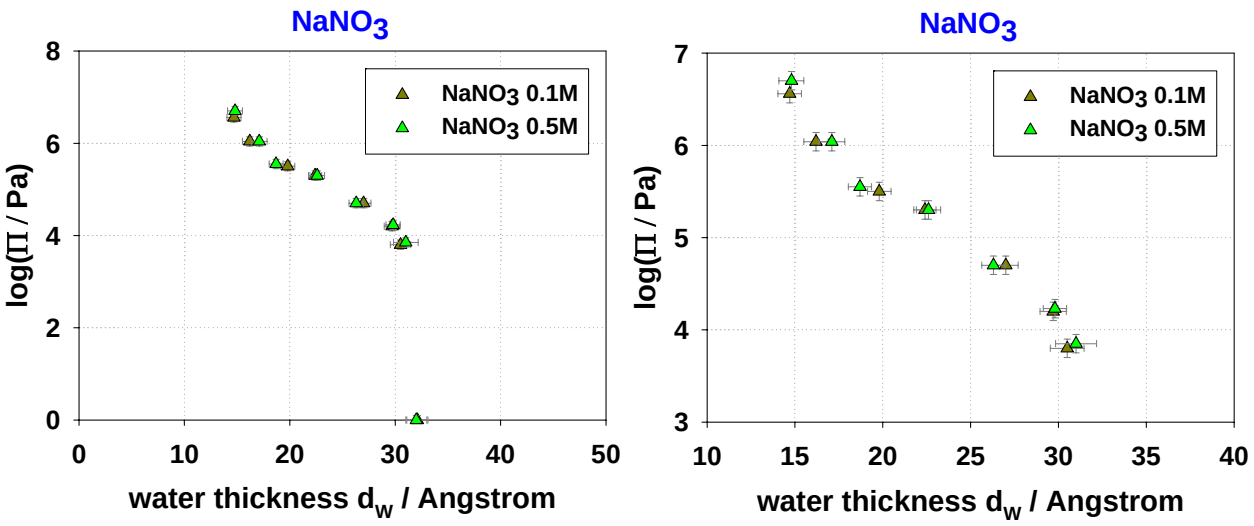

Figure 7-15. logΠ – d_w of DPPC in the presence of $NaNO_3$ at concentration 0.1M and 0.5M

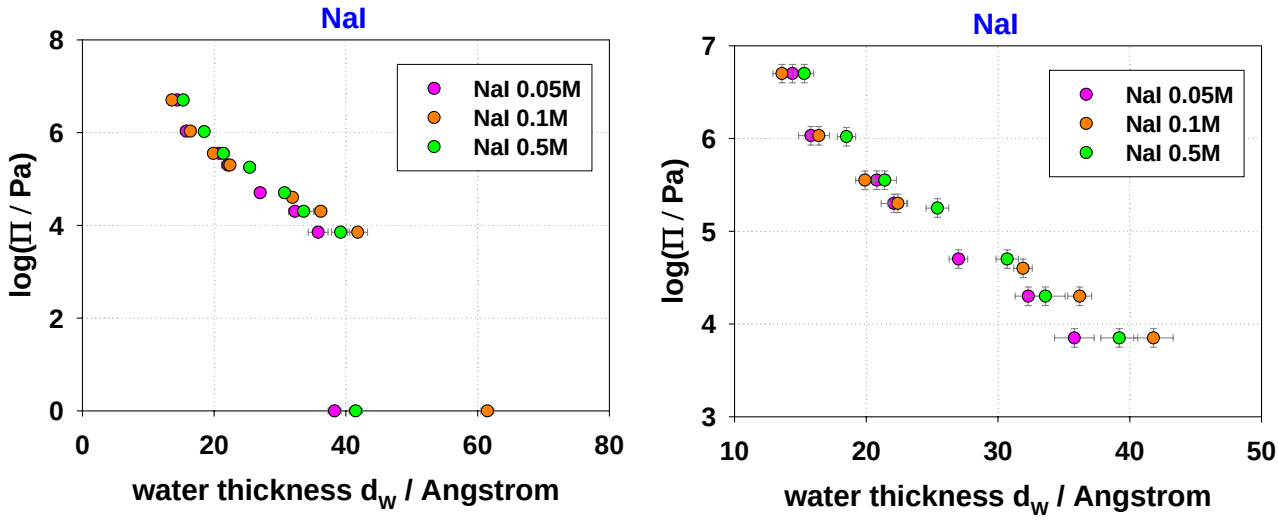

Figure 7-16. logΠ – d_w of DPPC in the presence of NaI at concentration 0.05M, 0.1M and 0.5M

As discussed before, NaI and NaSCN, have slightly different effects on d_w as a function of their concentration. This complex behaviour may be explained by two phenomena that determine the electrostatic repulsive force between the bilayers; these are ion binding and ion screening. The influence of NaI on d_w at a concentration of 0.05M is weak because the adsorption of I^- on the DPPC headgroups is still small. In contrast, the influence of NaI on d_w at a concentration of 0.5M is weak due to high screening. As a result, there will be an intermediate concentration for which the repulsion between the DPPC bilayers is highest.

NaSCN salt behaves differently, with the electrostatic repulsion decreasing consistently with increasing salt concentration.

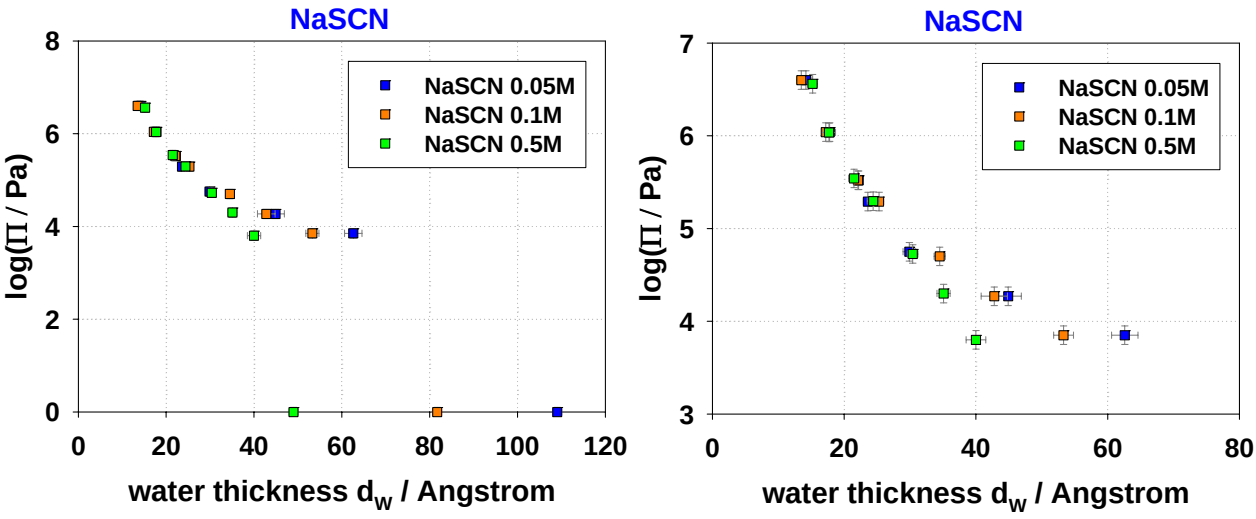

Figure 7-17. logΠ – d_w of DPPC in the presence of NaSCN at concentration 0.05M, 0.1M and 0.5M

This behaviour may be explained by the very strong binding of SCN^- on the DPPC headgroups. Even at small concentration (0.05M) the SCN^- ions bind more strongly to the DPPC molecules than the I^- ions, and thus the electrostatic repulsion that is generated is stronger than that observed in the presence of an equal concentration of I^-. As the concentration of NaSCN increases more SCN^- ions bind to the DPPC headgroups but apparently the increased binding is counterbalanced by the double-layer screening. It is possible that a maximum repulsive force between the bilayers might be observed for NaSCN concentrations lower than 0.05M, but such concentrations were not examined in our experiments.

The presence of salt was also found to influence the headgroup size of DPPC molecules by dehydration, especially in the presence of the less chaotropic ions, such as Br^-, as is observed in **Figures 7-8** to **7-10**. For this reason, the spacing of DPPC bilayers has been measured in a mixture of NaCl (less chaotropic) and NaI (chaotropic) salt solutions, as shown in **Figure 7-18**, in order to compare the effect of a strongly hydrophilic (Cl^-) and a strongly hydrophobic (I^-) ion on the structure of DPPC bilayers. A sequence of experiments was performed at a constant *total* [NaCl]+[NaI], changing the percentage of NaI from 0% to a 100%. The *total* salt concentration used was 0.1M and 0.5M.

Starting at 100% NaCl and adding NaI, we observe significant changes in the spacing at a percentage concentration of NaI larger than 20% in the solution. In addition, the water bilayer

separation, d_w, does not seem to follow a linear behaviour upon increasing the precentrage of NaI in the mixture. At a *total* salt concentration 0.5 M it appears to have a minimum value. Moreover, the effect on d_w, depends on the *total* salt concentration used. For example, as the total salt concentration *increases* the water bilayer separation *decreases* which can be attributed to the screening of the electrostatic repulsion between the lipid bilayers.

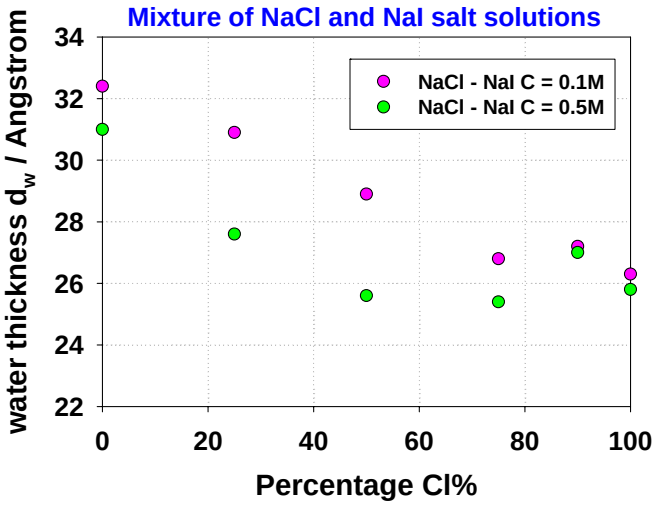

Figure 7-18. Water thickness of DPPC in a mixture of NaCl and NaI salt solutions at concentration 0.1M and 0.5M

The structure of the bilayers as a function of NaSCN concentration was also examined by Freeze Fracture Electron Microscopy since the presence of high SCN^- concentration in DPPC bilayers has been reported to induce an interdigitated phase (**Cunningham et al. 1986**). From **Figures 7-19** to **7-21**, it can be seen that the presence of NaSCN in DPPC bilayers even at a concentration of 0.5 M does not lead to an interdigitated phase. Instead, the ripple $P_{\beta'}$ phase is observed (**Meyer et al. 2001**). This phase is clearly observed at concentrations 0.05 M and 0.1 M, while at 0.5 M the ripple phase disappears. The main transition temperature from the liquid, L_α, to the ripple, $P_{\beta'}$, phase is 41 °C. It appears that during the handling stage of the samples they first pass through this transition before being frozen. However, it has been found by calorimetry (**Chapman et al. 1977; Cunningham et al. 1986; Sanderson et al. 1991**) that the presence of anions decrease the main transition temperature of phosphatidylcholine bilayers with SCN^- having the strongest effect. This is why in the presence of 0.5 M SCN^- the ripple phase is no longer observed.

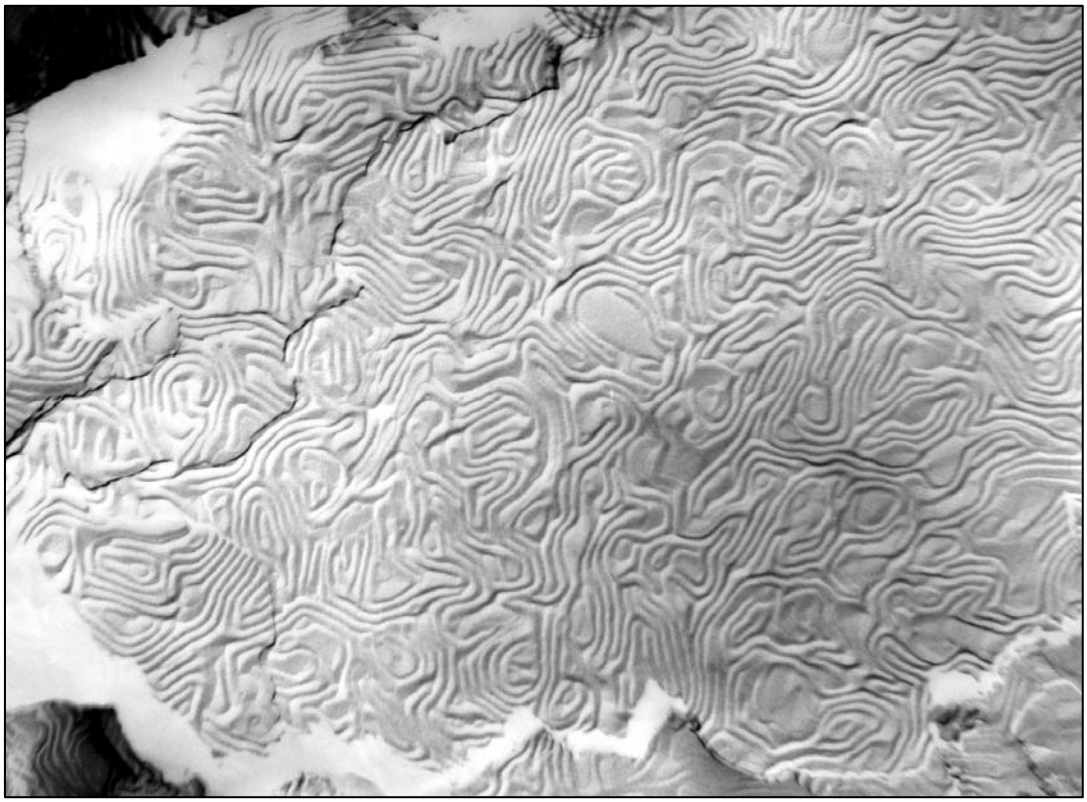

Figure 7-19. Freeze Fracture electron microscopy pictures of DPPC in 0.05M NaSCN Magnification x 22000

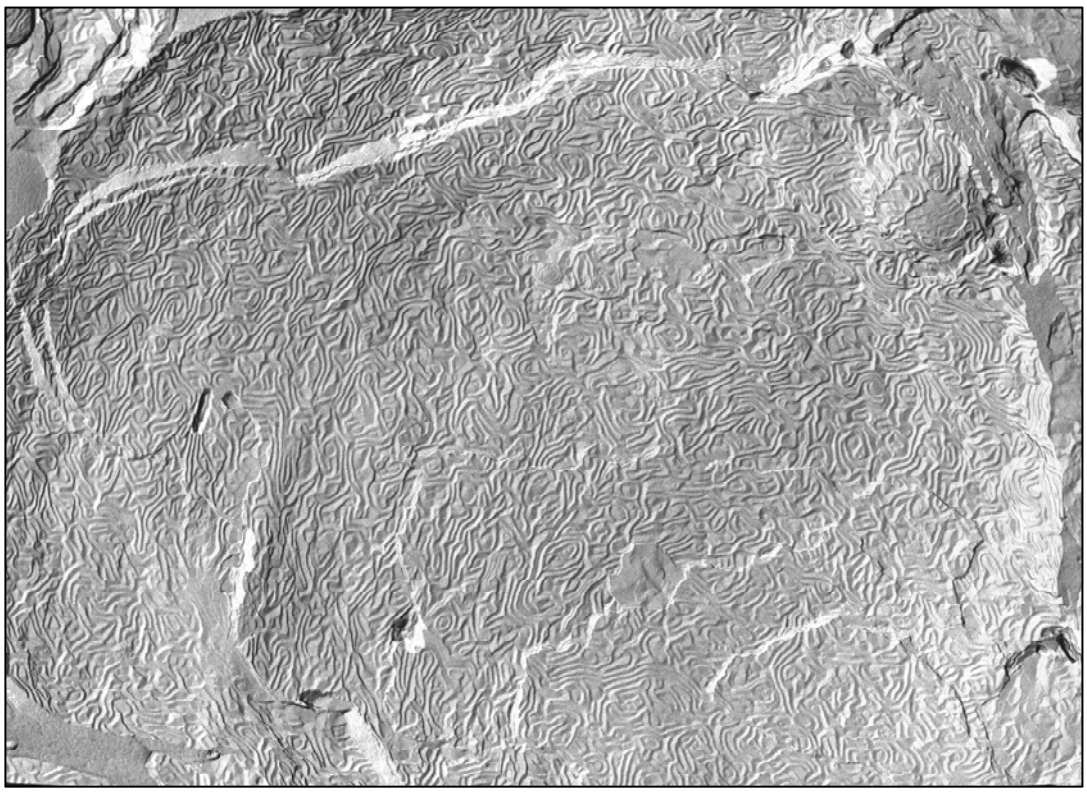

Figure 7-20. Freeze Fracture electron microscopy pictures of DPPC in 0.1M NaSCN Magnification x 13000

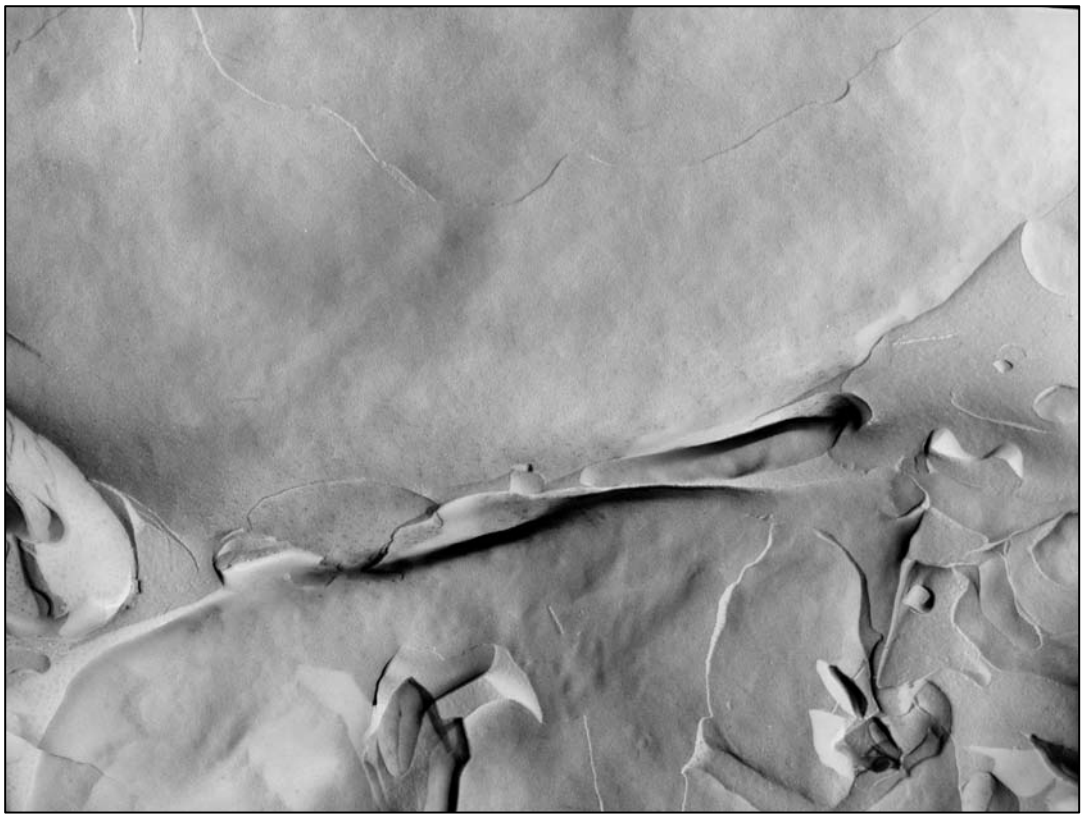

Figure 7-21. Freeze Fracture electron microscopy pictures of DPPC in 0.5M NaSCN Magnification x 13000

7.3 Fitting the osmotic pressure isotherms

7.3.1 Fitting the DPPC/Water isotherm

In order to fit the experimental results (logΠ – d_w data) of DPPC bilayers in the presence of NaX salts, it is important to fit first the isotherm of DPPC in pure water, which will be used as a reference. This allows the comparison with older literature results from the work of **Lis et al. 1982**, **Rand et al. 1989**, **McIntosh et al. 1993** and **Petrache et al. 1998**. The total osmotic pressure exerted between neutral phospholipid bilayers is given by the sum of the following interbilayer interactions (Hydration force, Van der Waals, and Undulation repulsive force) (see **Chapter 5**, **Section 5.4.1**):

$$\Pi = \Pi_{HYD} + \Pi_{UND} + \Pi_{VDW}$$

$$\Pi = P_0 \exp\left(-d_w/\lambda\right) + \frac{3\pi^2 (kT)^2}{128\kappa_c} \frac{1}{(d_w)^3} - \frac{A}{6\pi}\left[\frac{1}{(d_w^*)^3} + \frac{1}{(D+b_L)^3} - \frac{2}{(D)^3}\right] \qquad \textbf{Equation 7-1}$$

It is important to notice that there are two different ways to define the water bilayer separation d_w^* (**Figure 7-22**).

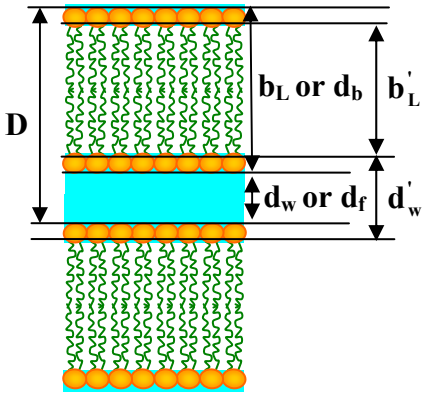

Figure 7-22. Definition of d_w, d_f and d_w'

A first assumption is that the lipid and water molecules pack into separate layers each characterized by its own Hamaker constant, and thus d_w^* is equal to d_w, the "real" water thickness as shown in **Figure 7-22**. d_w can be calculated by two different methods reported in

the literature: (i) one may calculate the lipid volume fraction φ_L which is related to the lipid bilayer thickness b_L and thus d_w is obtained using the expression $d_w = D - b_L$ where D is the repeat bilayer separation (see **Chapter 3**, **Section 3.6.6**), or (ii) one may construct an electron density profile of the bilayers whose peaks are related to the location of the lipid-water interfaces. The peak-to-peak distance plus a constant to include the polar group thickness is defined as the lipid bilayer thickness d_b. The remaining space is the water bilayer separation d_f. These alternative approaches of calculating the water bilayer separation (d_w or d_f) make a considerable difference in the way one estimates the distribution of water around the polar groups and therefore of bilayer separation and definition of bilayer contact. Alternatively, it can be assumed that the aqueous layer also includes the lipid headgroups, and thus d_w^* is equal to $d_w^{'}$ in **Figure 7-22**. In order to obtain $d_w^{'}$ and thus $b_L^{'}$ one must estimate the percentage of the molecular volume that is attributed to the headgroup in combination with the area per molecule so that the thickness of the headgroup region can be calculated and added to the known d_w that is estimated in advance as explained above. The two different ways to define the water bilayer separation influence only the profile of the Van der Waals interaction, since in the mathematical expressions for the hydration and undulation forces one uses the "real" thickness of the water layer, d_w. In this work both d_w and $d_w^{'}$ have been used to calculate the VDW interaction.

The results obtained by **Lis et al. 1982** for DPPC in water at T = 50°C are shown below.

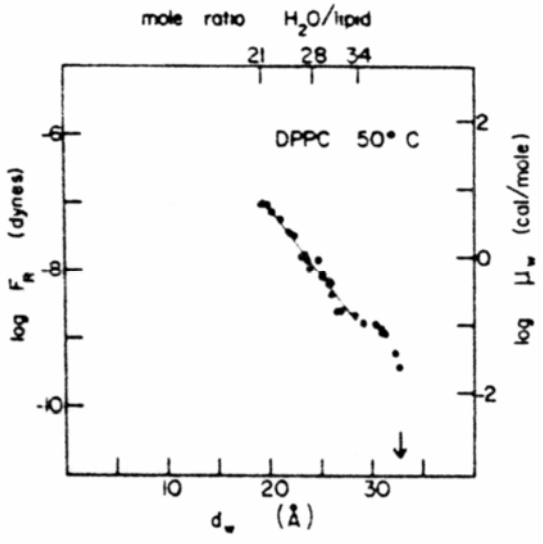

Figure 7-23. Plot of the net repulsive force Π (F_R) vs d_w for DPPC/Water at T = 50 °C (Lis et al. 1982)

The fitting on the force curve of **Figure 7-23** was carried out assuming that $F_R = F_{HYD} - F_{VDW}$ where F_R, F_{HYD}, and F_{VDW} are defined as $F = \Pi A$ where Π is the corresponding osmotic pressure, given in **Equation 7-1**, and A is the area per headgroup of DPPC. The repulsive undulation force was not taken into account by **Lis et al. 1982**

The Hamaker constant, A, was evaluated by equating Π_{VDW} with Π_{HYD} at d_w^{∞} (maximum-swelling separation) where Π was assumed to be zero. The results found for the Hamaker constant A, the hydration coefficient P_0, and the hydration decay length λ are given in **Table 7-8**. *In this study, the water bilayer separation for the calculation of the VDW interaction was defined as* d_w.

Continuing the work of **Lis et al. 1982**, **Rand** and **Parsegian** (**1989**) have fitted the hydration force to the experimental results of DPPC bilayers in water using two approaches: (i) the gravimetric method of **Luzzati** that calculates the water bilayer separation using the expression $d_w = D - b_L$ and (ii) the compressibility method taking into account the bilayer compressibility modulus K (dynes/cm^2), described as the fractional change in area for a unit change in bilayer tension. They also did not consider an undulation force. The results of the hydration coefficient P_0, and the hydration decay length λ are given in **Table 7-8**.

McIntosh et al. 1993 modeled the total pressure – distance relation (**Figure 7-24**) assuming that the total pressure Π between uncharged lipid bilayers can be written as the sum of three repulsive forces (hydration, undulation and an additional short-range steric repulsive force) and the attractive Van der Waals force. The equations used for fitting the experimental points for the hydration and Van der Waals forces are those given in **Equation 7-1**. The expression used for the short range steric force is very similar to that describing the hydration force given by:

$$\Pi_{VSR} = P_{VSR0}\exp\left(-d_f/\lambda_S\right) \qquad \textbf{Equation 7-2}$$

while for the repulsive undulation force the theoretical expression of **Evans** and **Needman (1987)** was used:

$$\Pi_{UND} = \frac{\pi kT}{32\lambda}\left(P_0/\kappa_c\lambda\right)^{1/2}\exp\left(-d_f/2\lambda\right) \qquad \textbf{Equation 7-3}$$

where κ_c is the bending rigidity. For the calculations of the Van der Waals attractive force d_f was used, water bilayer separation being defined as $d_f = D - d_b$ as shown in **Figure 7-22**. *The lipid bilayer thickness was considered constant for all the experimental points taken equal to* $d_b = 51.9 Å$. The equilibrium separation at maximum - swelling in water was found equal to $d_f = 15.4$Å. The results found for the different parameters are given in **Table 7-8**.

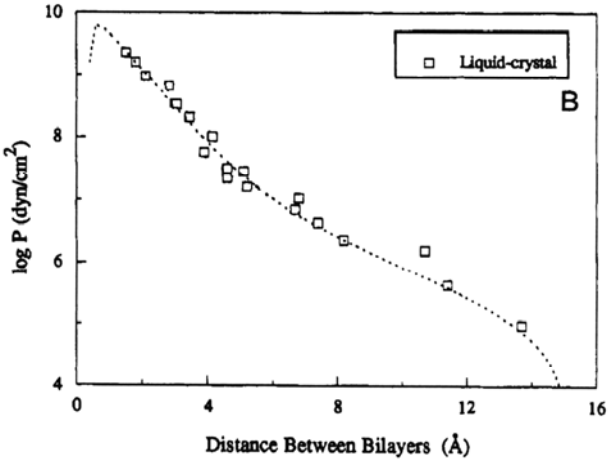

Figure 7-24. logΠ vs d_f for fluid egg PC bilayers (McIntosh et al. 1993)

Recently, **Petrache et al. 1998** have analyzed the osmotic pressure data of DPPC in water at T = 50 °C using the interbilayer interactions consisting of Van der Waals and hydration interactions given again by **Equation 7-1**, but also using a *modified* repulsive undulation force (Helfrich force) given by the following equation:

$$\Pi_{UND} = -\left(\frac{kT}{2\pi}\right)^2 \frac{1}{\kappa_c} \frac{d\sigma^{-2}}{d(d_f)} \qquad \textbf{Equation 7-4}$$

where κ_c is the bending modulus (fitting parameter) and σ is defined as the water spacing fluctuation given by:

$$\sigma^2 = \eta_l D^2/\pi^2 \qquad \textbf{Equation 7-5}$$

where η_l is the Caillé parameter which is experimentally known. The derivative $d\sigma^{-2}/d(d_f)$ is negative and thus $\Pi_{UND} > 0$.

As in the fitting analysis of **McIntosh et al. 1993**, d_f was used by **Petrache et al**. **1998** as the water bilayer separation for obtaining the Van der Waals interaction. Fitting results for different values of the parameters A, P_0, λ and κ_c are given in **Table 7-8**. **Figure 7-25** shows the theoretical fit for κ_c equal to κ_c =12 kT. The straight solid line indicates the fluctuation pressure, the dashed line shows the hydration pressure and the curved dotted line shows the Van der Waals pressure. The maximum water bilayer separation d_f for DPPC at T = 50 °C was found to be equal to d_f = 18 Å.

Table 7-8. Parameter values for several fits to logΠ – d_w force curves for DPPC in water g = Gravimetric method, c = Compressibility method

DPPC/Water Parameters	Lis et al.	Rand et al.		McIntosh et al.	Petrache et al.		
A (kT)	0.75	---	---	0.70	1.16	0.70	1.80
P_0 (Pa)	$10^{9.99}$	$10^{9.38}$ g	10^{10} c	$10^{7.6}$	10^{8}	$10^{7.96}$	$10^{7.76}$
λ (Å)	2.2	2.55 g	2.13 c	1.38	1.97	1.97	2.39
κ_c (kT)	---	---	---	25	12	24	24
K (dyne/cm^2)	---	---	145	---	---	---	---

The interbilayer forces, in our case, are studied by fitting the experimental results (logΠ – d_w curves) using appropriate models (see **Chapter 5**). The models contain several parameters that one must take into account, which are: the Hamaker constant A in kT units, the bending rigidity κ_c in kT units, the hydration coefficient P_0 (Pa), and the "characteristic" hydration decay length λ (Å).

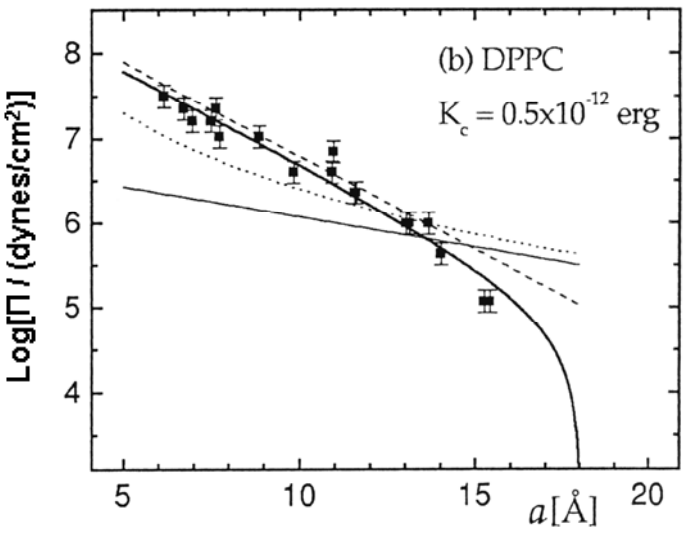

Figure 7-25. Fit for DPPC/Water at T = 50 °C (Petrache et al. 1998)

In principle one should use the full model equations containing all the adjustable parameters and carry out a nonlinear regression procedure. However, this would necessitate a much larger number of experimental points to be meaningful. One just cannot fit 4 parameters to 7 experimental points! We have therefore chosen a different fitting process: for a specific value of the Hamaker constant, A, the hydration decay length, λ, is set and the hydration coefficient, P_0, is varied over a broad range of values. For each A, λ, and P_0, we calculate the model deviation from the experimental points. The best value of P_0 (for each λ) is considered to be the one that has the smallest error, determined by the following equation:

$$\text{Error} = \sum_i \left(\frac{\Pi_{\text{theo, i}} - \Pi_{\text{exp, i}}}{\sigma_i} \right)^2 \qquad \textbf{Equation 7-6}$$

where σ_i is the standard deviation of each experimental point. An important point in the above process is that we demand from the beginning that the fitting curve passes through the maximum swelling point ($\log\Pi = 0$, $d_w = d_{max}$). *This fitting procedure is thus a conditional fit.* The procedure is facilitated considerably by the fact that there are some limitations in the values that the different parameters can take. For example, the Hamaker constant has been estimated to vary between 0.25 and 2.5 kT (**Rand et al. 1989; Israelachvili 1991; McIntosh et al. 1993; Parsegian 1993**), the bending rigidity is ranging between 10 and 50 kT (**Evans et al. 1990; Kummrow et al. 1991**), the hydration coefficient ranges between $10^{7.5}$ and 10^{10} Pa, and the "characteristic" decay length is expected to vary between 1.8 and 2.6 Å (**Lis et al. 1982; Rand et al 1989; McIntosh et al. 1993, Petrache et al. 1998**). These values are more or less established by various studies on neutral and charged lipid bilayers, that have been carried out in the past 20-30 years.

Before we continue with the fitting process, we first study the effect of each of the above parameters on the force curve ($\log\Pi - d_w$), e.g. the hydration coefficient, P_0, by changing the value of this parameter while keeping all the other parameters constant. This procedure helps us understand which part of the graph $\log\Pi - d_w$ is most strongly affected by each parameter. **Figure 7-26**, shows the effect of the hydration coefficient, P_0, on the $\log\Pi - d_w$ curve of DPPC in water. Here, the Hamaker constant, A, was taken equal to 1.0 kT, the bending rigidity, κ_c, was taken equal to 30 kT and the "characteristic" decay length, λ, was arbitrarily set to 1.8 Å. The hydration coefficient was varied from 10^8 to $10^{10.5}$ Pa. *Increasing the hydration coefficient leads to a parallel displacement of the fitting curves to higher water*

bilayer spacings (d_w) as the hydration coefficient increases. Since the hydration force dominates all other interactions as $d_w \rightarrow 0$, the hydration coefficient is essentially the intercept of the fitting curve with the logΠ axis.

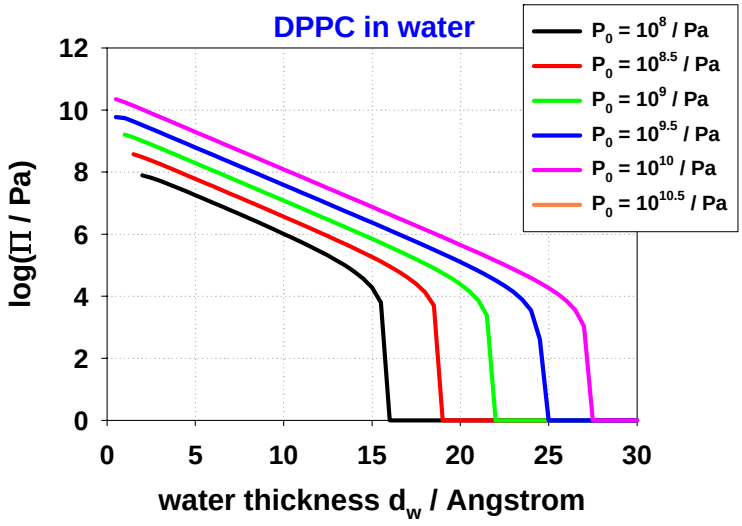

Figure 7-26. Fitting curves: A = 1.0 kT, κ_c = 30 kT, and λ = 1.8 Å

In **Figure 7-27** the effect of the hydration decay length, λ, was studied while the Hamaker constant and the bending rigidity were kept the same as in **Figure 7-26**. The hydration decay length was taken equal to $P_0 = 10^8$ Pa. From **Figure 7-27** we observe that the change of the hydration length influences strongly the slope of the fitting curves, which decreases upon increasing λ.

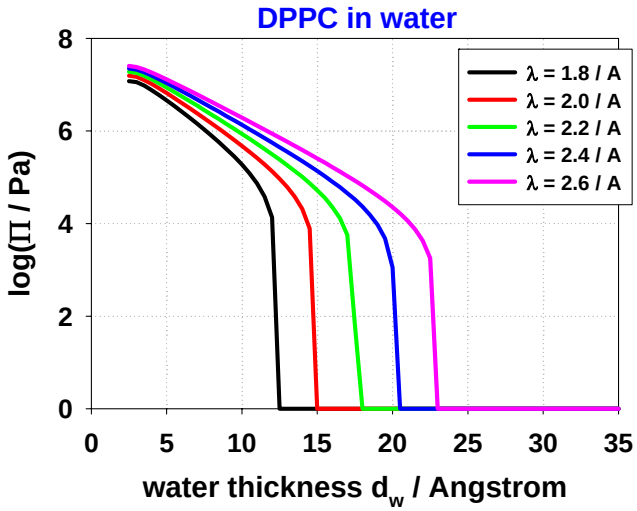

Figure 7-27. Fitting curves: A = 1.0 kT, κ_c = 30 kT, and $P_0 = 10^8$ Pa

The Hamaker constant, A, appears to affect the low-pressure part of the fitting curves as is shown in **Figure 7-28**, and thus it plays a significant role in the determination of the maximum swelling point.

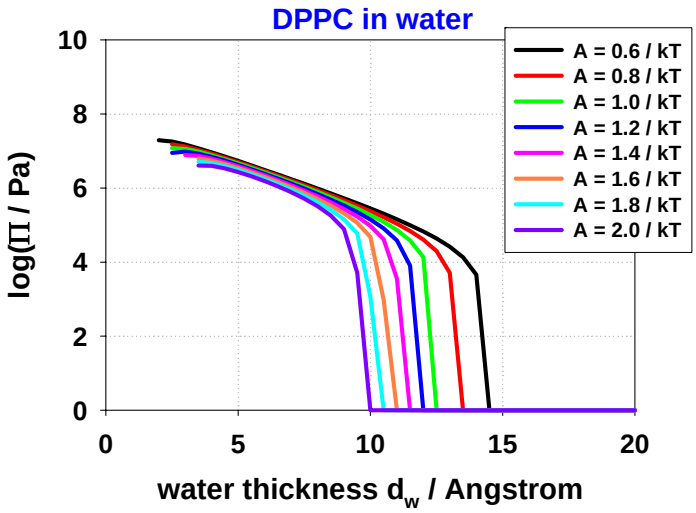

Figure 7-28. Fitting curves: $P_0 = 10^8$ kT, $\lambda = 1.8$ Å, and $\kappa_c = 30$ kT

Likewise, the bending rigidity, κ_c, influences the low-pressure part of the fitting curves, **Figure 7-29**, where it is important to check if they pass from the equilibrium separation point. Again, the values of the hydration length, λ, the hydration coefficient, P_0, and the bending rigidity are the same as those used before.

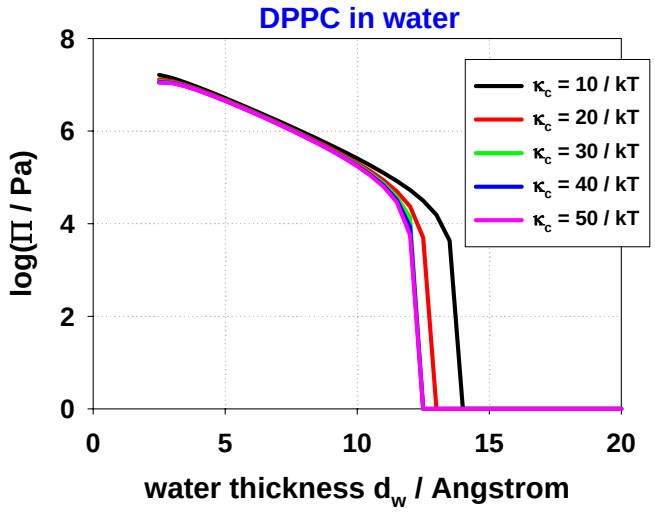

Figure 7-29. Fitting curves: A = 1.0 kT, $P_0 = 10^8$ Pa, and $\lambda = 1.8$ Å

Continuing with the *conditional fitting* process we give an example of the theoretical analysis using a Hamaker constant equal to A = 1.0 kT. As explained above for one specific value of the Hamaker constant (e.g. A = 1.0 kT) the hydration decay length, λ, is varied usually from 2.0 Å to 2.8 Å. For each value of λ the error function is calculated for a total of 1000 different values of P_0 (**Figure 7-30**). The bending rigidity, κ_c, is evaluated each time by requiring that the fitting curve passes exactly from the maximum swelling point. The results for each hydration length at the minimum error are given in **Table 7-9** and shown in **Figure 7-31**.

The parameter values that best describe our experimental results (logΠ - d_w) of DPPC in water for A = 1.0 kT are λ = 2.55 Å, P_0 = 8.67 x 10^8 Pa, κ_c = 14.2 kT with minimum error 13.6 as shown in **Table 7-9**.

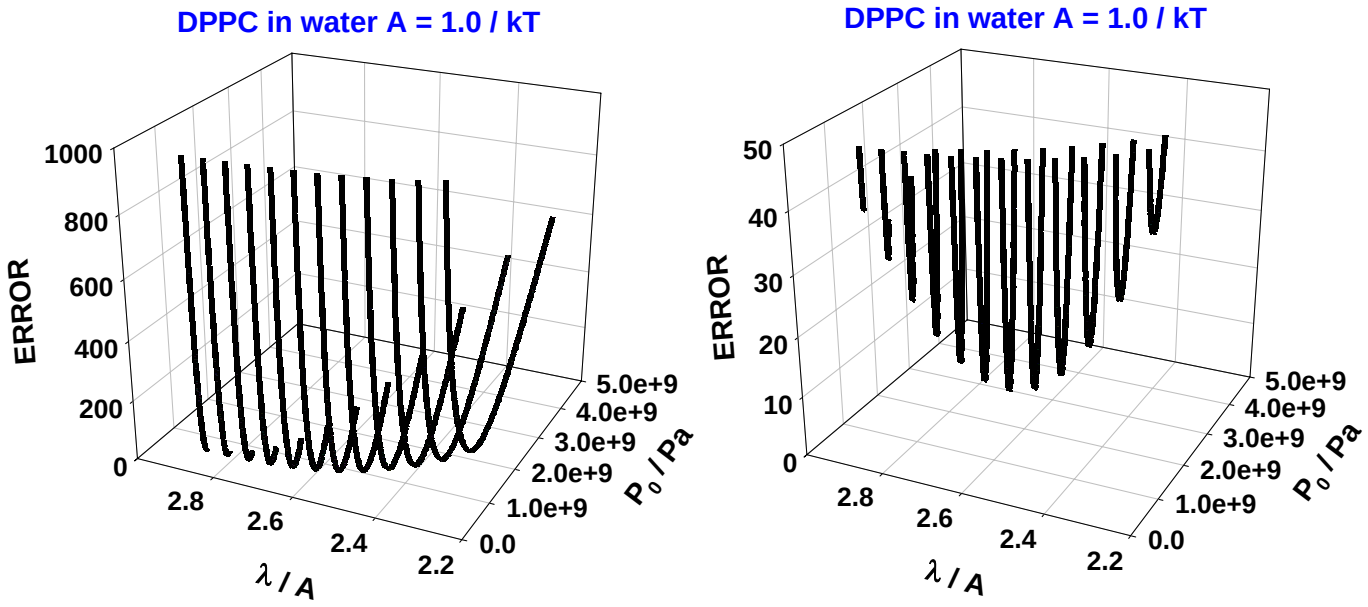

Figure 7-30. Conditional fitting curve: A = 1.0 kT

Table 7-9. Parameter values for DPPC in water for each value of hydration length λ. Hamaker constant A = 1.0 kT

P_0 / Pa	λ / Å	κ_c / kT	Error
2.113e+9	2.30	8.8853	36.50
1.738e+9	2.35	9.5164	26.90
1.445e+9	2.40	10.314	20.20
1.210e+9	2.45	11.296	15.90
1.021e+9	2.50	12.547	13.80
8.670e+8	2.55	14.224	13.60
7.412e+8	2.60	16.509	15.00
6.382e+8	2.65	19.905	17.90

5.528e+8	2.70	25.358	22.00
4.815e+8	2.75	35.476	27.20
4.216e+8	2.80	60.507	33.30
3.873e+8	2.85	249.21	40.40

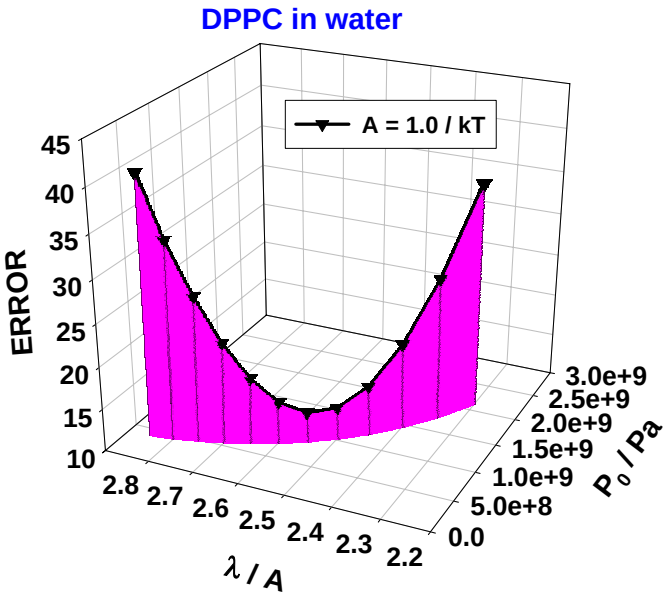

Figure 7-31. Parameter values for DPPC in water at minimum error A = 1.0 kT

The same theoretical analysis was followed for different values of the Hamaker constant and the results (at minimum error) are shown in **Table 7-10**. The results show that the hydration decay length, λ, and the hydration coefficient, P_0, are not greatly influenced by the change of the Hamaker constant.

Table 7-10. Parameter values using the conditional fitting process for DPPC bilayers in water

A / Kt	λ / Å	Po / Pa	κ_c / kT	Error
0.6	2.50	1.076e+9	180.24	13.5
0.7	2.55	8.616e+8	67.437	13.5
0.8	2.55	8.635e+8	30.016	13.5
0.9	2.55	8.647e+8	19.273	13.6
1.0	2.55	8.670e+8	14.224	13.6
1.2	2.55	8.700e+8	9.312	13.6
1.4	2.55	8.730e+8	6.923	13.7
1.6	2.55	8.770e+8	5.514	13.7
1.8	2.55	8.792e+8	4.576	13.8
2.0	2.55	8.820e+8	3.9120	13.9

On the contrary, the bending rigidity, κ_c, decreases significantly by increasing the Hamaker constant as shown in **Figure 7-32**. This indicates that the Hamaker constant and the bending rigidity are interdependent.

Analogous figures like **Figure 7-31** for each Hamaker constant used are given in **Appendix II**. *The Van der Waals interaction in this case was calculated taking as water bilayer separation equal to* d_w, *that is, the lipid and water are considered as two different layers.*

Similar analysis for DPPC in water was performed using d_w' as the water bilayer separation to the Van der Waals attractive force using as headgroup thickness $d_{head} \approx 3.5 - 4$ Å, which was calculated from the volumes of the component groups of L_α phosphatidylcholine bilayers (**Nagle et al. 2000**). The corresponding results (at minimum error) are shown in **Table 7-11**.

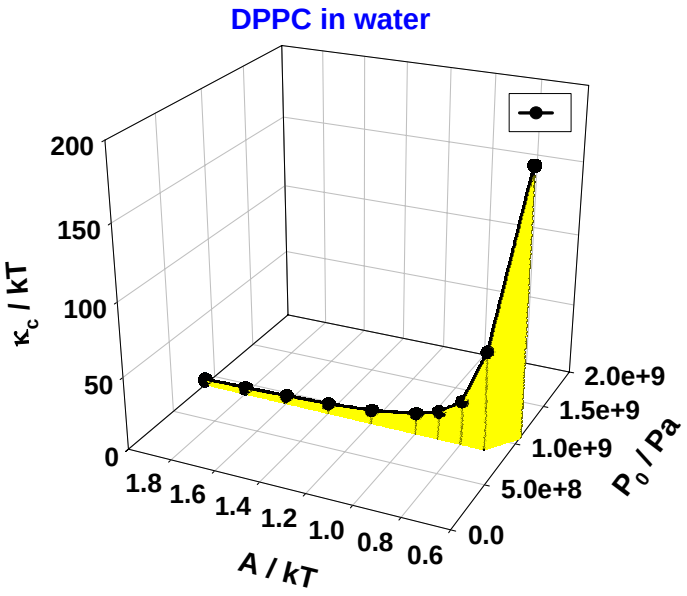

Figure 7-32. Reduction of bending rigidity by increasing the Hamaker constant

Table 7-11. Parameter values using the conditional fitting process for DPPC bilayers in water using d_w' as water bilayer separation to the VDW force

A / kT	λ / Å	Po / Pa	κ_c / kT	Error
1.4	2.50	9.950e+8	59.11	13.0
1.5	2.50	9.949e+8	39.03	13.0
1.6	2.50	9.944e+8	29.15	13.0
1.7	2.50	9.941e+8	23.24	13.0
1.8	2.50	9.942e+8	19.35	13.0
1.9	2.50	9.915e+8	16.46	13.0
2.0	2.50	9.927e+8	14.44	13.0

2.1	2.50	9.919e+8	12.80	13.0
2.2	2.50	9.915e+8	11.52	13.0

As it is seen from **Table 7-11**, in order to fit the logΠ – d_w curve of DPPC in water the Hamaker constant increases by almost 1 kT compared to the values found in **Table 7-10**. This increase was expected, since adding the headgroup thickness of the lipid molecule in the water bilayer separation greatly influences the Van der Waals interaction. In this case the Hamaker constant is equal to 1.8 ± 0.3 kT. In contrast, the hydration decay length, λ, and the hydration coefficient, P_0, are not influenced by changing the Hamaker constant.

As shown in **Table 7-10** and **Table 7-11**, the best set of parameters that can be used to fit the logΠ – d_w experimental results for DPPC in water is not obvious, since for values of the Hamaker constant from A = 0.8 to 1.2 kT or A = 1.6 to 2.1 kT there exist reasonable values for the bending rigidity (according to the literature), which provide excellent fits to the data. Other values of A must be excluded as possible solutions, because the bending rigidity associated with them deviates greatly from the published values. In **Figure 7-33** we present the best fitting curves for DPPC in water with A = 0.8 – 1.2 kT or A = 1.6 – 2.1 kT. It is seen that there is no actual difference between the theoretical fitting curves with different Hamaker constant.

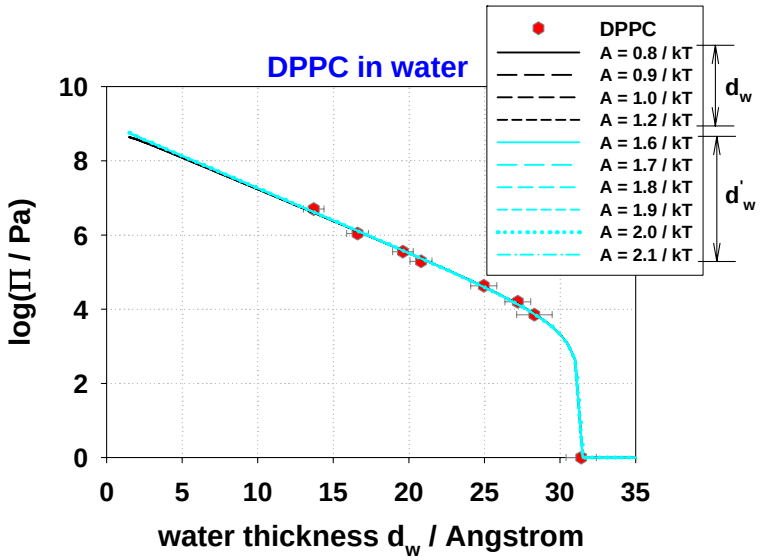

Figure 7-33. Conditional fitting results for DPPC in water with A = 0.8 – 1.2 kT or A = 1.6 – 2.1 kT

Comparing the results found here and those reported in **Table 7-8** by the previous researchers we see that our theoretical parameters do not agree with those found by the various research groups (**Lis et al. 1982**; **Rand et al. 1989; McIntosh et al. 1993**; **Petrache et al. 1998**). This

may be due to the fact that **Lis et al. 1982** and **Rand et al. 1989** calculated the hydration coefficient, P_0, and hydration length, λ, without taking into account the maximum swelling point, and thus properly using the Van der Waals attraction between the DPPC bilayers. Moreover, the difference in the way that the water bilayer separation was defined or the modified repulsive Helfrich force that was used by **McIntosh et al. 1993** and **Petrache et al. 1998** are responsible for the significant differences in the parameter values. Furthermore, **McIntosh et al. 1993** used an additional exponential steric repulsive force to fit the force curve of DPPC in pure water and as a result their various parameters deviate from the ones found by **Lis (1982)** and **Rand (1989)** and by us in the present work.

In conclusion, the values found for the different parameters by us and by various researchers over the years *are strongly model dependent,* and as a result no perfect agreement can be found.

Returning to our present results, we see that for DPPC in water we obtain excellent fits for A = (1.0 ± 0.2) kT, λ = (2.55 ± 0.05) Å, P_0 = (8.67 ± 0.06) x10^8 Pa and a range of κ_c values (from 9 to 30 kT) when the water bilayer separation d_w^* in the VDW force is taken equal to d_w. In addition, when d_w^* is taken equal to d_w', excellent fits are obtained for A = (1.8 ± 0.3) kT, λ = (2.50 ± 0.05) Å, P_0 = (9.94 ± 0.02) x10^8 Pa and a range of κ_c values (from 11 to 30 kT).

7.3.2 Fitting logΠ – d_w data for DPPC/Electrolyte solutions using the binding model

7.3.2.1 Fitting NaSCN results

In order to obtain binding constants of the anions on the headgroups of the DPPC molecules the experimental logΠ – d_w curves of DPPC in the presence of salt solutions of different concentrations are fitted according to the following procedure: All the parameters that have been obtained (P_0, λ, and κ_c) using the conditional fitting for DPPC in water (as explained before) are kept the same. P_0 and λ should not change since all the experimental data converge at high Π. κ_c should decrease by a few kT in the presence of salt solutions (**Brotons et al. 2005**) but the decrease is expected to be small compared to the values that we use and thus is not taken into account. The Hamaker constant should decrease by about 50% according to the theory (see **Chapter 5**). A binding constant K (M^{-1}) for the anions is introduced that

determines the electrostatic repulsive force generated between the lipid bilayers due to anion adsorption. The contribution of the electrostatic repulsion force Π_{ELE} to the total pressure acting between the lipid bilayers is calculated as explained in **Chapter 5**, **Section 5.4.4**. Different values for the binding constant are used until the best fit on the experimental results is found. An example of the fitting analysis for DPPC in the presence of a NaSCN solution of concentration 0.05 M is shown in **Figure 7-34**; SCN^- has the greatest effect on the $\log\Pi - d_w$ curves of DPPC compared to the other anions as shown in **Section 7.2**. d_w^* was set equal to d_w for the calculation of the VDW interaction. The values $P_0 = 8.635 \times 10^8$ Pa, $\lambda = 2.55$ Å, $\kappa_c = 30$ kT and A = 0.8 kT are chosen arbitrarily from **Table 7-10**.

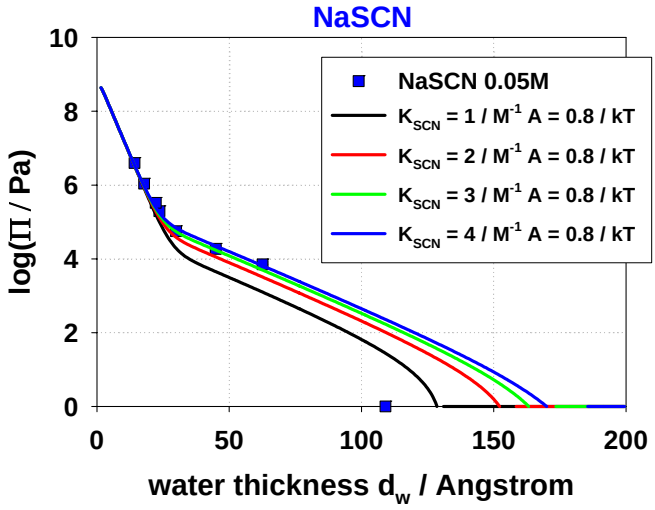

Figure 7-34. Fitting curves – Binding model for DPPC in the presence of 0.05 M NaSCN A = 0.8 kT, $P_0 = 8.635 \times 10^8$ Pa, $\lambda = 2.55$ Å, and $\kappa_c = 30$ kT

In **Figure 7-34**, one can see the influence of the electrostatic repulsion to the pressure – distance curve. As the binding constant increases the electrostatic repulsion increases. The binding constant that best describes the experimental data of **Figure 7-34** is equal to $K_{SCN} = 4$ M^{-1}. However, the fitting curve does not pass through the maximum swelling point and deviates towards higher values of d_w. This indicates that a bigger attractive interaction is needed to include the maximum swelling point in the fit. Since the VDW force is the only attractive interaction in this model, it follows that the Hamaker constant, A, must increase although this is not theoretically justified. The influence of the Hamaker constant on the $\log\Pi - d_w$ curves was studied in **Figure 7-28**, where it was shown that it affects the low-pressure part of the data and plays a significant role in the determination of the maximum swelling point. One could also consider increasing the bending rigidity modulus, κ_c, and thus

decreasing the repulsive undulation interaction, but the influence of κ_c on the logΠ – d_w curves is rather small, as shown in **Figure 7-29**.

Figure 7-35 illustrates the fitting results obtained by changing the Hamaker constant, A, from 0.8 to 4.0 kT and keeping P_0, λ, κ_c, and K_{SCN} the same as before (**Figure 7-34**).

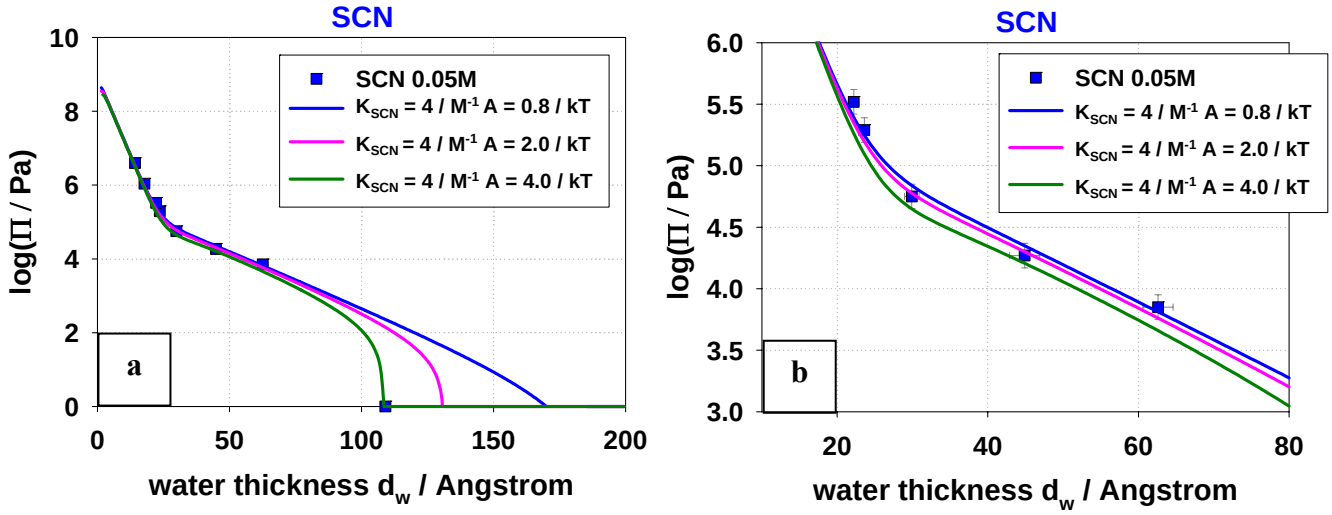

Figure 7-35. Fitting curves – Binding model for DPPC in the presence of NaSCN 0.05 M P_0 = 8.635 x 10^8 Pa, λ = 2.55 Å, and κ_c = 30 kT

Upon increasing the Hamaker constant by a factor of five (A = 4 kT) we produce a good fit to the logΠ – d_w curve of DPPC in the presence of 0.05 M NaSCN including the maximum swelling point. Further improvement can be achieved by varying slightly the binding constant K_{SCN} and the Hamaker constant A. The final fit is shown in **Figure 7-36** and the fitting parameters are K_{SCN} = 5.3 M^{-1}, A = 4.8 kT, P_0 = 8.635 x 10^8 Pa, λ = 2.55 Å, and κ_c = 30 kT.

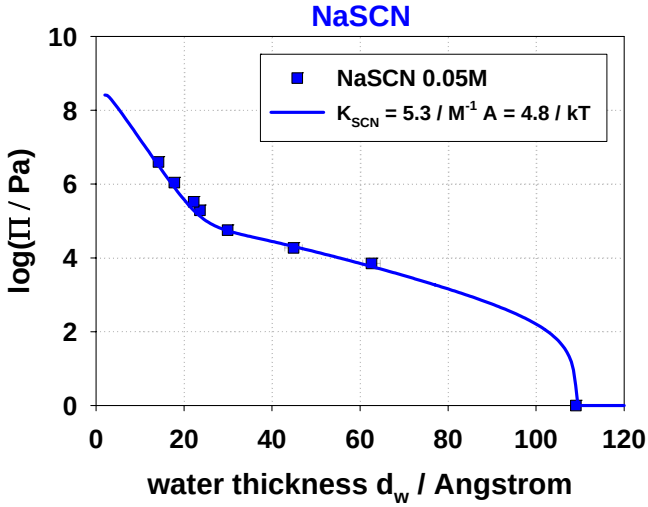

Figure 7-36. Fitting curves – Binding model for DPPC in the presence of 0.05 M NaSCN P_0 = 8.635 x 10^8 Pa, λ = 2.55 Å, and κ_c = 30 kT

The same fitting analysis was followed for DPPC in the presence of NaSCN solutions of concentrations 0.1 M and 0.5 M. The binding constants and Hamaker constants obtained for each salt concentration are given in **Table 7-12** and **Table 7-13**. The results in **Table 7-12** are obtained by using $\mathbf{d_w^* = d_w}$ for the VDW interaction and those of **Table 7-13** are obtained by using $\mathbf{d_w^* = d_w'}$. In the second case the hydration coefficient, P_0, the hydration length, λ, and the bending rigidity, κ_c, were chosen from **Table 7-11** as $P_0 = 9.94 \times 10^8$ Pa, $\lambda = 2.5$ Å, $\kappa_c = 29$ kT for A = 1.6 kT.

Table 7-12. Binding constants of SCN^- anions on the headgroups of DPPC molecules for different concentrations ($d_w^* = d_w$)

NaSCN $P_0 = 8.635 \times 10^8$ Pa, $\lambda = 2.55$ Å, $d_w^* = d_w$ (VDW)			
Concentration C / M	**Binding constant K_{SCN} / M^{-1}**	**Hamaker constant A / kT**	**STERN LAYER STL / Å**
0.05	5.3	4.8	----
0.1	6.0	2.7	----
0.5	for any K 80 40 6.0	0.8	---- (impossible to fit) 2 4 8

Table 7-13. Binding constants of SCN^- anions on the headgroups of DPPC molecules for different concentrations ($d_w^* = d_w'$)

NaSCN $P_0 = 9.940 \times 10^8$ Pa, $\lambda = 2.5$ Å, $d_w^* = d_w'$ (VDW)			
Concentration C / M	**Binding constant K_{SCN} / M^{-1}**	**Hamaker constant A / kT**	**STERN LAYER STL / Å**
0.05	5.0	7.0	----
0.1	5.5	4.2	----
0.5	for any K 80 5.0	1.6	---- (impossible to fit) 3 9

The results shown in **Tables 7-12** and **7-13** indicate that there is no significant difference in the calculated binding constants of the anions using the two different approaches for

calculating the water bilayer separation d_w^* and thus the Van der Waals attraction force. The general observation is that in order to fit the experimental data (including the maximum swelling point) the Hamaker constant *must be increased* by a factor of five for 0.05 M and 0.1 M NaSCN concentrations, for which the binding constants have about the same magnitude of $\approx 5.5\ M^{-1}$. On the contrary, for the 0.5 M NaSCN solution a binding constant of $> 80\ M^{-1}$ must be used to fit the experimental $\log\Pi - d_w$ data. Beyond a binding constant of $80\ M^{-1}$ the bilayers are apparently saturated with ions and the fitting becomes insensitive to the value of the binding constant. In fact, it is practically impossible to obtain a good fit, as shown in **Figure 7-37**.

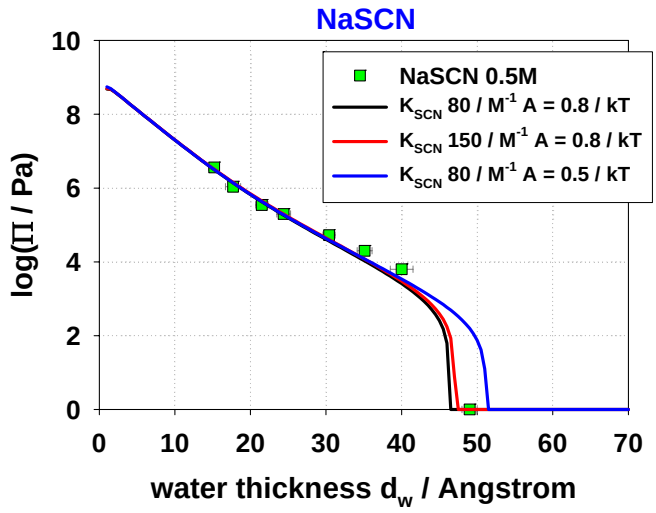

Figure 7-37. Fitting curves – Binding model for DPPC in the presence of 0.5 M NaSCN $P_0 = 8.635 \times 10^8$ Pa, $\lambda = 2.55$ Å, and $\kappa_c = 30$ kT

To improve the fit in this case and reduce the binding constant to values comparable to those found fot the lower NaSCN concentrations we must assume a very extensive "Stern" layer for Na^+ adsorption.

Figure 7-38 shows the fitting curve for DPPC in the presence of 0.5 M NaSCN with parameter values of $K_{SCN} = 6\ M^{-1}$, A = 0.8 kT, $P_0 = 8.635 \times 10^8$ Pa, $\lambda = 2.55$ Å, $\kappa_c = 30$ kT and Stern layer of 8 Å.

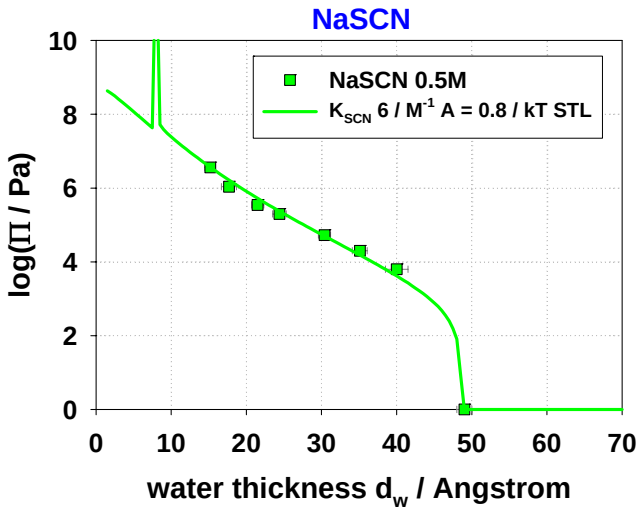

Figure 7-38. Fitting curves – Binding model for DPPC in the presence of 0.5 M NaSCN $P_0 = 8.635 \times 10^8$ Pa, $\lambda = 2.55$ Å, and $\kappa_c = 30$ kT

7.3.2.2 Fitting NaI, $NaNO_3$ and NaBr results

The same fitting procedure was followed for the logΠ – d_w data obtained in the presence of NaI solutions. **Tables 7-14** and **7-15** show the binding constants and the Hamaker constants obtained by fitting the experimental logΠ – d_w results of DPPC in the presence of NaI salt solutions of concentrations 0.05 M, 0.1 M and 0.5 M respectively.

Table 7-14. Binding constants of I^- anions on the headgroups of DPPC molecules for different concentrations ($d_w^* = d_w$)

NaI $P_0 = 8.635 \times 10^8$ Pa, $\lambda = 2.55$ Å, $d_w^* = d_w$ (VDW)			
Concentration C / M	**Binding constant K_I / M^{-1}**	**Hamaker constant A / kT**	**STERN LAYER STL / Å**
0.05	----	> 7.0	----
0.1	4.0	5.2	----
0.5	5.0	1.8	8

Table 7-15. Binding constants of I^- anions on the headgroups of DPPC molecules for different concentrations ($d_w^* = d_w'$)

NaI $P_0 = 9.940 \times 10^8$ Pa, $\lambda = 2.5$ Å, $d_w^* = d_w'$ (VDW)			
Concentration C / M	**Binding constant K_I / M^{-1}**	**Hamaker constant A / kT**	**STERN LAYER STL / Å**
0.05	----	> 8.0	----
0.1	3.5	8.0	----
0.5	4.5	3.0	8

The same observations as before apply in this case as well. In order to fit the experimental data including the maximum swelling point for concentrations of 0.05 M and 0.1 M, the Hamaker constant must increase considerably. In fact, for a concentration of 0.05 M NaI the increase of the Hamaker constant must be so big that the balance between the repulsive and attractive forces is not maintained and a satisfactory fit cannot be obtained!

For the concentration of 0.5 M NaI a binding constant of > 80 M^{-1} (saturated interface) is once more required to fit the experimental points, indicating that a bigger repulsive interaction is needed to include the maximum swelling point. A Stern layer of about 8 Å is assumed in order to obtain a binding constant comparable to those found for the lower concentrations.

For DPPC in $NaNO_3$ and NaBr solutions we have not attempted to fit the $\log\Pi - d_w$ curves due to the fact that there is no actual difference between the experimental results for both anions for concentrations between 0.1 M and 0.5 M (see **Figures 7-14** and **7-15**). In fact, the differences of these data with those of DPPC in water are very small, probably within the experimental error.

7.3.2.3 Fitting DPPC/Electrolyte data using the binding model. Further attempts and synopsis

To summarize, in order to be able to fit the $\log\Pi - d_w$ curves of DPPC in the presence of salts *using the binding model*, the Hamaker constant must increase very substantially for the low salt concentrations (0.05 M and 0.1 M), while an extra repulsion is required to fit the experimental results for DPPC both in NaSCN and NaI salt solutions of concentration 0.5 M. Increasing the Hamaker constant so much raises serious doubts about the real value of this fitting exercise, because theoretically the low frequency part of the Hamaker constant must

decrease in the presence of a salt solution by a factor proportional to $e^{-2\kappa D}$, where κ^{-1} is the Debye length of the solution. We thus anticipate that a 50% reduction of the Hamaker constant should roughly be expected when salts are present. The Hamaker constant was increased in our fit in order to accommodate the maximum swelling point. The main difficulty is associated with the assumption that the osmotic pressure is equal to 0 Pa at the maximum swelling point. However, the present of minute amounts of impurities, or the possibility of equilibrium of the swollen bilayers with a system of vesicles under tension, could easily increase the osmotic pressure at the maximum swelling point to a value of 100 – 200 Pa. This pressure is very small and is very hard to detect and measure precisely. One further possibility is the salting-in of lipids by the chaotropic salts, which might increase their solubility in solution. By excluding the maximum swelling point from the fitted data, one may be able to fit the rest of the data with reasonable values of the Hamaker constant and thus this must be studied. Moreover, the additional repulsive force that is required to fit the $\log\Pi - d_w$ curves in the presence of NaX solutions of concentration 0.5 M suggests the existence of an additional mechanism of repulsion, other than the electrostatic repulsion force produced between the lipid bilayers at high salt concentration. Assuming a Stern layer of the order of 8 Å is not an acceptable solution, since the Pauling radius for Na^+ is only 1 Å.

In consequence, we decided to fit the experimental $\log\Pi - d_w$ results without taking into account the maximum swelling point, hoping to obtain a good quantitative estimate of the magnitude of the binding constants of anions on the headgroups of the DPPC molecules. As a Hamaker constant, we assumed a value half of that found for DPPC in water (either A = 0.4 kT or A = 0.8 kT). **Figures 7-39** to **7-44** illustrate the best fitting curves found for DPPC in the presence of NaBr, $NaNO_3$, NaI and NaSCN of various concentrations. The binding constants obtained are given in **Table 7-16**. The results are the same either with hydration coefficient $P_0 = 8.635 \times 10^8$ and hydration decay length $\lambda = 2.55$ Å or with $P_0 = 9.94 \times 10^8$ and hydration decay length $\lambda = 2.5$ Å.

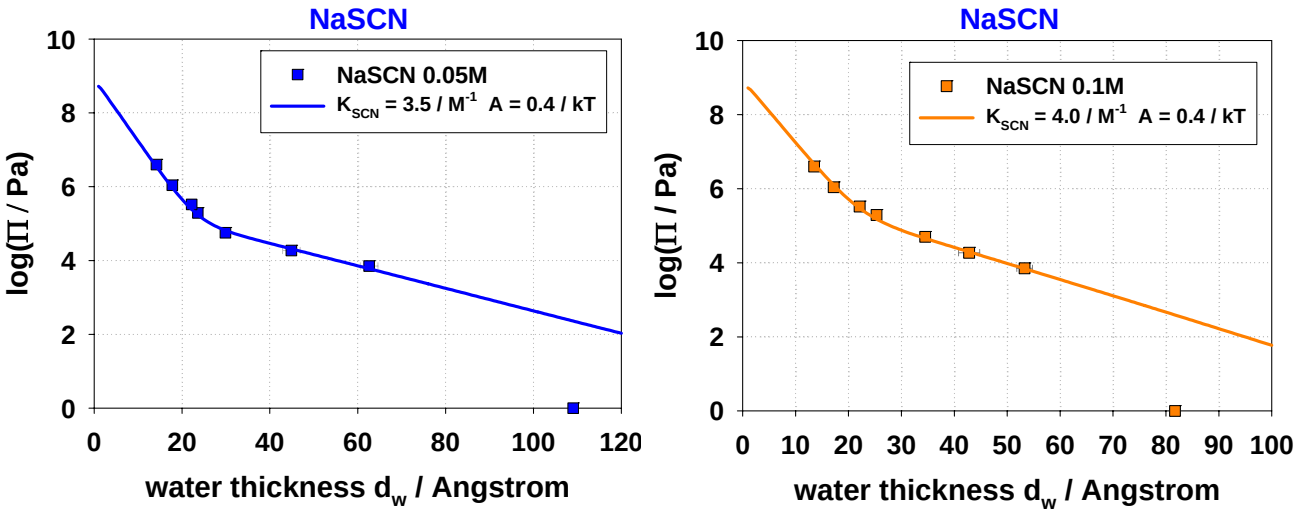

Figure 7-39. Fitting curves – Binding model for DPPC in the presence of 0.05 M NaSCN and 0.1M NaSCN P_0 = 8.635 x 10^8 Pa, λ = 2.55 Å, κ_c = 30 kT and A = 0.4 kT

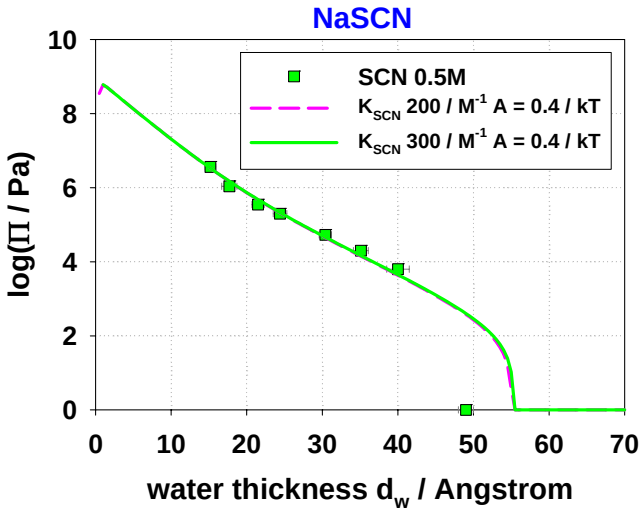

Figure 7-40. Fitting curves – Binding model for DPPC in the presence of 0.5 M NaSCN P_0 = 8.635 x 10^8 Pa, λ = 2.55 Å, κ_c = 30 kT and A = 0.4 kT

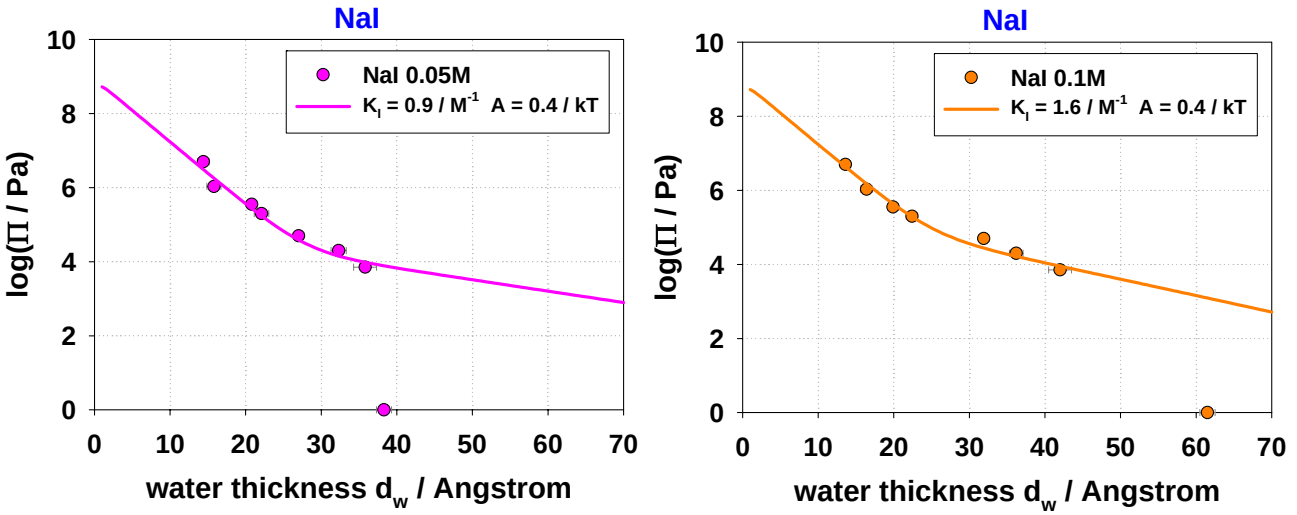

Figure 7-41. Fitting curves – Binding model for DPPC in the presence of 0.05 M NaI and 0.1 M NaI P_0 = 8.635 x 10^8 Pa, λ = 2.55 Å, κ_c = 30 kT and A = 0.4 kT

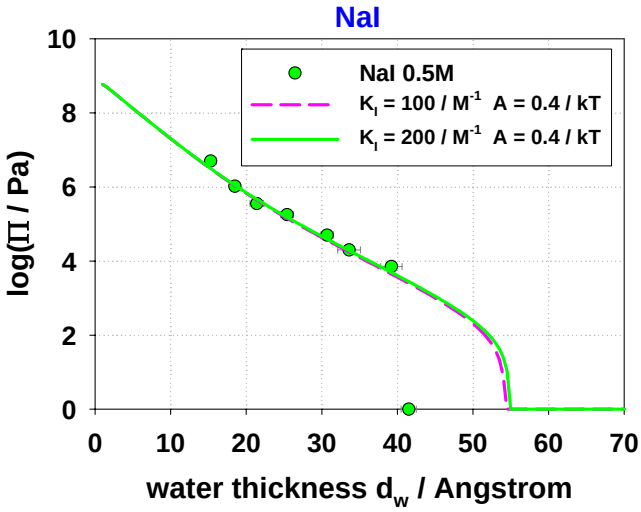

Figure 7-42. Fitting curves – Binding model for DPPC in the presence of 0.5 M NaI P_0 = 8.635 x 10^8 Pa, λ = 2.55 Å, κ_c = 30 kT and A = 0.4 kT

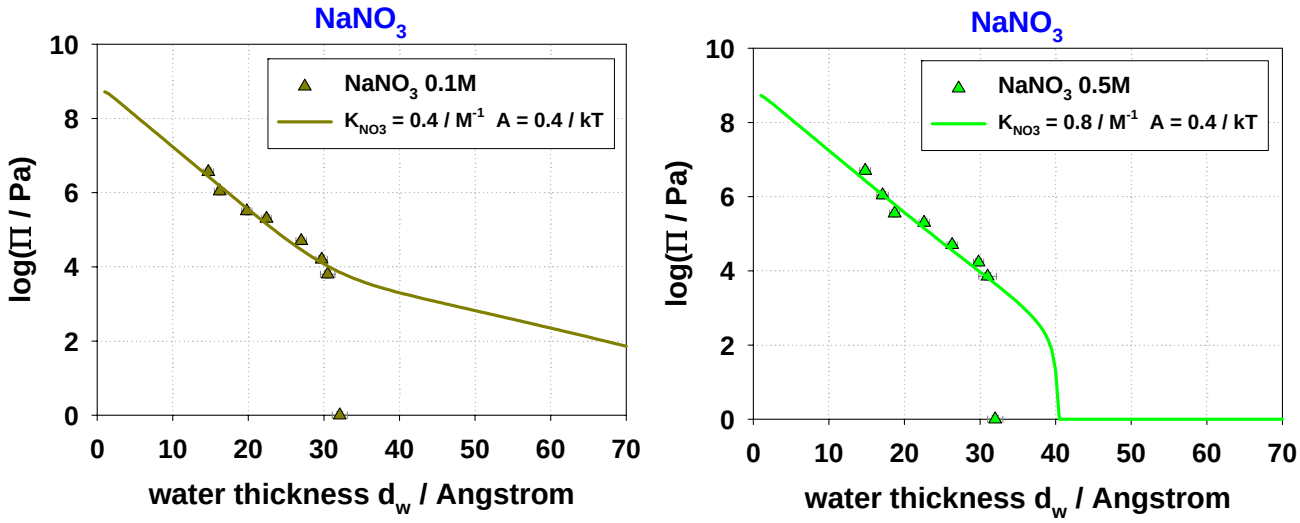

Figure 7-43. Fitting curves – Binding model for DPPC in the presence of 0.1 M $NaNO_3$ and 0.5 M $NaNO_3$ P_0 = 8.635 x 10^8 Pa, λ = 2.55 Å, κ_c = 30 kT and A = 0.4 kT

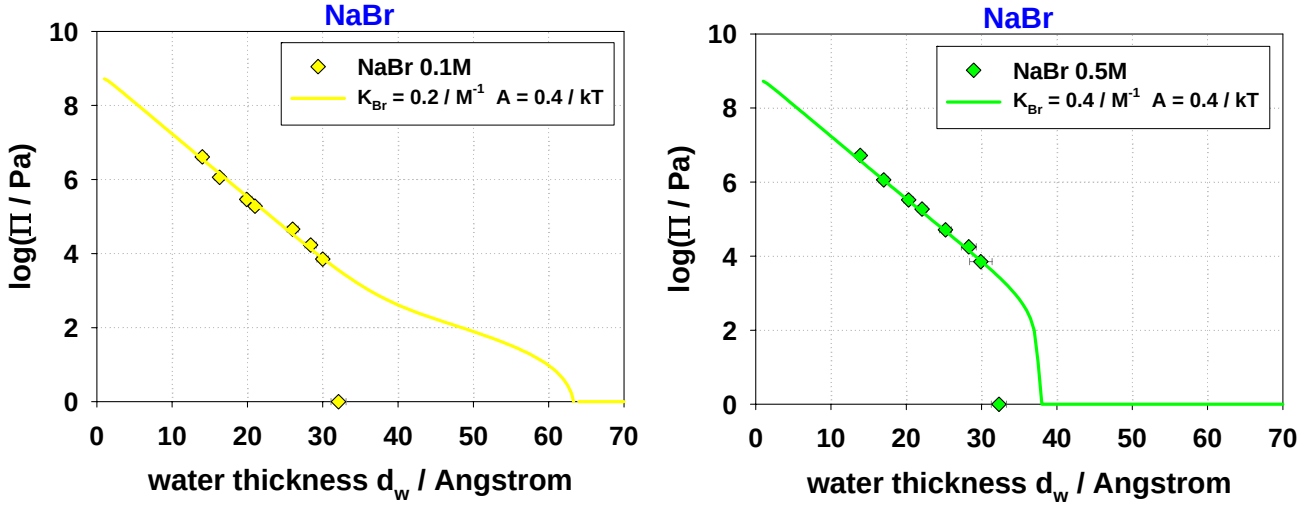

Figure 7-44. Fitting curves – Binding model for DPPC in the presence of 0.1 M NaBr and 0.5 M NaBr P_0 = 8.635 x 10^8 Pa, λ = 2.55 Å, κ_c = 30 kT and A = 0.4 kT

By comparing **Figures 7-39** to **7-44**, one observes the following general characteristics: At low concentrations of salt (0.05 M or 0.1 M) a fitting with reasonable parameters is possible, but it leaves out the maximum swelling point, as the fitting curves diverge to large osmotic pressures at large d_w distances. In contrast, at high salt concentration (0.5 M) much higher binding constants for the anions are necessary. Taking $d_w^* = d_w'$ and using a Hamaker constant equal to A = 0.8 kT (half of A = 1.6 kT for DPPC in water) the fitting curves are similar to those in **Figures 7-39** to **7-44**, with a small difference at large d_w (not shown). The electrostatic part of the $\log\Pi - d_w$ curves is not affected and consequently the binding constants of the anions are not modified.

Table 7-16. Binding constants of X^- anions on the headgroups of DPPC molecules for different concentrations

$P_0 = 8.635 \times 10^8$ Pa, $\lambda = 2.55$ Å, A = 0.4 kT				
Concentration C / M	**B. Constant K_{Br} / M^{-1}**	**B. Constant K_{NO3} / M^{-1}**	**B. Constant K_I / M^{-1}**	**B. Constant K_{SCN} / M^{-1}**
0.05	----	----	0.9 ± 0.1	3.5 ± 0.1
0.1	0.2 ± 0.1	0.4 ± 0.1	1.6 ± 0.1	4.0 ± 0.1
0.5	> 0.4	> 0.8	> 100	> 200

The results of **Table 7-16** show that the extracted binding constants according to the binding model depend on the anion used, but also on the concentration of the electrolyte solution. For example, if we compare the results obtained at the same salt concentration e.g. 0.1 M we see that the binding constants increase and follow the Hofmeister series of anions from $Br^- < NO_3^- < I^- < SCN^-$, but for increasing concentrations the binding constants increase. The effect is more pronounced when the chaotropic anions $I^-$and SCN^- are used, where it is seen that at high salt concentration binding constants larger than 100 M^{-1} (essentially surface charge saturation) are required to fit the data. This dependence of the binding constants on salt concentration severely limits the usefulness of these values for quantitative comparisons and hypotheses.

7.4 Fitting of logΠ – d_w curves in the presence of electrolytes using the diffuse lipid layer model

In this model, the anions are assumed to penetrate the headgroup plane of DPPC molecules without a specific binding to the headgroups of the lipid. Cations are assumed not to enter the headgroup plane. The osmotic pressure exerted between the lipid bilayers is calculated by using an attractive potential, U$_-$, of anions to the lipidic layer as explained in **Chapter 5**, **Section 5.4.5**. The attraction potential can be correlated with the binding constants of the anions calculated by the binding model. We have used a procedure identical to that of the binding model. **Figures 7-45** to **7-49** show the best fitting curves obtained for each salt solution for a specific value of U$_-$ at various concentrations with a Hamaker constant equal to 0.4 kT and a fixed lipid layer thickness δ = 4 Å, equal to the average headgroup size of a DPPC molecule.

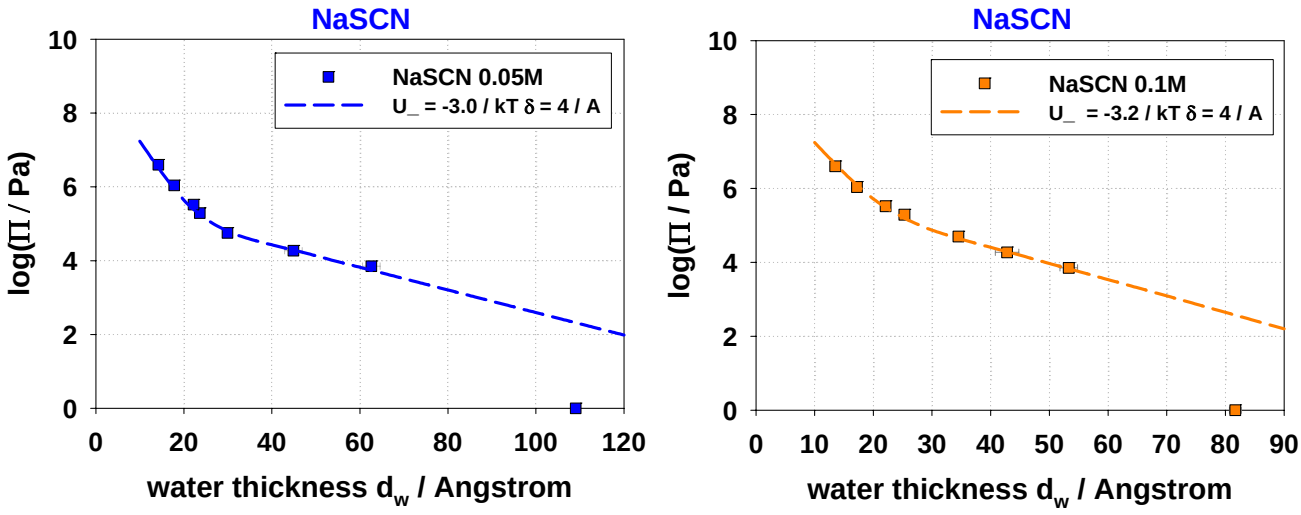

Figure 7-45. Fitting curves –Diffuse layer model for DPPC in the presence of 0.05 M NaSCN and 0.1 M NaSCN P_0 = 8.635 x 10^8 Pa, λ = 2.55 Å, κ_c = 30 kT and A = 0.4 kT

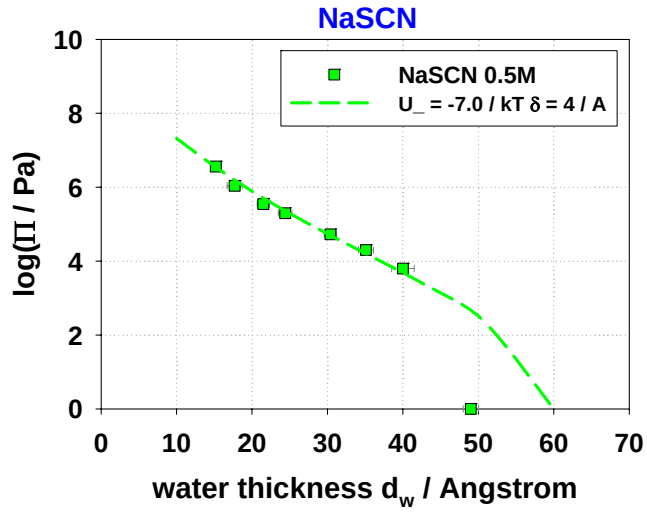

Figure 7-46. Fitting curves –Diffuse layer model for DPPC in the presence of 0.5 M NaSCN P_0 = 8.635 x 10^8 Pa, λ = 2.55 Å, κ_c = 30 kT and A = 0.4 kT

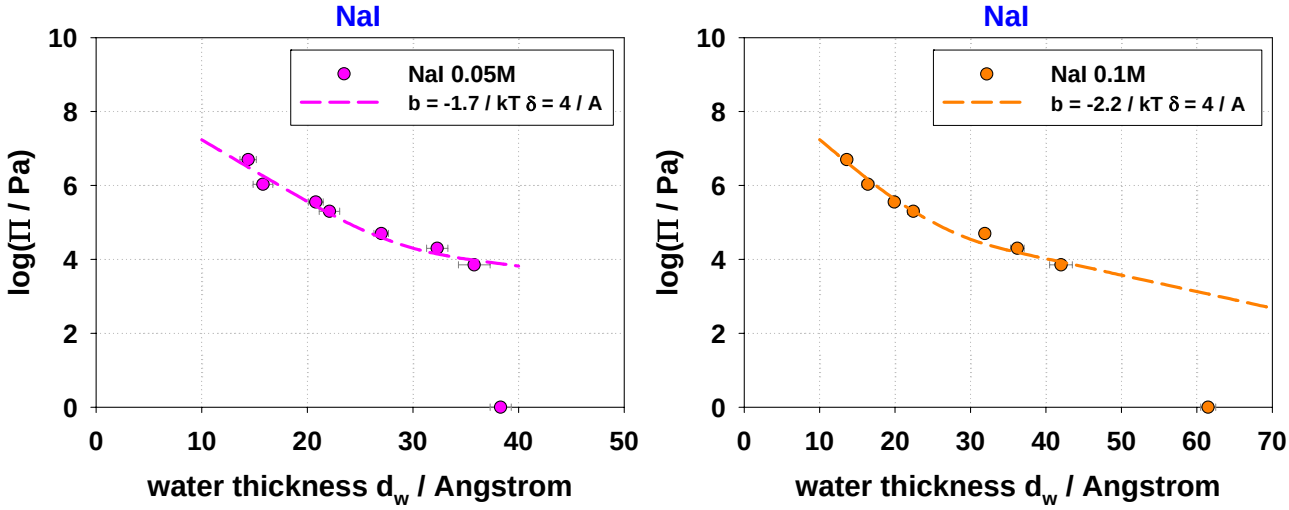

Figure 7-47. Fitting curves –Diffuse layer model for DPPC in the presence of 0.05 M NaI and 0.1 M NaI P_0 = 8.635 x 10^8 Pa, λ = 2.55 Å, κ_c = 30 kT and A = 0.4 kT

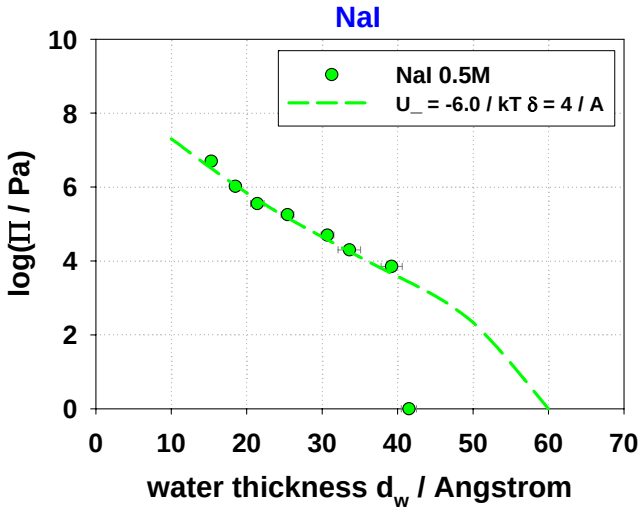

Figure 7-48. Fitting curves –Diffuse layer model for DPPC in the presence of 0.5 M NaI P_0 = 8.635 x 10^8 Pa, λ = 2.55 Å, κ_c = 30 kT and A = 0.4 kT

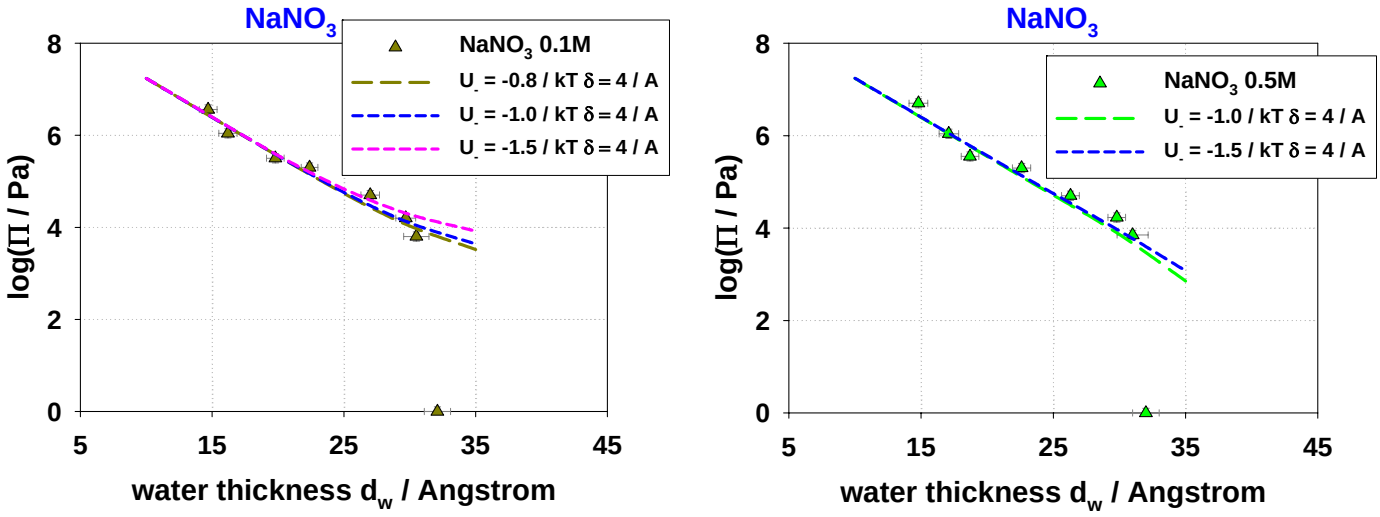

Figure 7-49. Fitting curves –Diffuse layer model for DPPC in the presence of 0.1 M $NaNO_3$ and 0.5 M $NaNO_3$ P_0 = 8.635 x 10^8 Pa, λ = 2.55 Å, κ_c = 30 kT and A = 0.4 kT

The fitting curves in **Figures 7-45** to **7-49** are very similar to those observed using the binding model, and in general, they demonstrate the same characteristics. Once more, upon using $d_w^* = d_w'$ with a Hamaker constant equal to A = 0.8 kT the fitting curves are not altered significantly and thus the interaction potential U_- of the anions remains the same as with A = 0.4 kT. In **Figure 7-49**, several fitting curves with different interaction potentials U_- are shown for both $NaNO_3$ concentrations. It is very difficult to decide which value of U_- best describes the experimental data. This is due to the fact that the DPPC bilayer properties are very weakly affected in the presence of NO_3^- anions and thus the uncertainty of U_- is high. The same applies to the NaBr results, which are not shown here. The interaction potentials U_- of the anions, as they have been obtained from the fits are summarized in **Table 7-17**.

Table 7-17. Interaction potentials of anions X^- for different concentrations of NaX salt solutions

P_0 = 8.635 x 10^8, λ = 2.55 Å, A = 0.4 kT				
Concentration C / M	**I. Potential U_{Br} / kT**	**I. Potential U_{NO3} / kT**	**I. Potential U_I / kT**	**I. Potential U_{SCN} / kT**
0.05	----	----	-1.70 ± 0.05	-3.00 ± 0.05
0.1	----	-0.8 ± 0.2 (?)	-2.2 ± 0.05	-3.20 ± 0.05
0.5	----	-1.5 ± 0.5 (?)	-6.00 ± 0.2	-7.00 ± 0.05

The results of **Table 7-17** illustrate that the interaction potentials depend on the anion and the concentration of the salt solution used. The interaction potentials increase and follow the Hofmeister series of anions $Br^- < NO_3^- < I^- < SCN^-$ for the same salt concentration; for different salt concentrations the interaction potentials increase with concentration. For salt concentrations equal to 0.5 M very big interaction potentials are required in order to fit the experimental data. Generally, the interaction potentials of anions estimated using the diffuse layer model demonstrate the same behavior as the binding constants presented in **Table 7-16**. In fact, the binding constants of anions obtained from the binding model can be roughly transformed to interaction potentials using the following approximate expression:

$$\delta A N_{AV} e^{-\frac{U_{-,i}}{kT}} \approx K_i \qquad \textbf{Equation 7-7}$$

where δ is the lipid layer thickness, A the headgroup area of the DPPC molecules in the presence of salt solutions, and N_{AV} is Avogadro's number. **Equation 7-7** can be derived if we assume that a lipid layer exerts a square-well attractive potential on the anions. As a result, a comparison of the two different models can be achieved. The results of the converted binding constants to interaction potentials of anions are given in **Table 7-18**.

Table 7-18. Interaction potentials of anions X^- calculated using Equation 7-7 for different concentrations of NaX salt solutions

P_0 = 8.635 x 10^8, λ = 2.55 Å, A = 0.4 kT			
C / M	**0.05 M**	**0.1 M**	**0.5 M**
Salts	**U_- / Kt**	**U_- / kT**	**U_- / Kt**
NaBr	----	-0.27	-0.94
$NaNO_3$	----	-0.9	-1.6
NaI	-1.70	-2.3	-6.31
NaSCN	-3.04	-3.18	-7.01

The results of **Table 7-18** point out that there is a very good agreement between the binding constants and the interaction potentials of anions, although the two models are based on a different picture of the lipid-electrolyte interface.

The conclusion reached from the above fitting analysis using either the binding model or the diffuse layer model is that at low salt concentrations one can fit the data with more or less comparable parameters (binding constants or interaction potentials) while at high salt concentrations both models fail to fit the experimental data with the same parameters as for small salt concentrations; bigger binding parameters are needed to fit the data. This suggests that an extra repulsion may be present at high salt concentrations, which must taken into account in the fitting models. It is possible that in the presence of very high concentrations of chaotropic ions the interface is considerably "softened" and the perpendicular headgroup fluctuations (protrusion forces) increase considerably. Another possibility is that the interfacial rigidity increases, leading to stronger undulation repulsion, although this is in contrast to theoretical considerations and is not visible as increased peak broadening of the SAXS peaks as shown in **Figure 7-50** for DPPC in the presence of NaSCN, which is the salt that has the strongest effect on the logΠ – d_w curves. In fact, the peaks appear to become thinner (less broad) as the electrolyte concentration increases.

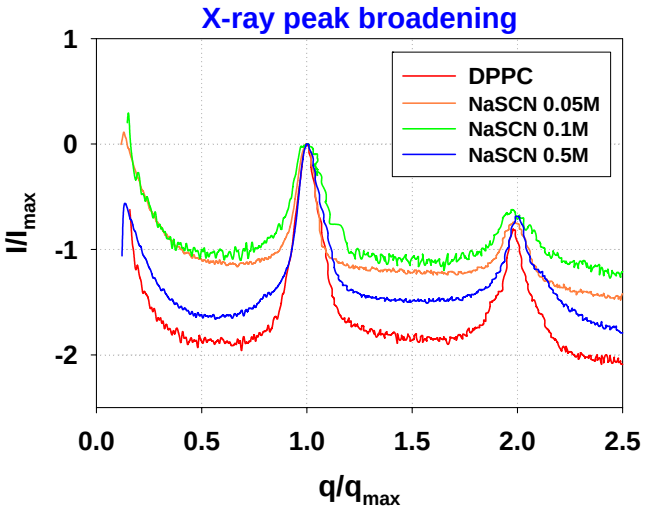

Figure 7-50. X-ray peak broadening dependence on NaSCN salt concentration

8 CHAPTER

MICELLE EXPERIMENTAL RESULTS

8.1 Introduction – Micelle/Ion interactions in aqueous solutions

In the final part of this thesis we have determined (using DLS and SLS) the physical properties of DPC micelles in water and in the presence of various NaX salt solutions. There are several advantages of using the zwitterionic surfactant dodecylphosphocholine (DPC) for such a study: (i) The interface is not charged initially, and the added salt produces a charging of the interface with a detectable increase of lateral electrostatic interactions. (ii) DPC micelles are very well characterized. DPC forms small spherical micelles in water, the main physical parameters of which, as they have been obtained by others, are given in **Chapter 4**. (iii) The use of single chain surfactants of easily measurable (incompressible) molecular volume V_{mol} provides a clear advantage since, if the globular shape of the micelles is ascertained, then as a consequence of surface and mass conservation one can estimate the aggregation number of the micelle, N, and the headgroup area, α, given by **Equations 3.7-19** and **3.7-20** (**Chapter 3**, **Section 3.7.5**) . The equilibrium area per head group of DPC monomers in the micelles is the main experimental result.

8.2 DLS Data Analysis

In order to find the critical micelle concentration of DPC micelles in water and in the presence of NaX salt solutions, we used the following process: We prepared samples of different surfactant concentrations in water and also in solutions of known salt concentration e.g. 0.45M or 1.35M, and we measured the intensity of the scattered light, I_S, at 60° for each sample using the Brookhaven BI-9000AT Digital correlator as explained in **Chapter 3**, **Section 3.7.4**. Before measuring the scattering intensity, the samples were filtered using a Whatman Inorganic membrane filter of 0.1μm cutoff or a Millex PVDF Durapore sterile filter of 0.1μm cutoff, and then centrifuged at a speed of 3000rpm for 1-2min to completely remove dust particles and other large-size contamination. The intensity of pure water was subtracted from the intensity of the scattered light, I_S, and the result was divided by the intensity of a reference solution such as benzene, I_B. Both I_S and I_W were measured several times during each experiment. As a result, the expression $\frac{I_S - I_W}{I_B}$ was obtained and used for each sample. This expression is plotted against the concentration of DPC in the samples and the cmc is obtained by fitting the experimental points (linear regression), for which the expression deviates from the initial horizontal line. As an example, the results obtained for DPC micelles in water are shown in **Table 8-1** and **Figure 8-1**. Each experiment was repeated five times and the values presented are the averages of the five measurements.

Table 8-1. Measured scattered light intensity for DPC micelles in water

DPC Concentration / mM	Reduced Intensity $(I_S - I_W)/I_B$
0.225	0.0
0.410	0.0
0.614	0.0
0.814	0.0
0.930	0.0
0.985	0.0
1.000	0.0
1.500	0.033
2.000	0.085
3.100	0.170
5.000	0.340
1.000	0.850

The linear regression of the experimental results (given with red colour in **Table 8-1)** is shown in **Figure 8-2**. The linear regression yields the equation y = 93.85x – 0.109 (R^2 = 0.9985) from which setting y = 0 we calculate the cmc of DPC in water. In this experiment, the cmc was found equal to 1.16 x 10^{-3} M or 1.16 mM.

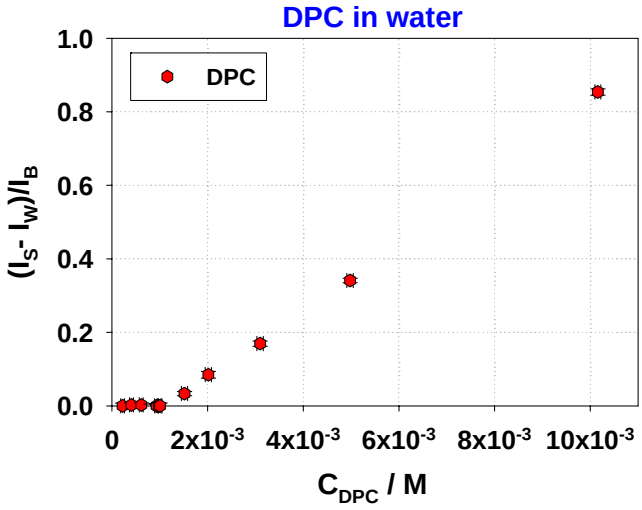

Figure 8-1. Reduced Intensity vs Concentration for DPC in water

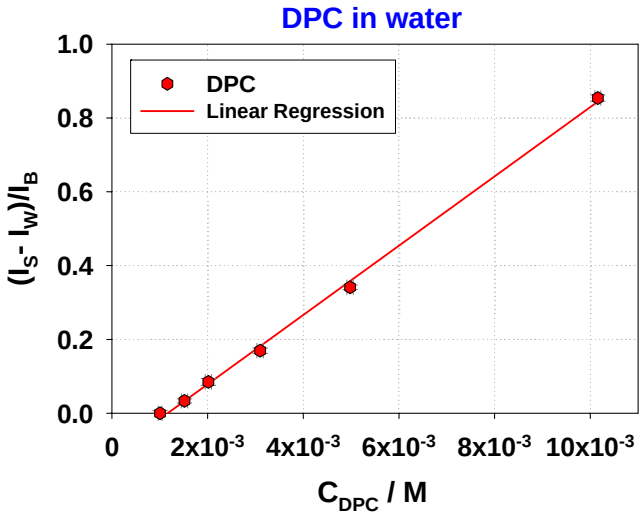

Figure 8-2. Linear Regression of reduced intensity vs concentration of DPC in water

The size of the DPC micelles was calculated using the standard method of cumulant expansion available in the BI-9000AT correlator software. Different approaches have been used, the best one being the Quadratic fit analysis for which

$$\ln[g_1(t_d)] \equiv K_1 t_d + \frac{K_2 t_d^2}{2!} \qquad \textbf{Equation 8.2-1}$$

where K_1 and K_2 are given in **Chapter 3**, **Equation 3.7-16**. **Figure 8-3** shows the size (diameter) of the DPC micelles in water, found by the DLS analysis **Equations 3.7-17** and **3.7-11**, as a function of the concentration of DPC. Each experimental point is an average of five independent measurements.

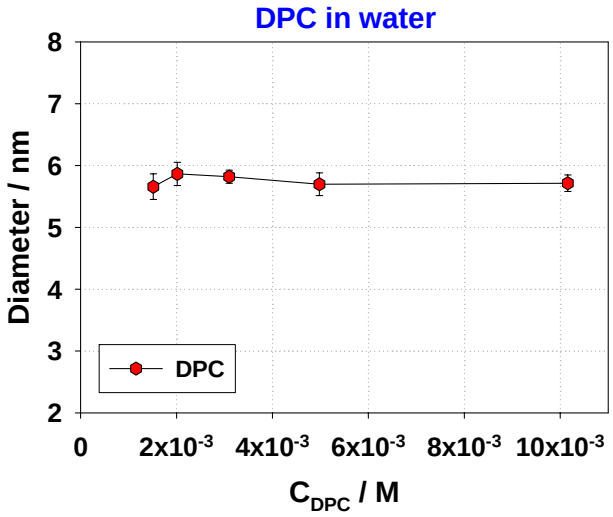

Figure 8-3. Size of DPC micelles in water calculated from the DLS data

The average value of the diameter of DPC micelles in water is ≈ 5.7 nm. The size of the DPC micelles found by DLS analysis is compared to the size found by the standard equations used for SLS as explained in **Chapter 3**, **Section 3.7.5**.

8.3 SLS Data Analysis

In order to find the size of DPC micelles in water using **Equation 3.7-18** we need to know the aggregation number and the mass of the DPC micelles. The mass of the micelles, M, is obtained from Debye's scattering theory:

$$\frac{KC}{R_\theta} = \frac{1}{P(\theta)}\left(\frac{1}{M} + 2BC\right) \qquad \textbf{Equation 8.3-1}$$

where R_θ is the Rayleigh ratio, C is the concentration of DPC micelles in the samples, B is the second virial coefficient, K is an optical constant and P(θ) is the form factor or the intraparticle structure factor. The optical constant K is defined as:

$$K = \frac{4\pi^2 n_B^2}{\lambda^4 N_{AV} R_B}\left(\frac{\partial n}{\partial C}\right)^2 \qquad \textbf{Equation 8.3-2}$$

where n_B and R_B are the refractive index and the Rayleigh ratio of the reference solution (Benzene), N_{AV} is Avogadro's number, λ is the wavelength of the laser beam (514 nm), and $\partial n/\partial C$ is the change of the refractive index of the samples with the concentration of DPC, which was measured (see below).

The intraparticle structure factor is defined as follows:

$$P(\theta) \approx \frac{1}{1+\frac{Q^2}{3}} \qquad \textbf{Equation 8.3-3}$$

Here Q = qR; q is the scattering vector and R the micellar radius. Assuming that qR << 1, due to the fact that the size of DPC micelles is small, the intraparticle structure factor tends to unity and thus is not taken into account.

In addition, we assume that the interparticle interactions are negligible, because the concentration of DPC micelles in the samples is small (Cmax = 5e-3 M), therefore they are not taken into account. Thus, the second virial coefficient B → 0 or S(q) → 1.

As a result, **Equation 8.3-1** is modified as follows:

$$\frac{KC}{R_\theta} = \frac{1}{M} \text{ or } R_\theta = KMC \qquad \textbf{Equation 8.3-4}$$

In our experimental analysis we used **Equation 8.3-4** to find the micellar mass of DPC in water and in the presence of salt solutions by plotting the intensity of the samples, taken as $I = (I_S - I_W)/I_B$, versus the concentration of DPC in the micelles taken as $C = [C_{DPC} - C_{cmc}]$ / (g/cm^3) as shown in **Figure 8-4** for DPC in water. By fitting the experimental results with a linear regression (R^2 = 0.999) we obtain the slope and the intercept of the regression line,

which in this case are equal to 270 cm^3/g and ≈ 0 respectively. The slope is equal to KM and can be used to estimate the DPC micellar mass, if we know in advance the optical constant K. In order to calculate the optical constant K we need to know the derivative $\partial n/\partial C$. We prepared samples of known surfactant concentration in water and we measured the refractive index, n, of each sample. **Figure 8-5** shows the plot of the measured refractive index, n, versus the concentration of DPC in the samples.

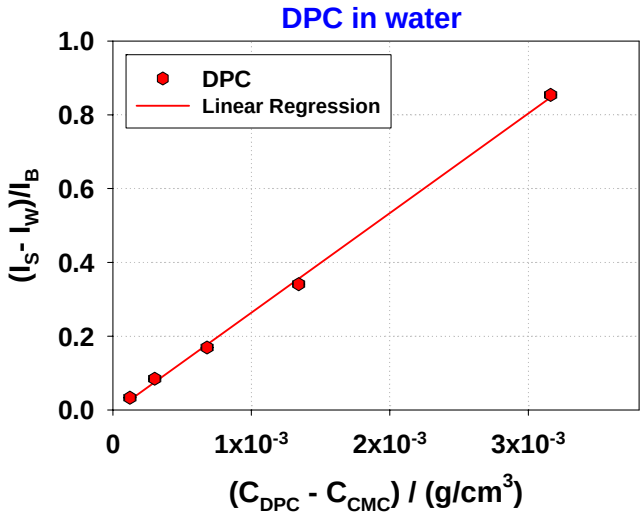

Figure 8-4. Static light scattering results for DPC in water

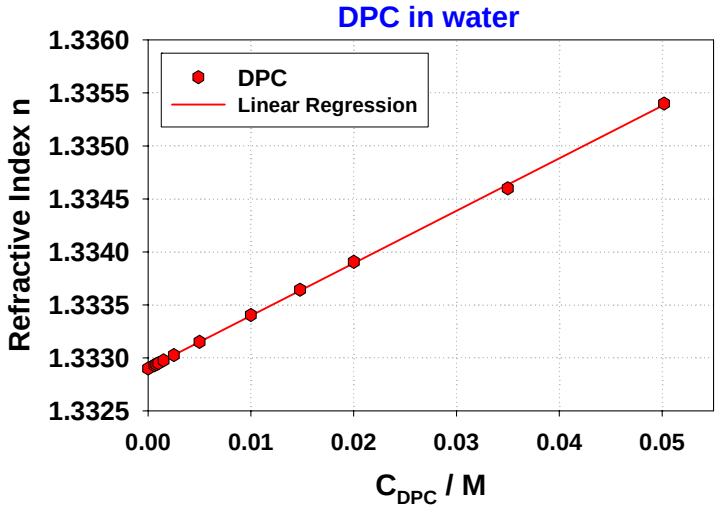

Figure 8-5. Refractive indices as function of DPC concentration in water

The slope of the graph (R^2 = 0.999) gives the change of the refractive index n with DPC concentration, $\partial n/\partial C$, which is equal to 0.1405 cm^3/g. As a result, the optical constant can be

calculated and then the micellar mass, M, and consequently the aggregation number, N, can be estimated.

Going one step further, we can estimate the area per headgroup, α, of DPC in water and in the presence of salt solutions using **Equation 3.7-20** (**Chapter 3, Section 3.7.5**). In order to do that, we need to know the aggregation number, and the radius R of the DPC micelles. To estimate the micellar radius we must know the molecular volume of DPC, V_{mol}, as is shown in **Equation 3.7-18** (**Chapter 3, Section 3.7.5**). V_{mol} can be calculated from density measurements of the solution as a function of the DPC mass fraction. For a solution containing n_1 molecules of the solvent (water) of molecular mass M_1 and molecular volume V_1 and n_2 molecules of the solute (DPC) of molecular mass M_2 and partial molar volume V_2, the volume $V_2 = V_{mol}$ is given by the following equation (**see Appendix III**):

$$V_2 = M_2\left(s + \frac{1}{\rho_0}\right) \qquad \textbf{(Equation III-9)}$$

where s is the slope of a graph of 1/ρ vs w% (ρ is the measured density of the samples) and ρ_0 is the density of pure water. **Table 8-2** and **Figure 8-6** show the experimental results 1/ρ vs w% obtained using an Anton Paar DMA 5000 density meter.

Table 8-2. Density of DPC aqueous solutions

w%	0.103	0.22	0.25	0.52	0.75	1.08
Inverse density 1/ρ / (ml/g)	1.0029	1.0028	1.0027	1.0025	1.0023	1.0021

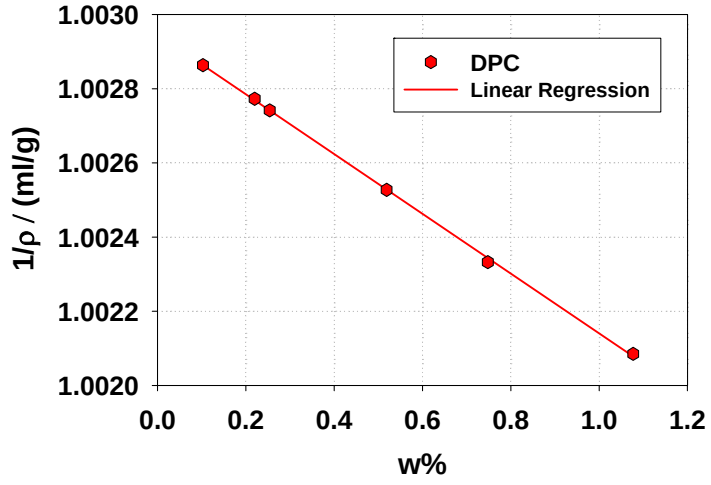

Figure 8-6. Density of DPC aqueous solutions at 25 °C

The linear regression of the plot 1/ρ vs w gives the equation y = (-0.8055)x + 1.0029, from which V_{mol} was found equal to 539 $Å^3$ and consequently the density of the DPC molecule is equal to ρ = 1.084 g/ml. Using **Equations 3.7-18** to **3.7-20** we have computed the surface area, α, of the DPC molecules in the micelles and all other physical parameters of DPC micelles in water. These are tabulated in **Table 8-3**.

Table 8-3. Physical parameters of DPC in water

Parameters	DPC in water
CMC / mM	1.16 ± 0.06
(dn/dC) / (cm^3/g)	0.1405 ± 0.0007
Aggregation number N	56.0 ± 1.4
Surface area α / $Å^2$	85.0 ± 2.2
Diameter / nm (DLS)	5.70 ± 0.05
Diameter / nm (SLS)	4.00 ± 0.05

Similar analysis as for DPC in water was made for DPC micelles in NaX salt solutions of concentrations 0.45M and 1.35M. The NaX salts used were NaCl, NaBr, $NaNO_3$, NaI, NaSCN and $NaClO_4$. **Figures 8-7** to **8-12** show plots of the intensity $(I_S - I_W)/I_B$ versus the concentration of DPC in the presence of NaX solutions. The graphs of $(I_S - I_W)/I_B$ vs the corrected concentration of the samples C = [C_{DPC} - C_{cmc}] (DPC micellar mass estimation) and the plots of the measured refractive index, n, versus the concentration of DPC ($\partial n/\partial C$ estimation) in the presence of salt solutions are given in **Appendix III**.

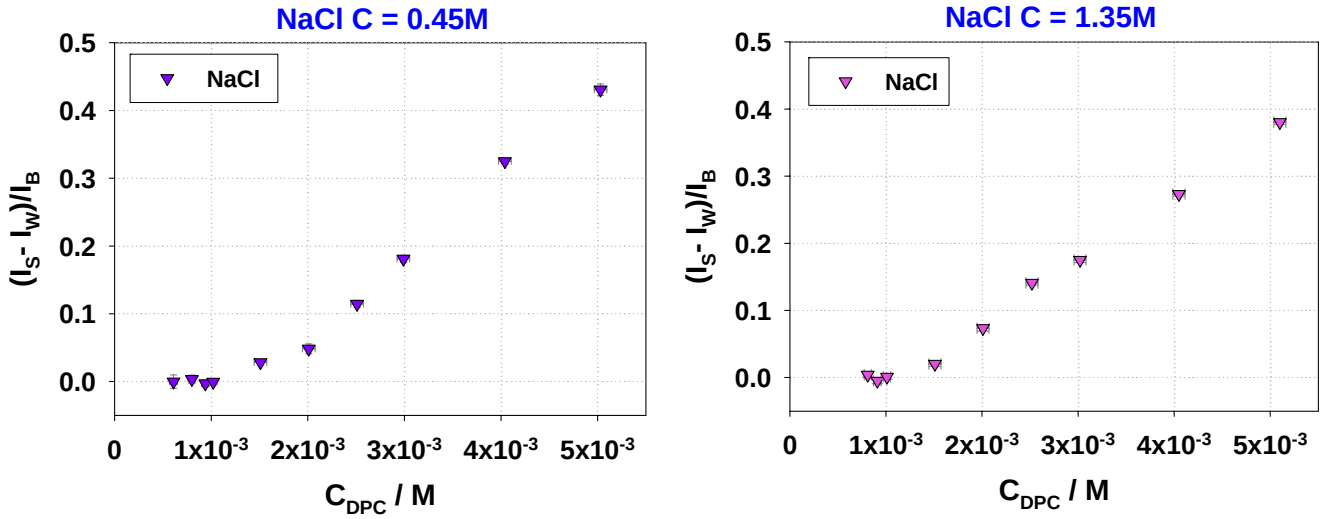

Figure 8-7. Reduced Scattered light Intensity vs Concentration of DPC in NaCl solutions

The physical properties of DPC micelles in NaX salt solutions are given in **Tables 8-4** and **8-5** while **Figure 8-13** to **8-16** show the effect of the concentration and ion type of the NaX salts on the physical properties of the DPC micelles.

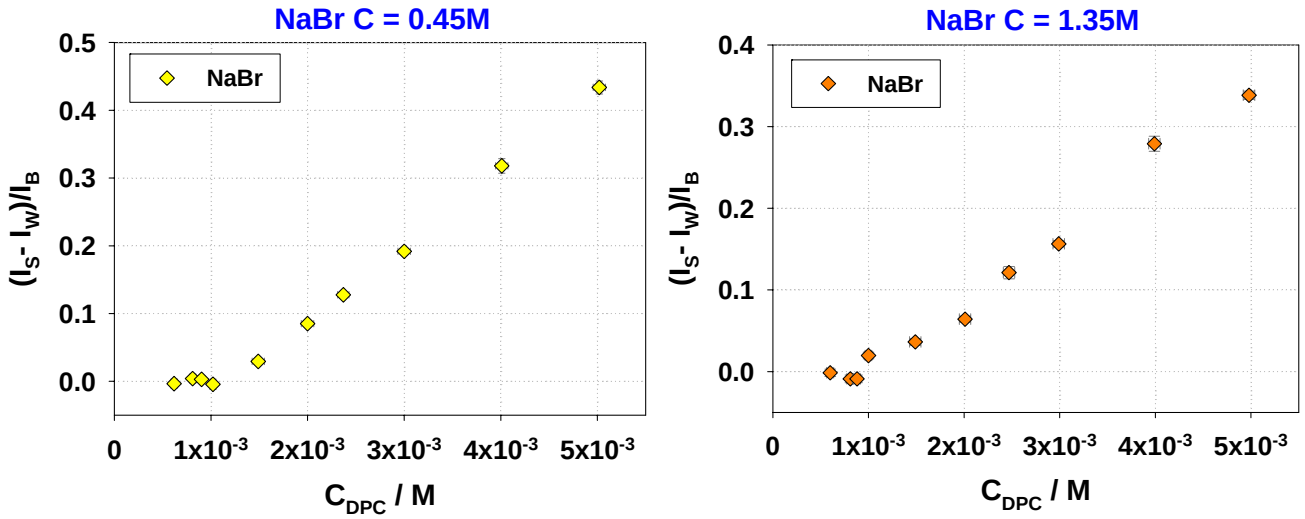

Figure 8-8. Reduced Scattered light Intensity vs Concentration of DPC in NaBr solutions

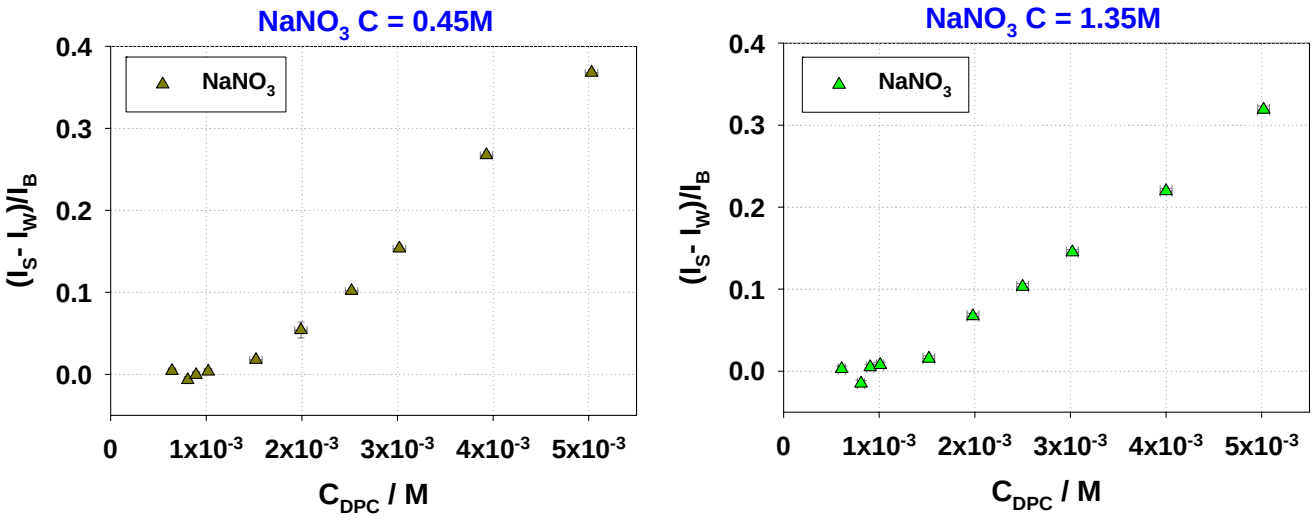

Figure 8-9. Reduced Scattered light Intensity vs Concentration of DPC in $NaNO_3$ solutions

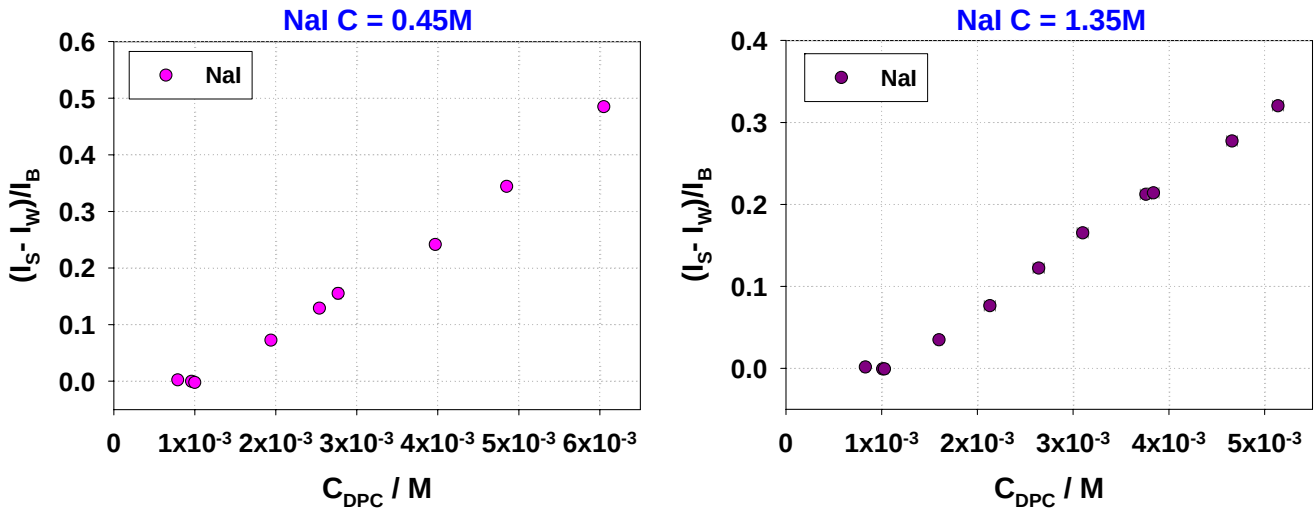

Figure 8-10. Reduced Scattered light Intensity vs Concentration of DPC in NaI solutions

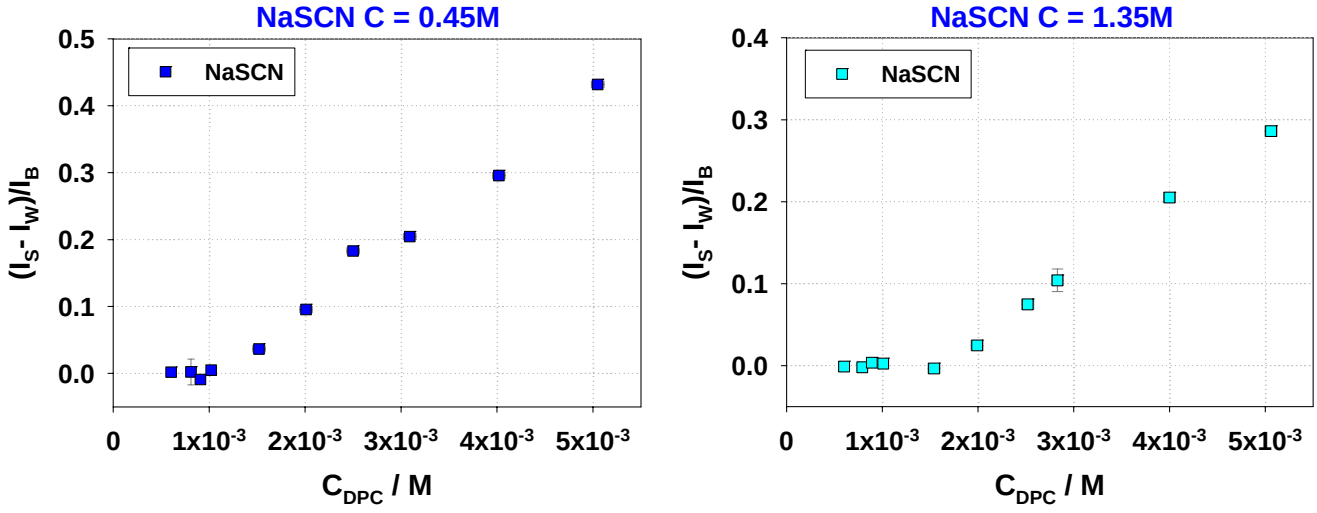

Figure 8-11. Reduced Scattered light Intensity vs Concentration of DPC in NaSCN solutions

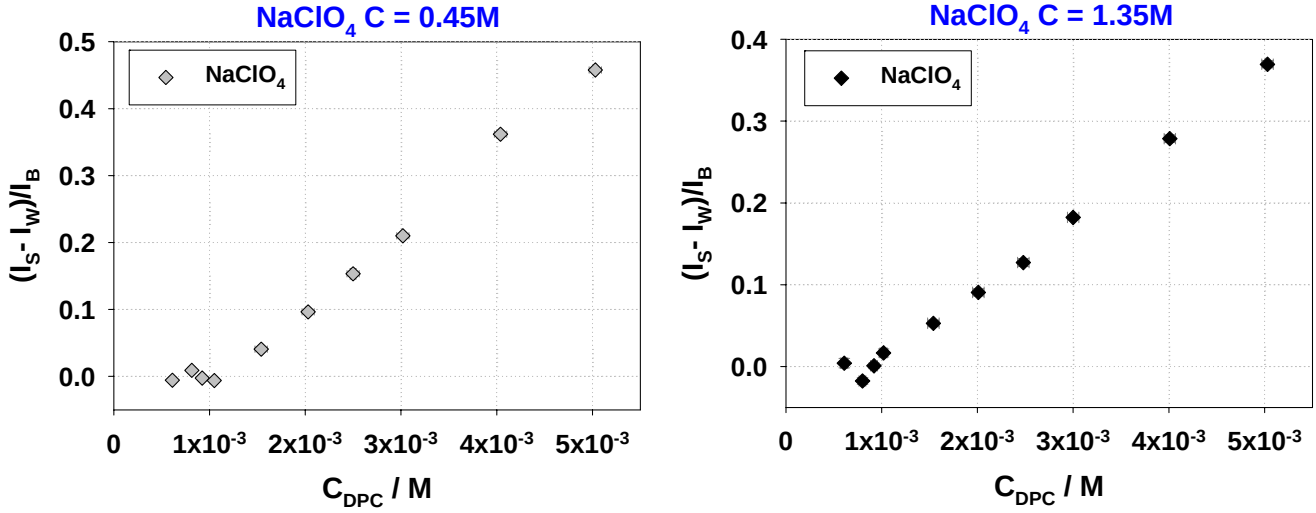

Figure 8-12. Reduced Scattered light Intensity vs Concentration of DPC in $NaClO_4$ solutions

Table 8-4. Physical properties of DPC micelles in the presence of NaCl, NaBr and $NaNO_3$

Concentration	Parameters	NaCl	NaBr	$NaNO_3$
0.45 / M	CMC / mM	1.460 ± 0.061	1.260 ± 0.042	1.460 ± 0.053
	(dn/dC) / (cm^3/g)	0.134 ± 0.006	0.138 ± 0.005	0.142 ± 0.006
	Aggregation number N	79.0 ± 6.3	70.0 ± 1.5	60.0 ± 2.5
	Surface area α / $Å^2$	75.0 ± 7.1	77.5 ± 2.0	81.8 ± 4.0
	Diameter / nm (DLS)	5.3 ± 0.2	5.8 ± 0.2	5.5 ± 0.2
	Diameter / nm (SLS)	4.3 ± 0.1	4.20 ± 0.05	3.90 ± 0.05
1.35 / M	CMC / mM	1.240 ± 0.042	1.180 ± 0.061	1.280 ± 0.050
	(dn/dC) / (cm^3/g)	0.138 ± 0.006	0.139 ± 0.007	0.134 ± 0.007
	Aggregation number N	59.0 ± 3.2	55.0 ± 3.3	55.0 ± 3.0
	Surface area α / $Å^2$	82.0 ± 5.3	84.0 ± 6.0	84.5 ± 5.4
	Diameter / nm (DLS)	5.2 ± 0.15	4.8 ± 0.2	4.30 ± 0.15
	Diameter / nm (SLS)	3.9 ± 0.1	3.8 ± 0.1	3.8 ± 0.1

Table 8-5. Physical properties of DPC micelles in the presence of NaI, NaSCN and $NaClO_4$

Concentration	Parameters	NaI	NaSCN	$NaClO_4$
0.45 / M	CMC / mM	1.280 ± 0.057	1.190 ± 0.055	1.230 ± 0.051
	(dn/dC) / (cm^3/g)	0.141 ± 0.008	0.148 ± 0.008	0.1138 ± 0.0002
	Aggregation number N	57.0 ± 5.7	58.0 ± 1.0	109.0 ± 2.2
	Surface area α / $Å^2$	82.5 ± 9.0	83.0 ± 1.8	67.0 ± 1.5
	Diameter / nm (DLS)	4.7 ± 0.3	4.50 ± 0.15	5.1 ± 0.1
	Diameter / nm (SLS)	3.9 ± 0.1	3.90 ± 0.05	4.80 ± 0.05
1.35 / M	CMC / mM	1.160 ± 0.052	1.620 ± 0.060	1.050 ± 0.056
	(dn/dC) / (cm^3/g)	0.139 ± 0.005	0.144 ± 0.009	0.165 ± 0.007
	Aggregation number N	49.0 ± 0.6	47.0 ± 2.0	40.0 ± 1.0
	Surface area α / $Å^2$	87.3 ± 1.3	89.0 ± 4.5	94.0 ± 3.5
	Diameter / nm (DLS)	3.0 ± 0.1	3.1 ± 0.2	4.8 ± 0.1
	Diameter / nm (SLS)	3.70 ± 0.05	3.6 ± 0.1	3.40 ± 0.05

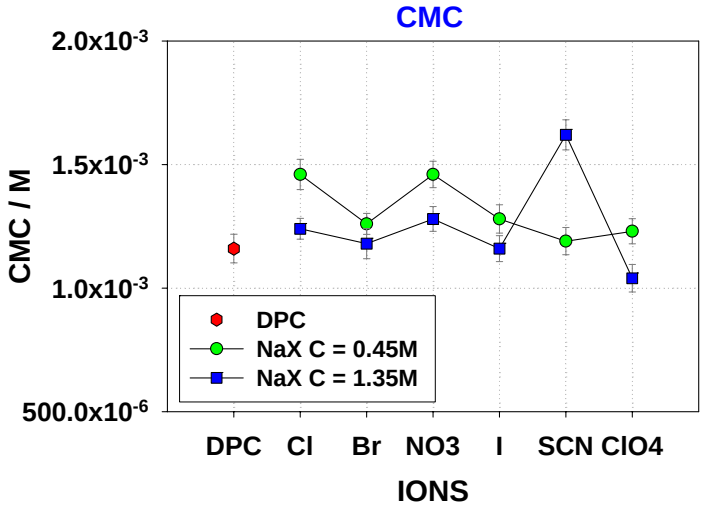

Figure 8-13. Critical micelle concentration of DPC in the presence of NaX salt solutions

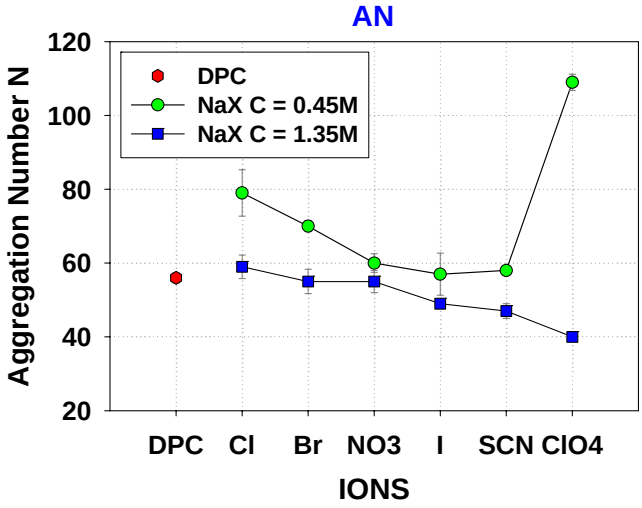

Figure 8-14. Aggregation number of DPC micelles in the presence of NaX salt solutions

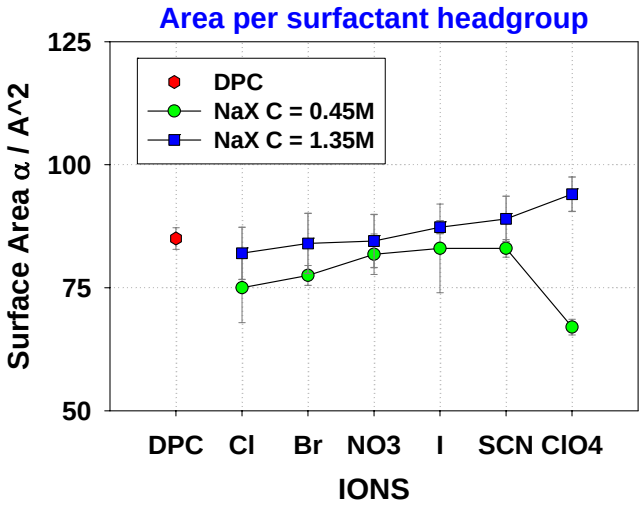

Figure 8-15. Area per headgroup of DPC micelles in the presence of NaX salt solutions

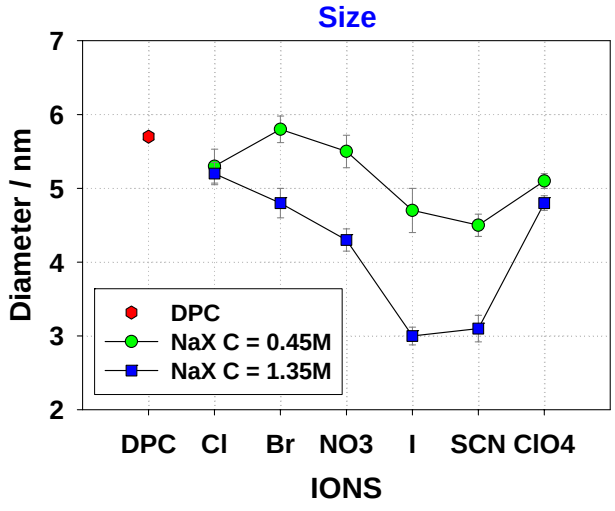

Figure 8-16. Diameter (DLS) of DPC micelles in the presence of NaX salt solutions

Figure 8-13 shows the effect of the concentration and the effect of the anion used in the NaX solutions on the cmc of DPC micelles. At a salt concentration of 0.45 M the cmc increases for all the anions in comparison with the cmc of DPC micelles in pure water. This may be explained by the increase of the electrostatic repulsion between the surfactant headgroups as the micelles acquire a surface charge due to ion-headgroup association. As a result, the cmc of DPC increases. On the contrary, the cmc of DPC micelles decreases when the concentration of NaX electrolytes increases further to 1.35M. The decrease of the cmc at higher salt concentrations is due to the screening of the electrostatic repulsion by the double layer formed. *The type of the anion in solution does not appear to have any influence on the cmc of DPC molecules.*

The effect of the concentration and type of the anion used on the aggregation number N of DPC micelles is shown in **Figure 8-14**. The aggregation number decreases with salt concentration but it also decreases when the anion in the aqueous solution changes from the hydrophilic (cosmotropic) Cl^- to the hydrophobic (chaotropic) SCN^-. The chaotropic anion ClO_4^- does not appear to have the same effect on the aggregation number as I^- and SCN^-, especially at NaX concentrations of 0.45M. This may be due to the change of the globular geometry of the micelles in the presence of ClO_4^-. In general, the effect of the anion type on the aggregation number, N, of DPC micelles follows the Hofmeister series.

The behaviour of the equilibrium area per headgroup of DPC micelles for the different anions used follows the behaviour of the aggregation number, as shown in **Figure 8-15**. That is, as the aggregation number *decreases* with concentration and type of the anion, the surface area of DPC micelles *increases* with concentration and type of anion used in the NaX salts. The effect of the anion type is more pronounced at small concentrations (0.45M). Hydrophilic anions, such as Cl^- and Br^-, appear to dehydrate the headgroup of the DPC molecules. The size of the headgroup of DPC micelles decreases in the presence of these ions compared to that in pure water, due to competition of the osmotic equilibrium of water between the surfactant headgroups and the specific anions. ClO_4^- deviates again from the general behaviour at 0.45M, indicating that the geometry of the DPC micelles is not maintained in the presence of this electrolyte.

Figure 8-16 shows the hydrodynamic size (diameter) of DPC micelles, as obtained by the numerical fit of the DLS software. From **Figure 8-16** it is apparent that the size of the DPC micelles is greatly affected both by the concentration of the electrolytes but also by the type of the anion in the NaX salts. The size of the DPC micelles decreases significantly with

concentration and type of the anion. The chaotropic anions I^- and SCN^- have the biggest influence on the micellar size for both concentrations. Generally, the effect on the size of the DPC micelles follows the Hofmeister series. The reason why the micellar size decreases with concentration and type of the anion is not obvious. It may be due to dehydration of the DPC molecules, to the change of the globular shape of the micelles in the presence of the anions, or even to the existence of interparticle interactions between the DPC molecules that were not considered in the present analysis.

8.4 Evaluation of free energy of micellization

The binding constants, K, of anions on DPC micelles are calculated using **Equation 5.2-11** (**Chapter 5**). Since the presence of a salt influences the head group size by dehydration as seen above, the comparison can only be made in relative terms. The Cl^- ion is used as a reference state without electrostatic lateral repulsion since we assume that Cl^- does not adsorb on the micelles. For the determination of the association constant, K, a theoretical model was used that connects the area per headgroup of DPC micelles with the free energy of micellization in the presence of anions.

The general relation between headgroup surface area and free energy of micellization is known (see **Chapter 5**, **Section 5.5.1**). The free energy F per mole of surfactant in the micelle is given by **Equation 5.5-1**:

$$F_m = \gamma(\alpha-\alpha_0) + \frac{C(\mu_{H_2O})}{\alpha-\alpha_0} + F_{el} \qquad \textbf{(Equation 5.5-1)}$$

α_0 was taken as $20 Å^2$. The micelle/water surface tension γ was chosen to be equal to $\gamma = 25$ mN/m a value often adopted in the literature for small micelles of single-chain surfactants. The constant C is adjusted so that the area per headgroup coincides with the observed value for the “reference” salt which is NaCl in the present study.

The procedure that is followed in order to find the apparent binding constant of anions on the headgroups of DPC is explained below:

In the absence of salt, the free energy of micellization is the sum of the first two terms in **Equation 5.5-1**. The constant C in this case is adjusted so that the minimum value of F_m is found at the equilibrium surface area of DPC micelles in pure water. In the presence of a non-

adsorbing anion, such as Cl^-, F_m keeps the same form as in the absence of salt, but the constant C is modified so that the minimization of F_m gives the correct area per headgroup. In the presence of an adsorbing salt like I^- or SCN^-, the free energy of micellization is given by **Equation 5.5-1** in which the electrostatic free energy is added. The first two terms are taken to be the same as in the case of the non-adsorbing salt, considered here to be our "reference" state since we assume that the hydration state of the surfactant headgroups does not change significantly when Cl^- is exchanged for another ion. To obtain the electrostatic term, F_{el}, one must first calculate the fraction of surfactant molecules on which anions are absorbed, x_b. This is given by the law of mass action and the Grahame equation (see **Chapter 5**). The solution is obtained by numerical iteration. The binding constant K in **Equation 5.2-11**, is adjusted in order to obtain the desired area per headgroup of DPC in the presence of an adsorbing anion.

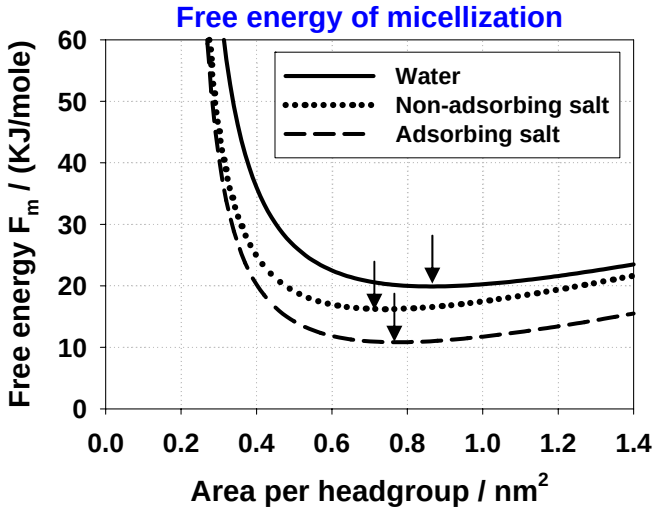

Figure 8-17. Evaluation of the free energy of micellization per surfactant vs area per molecule

Figure 8-17 shows the evaluation of free energy of micellization according to **Equation 5.5-1**. The position of the minimum gives the experimental equilibrium headgroup area in three different cases: without added salt (solid line), with a non-adsorbing salt (dotted line) and with an adsorbed anion (bottom line).

From the measured area increase, we have derived the apparent binding constant K (fitting parameter in the PB analysis). The results are given in **Table 8-6**.

The order of magnitude of x_b necessary to explain the sensitivity observed for the micellar mass versus the nature of the counter-ion is compatible with the Hofmeister series. Larger x_b are found for the more hydrophobic ions. However, the numbers obtained for x_b are not

credible. It is hard to imagine that 75% of the DPC molecules are charged by adsorption of an I^- or SCN^- ion.

Table 8-6. Measured increase of area per head-group for an overall salinity of 0.45M, binding constants K and percentage of ion-occupied surface sites

Parameters	Br^- vs Cl^-	NO_3^- vs Cl^-	I^- vs Cl^-	SCN^- vs Cl^-
Surface area of DPC per molecule at equilibrium over that in NaCl / Å^2	+3	+6	+7.5	+8
K / M^{-1}	20	340	1000	1200
x_b (percent coverage of surface sites by ions)	25%	55%	70%	75%

When the fitted constants K of **Table 8-6**, extracted at salinity 0.45M, are used to derive the area at equilibrium at the higher salinity of 1.35M, the agreement with experiment is only qualitative. It is clear that these binding constants exhibit strong concentration dependence, as was also found in the case of the DPPC monolayers and bilayers. The results of the DPC work verify that a standard chemical binding model is inappropriate for the treatment of Hofmeister anion interactions with lipid interfaces.

9 CHAPTER

DISCUSSION AND CONCLUSIONS

The effect of various NaX electrolytes on the three model systems studied in this thesis (monolayers, bilayers, and micelles) is significant and follows the Hofmeister series.

9.1 Conclusions from the monolayer study

The addition of electrolytes in the aqueous subphase of DPPC monolayers leads to a general increase of the surface pressure at a fixed area per molecule, which depends on the salt concentration and the type of anion in the subphase following the Hofmeister anion series. The increase of the surface pressure at a fixed area per molecule indicates a stabilization of the liquid-expanded phase of the monolayer. Experiments using Brewster angle microscopy have shown that in the presence of electrolytes the domains become rounder instead of more elongated implying that the electrostatic term, which determines their shape, decreases in the presence of salt. This can be understood as a screening effect, and it suggests that anions do not bind to the LC domains. GIXD and IRRAS experiments provide definite evidence that the structure of the LC phase is largely insensitive to the type and concentration of anions in the subphase. The lattice parameters and the ordering of the lipid molecules in the liquid-condensed phase remain essentially unaffected even at quite high electrolyte concentrations. The different results (alteration of the chain packing) found for NaI of concentration 1.5M are not the result of electrostatic interactions between I^- and the PC head group but can be explained by the formation of iodine in the subphase through a radical-mediated oxidation reaction. The hypothesis of the LE phase stabilization in the presence of electrolytes is

supported by IRRAS measurements, which show that on a NaI subphase the proportion of gauche conformers in the alkyl chains is considerably enhanced at low pressures, and that the LE/LC phase transition extends over a wider range of surface pressures. These findings suggest that anions partition into or bind to the looser liquid-expanded phase, thus providing entropic stabilization of that phase, but do not penetrate into or bind to the domains of the liquid-condensed phase. The emerging picture that can explain the above idea is shown in **Figure 9-1**.

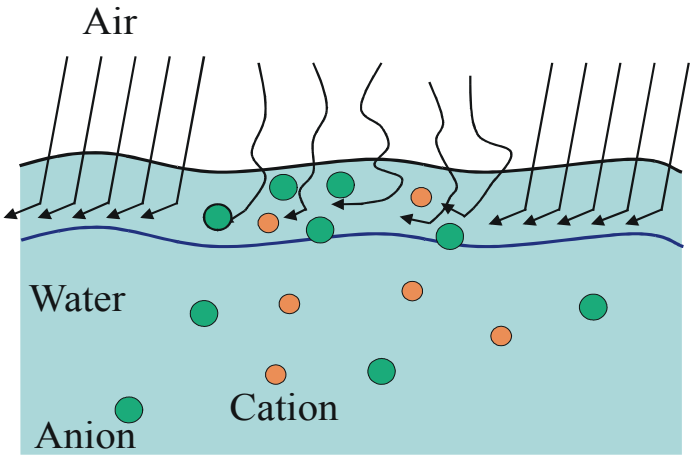

Figure 9-1. Schematic representation of the behavior of ions in a DPPC monolayer in the presence of both LE and LC phases

Here we see that ions penetrate into the disordered LE phase more easily, either binding to the lipids or partitioning in the phase in a more delocalized way. On the contrary, the ions do not interact strongly with the LC phase. The increase of the surface pressure, especially in the presence of the more chaotropic anions, can be understood by evoking two different but not necessarily contradictory pictures:

(a) There is preferential adsorption of anions compared with sodium in the head group region, which is greater for the more chaotropic anions. This adsorption may occur either through strong local binding or through dispersion forces. As a result the monolayer acquires an excess of negative charge, and there is an expansion of the LE phase at fixed pressure or equivalently an increased pressure at fixed area.

(b) There is no preferential binding, but the anions are expelled from the subphase and enter the disordered LE phase, because there is a free energy gain for water in this way leading to a net gain in free energy for the whole system. This monolayer penetration is stronger for the more chaotropic ions. This may or may not result in the creation of

excess negative charge, depending on the amount of cations that enter the LE phase as well. *The crucial result in this picture is an increase of the entropy of the LE phase, which is thus entropically stabilized.*

Various pieces of evidence from the monolayer experimental results appear to support mechanism (b): First, if anions are strongly and specifically bound to the lipids this should happen for the LC phase as well, which would presumably give completely different BAM images and GIXD results. The counter argument is that the LC phase is very ordered and that the positive choline groups are not available for ion binding, being ion-paired to neighboring phosphate groups in the crystal lattice. A second argument is based on the fact that many pressure-area isotherms appear to converge at high surface pressures and that infrared frequencies approach those of DPPC on pure water at high pressures. This implies that ions are "squeezed out" from the monolayer at high pressures, and it is not obvious how this would be possible if strong local binding was happening. **Kölsch et al. 2004** and **Krasteva et al. 2001** recently observed "squeezing-out" of ions or even different hydrophobic molecules such as sugars from monolayers. Moreover, a strong non-specific penetration of anions into lipid phases has been found in the recent Molecular Dynamics simulations of **Sachs et al. (2003 and 2004)**.

In order to elucidate which of the two mechanisms is really acting, two theoretical models have been used to study the interaction of anions with lipid interfaces. These models assume that either the anions bind to the phospholipid headgroups through a chemical reaction or they penetrate the headgroup plane of DPPC molecules driven by an attractive potential towards the lipid layer. The results indicate that a simple chemical binding model of the anions on the headgroups of the DPPC molecules cannot explain the increase of surface pressure observed in the presence of NaX salt solutions in the subphase. In contrast, the diffuse layer model (partitioning model) is able to fit the experimental data very well. The modelling results are evidence that the X^- ions do not bind to the headgroups of the DPPC molecules. Modelling supports the idea that the LE phase is entropically stabilized through ionic partitioning in the interfacial lipid layer. The interaction potentials obtained by the fitting analysis through the diffuse layer model are anion-but not concentration-dependent and follow the Hofmeister series. In addition, the interaction potentials have been correlated to various ionic properties such as the size, R_P, the partial molar volume, V, the polarizability, α_p, the hydration free energy, ΔG_{hyd}, and the ion softness. It was found that the correlation between the interaction

potentials and individual ionic properties is not satisfactory indicating that the mechanism of the Hofmeister effect does not depend on individual ionic properties.

9.2 Conclusions from the bilayer study

The experimental logΠ – d_w curves of DPPC bilayers in the presence of salt solutions obtained using the small angle X-ray scattering in combination with the osmotic stress technique show that the water bilayer separation, d_w, (for the same osmotic pressure) increases when salts are present, which is observed at all salt concentrations. The electrolyte influence on d_w is more pronounced at small osmotic pressures and becomes weaker as the osmotic pressure applied to the bilayers increases, implying that the hydration force between DPPC bilayers in pure water and in the presence of salts is similar. The increase of the water bilayer separation depends on the type of anion and follows the Hofmeister series with SCN^- having the strongest effect on d_w. The increase of d_w depends also on the concentration of the sodium salt solutions used. In the presence of NaBr and $NaNO_3$ salt solutions, d_w does not seem to change by varying the salt concentration. On the contrary, d_w is greatly affected by the concentration of NaI and NaSCN salt solutions. The effect of NaSCN salt on d_w *decreases* upon *increasing* the concentration from 0.05M to 0.5M. Interestingly, NaI is more effective at a concentration of 0.1M while 0.05M provides the smallest effect and 0.5M gives intermediate results.

The difference between the force curves (logΠ – d_w) of DPPC in water and in the presence of NaX solutions, especially in the cases of NaI and NaSCN, is believed to be due to the existence of an electrostatic repulsive force created by the adsorption of Br^-, NO_3^-, I^-, and SCN^- on the DPPC headgroups. The strength of this electrostatic repulsive force depends on the electrolyte concentration. As discussed before, NaI and NaSCN, have slightly different effects on d_w as a function of their concentration. This complex behaviour can be explained by two phenomena; these are ion binding on the lipids and ion screening that determine the electrostatic repulsive force between the bilayers.

Maximum swelling experiments have been performed in order to determine the maximum swelling of DPPC (logΠ = 0, $d_w = d_{max}$) in the presence of different NaX electrolytes. The experimental results show that the maximum water uptake by the bilayers is influenced both by the type of the anion and the concentration of the sodium salt solutions. The anions used influence the maximum swelling following the Hofmeister anion series. The maximum

swelling of DPPC in the presence of NaBr and $NaNO_3$ is not influenced by the salt concentration and is about the same as that of DPPC in pure water. On the contrary, the maximum swelling of DPPC is greatly influenced by the presence of NaI and NaSCN.

In addition, the headgroup area of DPPC molecules at the bilayer surfaces was computed and appears to be affected by the type and concentration of anions used. The chaotropic anions I^- and SCN^- are those that affect the most the DPPC headgroup area, A. In addition, Br^- and NO_3^- appear to dehydrate the headgroup area, which can be attributed to their hydrophilic character. The effect of the anions is more pronounced at small osmotic pressures. In addition, the DPPC headgroup area appears to decrease as the concentration of the electrolyte solution is increased. The headgroup area of DPPC molecules in bilayers is compared below to the headgroup area of DPC molecules in micelles in the presence of NaX electrolytes.

Moreover, the effect of the ionic competition between Cl^- and I^- on the DPPC bilayer structure has been studied. The water bilayer separation, d_w, was found to increase as the percentage of I^- in mixed solutions of constant *total* [NaCl]+[NaI] was increased. Furthermore, d_w, does not follow a linear behaviour with the increase of I^- ions in the mixed solution, but it has a minimum at 0.5M *total* salt concentration. The water bilayer separation, d_w, was found to decrease as the *total* concentration of the solutions increased indicating screening of the electrostatic repulsion between the lipid bilayers.

In order to study the interactions between the anions and the lipid bilayer phase the experimental results ($\log\Pi - d_w$) of DPPC bilayers in the presence of NaX salts were fitted, either using the binding model or the partitioning model adjusted for the lipid bilayer geometry. The fit of the DPPC curve in pure water was carried out by forcing from the beginning the fitting curve to pass through the maximum swelling point ($d_w = d_{max}$). In addition, for a specific value of the Hamaker constant, A, the hydration decay length, λ, was set and the hydration coefficient, P_0, was varied over a broad range of values. For each A, λ, and P_0, we calculated the model deviation from the experimental points. The best value of P_0 (for each λ) was considered to be the one with the smallest deviation from experiment. Using either d_w or $d_w^{'}$ as the water bilayer separation we obtained excellent fits for DPPC in water for A = (1.0 ± 0.2) kT, λ = (2.55 ± 0.05) Å, P_0 = (8.67 ± 0.06) x10^8 Pa and a range of κ_c values (from 9 to 30 kT) if the water bilayer separation in the VDW force was taken equal to d_w. When the water bilayer separation was taken equal to $d_w^{'}$, excellent fits were obtained for A = (1.8 ± 0.3) kT, λ = (2.50 ± 0.05) Å, P_0 = (9.94 ± 0.02) x10^8 Pa and a range of κ_c values (from 11 to 30 kT). In the second case the Hamaker constant increases by almost 1 kT

compared to the values found for water bilayer separation equal to d_w. This increase was expected, since the change of the water bilayer separation greatly influences the Van der Waals interaction. The theoretical parameters found in this thesis for DPPC in pure water do not agree with those found by previous research groups (**Lis et al. 1982**; **Rand et al. 1989; McIntosh et al. 1993**; **Petrache et al. 1998**). This may be due to the different theoretical approach each of these groups uses to compute the various theoretical parameters. In general, the values found for the different parameters by us and by various researchers over the years *are strongly model dependent,* and as a result no perfect agreement can be expected.

Upon fitting the $\log\Pi - d_w$ curves of DPPC in the presence of NaX salts (including the maximum swelling point), *using the binding model*, it was observed that the Hamaker constant must increase very substantially for the low salt concentrations (0.05 M and 0.1 M) while an extra repulsion is required to fit the experimental results for DPPC both in NaSCN and NaI salt solutions of concentration 0.5 M, as indicated by the large values of the association constants needed to fit the electrostatic part of the $\log\Pi - d_w$ curves. The only way to improve the fit for high salt concentrations and thus reduce the binding constant to values comparable to those found for the lower NaX concentrations, is to assume the existence of a very extensive "Stern" layer for Na^+ adsorption. However, assuming a Stern layer of the order of 8 Å is not an acceptable solution, since the Pauling radius for Na^+ is only 1 Å. The additional repulsive force that is required to fit the $\log\Pi - d_w$ curves in the presence of NaX solutions of concentration 0.5 M supports the existence of an additional mechanism of repulsion, other than the electrostatic repulsion force produced between the lipid bilayers at high salt concentration and is something that must be studied in the future.

Moreover, increasing the Hamaker constant so much creates serious doubts about the significance of this fitting exercise, because the low frequency part of the Hamaker constant must decrease theoretically in the presence of a salt solution by a factor proportional to $e^{-2\kappa D}$, where κ^{-1} is the Debye length of the solution. *The Hamaker constant was increased in our fit in order to accommodate the maximum swelling point.* The possibility that the osmotic pressure at maximum swelling is not exactly zero but has a very small value of about 100 – 200 Pa, due either to the presence of minute impurities or to the equilibrium of the swollen bilayers with a system of vesicles under tension, creates doubts about the accuracy of the maximum swelling point. Consequently, the experimental $\log\Pi - d_w$ results were fitted without taking into account the maximum swelling point, using again the *binding model*. The extracted binding constants were similar to those when the maximum swelling point was

taken into account in the fitting process. Binding constants depend on the anion used but also on the concentration of the electrolyte solution. This dependence of binding constants on salt concentration severely limits the usefulness of these values for quantitative comparisons and hypotheses.

The diffuse layer model was also used in order to calculate the osmotic pressure exerted between the lipid bilayers by assuming an attractive potential, U_-, of anions to the lipidic layer. The fitting results obtained are very similar to those observed using the binding model, and in general, they demonstrate the same characteristics. The interaction potentials depend on the anion and the concentration of the salt solution used. The interaction potentials increase and follow the Hofmeister series of anions for the same salt concentration; for different salt concentrations, the interaction potentials increase with concentration. For salt concentrations equal to 0.5 M, very large interaction potentials are required in order to fit the experimental data. Generally, the interaction potentials of anions estimated using the diffuse layer model are equivalent to the binding constants, although the two models are based on a different picture of the lipid-electrolyte interface.

The conclusions reached from the fitting analysis of the $\log\Pi - d_w$ curves of DPPC in the presence of various salts solutions are the following: at low salt concentrations one can fit the data with more or less comparable parameters (binding constants or interaction potentials) while at high salt concentrations much larger parameter values (binding constants) are needed to fit the data. This indicates that an extra repulsion is present at high salt concentrations that must be introduced into the fitting models. One possibility for the existence of an extra repulsion force is that in the presence of very high concentrations of chaotropic ions the interface is considerably "softened" and the perpendicular headgroup fluctuations (protrusion forces) increase considerably. Another possibility is that the interfacial rigidity increases, leading to stronger undulation repulsion, although this is not supported by theoretical considerations, and is not visible as increased SAXS peak broadening in our experiments. The "basis" of a possible extra repulsion force is something that could be studied in the future.

9.3 Conclusions from the micellar study

The effect of different sodium salt solutions on the physicochemical properties of DPC micelles was studied using DLS. The following table (**Table 9-1**) illustrates how the critical micelle concentration (cmc), the aggregation number (N), the surface area (α), and the

micellar hydrodynamic diameter are influenced by the concentration used in the presence of DPC micelles. In general, as the salt concentration increases, the critical micelle concentration, the aggregation number and the micellar diameter decrease. On the contrary, the surface area of a DPC molecule appears to increase with the concentration of the salt solution.

Table 9-1. Effect of the salt concentration on the physicochemical properties of DPC micelles

NaX salt concentration	**Micellar physicochemical properties**	
↑ **(Increases 0.45 M to 1.35 M)**	Critical micelle concentration	↓
	Aggregation number	↓
	Surface area	↑
	Micellar diameter	↓

The decrease of the cmc at higher salt concentrations may be explained by the screening of the electrostatic repulsion due to the double layer formed. However, the reason why the micellar size decreases with concentration and type of the anion is not obvious. It may be explained by dehydration of the DPC molecules, or the existence of interparticle interactions between the DPC molecules that were not considered in the theoretical analysis.

The type of the anion used in the NaX salt solutions also influences the physicochemical properties of DPC micelles. Generally, the micellar properties follow the Hofmeister series. The chaotropic anions I^- and SCN^- have the strongest effect on all micellar properties with the exception of the cmc, which appears not to be affected by the type of the anion in solution.

The theoretical binding model adjusted for the micellar geometry was used to obtain binding constants of anions to the headgroups of the DPC micelles. The calculation of the binding constants was made only in relative terms since the presence of a salt is known to dehydrate the headgroup of DPC micelles. As a result, the Cl^- ion was used as a reference state.

The binding constants, K, of anions on DPC micelles follow the Hofmeister series. Thus, larger x_b and K are found for the more hydrophobic (chaotropic) ions. However, the binding constants exhibit strong concentration dependence, as was also found in the case of the DPPC monolayers and bilayers.

9.4 Correlations between results from different geometries

Different common parameters which were extracted by the experimental or the theoretical analysis of the effect of NaX electrolytes on the above three models systems can be compared. For example, the change of the surface area of DPC micelles can be compared to the change of the headgroup area of DPPC bilayers in the presence of various electrolytes as seen in **Table 9-2**.

Table 9-2. Comparison of headgroup area computed for bilayers and micelles in the presence of NaX salts at different concentrations

NaX salt concentration	Headgroup area		Anion type	Headgroup area	
	Bilayers	Micelles		Bilayers	Micelles
↑ **(Increases)**	↓	↑	**Hofmeister series (cosmotropic to chaotropic anions)**	follows the Hofmeister series	follows the Hofmeister series

Table 9-2 shows that the headgroup area does not follow the same trend for bilayers and micelles as the concentration of the salt solution increases. The headgroup area of DPPC bilayers decreases while the headgroup area of DPC micelles increases with salt concentration. In contrast, both depend on the anion type used and both follow the Hofmeister anion series. The increased area per headgroup in micelles upon increasing the salt concentration is expected and is due to charging through ion binding. The decreased area per headgroup in bilayers upon increasing salt concentration is a subtle effect that can be attributed to headgroup hydration.

The obtained binding constants and partitioning constants in the three model systems can also be compared. Although it was not possible to compute unique ionic binding constants for the monolayer, bilayer and micellar geometry a rough correlation between the values of K for the bilayers and those of the monolayers and micelles, which best describe the experimental data at low salt concentrations, is presented in **Figure 9-2**.

The partitioning constants computed for the monolayer geometry are concentration independent and thus they cannot be directly correlated to the partitioning constants calculated for lipid bilayers, which demonstrate concentration dependence. However, a correlation between mean values of U- obtained for the bilayers at low salt concentration and those of the monolayers is presented in **Figure 9-3**.

Figures 9-2 and **9-3** show that the correlation of ion-binding parameters between the three geometries is good for most of the anions used. This implies that similar ion-interface interactions take place in the three geometries and thus the mechanism of action of Hofmeister anions is the same. SCN^- deviates from the linear correlation in all cases, indicating an alteration of the monolayer properties at the air-water interface. This may be due to the fact that SCN^- is a non-symmetrical (non-spherical) ion with an uneven distribution of electrons, that is apparently capable of specific interactions with lipid monolayers disturbing thus the molecular arrangement at the air-water interface.

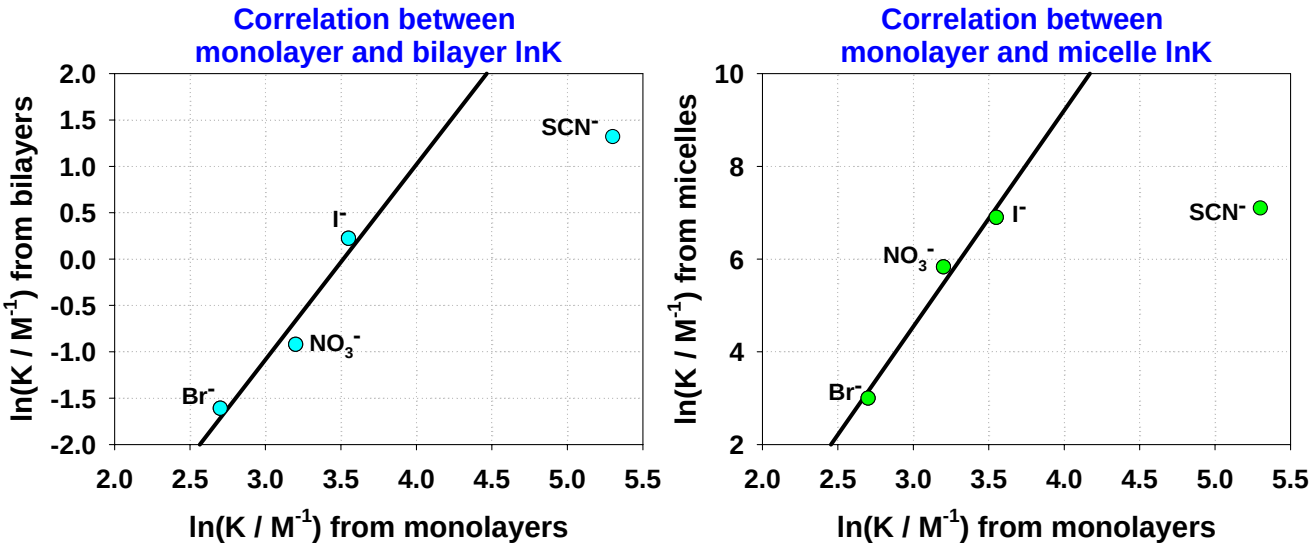

Figure 9-2. Correlation between the lnK's of the monolayer, bilayer and micellar geometries as they have been computed from the theoretical binding model

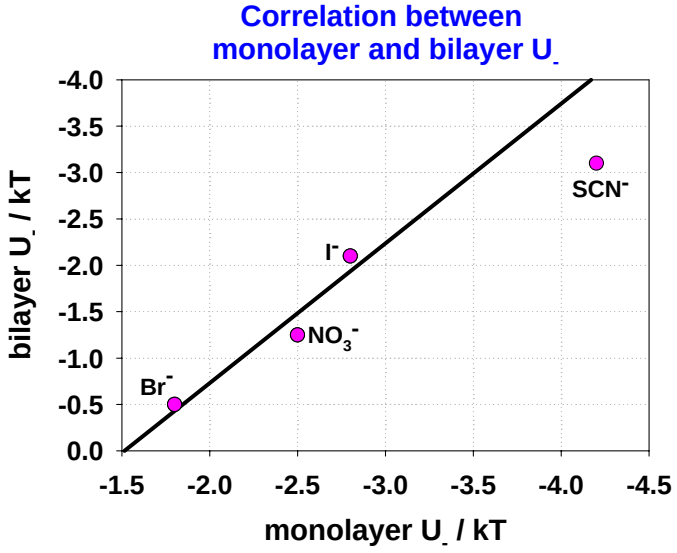

Figure 9-3. Correlation between the U_-'s of the monolayer and bilayer geometries as they have been computed from the theoretical diffuse layer model

9.5 Final discussion and future work

In conclusion, the presence of various salt solutions has a great effect on the properties of the three model systems used in this study. The effects always follow the Hofmeister series and depend on the salt concentration. The main goal of this thesis, which was to advance the understanding of the mechanism of action of Hofmeister anions, has been achieved to a significant extent. *From all geometries studied*, the results of the binding studies support the idea that the interaction of anions is not through some type of local chemical binding. The monolayer appears to be the best model system since the impact of ions is related to $\Delta\pi_{el}$, a directly measurable property. The bilayers are not such a good model system, since their theoretical analysis involves a number of interactions, for none of which the extent of the salt influence is a priori known. The same applies to micelles, where the quantity with which we monitor the salt effect (headgroup area) is very indirectly obtained from experiments.

The following questions are left open for the time being and can be considered as work for the future:

- The diffuse layer model must be applied to the micellar geometry as well. It is expected to provide better results than the binding model, since the outcome in this case (the headgroup area) is related to lateral stresses.
- The theoretical binding models adjusted for each geometry must be reconsidered since the association constants that emerge always "suffer" from salt concentration dependence. The models must be modified to test additional possibilities such as the presence of induction and dispersion forces.
- More precise maximum swelling experiments for DPPC in the presence of NaX salt solutions, especially in the presence of the chaotropic anions I^- and SCN^- must be carried out, in order to determine the osmotic pressure under these conditions. If the "limiting" osmotic pressure is nonzero this could modify the Hamaker constants derived from the present theoretical models.
- The "source" of the possible additional repulsive force that appears in DPPC bilayers at high salt concentrations must be studied. This can be done with experiments (micropipette methods, deformation via applied electric fields etc) that can measure the steric repulsive forces that arise due to the presence of anions.
- Electrical properties such as the electrostatic surface potential induced by the presence of anions can be directly measured through measurements of the surface potential of

monolayers and electrophoresis or fluorescence studies using fluorescent dyes applied to the bilayer and micellar geometry.

- Alternate lipid interfaces may be examined. For example other phospholipid molecules can be used which can be charged or zwitterionic, e.g. the important ethanolamine headgroup could be examined as a model, since it can be charged by pH modification and thus provides one additional dimension to the investigation of specific salt effects. In addition, proteins or even reverse micelles can be used as model systems to study the Hofmeister effect.

I APPENDIX

MONOLAYER DATA ANALYSIS

Surface pressure – Area per Molecule isotherms of DPPC in the presence of NaX salt solutions

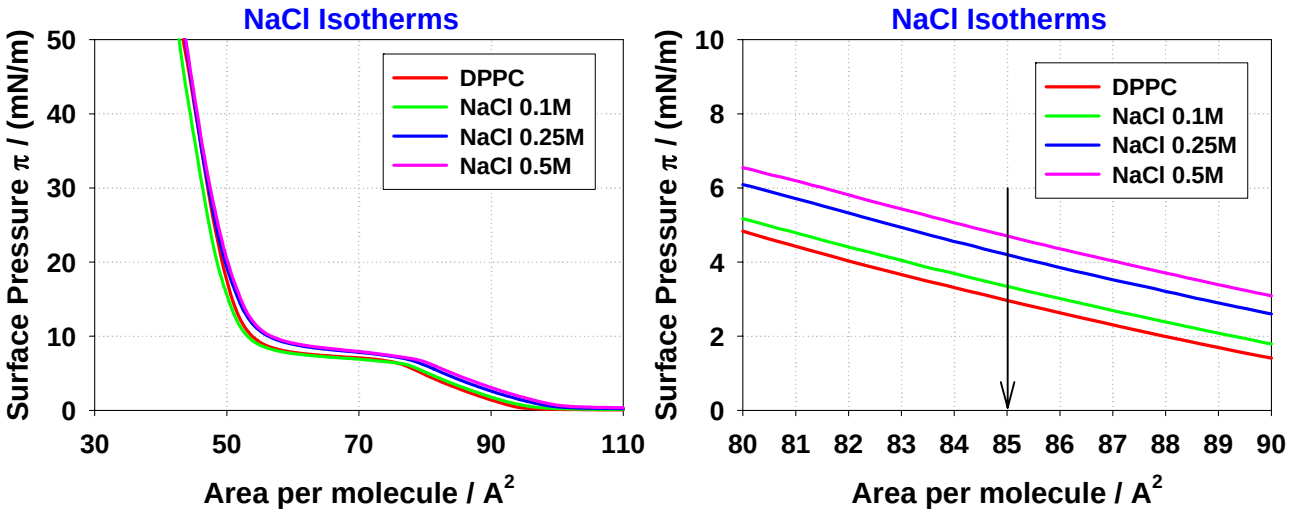

Figure 0-1. Surface pressure vs molecular area isotherms of DPPC on NaCl salt solutions of various concentrations at T = 22 ± 0.1°C

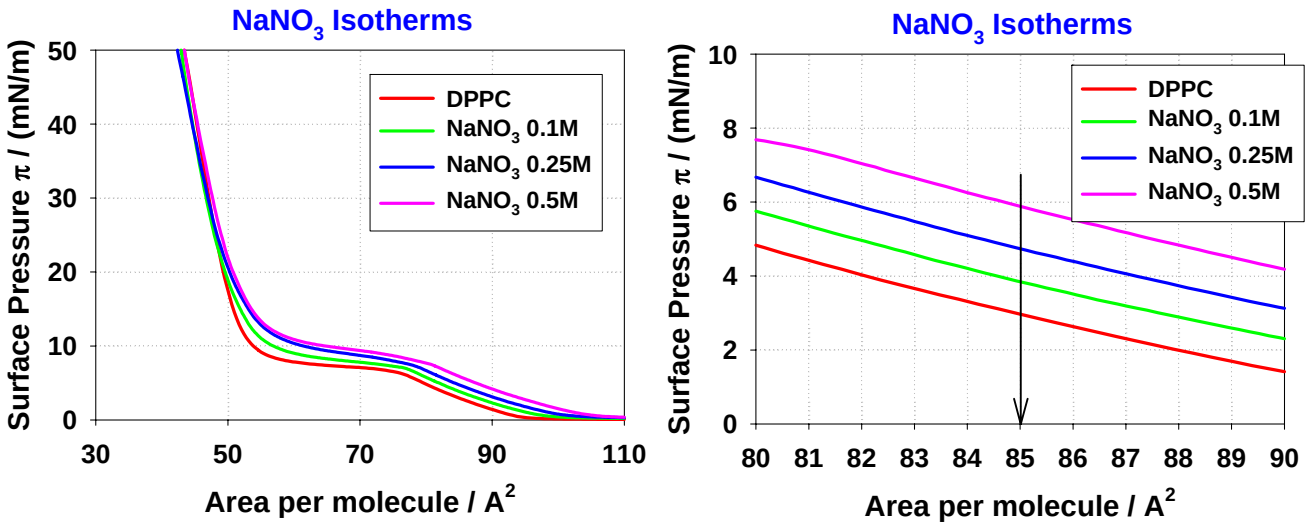

Figure 0-2. Surface pressure vs molecular area isotherms of DPPC on $NaNO_3$ salt solutions of various concentrations at T = 22 ± 0.1°C

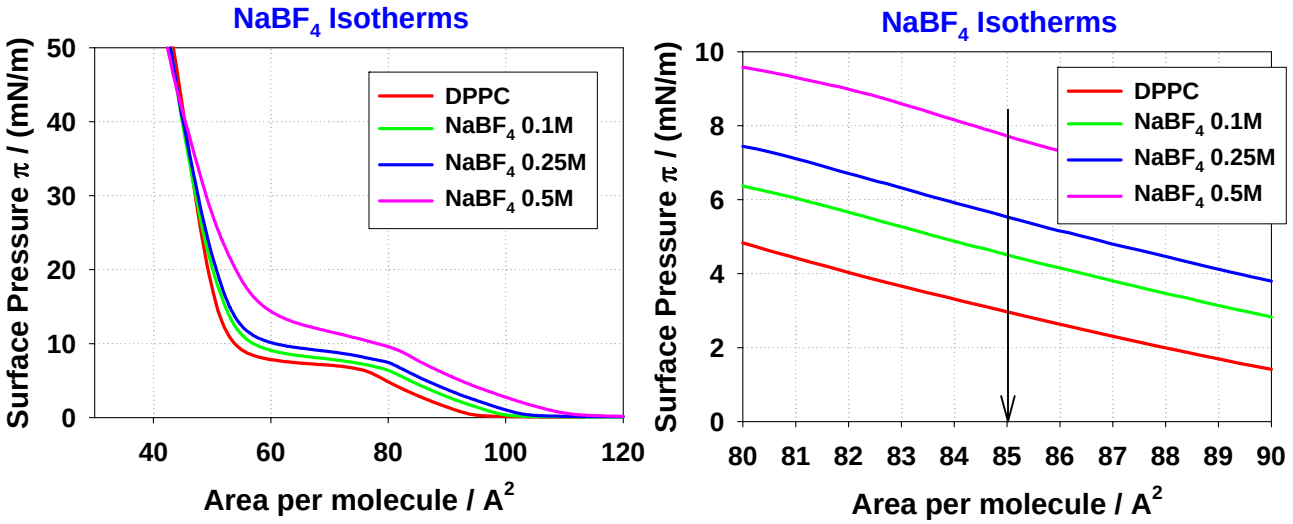

Figure 0-3. Surface pressure vs molecular area isotherms of DPPC on $NaBF_4$ salt solutions of various concentrations at T = 22 ± 0.1°C

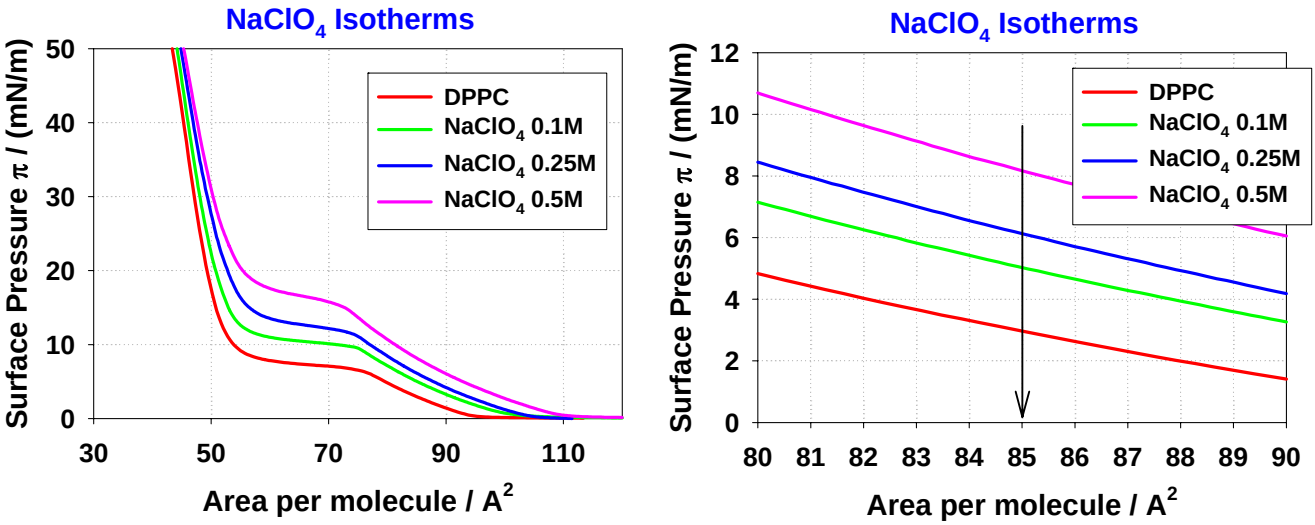

Figure 0-4. Surface pressure vs molecular area isotherms of DPPC on $NaClO_4$ salt solutions of various concentrations at T = 22 ± 0.1°C

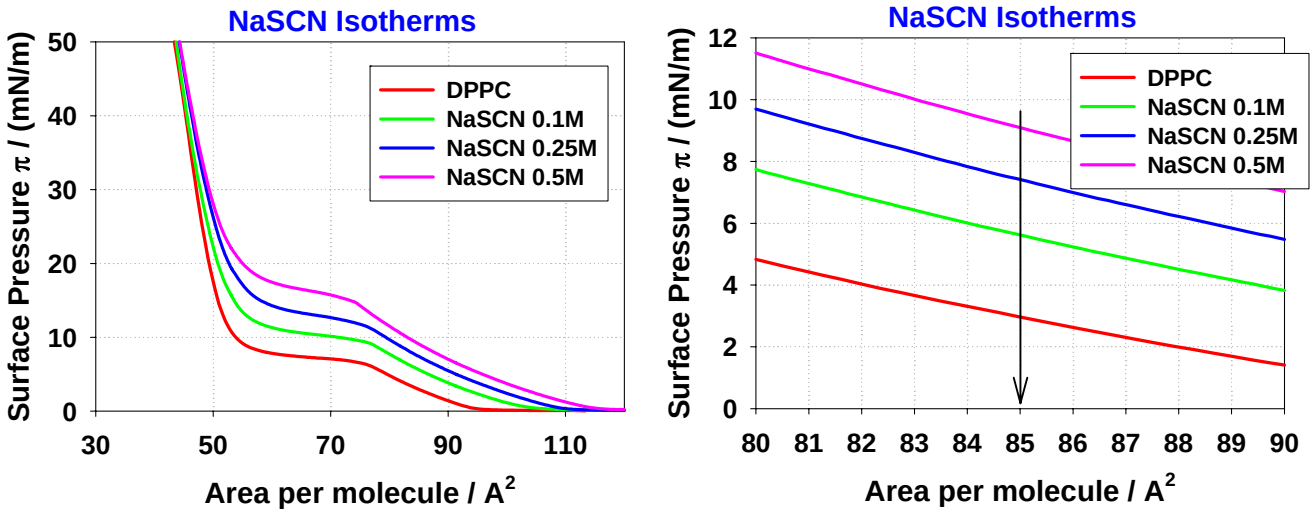

Figure 0-5. Surface pressure vs molecular area isotherms of DPPC on NaSCN salt solutions of various concentrations at T = 22 ± 0.1°C

II APPENDIX

BILAYER DATA ANALYSIS

Osmotic Pressure

The osmotic pressure exerted on DPPC bilayers by PEG solutions is calculated according to **Equation 3.5-9** which is the following:

$$\Pi\ (\mathrm{dyn/cm^2}) = -1.31 \times 10^6 G^2 T + 141.8 \times 10^6 G^2 + 4.05 \times 10^6 G$$

The experimental error of the osmotic pressure is calculated taking into account the experimental errors of the constituent masses (mPEG, mH_2O or mSalt) and the experimental error of the temperature (T) as shown in **Table 0-1**. The effect of a salt on the osmotic pressure of PEG solutions is discussed below in connection with the discusssion in **Section 3.5.5**.

Water bilayer separation d_w

The water bilayer separation, d_w, is calculated according to **Equation 3.6-14** ($d_w = D - b_L$). In order to calculate d_w we need to know the repeat distance D and the thickness b_L of DPPC bilayers in the presence of salt solutions. The bilayer repeat distance, D, is observed from the Bragg peak positions using **Equation 3.6-12** ($q = \frac{2\pi}{D}$). The bilayer thickness b_L can be calculated using **Equation 3.6-13** ($b_L = \varphi_L D$ - maximum swelling law). The lipid volume

fraction, φ_L, is obtained according to **Equation 3.6-10** ($\varphi_L = \left[1 + \frac{(1-c)\bar{v}_w}{c\bar{v}_L}\right]^{-1}$) by measuring the amount of water and thus the amount of lipid in the samples, using the Karl Fischer method as discussed in **Chapter 3**, **Section 3.9**. For more accurate results on bilayer thickness, a graph of b_L vs φ_L is plotted and all point that deviate from the linear plot are excluded. As a result, a new equation y = ax + b that fits the experimental points is obtained and using the values of the slope a, and intercept b new values of b_L can be recalculated.

Maximum swelling

The maximum swelling of DPPC lamellar phases in the absence and in the presence of salt solutions is found through graphs of D vs $1/\varphi_L$ (see **Section 3.6.5**). In this case φ_L is known in advance and D is obtained as explained above. The maximum swelling is defined as the point where the bilayer repeat spacing D does not change with the lipid volume fraction φ_L.

An example of the data analysis is given below for DPPC/water in the absence of salt. The osmotic pressure exerted by the PEG solution on seven samples of DPPC named DPPC1, DPPC2, etc is given in **Table 0-1**.

Table 0-1. Osmotic pressure of PEG solutions exerted on DPPC bilayers

Parameters	DPPC1	DPPC2	DPPC3	DPPC4	DPPC5	DPPC6	DPPC7
mPEG (g)	0.5533	1.0453	2.0215	4.8031	6.4080	10.4253	17.6072
mH_2O (g)	39.4514	38.9920	38.0135	35.2281	33.6201	29.6636	22.4058
mtot (g)	40.0047	40.0372	40.0350	40.0312	40.0281	40.0889	40.0130
G	0.014	0.0285	0.0555	0.136	0.191	0.351	0.786
logΠ (dynes/cm^2)	4.85	5.25	5.65	6.29	6.55	7.05	7.70
logΠ (Pa)	**3.855 ± 0.003**	**4.200 ± 0.006**	**4.630 ± 0.008**	**5.290 ± 0.011**	**5.550 ± 0.012**	**6.040 ± 0.013**	**6.700 ± 0.014**

e.g. the calculation of the osmotic pressure exerted on sample DPPC1 using **Equation 3.5-9** is as follows:

Π (dyn/cm^2) = -1.31 x $10^6 G^2 T$ + 141.8 x $10^6 G^2$ + 4.05 x $10^6 G$

Π (dyn/cm^2) = -1.31 x $10^6 (0.014)^2 (50)$ + 141.8 x $10^6 (0.014)^2$ + 4.05 x $10^6 (0.014)$

Π (dyn/cm^2) = 71655, Π (Pa) = 7165.5

logΠ (Pa) = 3.85

Table 0-1 shows the experimental error of the osmotic pressure taking into account only the experimental error of the masses (mPEG, mH_2O) and the temperature (T). We see that the relative error in logΠ is very small (3% maximum). The effect of a salt on the osmotic pressure of PEG for two concentrations G = 0.015 and G = 0.79 was discussed in **Chapter 3**, **Section 3.5.4**, where it was shown that even a 40% error in the osmotic pressure of PEG corresponds to a much smaller error in logΠ. We have accordingly decided to use an experimental error of 20% in Π, introducing an error of ± 0.1 to reported logΠ values assuming that in this way we are covering the uncertainty introduced by the salt. Thus, logΠ of PEG in the presence of salt solutions is always taken to be equal to logΠ ± 0.1 (Pa).

The bilayer repeat distances D, for the seven samples under osmotic stress are given in **Table 0-2,** which was calculated using the small angle X-ray scattering technique, plotting intensity versus q as shown in **Figure 0-1**.

Table 0-2. Bilayer repeat distance of DPPC/water under OS

Parameter	DPPC1	DPPC2	DPPC3	DPPC4	DPPC5	DPPC6	DPPC7
D (Å)	63.3	62.4	60.85	57.1	56.7	54.7	53.0

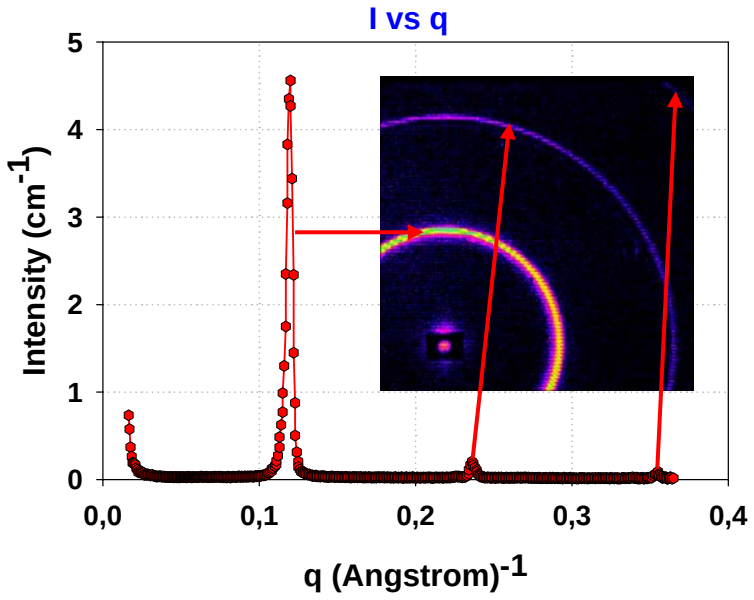

Figure 0-1. Bragg peak position and bilayer repeat spacing

The lipid volume fraction φ_L for each sample is given in **Table 0-3**.

Table 0-3. Volume fraction of DPPC as defined by the Karl Fischer technique

Parameter	DPPC1	DPPC2	DPPC3	DPPC4	DPPC5	DPPC6	DPPC7
mSample (g)	0.0169	0.0213	0.0152	0.0244	0.0226	0.0193	0.0222
mEtOH (g)	0.803	0.857	0.803	0.790	0.749	0.778	0.910
VEtOH (ml)	1.013	1.081	1.012	0.996	0.945	0.982	1.148
V(per injection) (ml)	0.0515	0.0515	0.0515	0.0515	0.0515	0.0515	0.0515
Qty water in pure EtOH (µg)	18	21	27	32	38	43	47
Qty water in the sample (µg)	435.7	476.7	329.7	508.3	461	355.7	303.3
Qty water in the lipid (µg)	417.7	455.7	302.7	476.3	423	312.7	256.3
m(lipid+water) (mg)	0.86	1.01	0.77	1.26	1.23	1.02	0.99
m(lipid) (mg)	0.442	0.576	0.47	0.787	0.804	0.705	0.736
W%	51.39	55	60.8	62.3	65.5	69.3	74.2
φ_L%	**51.6 ± 1.6**	**55.25 ± 1.00**	**61.05 ± 1.0**	**62.5 ± 0.8**	**65.7 ± 0.6**	**69.5 ± 0.7**	**74.3 ± 0.5**

e.g. the calculation of the lipid volume fraction φ of the sample DPPC1 is as follows:

m(lipid+water) = [V(per injection) x mSample] / VEtOH

m(lipid+water) = [0.0515 x 0.0169] / 1.013 = 8.59×10^{-4} g = 0.86 mg

m(lipid) = m(lipid+water) - Qty water in the lipid

m(lipid) = $8.59 \times 10^{-4} - 417.7 \times 10^{-6} = 4.42 \times 10^{-4}$ g = 0.442 mg

w% = [m(lipid) / m(lipid+water)] x 100 = [0.442 / 0.86] x 100 = 51.39

$\varphi_L = \left[1 + \frac{(1-c)\bar{v}_w}{c\bar{v}_L}\right]^{-1}$ where c = w (weight percentage) and $\bar{v}_w$ and $\bar{v}_L$ are the water and lipid partial specific volumes

$\varphi_L\% = \left[1 + \frac{(1-0.5139)\times 1}{0.5139 \times 1.0091}\right]^{-1} \text{x } 100 = 51.6$

The bilayer thickness for each sample is given in **Table 0-4**.

Table 0-4. Bilayer thickness of DPPC samples

Parameter	DPPC1	DPPC2	DPPC3	DPPC4	DPPC5	DPPC6	DPPC7
b_L (Å)	32.70 ± 1.05	34.4 ± 0.7	37.1 ± 0.7	35.7 ± 0.5	37.2 ± 0.5	38.0 ± 0.5	39.40 ± 0.45

e.g. the calculation of the bilayer thickness of the sample DPPC1 is as follows:

$b_L = \varphi_1 \times D_1 = 0.516 \times 63.3 = 32.70$ (Å)

As mentioned before, for more accurate results a graph of b_L vs φ_L is plotted and any point that deviates from the linear plot is not taken into account. The graph of b_L vs φ_L for pure DPPC is shown in **Figure 0-2**. The bilayer thickness for each sample of DPPC is plotted as obtained from the experimental measurements *(red points)*. The point which corresponds to b_L = 32.70 and φ_L = 51.6%, (sample 1), is omitted from this graph, since it is close to the maximum swelling of DPPC.

Two points deviate from the *red linear regression curve* (y = ax + b) which is characterized by $R^2 = 0.8834$, $a = 0.2456$ *and* $b = 21.0800$. These two points are excluded to obtain a second *linear regression curve (blue curve)* with $R^2 = 0.9985$, $a = 0.2600$ *and* $b = 20.0$. The bilayer thickness is then recalculated from equation $b_L = a(\varphi_L\%) + b$ using the a and b values found from the second linear regression and plotted in φ_L% for DPPC in water, **Figure 0-2**. **Table 0-5** shows the new values of b_L as they have been recalculated.

Table 0-5. New values of DPPC bilayer thickness

Parameter	DPPC1	DPPC2	DPPC3	DPPC4	DPPC5	DPPC6	DPPC7
b_L (Å)	33.4	35.0	35.9	36.3	37.1	38.1	39.3

Comparing b_L values in **Table 0-4** and **II-5** we see that for some samples the differences can be considerable, up to 1 Å.

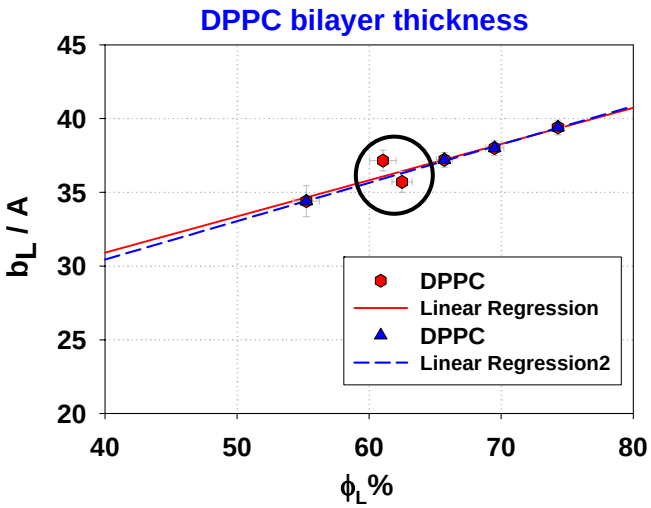

Figure 0-2. b_L versus φ_L% for DPPC in water

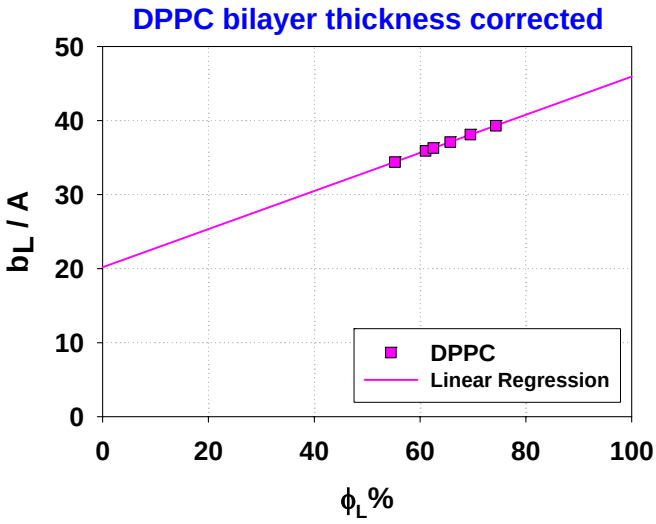

Figure 0-3. DPPC bilayer thickness

The water bilayer spacings, d_w, are given in **Table 0-6**.

Table 0-6. Water bilayer spacings for DPPC bilayers in water

Parameter	DPPC1	DPPC2	DPPC3	DPPC4	DPPC5	DPPC6	DPPC7
d_w (Å)	**29.9** ± 1.2	27.2 ± 0.9	24.95 ± 0.85	20.8 ± 0.7	19.6 ± 0.7	16.6 ± 0.7	13.7 ± 0.7

e.g. the calculation of the water bilayer spacing for sample DPPC1 is as follows:

$d_w = D - b_L = 63.3 – 33.4 = 29.9$Å

The value of d_w for sample DPPC1 (red color) is not correct. The reason for this is discussed below.

The maximum swelling of DPPC bilayers in water is estimated in **Figure 0-4**.
The maximum swelling is defined as the point where the bilayer repeat spacing D does not change anymore with the lipid volume fraction φ_L. Thus the maximum swelling of DPPC in pure water is $\varphi_L \approx 52.6\%$ as it is found from
Figure 0-6. The DPPC bilayer thickness is calculated using the maximum swelling law ($D_{max} = b_L/\varphi_L$) and is equal to $b_L = 34.9$ Å ($D_{max} = 66.3$ Å). The water bilayer spacing, d_w, at the maximum swelling is $d_w = 31.4$ Å.

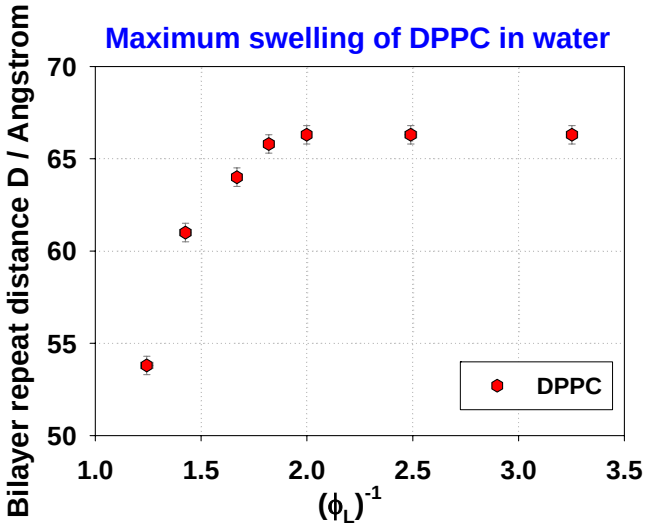

Figure 0-4. Plot of D vs $(\varphi_L)^{-1}$ for DPPC/water for the estimation of maximum swelling

Figure **0-6** shows that the experimental points for small b_L/φ_L do not follow a linear relationship (see **Chapter 8**, **Figures 8-3** and **8-4**) as they should according to the swelling law which is valid up to the maximum swelling. This was also found by **Lis et al. 1982** who have studied the swelling of various lipids including DPPC at T = 50 °C as shown in **Figure** 0-5.

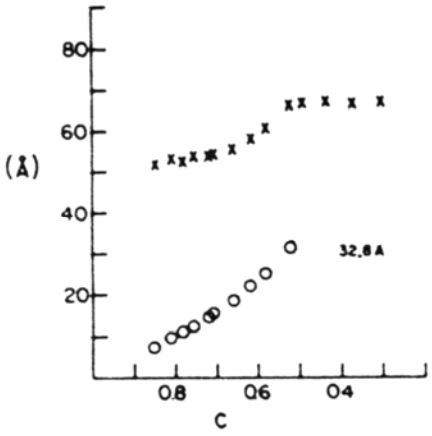

Figure 0-5. Lamellar repeat spacing (x) and water bilayer separation (o) of DPPC bilayers at T = 50 °C (Lis et al. 1982)

The fact that the maximum swelling of DPPC is φ_L = 52.6% indicates that the bilayer thickness of the sample DPPC1 is incorrect, because the swelling law is not valid for lipid volume fractions smaller than the limiting volume fraction of the lipid at the maximum swelling. For this reason the experimental point which corresponds to b_L = 32.70 Å and φ_L = 51.6% for the sample DPPC1 is not taken into account at the plot of b_L versus φ_L%.

Moreover, the water bilayer separation d_w for the sample DPPC1 as shown in **Table 0-6** is not correct for the same reason.

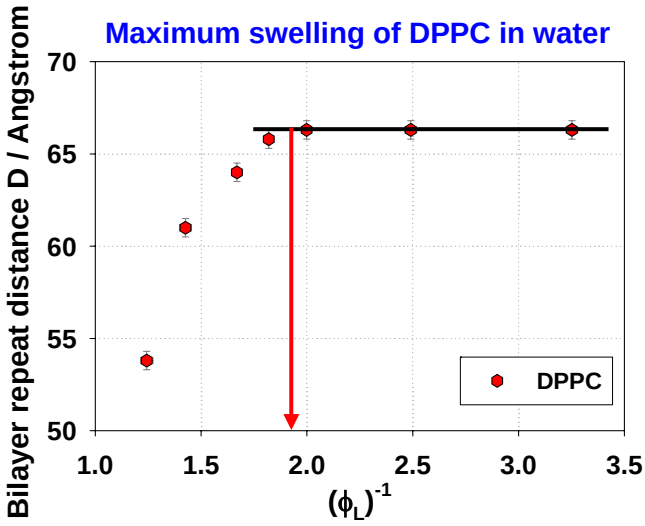

Figure 0-6. Maximum swelling of DPPC

Headgroup area A

The headgroup area, A, of DPPC molecules can be calculated according to **Equation 3.6-15** ($A = \frac{2x10^{24} \cdot MW \cdot \overline{v_L}}{b_L \cdot N_{AV}}$). The headgroup area, A, for each sample (DPPC1, etc.) is given in **Table 0-7**.

Table 0-7. Headgroup area of DPPC samples

Parameter	DPPC1	DPPC2	DPPC3	DPPC4	DPPC5	DPPC6	DPPC7
A (Å^2)	70.3 ± 2.0	70.0 ± 1.4	68.5 ± 1.3	67.8 ± 1.0	66.3 ± 0.8	64.6 ± 0.9	62.3 ± 0.7

Fitting Analysis of DPPC/ Water

Table 0-8 to **II-16** give the parameter values that have been found by the conditional fitting for different values of a Hamaker constant using $d_w^* = d_w$. **Figures II-7** to **II-15** show correspondingly the change of the hydration coefficient, P_0, as the hydration decay length, λ, increases for the various values of the Hamaker constant.

Table 0-8. Conditional fit: A = 0.6 kT

P_0 / Pa	λ / Å	κ_c / kT	Error
8.320e+9	2.00	13.439	173.30
6.410e+9	2.05	15.610	137.40
5.013e+9	2.10	14.398	107.30
3.965e+9	2.15	17.174	82.70
3.170e+9	2.20	19.202	62.70
2.565e+9	2.25	22.035	46.90
2.093e+9	2.30	26.097	34.70
1.725e+9	2.35	32.444	25.60
1.433e+9	2.40	43.757	19.20
1.200e+9	2.45	69.114	15.30
1.076e+9	2.50	180.24	13.50

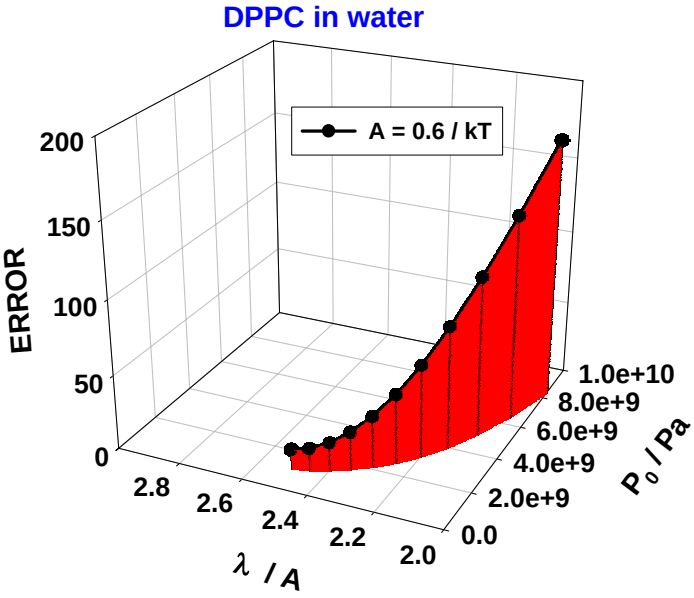

Figure 0-7. Parameter values for DPPC in water at minimum error (A = 0.6 kT)

In **Figures II-7** and **II-8** the curves stop abruptly and as a result a minimum is not observed due to fact that a negative osmotic pressure is obtained for the specific parameter values that we used for the conditional fitting procedure, which are A = 0.6 kT and A = 0.7 kT respectively.

Table 0-9. Conditional fit: A = 0.7 kT

P_0 / Pa	λ / Å	κ_c / kT	Error
8.340e+9	2.00	10.748	175.30
6.460e+9	2.05	11.383	138.82
5.030e+9	2.10	12.101	108.40
3.975e+9	2.15	13.018	83.60
3.180e+9	2.20	14.162	63.40
2.573e+9	2.25	15.646	47.50
2.098e+9	2.30	17.585	35.10
1.728e+9	2.35	20.241	25.90
1.435e+9	2.40	24.140	19.50
1.202e+9	2.45	30.349	15.50
1.015e+9	2.50	41.482	13.60
8.616e+8	2.55	67.437	13.50
7.379e+8	2.60	203.61	15.10

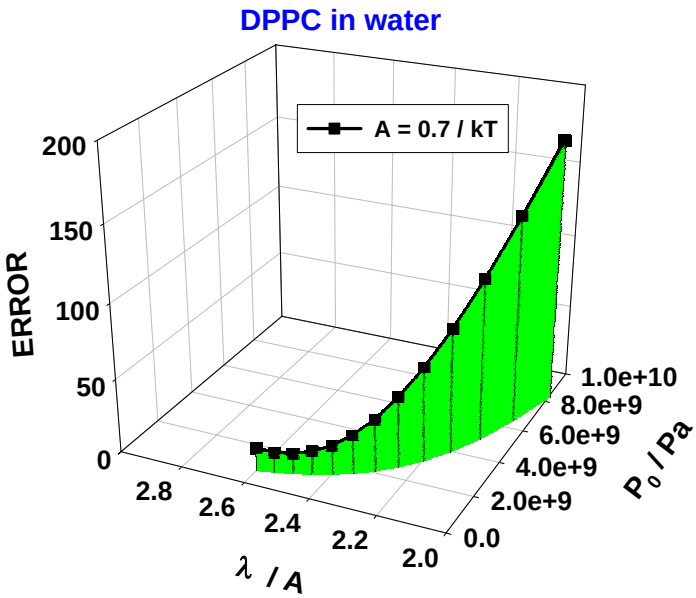

Figure 0-8. Parameter values for DPPC in water at minimum error (A = 0.7 kT)

Table 0-10. Conditional fit: A = 0.8 kT

P_0 / Pa	λ / Å	κ_c / kT	Error
2.105e+9	2.30	13.261	35.50
1.732e+9	2.35	14.725	26.20
1.438e+9	2.40	16.694	19.70
1.204e+9	2.45	19.405	15.60
1.017e+9	2.50	23.411	13.60
8.635e+8	2.55	30.016	13.50
7.389+8	2.60	42.594	15.10
6.360e+8	2.65	75.433	18.00

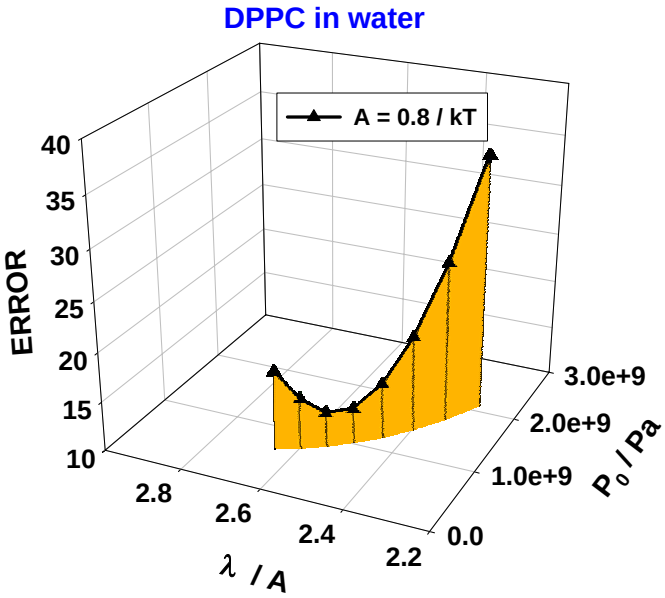

Figure 0-9. Parameter values for DPPC in water at minimum error (A = 0.8 kT)

Table 0-11. Conditional fit: A = 0.9 kT

P_0 / Pa	λ / Å	κ_c / kT	Error
2.1071e+9	2.30	10.644	36.00
1.7360e+9	2.35	11.566	26.60
1.4400e+9	2.40	12.735	19.90
1.2058e+9	2.45	14.253	15.80
1.0186e+9	2.50	16.355	13.70
8.6471e+8	2.55	19.273	13.60
7.4050e+8	2.60	23.802	15.00
6.3743e+8	2.65	31.520	17.90
5.5188e+8	2.75	47.731	22.10
4.8100e+8	2.75	10.293	27.30
4.1480e+8	2.80	24.785	33.70

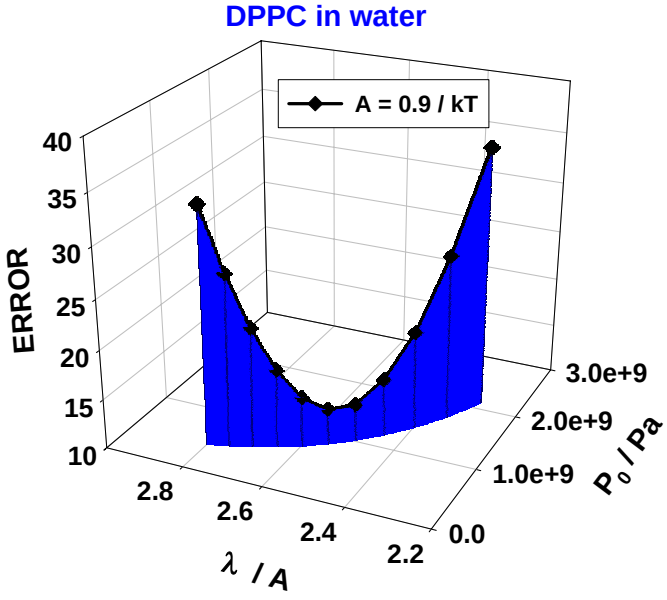

Figure 0-10. Parameter values for DPPC in water at minimum error (A = 0.9 kT)

Table 0-12. Conditional fit: A = 1.2 kT

P_0 / Pa	λ / Å	κ_c / kT	Error
2.120e+9	2.30	6.679	37.40
1.746e+9	2.35	7.034	27.60
1.451e+9	2.40	7.457	20.70
1.215e+9	2.45	7.957	16.20
1.025e+9	2.50	8.564	14.00
8.700e+8	2.55	9.312	13.60
7.440e+8	2.60	10.249	14.90
6.406e+8	2.65	11.467	17.70
5.544e+8	2.75	13.073	21.70
4.827e+8	2.75	15.316	26.90
4.227e+8	2.80	18.685	33.00
3.721e+8	2.85	24.252	39.90

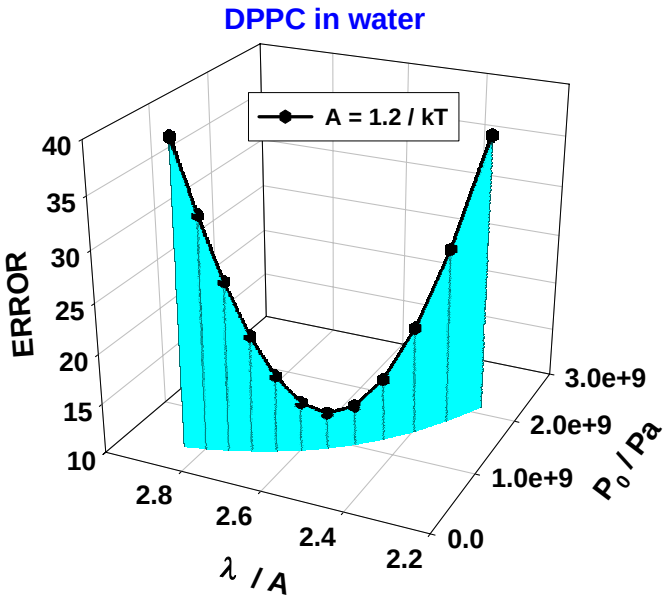

Figure 0-11. Parameter values for DPPC in water at minimum error (A = 1.2 kT)

Table 0-13. Conditional fit: A = 1.4 kT

P_0 / Pa	λ / Å	κ_c / kT	Error
2.132e+9	2.30	5.355	38.30
1.757e+9	2.35	5.582	28.30
1.457e+9	2.40	5.840	21.20
1.220e+9	2.45	6.147	16.60
1.027e+9	2.50	6.500	14.20
8.730e+8	2.55	6.923	13.70
7.468e+8	2.60	7.432	14.90
6.420e+8	2.65	8.041	17.50
5.562e+8	2.75	8.816	21.50
4.840e+8	2.75	9.776	26.60
4.240e+8	2.80	11.063	32.60
3.735e+8	2.85	12.803	39.50

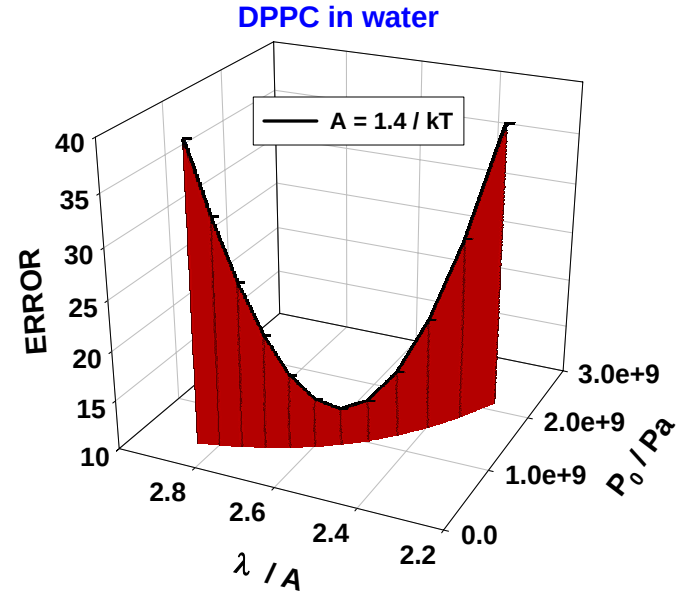

Figure 0-12. Parameter values for DPPC in water at minimum error (A = 1.4 kT)

Table 0-14. Conditional fit: A = 1.6 kT

P_0 / Pa	λ / Å	κ_c / kT	Error
2.144e+9	2.30	4.468	39.30
1.765e+9	2.35	4.624	29.00
1.462e+9	2.40	4.799	21.70
1.225e+9	2.45	5.008	16.90
1.031e+9	2.50	5.237	14.40
8.770e+8	2.55	5.514	13.70
7.484e+8	2.60	5.823	14.80
6.438e+8	2.65	6.195	17.40
5.583e+8	2.75	6.650	21.30
4.856e+8	2.75	7.182	26.30
4.252e+8	2.80	7.849	32.20
3.743e+8	2.85	8.691	39.10

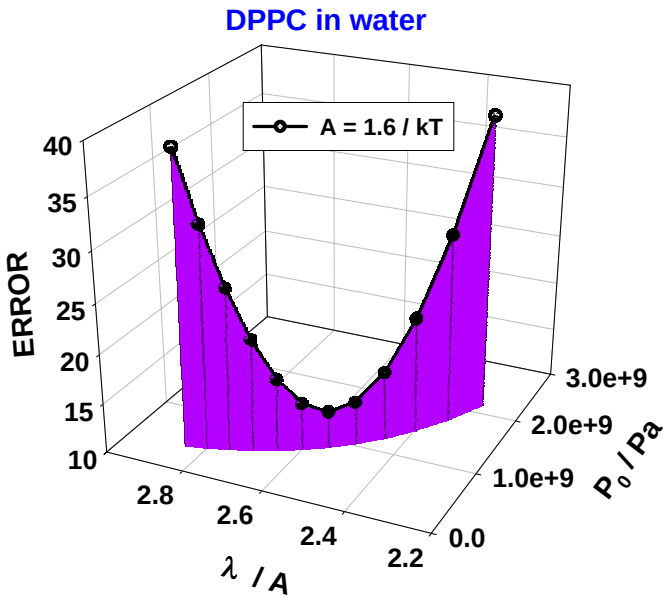

Figure 0-13. Parameter values for DPPC in water at minimum error (A = 1.6 kT)

Table 0-15. Conditional fit: A = 1.8 kT

P_0 / Pa	λ / Å	κ_c / kT	Error
2.150e+9	2.30	3.830	40.20
1.770e+9	2.35	3.945	29.80
1.470e+9	2.40	4.076	22.20
1.226e+9	2.45	4.219	17.30
1.035e+9	2.50	4.386	14.60
8.792e+8	2.55	4.576	13.80
7.520e+8	2.60	4.795	14.80
6.468e+8	2.65	5.044	17.30
5.597e+8	2.75	5.334	21.00
4.875e+8	2.75	5.678	26.00
4.264e+8	2.80	6.083	31.90
3.753e+8	2.85	6.578	38.70

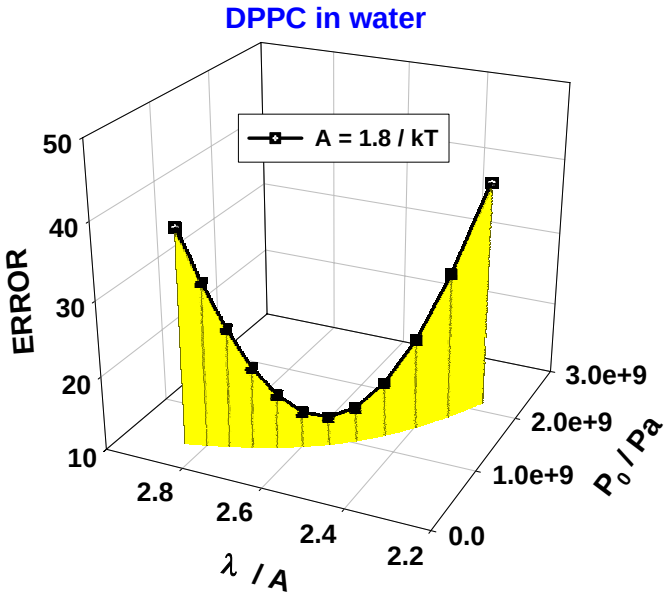

Figure 0-14. Parameter values for DPPC in water at minimum error (A = 1.8 kT)

Table 0-16. Conditional fit: A = 2.0 kT

P_0 / Pa	λ / Å	κ_c / kT	Error
2.160e+9	2.30	3.355	41.20
1.780e+9	2.35	3.443	30.50
1.472e+9	2.40	3.538	22.80
1.235e+9	2.45	3.650	17.60
1.038e+9	2.50	3.773	14.80
8.820e+8	2.55	3.912	13.90
7.540e+8	2.60	4.071	14.80
6.486e+8	2.65	4.249	17.10
5.612e+8	2.75	4.453	20.80
4.880e+8	2.75	4.692	25.70
4.275e+8	2.80	4.966	31.50
3.764e+8	2.85	5.290	38.30

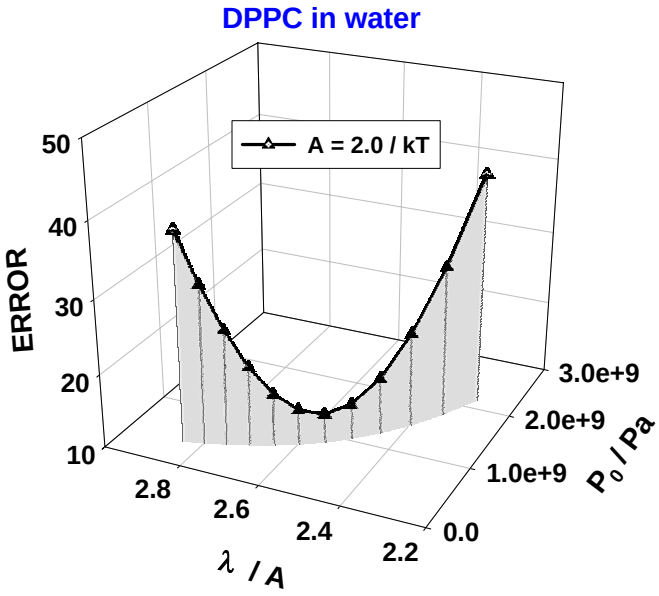

Figure 0-15. Parameter values for DPPC in water at minimum error (A = 2.0 kT)

III APPENDIX

MICELLE DATA ANALYSIS

DPC micellar mass (M) estimation in the presence of NaX salt solutions

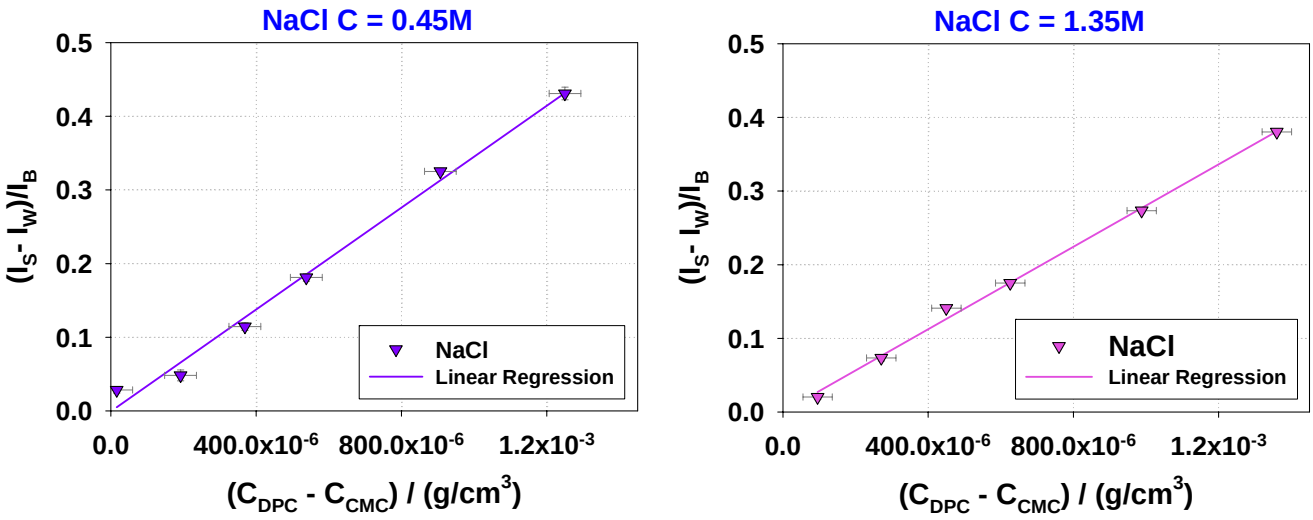

Figure 0-1. Static light scattering results for DPC in NaCl solutions

Linear Regression (y = ax + b)	NaCl 0.45M	NaCl 1.35M
B	-4.77e-4	2.42e-4
A	3.45e+2	2.80e+2
R^2	9.90e-1	9.97e-1
K (cm^{3}mol/g^2)	1.25e-2	1.34e-2
M (g/mol)	2.76e+4	2.09e+4

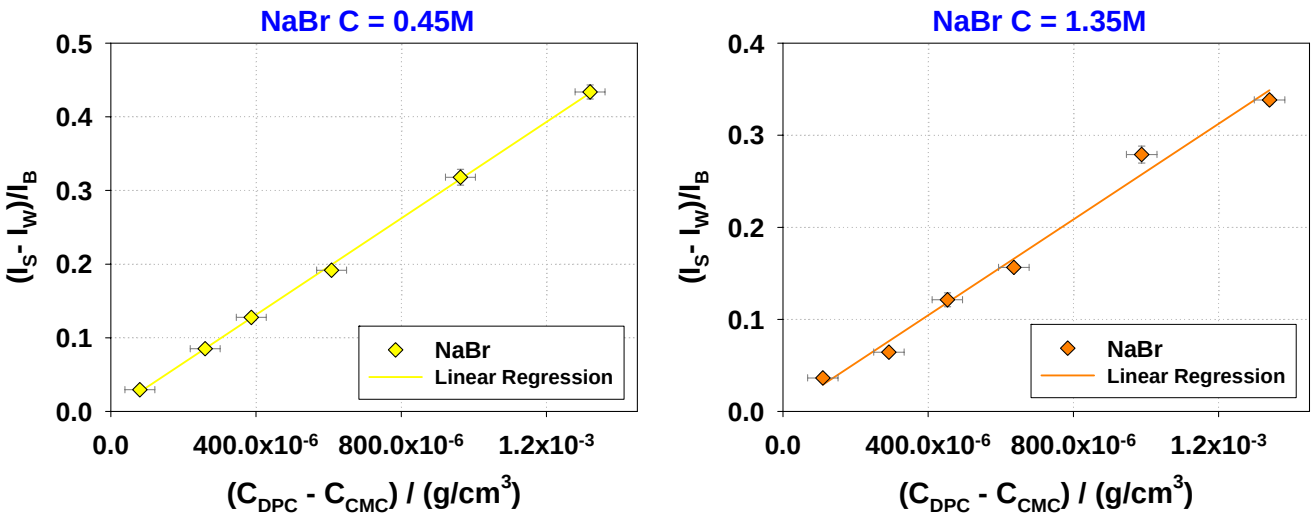

Figure 0-2. Static light scattering results for DPC in NaBr solutions

Linear Regression (y = ax + b)	NaBr 0.45M	NaBr 1.35M
B	7.12e-5	3.90e-4
A	3.27e+2	2.60e+2
R^2	9.99e-1	9.88e-1
K (cm^3mol/g^2)	1.33e-2	1.34e-2
M (g/mol)	2.46e+4	1.94e+4

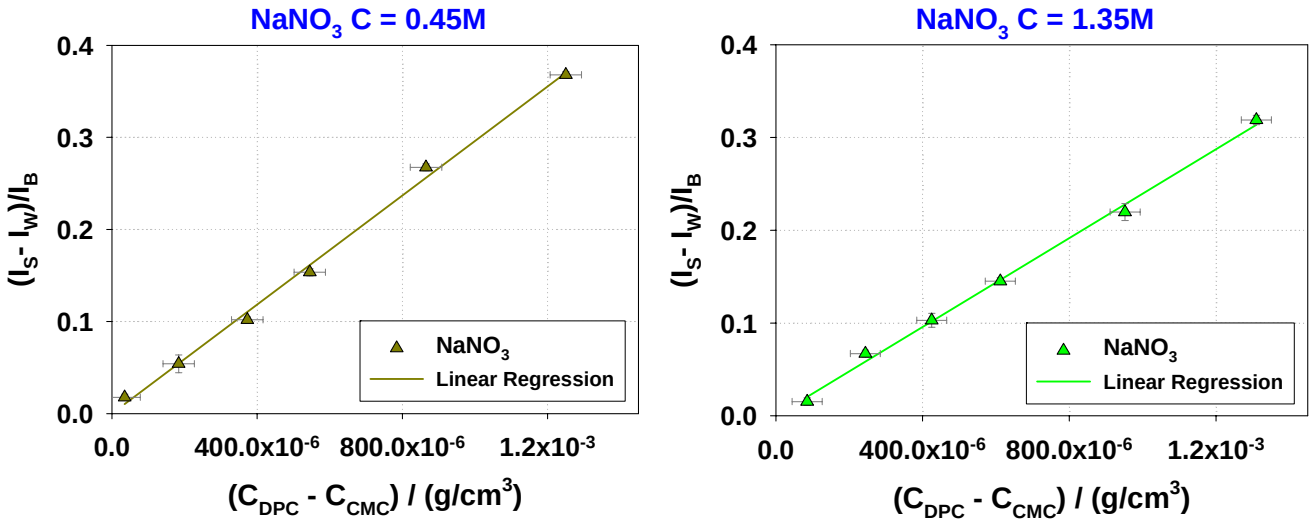

Figure 0-3. Static light scattering results for DPC in $NaNO_3$ solutions

Linear Regression (y = ax + b)	$NaNO_3$ 0.45M	$NaNO_3$ 1.35M
B	-5.40e-5	-1.10e-4
A	2.96e+2	2.39e+2
R^2	9.96e-1	9.97e-1
K (cm^3mol/g^2)	1.41e-2	1.25e-2
M (g/mol)	2.10e+4	1.92e+4

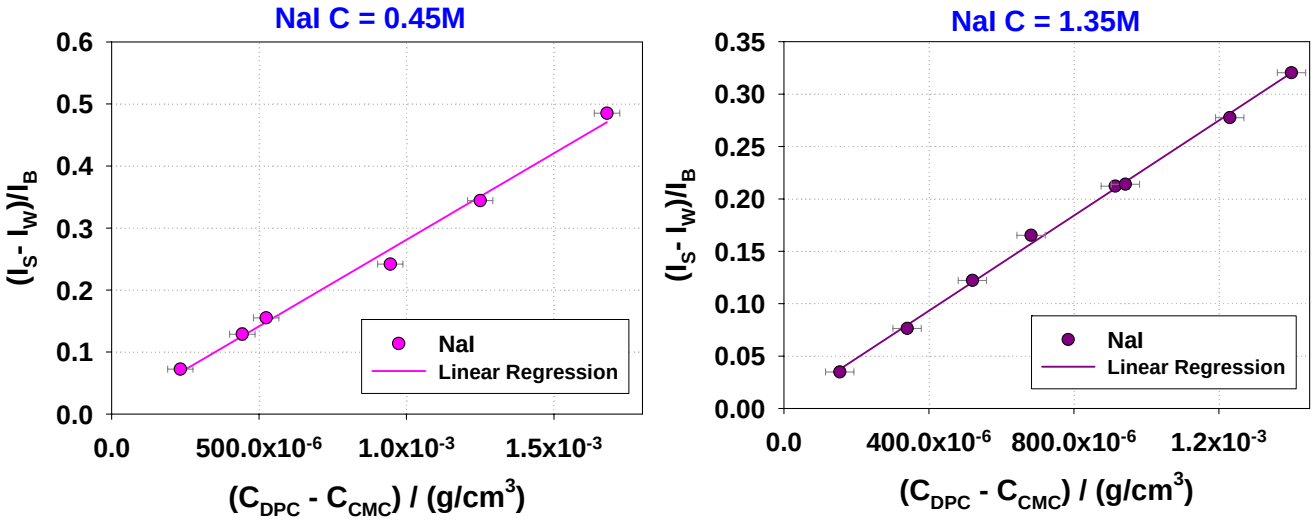

Figure 0-4. Static light scattering results for DPC in NaI solutions

Linear Regression (y = ax + b)	NaI 0.45M	NaI 1.35M
B	1.87e-3	2.44e-3
A	2.79e+2	2.26e+2
R ²	9.92e-1	9.98e-1
K (cm^3mol/g^2)	1.39e-2	1.31e-2
M (g/mol)	2.01e+4	1.73e+4

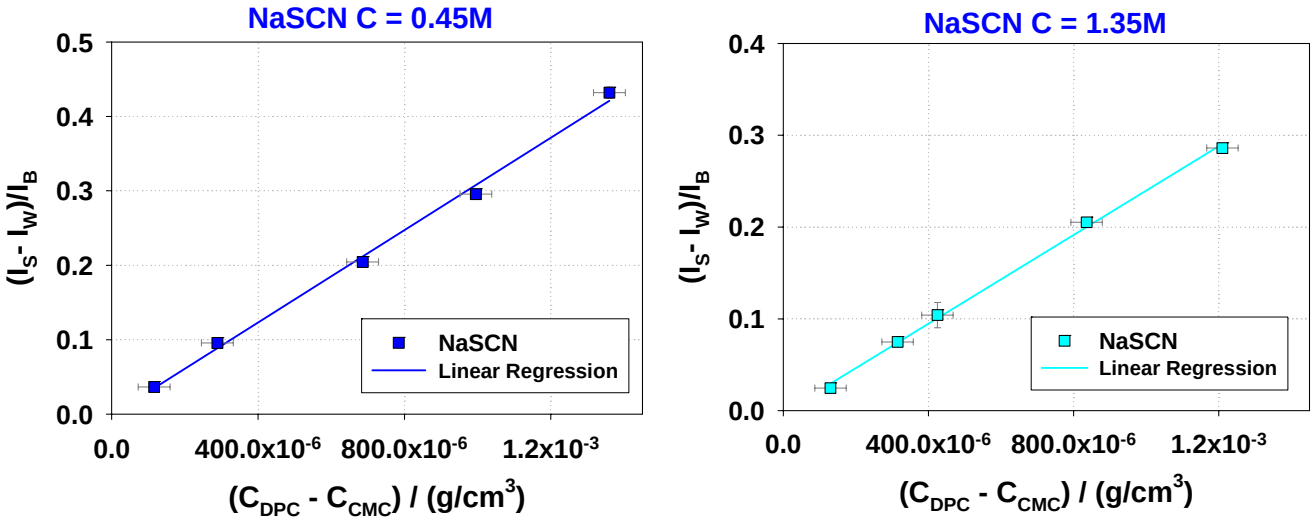

Figure 0-5. Static light scattering results for DPC in NaSCN solutions

Linear Regression (y = ax + b)	NaSCN 0.45M	NaSCN 1.35M
B	-9.58e-4	-2.04e-3
A	3.10e+2	2.41e+2
R ²	9.96e-1	9.98e-1
K (cm^3mol/g^2)	1.53e-2	1.46e-2
M (g/mol)	2.03e+4	1.65e+4

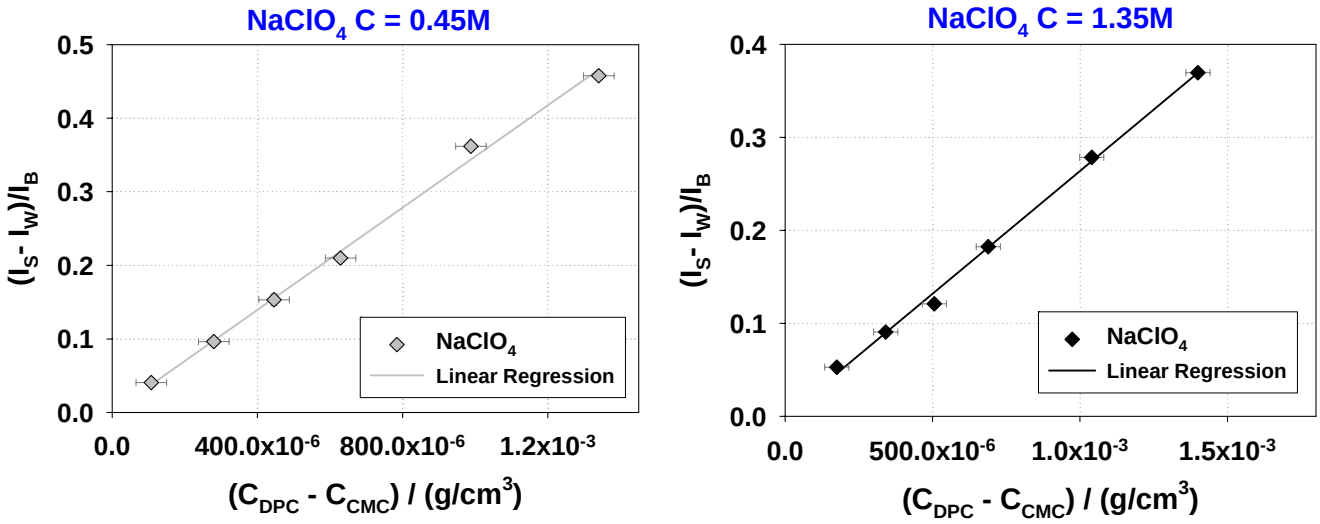

Figure 0-6. Static light scattering results for DPC in $NaClO_4$ solutions

Linear Regression (y = ax + b)	$NaClO_4$ 0.45M	$NaClO_4$ 1.35M
B	3.5e-4	-2.4e-4
A	3.47e+2	2.64e+2
R^2	9.97e-1	9.97e-1
K (cm^3mol/g^2)	9.10e-2	1.90e-2
M (g/mol)	3.82e+4	1.39e+4

Refractive index, n, of DPC solutions in the presence of NaX salts

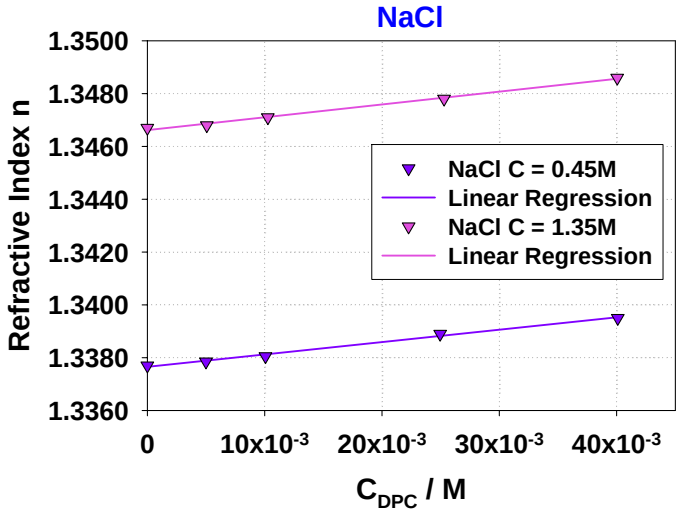

Figure 0-7. Refractive indices as a function of DPC concentration in NaCl solutions

Linear Regression (y = ax + b)	NaCl 0.45M	NaCl 1.35M
b	1.3376	1.3466
$a = \left(\frac{\partial n}{\partial C}\right)$ (1/M)	4.68e-2	4.85e-2
R^2	9.93e-1	9.94e-1

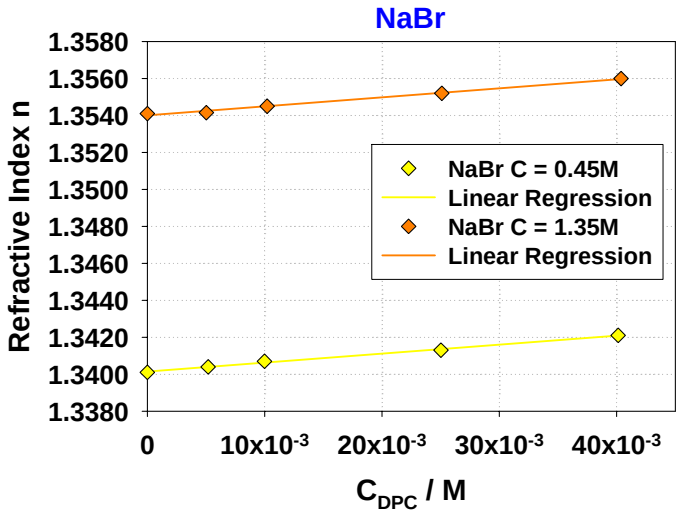

Figure 0-8. Refractive indices as a function of DPC concentration in NaBr solutions

Linear Regression (y = ax + b)	NaBr 0.45M	NaBr 1.35M
b	1.3401	1.3540
$a = \left(\frac{\partial n}{\partial C}\right)$ (1/M)	4.84e-2	4.87e-2
R^2	9.96e-1	9.92e-1

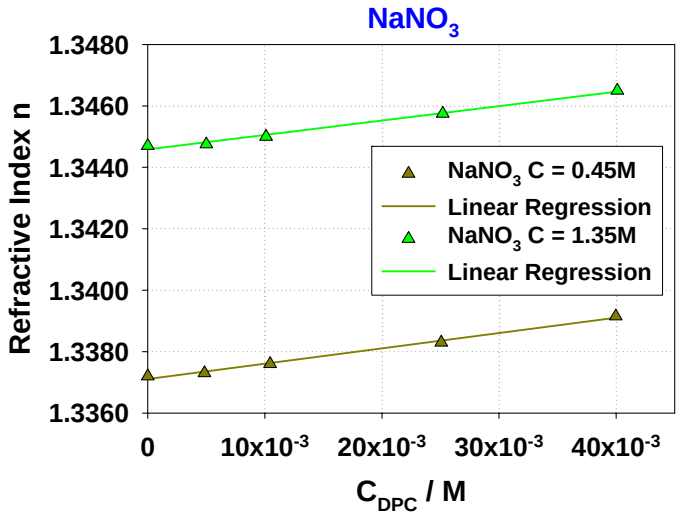

Figure 0-9. Refractive indices as a function of DPC concentration in $NaNO_3$ solutions

Linear Regression (y = ax + b)	$NaNO_3$ 0.45M	$NaNO_3$ 1.35M
b	1.3371	1.3446
$a = \left(\frac{\partial n}{\partial C}\right)$ (1/M)	4.97e-2	4.68e-2
R^2	9.93e-1	9.90e-1

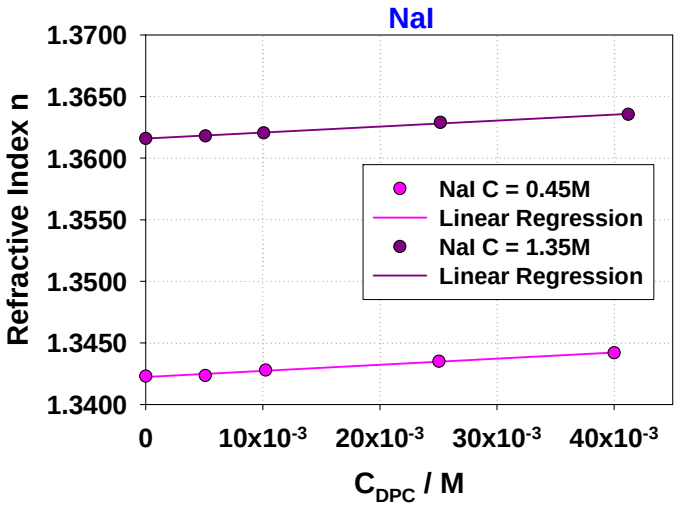

Figure 0-10. Refractive indices as a function of DPC concentration in NaI solutions

Linear Regression (y = ax + b)	NaI 0.45M	NaI 1.35M
b	1.3422	1.3616
$a = \left(\frac{\partial n}{\partial C}\right)$ (1/M)	4.95e-2	4.87e-2
R^2	9.90e-1	9.96e-1

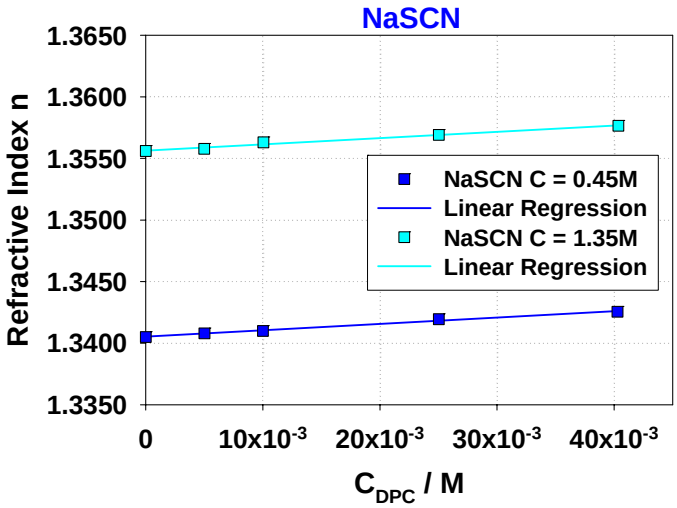

Figure 0-11. Refractive indices as a function of DPC concentration in NaSCN solutions

Linear Regression (y = ax + b)	NaSCN 0.45M	NaSCN 1.35M
b	1.3405	1.3556
$A = \left(\frac{\partial n}{\partial C}\right)$ (1/M)	5.19e-2	5.07e-2
R^2	9.92e-1	9.87e-1

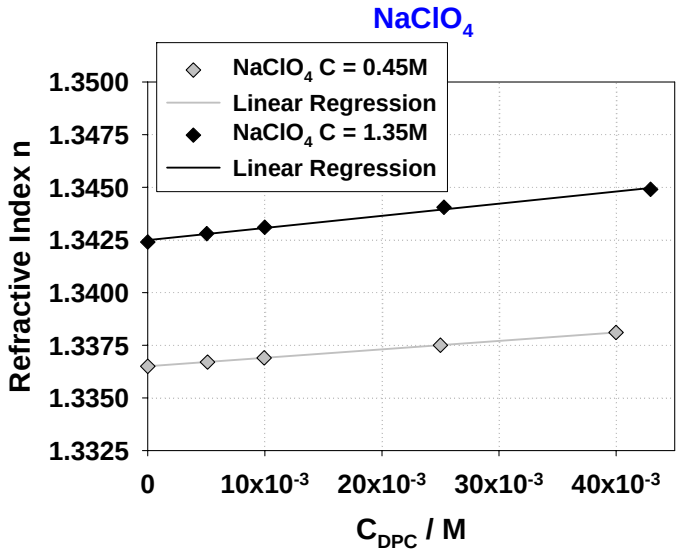

Figure 0-12. Refractive indices as a function of DPC concentration in $NaClO_4$ solutions

Linear Regression (y = ax + b)	$NaClO_4$ 0.45M	$NaClO_4$ 1.35M
B	1.3365	1.3425
$A = \left(\frac{\partial n}{\partial C}\right)$ (1/M)	4.00e-2	5.78e-2
R^2	9.99e-1	9.94e-1

Calculation of the molecular volume from density measurements

The molecular volume, V_{mol}, of a solute in a solution can be obtained by density measurements. For a solution containing n_1 molecules of the solvent (water) of molecular mass M_1 and partial molar volume V_1 and n_2 molecules of the solute (DPC) of molecular mass M_2 and partial molar volume V_2, the density is given by the following expression:

$$\rho = \frac{M_{tot}}{V_{tot}} = \frac{n_1 M_1 + n_2 M_2}{n_1 V_1 + n_2 V_2} \qquad \textbf{Equation 0-1}$$

For relatively low solute concentrations we can assume that the partial molar volume of water, V_1, is practically identical to its molar volume, V_{1m}.

The mass fraction of the solute is:

$$x = \frac{n_2 M_2}{n_1 M_1 + n_2 M_2} \qquad \textbf{Equation 0-2}$$

The density of pure water is:

$$\rho_0 = \frac{M_1}{V_{1m}} \qquad \textbf{Equation 0-3}$$

Equations III-1 to **III-3** are a system of three equations with three unknown parameters (n_1/n_2, V_1 and V_2). Combining **Equations III-1** and **III-3** we get:

$$n_1 M_1 \left(\frac{\rho}{\rho_0} - 1 \right) = n_2 \left(M_2 - \rho V_2 \right) \qquad \textbf{Equation 0-4}$$

Equation III-2 can be written also as follows:

$$n_1 M_1 x = n_2 M_2 \left(1 - x \right) \qquad \textbf{Equation 0-5}$$

One obtains from these two last relations (**Equation III-4** and **Equation III-5**):

$$V_2 = M_2 \left[\frac{1}{\rho_0} - \frac{1}{x} \left(\frac{1}{\rho_0} - \frac{1}{\rho} \right) \right] \qquad \textbf{Equation 0-6}$$

which can be rewritten in the following:

$$\frac{1}{\rho} = x \left(\frac{V_2}{M_2} - \frac{1}{\rho_0} \right) + \frac{1}{\rho_0} \qquad \textbf{Equation 0-7}$$

Equation III-7 implies that a plot of 1/ρ vs x is a straight line with slope equal to:

$$s = \frac{V_2}{M_2} - \frac{1}{\rho_0} \qquad \textbf{Equation 0-8}$$

From the slope, s, we can compute the partial molar volume of the solute, V_2, according to:

$$V_2 = M_2\left(s + \frac{1}{\rho_0}\right) \qquad \textbf{Equation 0-9}$$

REFERENCES

Afzal, S.; Tesler, W. J.; Blessing, S. K.; Collins, J. M.; Lis, L. J. "Hydration Force between Phosphatidylcholine Surfaces in Aqueous Electrolyte Solutions" *J. Col. Int. Scien.* **1983**, 97, 303.

Akutsu, H.; Seelig, J. "Interaction of Metal Ions with Phosphatidylcholine Bilayer Membranes" *Biochemistry* **1981**, 20, 7366.

Albrecht, O.; Gruler, H.; Sackmann, E. "Polymorphism of phospholipid monolayers" *J. Phys.* **1978**, 39, 301.

Altenbach, C.; Seelig, J. "Ca^{2+} Binding to Phosphatidylcholine Bilayers as studied by Deuterium Magnetic Resonance. Evidence for the formation of a Ca^{2+} complex with two phospholipid molecules" *Biochemistry* **1984**, 23, 3913.

Babu, C. S.; Lim, C. "Theory of Ionic Hydration: Insights from Molecular Dynamic Simulations and Experiment" *J. Phys. Chem. B.* **1999**, 103, 7958.

Baptista, M. S.; Politi, M. J. "Dipole oriented anion binding and exchange in zwitterionic micelles" *J. Phys. Chem.* **1991**, 95, 5936.

Bartucci, R.; Belsito, S.; Sportelli, L. "Neutral lipid bilayers interacting with chaotropic anions" *Chem. Phys. Lipids* **1996**, 79, 171.

Ben-Shaoul, A; Gelbart, W. M. "Theory of chain packing in amphiphilic aggregates" *Ann. Rev. Phys. Chem.* **1985**, 36, 179.

Berdysheva-Desert, O. "Etudes Specturales et Spectroscopique de l'interaction de polyamines naturelles et siliciees avec de couches monomoleculaires de phospholipides" **2004**, Thesis, University of Paris VI, Paris, France.

Bin, X.; Zawisza, I.; Goddard, J.D.; Lipkowski, J. "Electrochemical and PM-IRRAS Studies of the Effect of the Static Electric Field on the Structure of the DMPC Bilayer Supported at the Au (111) Electrode Surface" *Langmuir* **2004**, 21, 330.

Birdi, K. S. "Lipid and Biopolymer Monolayers at the Liquid Interfaces" 1989, Plenum Press, New York.

Blaudez, D.; Buffeteau, T.; Desbat, B.; Turlet, J. M. "Infrared and Raman spectroscopies of monolayers at the air-water interface" *Cur. Op. Col. Inter. Sci.* **1999**, 4, 265.

(a) Boström, M.; Williams, D. R. M.; Ninham, B. W. "Surface Tension of Electrolytes: Specific Ion Effects Explained by Dispersion Forces" *Langmuir* **2001**, 17, 4475. (b) Boström,

M.; Graig, V. S. J.; Albion, R.; Williams, D. R. M.; Ninham, B. W. “Hofmeister Effects in pH Measurements: Role of Added Salt and Co-Ions” *J. Phys. Chem. B* **2003**, 107, 2875.

Braslau, A.; Deitsch, M.; Pershan, P. S.; Weiss, H.; Als-Nielsen, J.; Bohr, J. “Surface Roughness of Water Measured by X-Ray Reflectivity” *Phys. Rev. Let.* **1985**, Vol. 54, No. 2, 114.

Brezesinski, G.; Scalas, E.; Struth, B.; Moehwald, H.; Bringezu, F.; Gehlert, U.; Weidemann, G.; Vollhardt, D. “Relating Lattice and Domain Structures of Monoglyceride Monolayers” *J. Phys. Chem.* **1995**, 99, 8758.

Brochsztain, S.; Filho, P. B.; Toscano, V. G.; Chaimovich, H.; Politi, M. J. “Ion binding and selectivity in zwitterionic micelles” *J. Phys. Chem.* **1990**, 94, 6781.

Brotons, G.; Dubois, M.; Belloni, L.; Grillo, I.; Narayanan, T.; Zemb, T. “The role of counterions on the elasticity of highly charged lamellar phases: A small-angle x-ray and neutron-scattering determination” *J. Chem. Phys.* **2005**, 123, 024704.

Buffeteau, T.; Desbat, B.; Turlet, J. M. “Polarization Modulation FT-IR Spectroscopy of Surfaces and Ultra-thin Films: Experimental Procedure and Quantitative Analysis” *Appl. Spec.* **1991**, Vol. 45, No. 3, 380.

Bunton, C. A.; Mhala, M. M.; Moffatt, J. R. “Nucleophilic Reactions in zwitterionic micelles of Amine Oxide or Betaine Sulfonate surfactants” *J. Phys. Chem.* **1989**, 93, 854.

Cacace, M. G.; Landau, E. M.; Ramsden, J. J. “The Hofmeister series: salt and solvent effects on interfacial phenomena” *Q. Rev. Biophys.* **1997**, 30, 241.

Camoes, M. F.; Lito, M. J. G.; Ferra, M. I. A.; Covington, A. K. “Consistency of pH standard values with the corresponding thermodynamic acid dissociation constants” *Pure Appl. Chem.* **1997**, 69, 1325.

Chaplin, M. F. “A proposal for the structuring of water” *Biophys. Chem.* **1999**, 83, 211.

(a) Chapman, D.; Williams, R. M.; Ladbrooke, B. D. “Physical studies of phospholipids. VI. Thermotropic and lyotropic mesomorphism of some 1,2-diacyl-phosphatidylcholines (lecithins)” *Chem. Phys. Lipids* **1967**, 1, 445. (b) Chapman, D.; Peel, W. E.; Kingston, B.; Lilley, T. H. “Lipid phase transitions in model biomembranes. The effect of ions on phosphatidylcholine bilayers” *Biochim. Biophys. Acta* **1977**, 464, 260.

Chaudhuri, A.; Loughlin, J. A.; Romsted, L. S.; Yao, J. “Arenediazonium salts: New probes of the interfacial compositions of association colloids. 1. Basic approach, methods, and illustrative applications” *J. Am. Chem. Soc.* **1993**, 115, 8351.

Clarke, R. J.; Lüpfert, C. “Influence of Anions and Cations on the Dipole Potential of Phosphatidylcholine Vesicles: A Basis for the Hofmeister Effect” *Biophysical J.* **1999**, 76, 2614.

(a) Collins, K. D.; Washabaugh, M. W. “The Hofmeister effect and the behaviour of water at interfaces” *Q. Rev. Biophys.* **1985**, 18, 323. (b) Collins, K. D. “Charge density-dependent strength of hydration and biological structure” *Biophys. J.* **1997**, 72, 65.

Corti, M. “Physics of Amphiphiles. Micelles, Vesicles and Microemulsions” **1983**, Chapter X, 122.

(a) Cuccovia, I. M.; N. da Silva, I.; Chaimovich, H.; “New method for estimating the degree of ionisation and counterion selectivity of cetytrimethylammonium halide micelles: Chemical trapping of free counterions by water soluble arenediazonium ion” *Langmuir* **1997**, 13, 647. (b) Cuccovia, I. M.; Romsted, L. S.; Chaimovich, H. “Determination of halide concentrations at the interface of zwitterionic micelles by chemical trapping: Influence of the orientation of the dipole and the nature of the cation” *J. Colloid Int. Sci.* **1999**, 220, 96.

(a) Cunningham, B. A.; Lis, L. J. “Thiocyanate and bromide ions influence the bilayer structural parameters of phosphatidylcholine bilayers” *Biochim. Biophys. Acta* **1986**, 861, 237. (b) Cunningham, B. A.; Lis, L. J.; Quinn, P. J. “The Influence of Monovalent Anions on Dipalmitoylphosphatidylcholine Bilayer Phase Transitions: A Time Resolved X-Ray Diffraction Study” *Mol. Cryst. Liq. Cryst.* **1986**, 141, 361. (c) Cunningham, B. A.; Lis, L. J. “Interactive Forces between Phosphatidylcholine Bilayers in Monovalent Salt Solutions” *J. Coll. Int. Scien.* **1988**, 128, 15.

Davies, J. T.; Rideal, E. K. “Interfacial Phenomena” **1963**, Academic Press, New York and London.

(a) Dluhy, R. A; Cornell, D. G. “In Situ Measurement of the Infrared Spectra of Insoluble Monolayers at the Air-Water Interface” *J. Phys. Chem.* **1985**, 89, 3195. (b) Dluhy, R. A. “Quantitative External Reflection Infrared Spectroscopy Analaysis of Insoluble Monolayers Spread at the Air-Water Interface” *J. Phys. Chem.* **1986**, 90, 1373. (c) Dluhy, R. A.; Wright, N. A.; Griffiths, P. R. “In Situ Measurements of the FT-IR Spectra of Phospholipid Monolayers at the Air/Water Interface” *App. Spect.* **1988**, Vol. 42, No. 1, 138. (d) Dluhy, R. A.; Stephens, S. M.; Widayati, S.; Williams, A. D. “Vibrational spectroscopy of biological monolayers. Applications of IR and Raman spectroscopy to biomembrane model systems at interfaces” *Spectrochimica Acta A* **1995**, 51, 1413.

Dubois, M.; Zemb, T.; Fuller, N.; Rand, R. P.; Parsegian V. A. "Equation of state of charged bilayer system: measure of the entropy of the lamellar – lamellar transtition in DDABr" *J. of Chem. Phys.* **1998**, 109, 8731.

Evans, D. F.; Wennerstrom, H. "The Colloidal Domain. Where Physics, Chemistry, Biology, and Technology Meet" **1999**, 2nd Edition, VCH Publishers, New York.

Feder, A. "Optical Studies of Monolayers at the Air/Water Interface" **1997**, Thesis, Harvard University, Cambridge, Massachusetts.

Feller, S. E.; Venable, R. M.; Pastor, R. W. "Computer Simulation of a DPPC Phospholipid Bilayer: Structural Changes as a Function of Molecular Surface Area" *Langmuir* **1977**, 13, 6555.

Franks, G. V. "Zeta Potentials and Yield Stresses of Silica Suspensions in Concentrated Monovalent Electrolytes: Isoelectric Point Shift and Additional Attraction" *J. Colloid Interface Sci.* **2002**, 249, 44.

Frisken, B. J. "Revisiting the method of cumulants for the analysis of dynamic light-scattering data" *Appl. Optics* **2001**, Vol. 40, No. 24, 4087.

Gaillon L.; Lelievre J.; Gaboriaud R. "Counterion Effects in Aqueous Solutions of Cationic Surfactants: Electromotive Force Measurements and Thermodynamic Model" *J. Colloid Int. Sci.* **1999**, 213, 287.

Gehlert, U.; Weidemann, G.; Vollhardt, D. "Morphological Features in 1-Monoglyceride Monolayers" *J. Colloid Int. Sci.* **1995**, 174, 392.

Gelbart, W. M.; Ben-Shaul, A.; Roux, D. "Micelles, Membranes, Microemulsions, and Monolayers", **1994**, Springer, New York.

Goddard, E. D.; Kao, O.; Kung, H. C. "Monolayer properties of fatty acids IV. Influence of cation at high pH" *J. Colloid Int. Sci.* **1967**, 24, 297.

Gordziel, S. A.; Flanagan, D. R.; Swarbrick, J. "Interaction of monomolecular films of biological significance with heavy metal ions and complexes at the air-water interface" *J. Colloid Int. Sci.* **1982**, 86, 178.

Grigoriev, D.; Krustev, R.; Miller, R.; Pison, U. "Effect of Monovalent Ions on the Monolayers Phase Behavior of the Charged Lipid DPPG" *J. Phys. Chem. B* **1999**, 103, 1013.

Hall, D. L.; Darke, P. L. "Activation of the herpes simplex virus type I protease" *J. Biol. Chem.* **1995**, 270, 22697.

Hallet, F. R. "Encyclopedia of Spectroscopy and Spectrometry" **2000**, Vol. 3, 2067, Academic Press, London.

Hauser, H.; Hinckley, C. C.; Krebs, J.; Levine, B. A.; Philips, M. C.; Williams, R. J. P. "The interaction of ions with phosphatidylcholine bilayers" *Biochim. Biophys. Acta* **1977**, 468, 364.

Hecht, E. "Optics" **1987**, Addison-Wesley, Reading.

Heimenz, P. C.; Rajagopalan, R. "Principles of Colloid and Surface Chemistry" **1997**, Marcel Dekker, Inc., New York.

Helm, C. A.; Laxhuber, L.; Lösche, M.; Möhwald, H. "Electrostatic interactions in phospholipid membranes I: Influence of monovalent ions" *Colloid Polym. Sci.* **1986**, 264, 46.

Hènon, S.; Meunier, J. "Microscope at the Brewster angle: Direct observation of first-order phase transitions in monolayers" *J. Rev. Sci. Instrum.* **1991**, 62, 936.

Hochachka, P. W.; Somero, G. N. "Biochemical Adaptation" Princeton, NJ: Princeton University Press, **1984**.

Hofmeister, F. "Zur Lehre von der Wirkung der Salze. II" *Arch. Exp. Pathol. Pharmakol.* **1888**, 24, 247.

Hönig, H.; Möbius, D. "Direct Visualization of Monolayers at the Air-Water Interface by Brewster Angle Microscopy" *J. Phys. Chem.* **1991**, 95, 4590.

Hribar, B.; Southall, N. T.; Vlachy, V.; Dill, K. A. "How Ions Affect the Structure of Water" *J. Am. Chem. Soc.* **2002**, 124, 12302.

Hunt, R. D.; Mitchell, M. L.; Dluhy, R. A. "The Interfacial Structrure of Phospholipid Monolayer Films: An Infrared Reflectance Study" *J. Mol. Struc.* **1989**, 214, 93.

Hunter, R. J. "Foundations of Colloid Science" **2001**, 2nd Edition, Oxford University Press, New York.

Hyde, T. S. "Identification of Lyotropic Liquid Crystalline Mesophases" **2001**, *Handbook of Applied Surface and Colloid Chemistry*, Chapter 16, John Wiley and Sons, Ltd.

Ikeda, S.; Ozeki, S.; Tsunoda, M. "Micelle Molecular Weight of Dodecyltrimethylammonium Chloride in Aqueous Solutions and the Transition of Micelle Shape in Concentrated NaCl Solutions" *J. Colloid Int. Sci.* **1980**, 73, 27.

Imae, T.; Ikeda, S. "Characteristics of rodlike micelles of cetytrimethy-ammonium chloride in aqueous NaCl solutions: their flexibility and the scaling laws in dilute and semidilute regimes" *Colloid Poly. Sci.* **1987**, 265, 1090.

Israelachvili, J., "Intermolecular and Surface Forces", **1991**, 2nd Edition, Academic Press, New York.

Jarvis, N. L.; Scheiman, M. A. "Surface potentials of aqueous electrolyte solutions" *J. Phys. Chem.* **1968**, 72, 74.

(a) Jendrasiak, G. L. “Hallide interaction with phospholipids: proton magnetic resonance studies” *Chem. Phys. Lipids* **1972**, 9, 133. (b) Jendrasiak, G. L.; Smith, R.; Ribeiro, A. A. “Chaotropic anion-phosphatidylcholine membrane interactions: an ultra high field NMR study” *Biochim. Biophys. Acta* **1993**, 1145(1), 25.

Jensen, T. R.; Balashev, K.; Bjørnholm, T.; Kjaer, K. “Novel methods for studying lipids and lipases and their mutual interaction at interfaces. Part II. Surface sensitive synchrotron X-ray scattering” *Biochimie* **2001**, 83, 399.

Johnson, C. S. Jr.; Gabriel, D. A. “Laser Light Scattering”, **1994,** Dover Classics of Science and Mathematics, New York.

Jönsson, B.; Lindmann, B. “Surfactants and Polymers in Aqueous Solution” **1998**, John Wiley and Sons, Chichester.

(a) Jungwirth, P.; Tobias, D. J. “Surface effects on aqueous ionic solvation: A molecular dynamics simulation study of NaCl at the air/water interface from infinite dilution to saturation” *J. Phys. Chem. B.* **2000**, 104, 7702. (b) Jungwirth, P.; Tobias, D. J. “ Ions at the Air/Water Interface” *J. Phys. Chem. B.* **2002**, 106, 6361.

Jyoti, A.; Prokop, A. M.; Li, J.; Vollhardt, D.; Kwok, D. Y.; Miller, R.; Möhwald, H; Neumann, A. W. “An investigation of the compression rate dependence on the surface pressure-surface area isotherm for a dipalmitoylphosphatidylcholine monolayer at the air/water interface” *Colloid and Surfaces A: Phys. Eng. Asp.* **1996**, 116, 173.

(a) Kaganer, V. M.; Peterson, I. R.; Kenn, R. M.; Shih, M. C.; Durbin, M.; Dutta, P. “Tilted Phases of fatty acid monolayers” *J. Chem. Phys.* **1995**, 102, 9412. (b) Kaganer, V. M.; Möhwald, H.; Dutta, P. “Structure and phase transitions in Langmuir monolayers” *Rev. Mod. Phys.* **1999**, Vol. 71, No. 3, 779.

Kane, S. A.; Compton, M.; Wilder, N. “Interactions Determining the Growth of Chiral Domains in Phospholipid Monolayers: Experimental Results and Comparison with Theory” *Langmuir* **2000**, 16, 8447.

Karlström, G.; Hagberg, D. “Toward an Understanding of the Hofmeister Effect: A Computer Game with Dipoles and an Ion” *J. Phys. Chem.* **2002**, 106, 11585.

Kellaway, L.; Warr. G. G.; “The effect of the head-group on selectivity counterion binding to cationic surfactants” *J. Colloid Int. Sci.* **1997**, 193, 312.

Kenn, R. M.; Böhn, C.; Bibo, A. M.; Peterson, I. R.; Möhwald, H.; Als-Nielsen, J.; Kjaer, K. “Mesophases and Crystalline Phases in Fatty Acid Monolayers” *J. Phys. Chem.* **1991**, 95, 2092.

Keiper, J.; Romsted, L. S.; Yao, J.; Soldi, V.; "Interfacial compositions of cationic and mixed non-ionic micelles by chemical trapping: a new method for characterizing the properties of amphiphilic aggregates" *Colloids and Surfaces A: Phys. Eng. Asp.* **2001**, 176, 53.

Kmetko, J.; Datta, A.; Evmenenko, G.; Dutta, P. **"**The Effects of Divalent Ions on Langmuir Monolayer and Subphase Structure: A Grazing-Incidence Diffraction and Bragg Rod Study" *J. Phys. Chem. B* **2001**, 105, 10818.

Knock, M. M.; Bain, C. D. "Effect of Counterion on Monolayers of Hexadecyltrimethylammonium Halides at the Air-Water Interface" *Langmuir* **2000**, 16, 2857.

Koppel, D. E. "Analysis of Macromolecular Polydispersity in Intensity Correlation Spectroscopy: The Method of Cumulants" *J. Chem. Phys.* **1972**, Vol. 57, No. 11, 4814.

Kölsch, P.; Motschmann, H. "A Method for Direct Determination of the Prevailing Counterion Distribution at a Charged Surface" *J. Phys. Chem. B* **2004**, 108, 18659.

Krasteva, N; Vollhardt, D.; Brezesinski, G.; Möhwald, H. "Effect of sugars and dimethyl sulfoxide on the structure and phase behaviour of DPPC monolayers" *Langmuir* **2001**, 17, 1209.

Krüger, P.; Lösche, M. "Molecular chirality and domain shapes in lipid monolayers on aqueous surfaces", *Phys. Rev. E* **2000**, Vol. 62, No. 5, 7031.

Kuzmenko, I.; Rapaport, H.; Kjaer, K.; Als-Nielsen, J.; Weissbuch, I.; Lahav, M.; Leslie, L. "Design and Characterization of Crystalline Thin Film Architectures at the Air-Liquid Interface: Simplicity to Complexity" *Chem. Rev.* **2001**, 101, 1659.

Kwok, W. M.; Shimotake, J. E.; Lis, L. J. "Effect of Ion Species on Interactive Forces between Phosphatidylcholine Bilayers" *Mol. Cryst. Liq. Cryst.* **1986**, 132, 181.

Langmuir, I.; Schaefer, V. J. "The effect of Dissolved salts on insoluble monolayers" *J. Am. Chem. Soc.* **1937**, 59, 2400.

Leikin, S.; Prasegian, V. A.; Rau, D. C.; Rand, R. P. "Hydration Forces" *Ann. Rev. Phys. Chem.* **1993**, 44, 369.

Leontidis, E. "Hofmeister anion effects on surfactant self-assembly and the formation of mesoporous solids" *Cur. Opin. Coll. Int. Sci.* **2002**, 7, 81-91.

Lewith, S. "Zur Lehre von der Wirkung ser Salze. I" *Arch. Exp. Phathol. Pharmakol.* **1888**, 24, 1.

Li, J. B.; Miller, R.; Volldardt, D.; Möhwald, H. "Spreading concentration effect on the morphology of phospholipid monolayers" *Thin Solid Films* **1998**, 327-329, 84.

Lin, Z.; Cai, J. J.; Scriven, L. E.; Davis, H. T. "Spherical-to-Wormlike Micelle Transition in CTAB Solutions" *J. Phys. Chem.* **1994**, 98, 5984.

Lipowsky, R. “Generic Interactions of Flexible Membranes”, *Handbook of Biological Physics*, **1995**, Vol.1, Chapter 11, Elsevier Science.

(a) Lis, L. J.; Parsegian, V. A.; Rand, R. P. “Binding of Divalent Cations to Dipalmiotylphosphatidylcholine Bilayers and its Effect on Bilayer Interaction” *Biochemistry*, **1981**, 20, 1761. (b) Lis, L. J.; Lis, W. T.; Parsegian, V. A.; Rand, R. P. “Adsorption of Divalent Cations to a Variety of Phosphocholine Bilayers” *Biochemistry*, **1981**, 20, 1771. (c) Lis, L. J.; McAlister, M; Fuller, N.; Rand, R. P.; Parsegian, V. A. “Interactions between neutral phospholipids bilayer membranes” *Biophysical J.* **1982**, 37, 657. Loosley-Millan, M.; Rand, R. P.; Parsegian, V. A. “Effects of Monovalent Ion Binding and Screening on Measured Electrostatic Forces between Charged Phospholipid Bilayers” *Biophys. J.* **1982**, 40, 221.

Loschilova, E.; Karvaly, B. “Laser Raman studies of molecular interactions with phosphatidylcholine multilayers. II. Effects of mono- and divalent ions on the bilayer structure” *Biochim. Biophys. Acta* **1988**, 514(2), 274.

Lösche, M.; Möhwald, H. “Electrostatic interactions in phospholipid membranes : II. Influence of divalent ions on monolayer structure” *J. Colloid Int. Sci.* **1989**, 131, 56.

Loughlin, J. A.; Romsted, L. S.; “A new method for estimating counter-ion selectivity of a cationic association colloid: Trapping of interfacial chloride and bromide counter-ions by reaction with micellar bound aryldiazonium salts” *Colloids and Surfaces* **1990**, 48, 123.

Lyklema, J. “Fundamentals of Interface and Colloid Science” **2000**, Vol. 1, Academic Press.

MacRitchie, F. “Chemistry at Interfaces” **1990**, Academic Press, San Diego.

(a) Marcus, Y. “Thermodynamics of Solvation of Ions. Part 5. Gibbs Free Energy of Hydration at 298.15 K” *J. Chem. Soc. Faraday Trans* **1991**, 87, 2995. (b) Marcus, Y. “Ion Properties” **1997**, Marcel Dekker, Inc. New York.

Marra, J. “Effects of counterion specificity on the interactions between quaternary ammonium surfactants in monolayers and bilayers” *J. Phys. Chem.* **1986**, 90, 2145.

(a) McConlogue, C. W.; Vandelrick, T. K. “A Close Look at Domain Formation in DPPC Monolayers” *Langmuir* **1997**, 13, 7158. (b) McConlogue, C. W.; Vandelrick, T. K. “Molecular Determinants of Lipid Domain Shape” *Langmuir* **1999**, 15, 234.

McDonald, P. M.; Seelig, J. “Anion binding to neutral and positively charged lipid membranes” *Biochemistry* **1988**, 27, 6769.

(a) McIntosh, T. J.; Simon, S. A. “Hydration and Steric Pressures between Phospholipid Bilayers” *Ann. Rev. Biophys. Biomol. Struct.* **1994**, 23, 27. (b) McIntosh, T. J.; Simon, S. A. “Contributions of Hydration and Steric (Entropic) Pressures to the Interactions between

Phosphatidylcholine Bilayers: Experiments with the Subgel Phase" *Biochemistry* **1993**, 32, 8374.

McLaughlin, S.; Bruder, A.; Chen, S.; Moser, C. "Chaotropic anions and the surface potential of bilayer membranes" *Biochim. Biophys. Acta* **1975**, 394, 304.

(a) Mendelson, R.; Brauner, J.W.; Gericke, A. "External Infrared Reflection Absorption Sepectrometry of Monolayer Films at the Air-Water Interface" *Ann. Rev. Phys. Chem.* **1995**, 46, 305. (b) Mendelson, R.; Moore, D. J. "Vibrational spectroscopic studies of lipid domains in biomembranes and model systems" *Chem. Phys. Lip.* **1998**, 96, 141. (c) Mendelson, R.; Flach, C. R. "Infrared Reflection-Absorption Spectrometry of Monolayer Films at the Air-Water Inteface" *Handbook of Vibrational Spectroscopy* **2002**, Vol. 2, J. Wiley and Sons.

Meyer, H. W.; Richter, W. "Freeze-Fracture studies on lipids and membranes" *Micron* **2001**, 32, 615.

(a) Michel, B. E.; Kaufmann, M. R. "Osmotic Pressure of Polyethylene Plycol 6000" *Plant Physiol.* **1973**, 51, 914. (b) Michel, B. E. "Evaluation of the water potentials of solutions of polyethylene glycol 8000 both in the absence and the presence of other solutes" *Plant. Physiol.* **1983**, 72, 66.

Miňones Jr, J.; Rodriguez Patino, J. M.; Conde, O.; Carrera, C.; Seoane, R. "The effect of polar groups on structural characteristics of phospholipid monolayers spread at the air-water interface" *Colloids and Surfaces A: Phys. Eng. Aspects* **2002**, 203, 273.

Mitchell, M. L.; Dluhy, R. A. "In Situ FT-IR Investigation of Phospholipid Monolayer Phase Transitions at the Air-Water Interface" *J. Am. Chem. Soc.* **1988**, 110, 712.

Morgan, J. D.; Napper, D. H.; Warr, G. G.; Nicol, S. K.; "Measuremnt of the selective adsorption of ions at the air/surfactant solution interfaces" *Langmuir* **1994**, 10, 797.

Morini M.A.; Schulz P.C.; Puig J.E. "Counterion specificity of the micelle surface and it's implications on micellar catalysis" *Colloid Polym Sci.* **1996**, 274, 662.

Moy, V. T.; Keller, D. J.; Gaub, H. E.; McConnell, H. M. "Long-Range Molecular Orientational Order in Monolayer Solid Domains of Phospholipid" *J. Phys. Chem.* **1986**, 90, 3198.

Nagle J. F.; Tristam – Nagle, S. "Structure of lipid bilayers" *Biochim. Biophys. Acta* **2000**, 1469, 159.

Nieto-Suarez, M.; Vila-Romeu, N.; Dynarowicz-Latka, P.; Prieto, I. "The influence of inorganic ions on the properties of nonionic Langmuir monolayers" *Colloids and Surfaces A: Phys. Eng. Asp.* **2004**, 249, 11.

(a) Ninham, B. W.; Parsegian, V. A. "Van der Waals forces. Special characteristics in lipid-water systems and a general method of calculation based on the Lifshitz theory" *Biophys. J.* **1970**, 10, 646. (b) Ninham, B. W.; Yaminsky, V. "Ion Binding and Ion Specificity: The Hofmeister Effect and Onsager and Lifshitz Theories" *Langmuir* **1997**, 13, 2097.

Onsager L.; Samaras, N. N. T. "The surface tension of Debye-Hückel electrolytes" *J. Chem. Phys.* **1934**, 2, 528.

(a) Parsegian, V. A.; Rand, R. P.; Fuller, N. L.; Rau, D. C. "Osmotic Stress for the Direct Measurement of Intermolecular Forces" *Meth. Enzym.* **1986**, 127, 400. (b) Parsegian, V. A.; Rand, R. P.; Rau, D. C. "Lessons from the Direct Measurement of Forces Between Biomolecules" *Physics of Complex and Supermolecular Fluids* **1987**, John Wiley and Sons, New York, Chichester, Brisbane, Toronto, Singapore.

Petrache, H. I.; Gouliaev, N.; Nagle-Tristram, S.; Zhang, R. ; Suter, R. M. ; Nagle, J. F. "Interbilayer interactions from high-resolution x-ray scattering" *Phys. Rev. E* **1998**, 57, 7014.

Petrov, J. G.; Brezesinski, G.; Kratseva, N.; Möhwald, H. "Langmuir Monolayers with Fluorinated Groups in the Hydrophilic Head: 2. Morphology and Molecular Structure of Trifluoroethyl Behenate and Ethyl Behenate Monolayers" *Langmuir* **2001**, 17, 4581.

Petty, M. C., "Langmuir-Blodgett films An Introduction" **1996,** Cambridge University Press.

Pryzyczyna, A.; Rózycka-Roszk, B.; Langner, M. "The Effect of Selected Anions on Dipalmitoylphosphatidylcholine Phase Transitions" *Z. Naturforsch.* **2002**, 57c, 712.

Pyper, N. C.; Pike, C. G.; Edwards, P. P. "The polarizabilities of species present in ionic solutions" *Mol. Phys.* **1992**, 76, 353.

(a) Rand, R. P.; Fuller, N.; Parsegian, V. A.; Rau, D. C. "Variation in hydration forces between neutral phospholipid bilayers: evidence for hydration attraction" *Biochemistry* **1988**, 27, 7711. (b) Rand, R. P.; Parsegian, V. A. "Hydration forces between phospholipid bilayers" *Bioch. Biophys. Acta* **1989**, 988, 351.

Rapaport, H.; Kuzmenko, I.; Berfeld, M.; Kjaer, M.; Als-Nielsen, J.; Popovitz-Biro, R.; Weissbuch, I.; Lahav, M.; Leiserowitz, L. "From Nucleation to Engineering of Crystalline Architectures at the Air-Water Interfaces" *J. Phys. Chem.* **2000**, 104, 1399.

Rappolt, M.; Pabst, G.; Amenitsch, H.; Laggner, P. "Salt-induced phase separation in the liquid crystalline phase of phosphatidylcholine" *Colloids and Surfaces A: Phys. Eng. Asp.* **2001**, 183-185, 171.

Ray, A.; Nemethy, G. "Effects of ionic protein denaturants on micelle formation by nonionic detergents" *J. Am. Chem. Soc.* **1971**, 93, 6787.

Roberts, G. "Langmuir-Blodgett Films" **1990**, Plenum Press, New York and London.

Roux, M.; Bloom, M. "Ca^{2+}, Mg^{2+}, Li^{+}, Na^{+}, K^{+}, Distributions in the Headgroup Region of Binary Membranes of Phosphatidylcholine as seen by Deuterium NMR" *Biochemistry* **1990**, 29, 7077.

Rydall J. R.; McDonald, P. M. "Investigation of anion binding to neutral lipid membranes using ^{2}H NMR" *Biochemistry* **1992**, 31, 1092.

(a) Sachs, J. N.; Woolf, T. B. "Understanding the Hofmeister Effect in Interactions between Chaotropic Anions and Lipid Bilayers: Molecular Dynamics Simulations" *J. Am. Chem. Soc.* **2003**, 125, 8742. (b) Sachs, J. N.; Nanda, H.; Petrache, H. I.; Woolf, T. B. "Changes in Phosphatidylcholine Headgroup Tilt and Water Order Induced by Monovalent Salts: Molecular Dynamics Simulations" *Biophys. J.* **2004**, 86, 3772.

Sanderson, P. W.; Lis, L. J.; Quinn, P. J.; Williams, W. P. "The Hofmeister effect in relation to membrane lipid phase stability" *Biochim. Biophys. Acta* **1991**, 1067, 43.

Santos, N. C.; Castanho, A. R. B. "Teaching Light Scattering Spectroscopy: The Dimension and Shape of Tobacco Mosaic Virus" *Biophysical J.* **1996**, 71, 1641.

Scarpa, M. V.; Maximiano, F. A.; Chaimovich, H.; Cuccovia, I. M. "Interfacial Concentrations of Chloride and Bromide and Selectivity for Ion Exchange in Vesicles Prepared with Dioctadecyldimethylammonium Halides, Lipids, and Their Mixtures" *Langmuir* **2002**, 18, 8817.

Schott, H.; Royce, A. E.; Han, S. K. "Effect of inorganic additives on solutions of non-ionic surfactant VII. Cloud point shift values of individual ions" *J. Colloid Int. Sci.* **1984**, 98,196.

Seddon, J. M.; Templer, R. H. "Polymorphism of Lipid-Water Systems" **1995**, *Handbook of Biological Physics*, Vol. 1, Chapter 3, Elsevier Science B.V.

Shah, D. O.; Schulman, J. H. "Binding of metal ions to monolayers of lecithins, plasmalogen, cardiolipin, and dicetyl phosphate" *J. Lipid. Res.* **1965**, 6, 341.

Siegel, S.; Vollhardt, D.; Cadenhead, D.A. "Effect of the hydroxy group position on the monolayer characteristics of hydroxypalmitic acids" *Colloids and Surfaces A: Physicochem. Eng. Aspects* **2005**, 256, 9.

Simon, S. A.; Lis, L. J.; Kauffmann, J. W.; Macdonald, R. C. "A calorimetric and monolayer investigation of the influence of ions on the thermodynamic properties of phosphatidylcholine" *Biochim. Biophys. Acta* **1975**, 375, 317.

Szleifer, I; Ben-Saul, A.; Gelbart, W. M. "Statistical thermodynamics of molecular organization in mixed micelles and bilayers" *J. Chem. Phys.* **1987**, 86, 7094.

Tadmor, R. "The London-van der Waals interaction energy between objects of various geometries" *J. Phys. Cond. Matter* **2001**, 13, L195.

(a) Tatulian, S. A. "Effect of lipid phase transition on the binding of anions to dimyristoylphosphatidylcholine liposomes" *Biochim. Biophys. Acta* **1983**, 736, 189. (b) Tatulian, S. A.; Gordeliy, V. I.; Sokolova, A. E.; Syrykh, A. G. "A neutron diffraction study of the influence of ions on phospholipid membrane interactions" *Biochim. Biophys. Acta* **1991**, 1070(1), 143.

Teppner, R.; Haage, K.; Wantke, D.; Motschmann, H. "On the Internal Structure of an Adsorption Layer of an Ionic Soluble Surfactant. The Buildup of a Stern Layer Monitored by Optical Means" *J. Phys. Chem. B* **2000**, 104, 11489.

Thalody, B. P.; Warr, G. G.; "The selective binding of benzoate and hydroxybenzoate ions at cationic surfactant solution/air interfaces" *J. Colloid Int. Sci.* **1995**, 175, 297.

Ulman, A. "An Introduction to Ultrathin Organic Films: From Langmuir-Blodgett to Self Assemblie" **1991** Academic Press.

(a) Vollhardt, D. "Morphology and Phase behavior of monolayers" *Adv. Coll. Int. Sci.* **1996**, 64, 143. (b) Vollhardt, D. "Morphology of Monolayers at the Air-Water Interface" in *Encyclopedia of Surface and Colloid Science* Editor Hubbard, A., Marcel Dekker, New York **2002**, 3585. (c) Vollhardt, D. "Supramolecular organisation in monolayers at the air/water interface" *Materials Science and Engineering C 22* **2002**, 121.

(a) Weidemann, G.; Gehlert, U.; Vollhardt, D. "Inner Structure of Condensed Phase Domains in Monolayers at the Air-Water Interface" *Langmuir* **1995**, 11, 864. (b) Weidemann, G.; Vollhardt, D. "Long Range Tilt Orientational Order in Phospholipid Monolayers: A Comparison of the Order in the Condensed Phases of Dimyristoyl-Phosphatidylethanolamine and Dipalmitoyl-Phospahtidylcholine" *Colloids Surf. A* **1995**, 100, 187. (c) Weidemann, G.; Vollhardt, D. "Long-range tilt orientational order in phospholipid monolayers: a comparative study" *Biophys. J.* **1996**, 70, 2758. (d) Weidemann, G.; Brezesinksi, G.; Vollhardt, D.; Möhwald, H. "Disorder in Langmuir Monolayers. 1. Disorder Packing of Alkyl Chains" *Langmuir* **1998**, 14, 6485.

Weissenborn, P. K.; Pugh, R. J. "Surface Tension of Aqueous Solutions of Electrolytes: Relationship with Ion Hydration, Oxygen Solubility, and Bubble Coalescence" *J. Colloid Interface Sci.* **1996**, 184, 550.

Werkman, P. J.; Schouten, A. J. "Morphological Changes of Monolayers of Two Polymerizable Pyridine Amphiphiles upon Complexation with Cu(II) Ions at the Air-Water Interface" *Langmuir* **1998**, 157.

Wright, E. M.; Diamond, J. M. "Anion selectivity in biological systems" *Physiol. Rev.* **1977**, 57, 109.

Wu, F.; Gericke, A.; Flach, C. R.; Mealy, T. R.; Seaton. B. A.; Mendelsohn, R. "Domain Structure and Molecular Conformation in Annexin V/1,2-Dimyristoyl-sn-Glycero-e-Phospate/Ca^{2+} Aqueous Monolayers: A Brewster Angle Microscopy/ Infrared Reflection-Absorption Spectroscopy Study" *Biophysical J.* **1998**, 74, 3273.

Yamaouchi, A.; Matsubara, A.; Kimuzuka, H.; Abood, L. A. "Differential effect of sodium and potassium on calcium adsorption to stearic acid monolayers" *Biochim. Biophys. Acta* **1968**, 150, 181.

Zemb, T.; Belloni, L.; Dubois, M.; Aroti, A.; Leontidis, E. "Can we use area per surfactant as a quantitative test model of specific ion effects?" *Cur. Op. Col. Int. Sci.* **2004**, 9, 74.

Zhang, L.; Somasundaran, P.; Maltesh, C. "Electrolyte effects on the surface tension and micellization of n-Dodecyl β-D-Maltoside solutions" *Langmuir* **1996**, 12, 2371.